Measured and Calculated Structures of a Multi-Layer Altocumulus Cloud

by

Stefan N. Tulich

Department of Atmospheric Science
Colorado State University
Fort Collins, Colorado

Colorado State University

Department of Atmospheric Science

Paper No. 647

ABSTRACT

MEASURED AND CALCULATED STRUCTURES
OF A MULTI-LAYER ALTOCUMULUS CLOUD

Phase 1 of the Complex Layered Cloud Experiment (CLEX) took place during June 1996 in the central Great Plains of the United States. Its primary purpose was to obtain both in-situ and remotely sensed measurements of middle and upper level non-precipitating layered clouds. On June 25, 1996, as a part of CLEX-1, an in-situ aircraft measurement experiment was performed within a complex and dissipating multi-layered altocumulus cloud system. At the start of the experiment (16:30 -17:00 UTC), the cloud system was observed to consist of two separate layers. The upper layer was stratiform in appearance with its top at roughly 5800 m; the lower layer was cumuliform in appearance with its base at roughly 5125 m. In certain regions of the cloud system, cumuliform cloud elements from the lower layer appeared to be rising into the stratiform layer. Aircraft measurements of both cloud layers were obtained during a number of straight and level flight legs. At the end of the experiment (17:30 -18:00 UTC), the cloud system was observed to consist solely of the upper stratiform layer; the cumuliform layer was no longer apparent. The top and base of the stratiform layer were measured to be at roughly 6000 and 5830 m. Aircraft measurements of the cloud system and its environment were obtained during a spiral sounding profile.

In this research, the aircraft measurements and a radiative transfer model were used to examine the liquid phase microphysical, thermodynamic, kinematic and radiative structures of the multi-layered altocumulus cloud system observed at the start and end of the experiment. Our results can be summarized as follows. The structures of the cloud system at the start of the experiment are similar to those observed in the boundary-layer cloud type: cumulus rising into stratocumulus. Microphysical measurements show that the cumulus layer was composed of horizontally separated liquid water cloud elements while the stratiform layer was composed of an almost continuous distribution. Thermodynamic measurements indicate that the

MEASURED AND CALCULATED STRUCTURES OF A MULTI-LAYER ALTOCUMULUS CLOUD

by

Stefan Tulich

Department of Atmospheric Science

Spring 1998

stratiform layer was situated below a dry and absolutely stable layer of air, while the cumuliform layer was situated in a moist and conditionally unstable layer. Vertical velocity measurements suggest that, within the cumuliform layer, regions of rising motion were relatively intense and narrow while regions of sinking motion were weak but broad. Near the top of the stratiform layer, regions of intense rising and sinking motion were observed. Solar and thermal radiative transfer calculations indicate that the cloud system was being radiatively destabilized.

The structures of cloud system at the end of the experiment are similar to those observed in the boundary layer cloud type: stratocumulus. Microphysical measurements indicate that the cloud layer was composed of horizontally separated cloud elements, in which, cloud droplet sizes and the liquid water content increased with height. Thermodynamic measurements indicate that that the cloud layer was positioned at the base of dry and relatively deep absolutely stable layer of air. Evidence of cloud-top entrainment is found. Solar and thermal radiative transfer calculations suggest that the cloud layer was undergoing intense radiative destabilization.

Based on the similarities in structures, we conclude that dynamic processes which occur in the previously mentioned boundary layer cloud types also occurred in the observed altocumulus cloud system. However, because the observed cloud system was not coupled to a well mixed surface-based marine layer, it did not have a constant supply of moisture to maintain itself against those processes which generally act to dry out layered clouds. This might explain the dissipation of the cloud system.

ACKNOWLEDGEMENTS

This research was funded by the Center for Geosciences, Phase II at CIRA/CSU under Department of Defense grant #DAAH04-94-G-0420 and by NASA grant #NAG5-3449.

TABLE OF CONTENTS

LIST OF TABLES

LIST OF FIGURES

LIST OF SYMBOLS

Symbol		
N_i	-	FSSP measured number concentration of cloud droplets in in size channel i
ρ_w	-	density of water
d_i	-	FSSP measured diameter of cloud droplet in size channel i
Δd_i	-	width of size channel i
d_e	-	effective diameter
r_e	-	effective radius
θ_v	-	virtual potential temperature
θ	-	potential temperature
r_v	-	water vapor mixing ratio
r_l	-	liquid water mixing ratio
r_i	-	ice water mixing ratio
B	-	buoyancy force
g	-	acceleration due to gravity
$\theta_{v\ parcel}$	-	virtual potential temperature of an air parcel
$\theta_{v\ environment}$	-	virtual potential temperature of the environment
γ -	-	environmental lapse rate of virtual potential temperature
Γ_s	-	saturated adiabatic lapse rate of virtual potential temperature
Γ_d	-	dry adiabatic lapse rate of virtual potential temperature
$\vec{u}$	-	velocity of air with respect to rotating Earth
$\vec{u}_p$	-	velocity of aircraft with respect to rotating earth
$\vec{u}_a$	-	velocity of air with respect to aircraft
R_i	-	Richardson number

S	-	vertical wind shear
J_l	-	lth associate Legendre coefficients
P_l	-	lth normalized associate Legendre polynomials
μ	-	cosine of the zenith angle
N_μ	-	number of Gaussian quadrature angles (discrete ordinates)
s_k	-	height of vertical grid point k
μ_j	-	cosine of Gaussian quadrature angle (discrete ordinat)
L	-	order of spherical harmonic expansion
I	-	radiance
σ_{ext}	-	extinction due to scattering and absorption
ω_j	-	normalized Gauss-Legendre quadrature weights
ϖ_0	-	single scatter albedo
χ_l	-	lth Legendre coefficient of the scattering phase function
$P(\mu)$	-	scattering phase function
S_l	-	lth Legendre coefficient of the solar pseudo-source and/or thermal source
$B[T]$	-	Planck blackbody radiance for temperature T
F_0	-	Downwelling solar flux on horizontal plane
μ_0	-	cosine of the solar zenith angle
τ_s	-	optical path from height s to the upper domain boundary along the solar direction
F^+	-	upwelling hemispheric flux on horizontal plane
F^-	-	downwelling hemispheric flux on horizontal plane
F_{net}	-	net hemispheric flux
$\bar{I}$	-	angular mean radiance
r	-	radius of a cloud droplet
$n(r)$	-	normalized modified gamma distribution
G	-	cross sectional area of particles

v_e	-	effective radius variance
σ_e^s	-	extinction cross section
x	-	size parameter
g	-	asymmetry parameter
o	-	arbitrary optical property
$E(\lambda)$	-	distribution of solar or thermal energy within a spectral band
P_{HG}	-	Henyey-Greenstein phase function
ode	-	extinction optical depth
oda	-	absorption depth due
σ	-	standard deviation

LIST OF ACRONYMS

Acronym		
2D-C	-	two dimensional optical particle probe
Ac	-	Altocumulus
ARM	-	Atmospheric Radiation Measurements Program
cloud layer 1	-	cloud layer used in sensitivity study
cloud layer 2	-	cloud layer used in sensitivity study
cloud layer 3	-	cloud layer used in sensitivity study
cloud layer A	-	lower cumuliform cloud layer visually observed in southern portion of the J25acs between 16:30 and 17:05 UTC
cloud layer B	-	upper stratiform cloud layer visually observed in both southern and northern portion of the J25acs between 16:30 and 17:20 UTC
cloud layer C	-	lower cumuliform cloud layer observed in northern portion of the J25acs between 17:05 and 17:20 UTC
cloud layer D	-	stratiform cloud layer visually observed in the northern portion of the J25acs between 17:40 and 18:10 UTC
CART	-	Cloud and Atmospheric Radiation Testbed
CLEX	-	Complex Layered Cloud Experiment
CKDFU	-	Correlated k-Distribution Method of Fu et al. (1991)
data group A	-	set of aircraft measurements collected during level flight legs A_u and A_l
data group B	-	set of aircraft measurements collected during level flight legs B_u, B1, and B2
data group C	-	set of aircraft measurements collected during level flight legs C_u and C_l
data group D	-	set of aircraft measurements collected during S1 profile
data group M	-	set of aircraft measurements collected during level flight leg M
flight leg A_l	-	lower level flight leg through cloud layer A

flight leg A_u	-	upper level flight leg through cloud layer A
flight leg B_u	-	upper level flight leg through cloud layer B
flight leg B1	-	first lower level flight leg through cloud layer B
flight leg B2	-	second lower level flight leg through cloud layer B
flight leg C_l	-	lower level flight leg through cloud layer C
flight leg C_u	-	upper level flight leg through cloud layer C
flight leg L0-L12	-	set of level flight legs used to measure J25acs
flight leg P0-P7	-	set of profile flight legs used to measure J25acs
flight leg S1	-	spiral sounding flight leg used to measure J25acs and its environment
FSSP	-	Forward Scattering Spectrometer Probe
GOES	-	Geostationary Operational Environmental Satellite
IBTM	-	infrared brightness temperature map
J25 experiment	-	June 25, 1996 aircraft measurement experiment
J25acs	-	June 25, 1996 complex multi-layered altocumulus cloud system
LES	-	Large-scale Eddy Simulation model
MIEAVG	-	Mie Band Averaging optical property code
NCAR	-	National Center for Atmospheric Research
NCAR RAF	-	NCAR Research Aircraft Facility
SGP	-	Southern Great Plains Site
SHACC	-	Spherical Harmonic Accuracy
SHDOM	-	Spherical Harmonic Discrete Ordinate Method
SOLACC	-	Solution Accuracy
SSM/I	-	Special Sensor Microwave Imager
SSM/T	-	Special Sensor Microwave Temperature
UTC	-	Coordinated Universal Time
UWRAF	-	University of Wyoming Research Aircraft Facility

CHAPTER I

INTRODUCTION

Altocumulus (Ac) clouds form in layers at middle levels of the atmosphere, and together with altostratus clouds, cover approximately 22 % of the Earth's surface (Heymsfield et al 1991; Warren 1986, 1988). They modify the flows of both incoming solar and outgoing thermal radiation, and thus, the distribution of diabatic heating within the atmosphere. Because atmospheric circulations are primarily driven by this distribution , Ac clouds play a role in determining both the Earth's climate and regional weather patterns. Hence, to predict either weather or climate, requires that they be realistically represented within numerical weather prediction and global climate models. However, Tiedke (1993) states that "the lack of knowledge of cloud processes" is a fundamental limitation thwarting the parameterization of all cloud types. Because of the limited number of in-situ observational studies within Ac clouds, the physical processes which are important for their formation, maintenance, and dissipation are perhaps the least well understood. In this research, we attempted to increase our knowledge of physical processes which occur in Ac clouds layers by performing an in-situ observational study of a cloud observed during the phase 1 Complex Layered Cloud Experiment, CLEX-1.

The Complex Layered Cloud Experiment was initiated to obtain a new observational dataset within extensive middle and upper level layered non-precipitating clouds. Its primary scientific objectives were to increase our understanding of the morphology and physical processes which occur in these cloud types. The phase 1 experiment took place between June 21-29, 1996 and focused on the central Great Plains of the Continental United States between 34-43 N and 95-104 W (Fig. 1.1). The observational strategy was to measure middle and upper level layered clouds using in-situ and passive and active remote sensing measurement platforms. The main remote sensing platforms were the NASA/JPL DC-8 94 GHz airborne cloud radar, the SSM-I microwave imager, and the SSM/T microwave sounder. The main in-situ

platform was the University of Wyoming King Air (N2Uw) airborne meteorological measurement system. A variety of ground based radiation measurements and atmospheric sounding measurements were taken at the U.S. Southern Great Plains Arm-Cart site. ASOS and SAO data, NWS Rawinsonde and CLEX sonde measurements, NCEP and ECMW analyses were also collected. During the experiment, a number of middle and upper level layered clouds were measured. In this research, we focused on an Ac cloud measured in-situ by the N2Uw on June 25, 1996.

On June 25, 1996 between 16:30 and 18:10 UTC, an in-situ aircraft measurement experiment was performed within a complex and dissipating multi-layered altocumulus cloud system over Emporia, Kansas. We will refer to the experiment and the complex cloud system as the J25 experiment and the J25acs, respectively. Figs 1.1 and 1.2 show the location of the experiment and a GOES-8 0.7 μm satellite image focused on the J25acs at the start of the experiment. A summary of the experiment is given below.

Between 16:30 and 17:05, aircraft measurements were obtained during five straight and level flight legs positioned in the southern portions of the J25acs. The location of these flight legs is indicated in Fig. 1.2. During this time period, the J25acs was observed to be roughly 900 km ^{2} in horizontal extent and to consist of two separate layers. The upper layer was stratiform in appearance and the lower layer was cumuliform in appearance. Some of the lower layer cumuli appeared to be merged with or rising into the upper stratiform layer. The top of the stratiform layer was observed to be smooth and to consist of mounded elements. Two straight and level flight legs were executed in the base and middle portions of the cumuliform cloud layer. Three straight and level flight legs were executed in the top and middle portions of the stratiform cloud layer. The headings and lengths of the flight legs through the cumuliform cloud layer were different than those in the stratiform layer.

Between 17:10 and 17:20, aircraft measurements were obtained during three level flight legs in the northern portions of the J25acs. Fig. 1.3 shows a GOES-8 0.7 μm satellite image focused on the J25acs at 17:15 UTC. The horizontal extent of the J25acs at this time was estimated to be roughly 400 km^2. The region of aircraft sampling is indicated by the small white box. In this region, the cloud system was observed to possess the same multi-layered cloud structure as observed previously. However, the two layers were separated by a cloud free layer of air and the base of the cumuliform layer was lower than that

previously observed. A level flight leg was made in the clear layer of air separating the two layers and two straight and level flight legs were executed in the top and middle portions of the cumuliform cloud layer..

Between roughly 17:30 and 18:00, aircraft measurements of the J25acs and its environment were obtained during a spiral sounding profile. Fig. 1.4 shows a GOES-8 0.7 μm satellite image focused on the J25acs at 17:45 UTC. The approximate location of the aircraft spiral sounding is indicated by the smaller white box. The J25acs, at this time, was estimated to be roughly 25 km^2. During the spiral sounding, the lower cumuliform layer was no longer apparent and the upper stratiform cloud layer appeared to consist of smoothed and cellular cloud elements.

Objectives of this Research

The primary objectives of this research were to use aircraft measurements collected during the J25 experiment and a radiative transfer model to examine the microphysical (liquid phase), thermodynamic, kinematic and radiative structures of the J25acs. The obstacles which confronted this research were as follows:

1) The aircraft measurements represented a limited sample of observations within a complex and dissipating multiple layered cloud system.
2) The aircraft measurements were not obtained in a systematic fashion.

To overcome these obstacles, we first broke down the set of aircraft measurements into groups. Within each group, measurements were obtained in a systematic fashion and the observed cloud structure was similar over the time period in which they were obtained. The measurements in these groups were analyzed separately. The relationships between each group of measurements were examined to infer the spatial and temporal trends in the structure of the J25acs.

Hypothesis

The visual appearance of the J25acs observed between 16:30-17:00 UTC was similar to that of the boundary-layer cloud type, cumulus rising into stratocumulus. The visual appearance of the J25acs observed between 17:30 and 18:00 UTC was similar to that of stratocumulus. Based on these similarities,

we hypothesized that the measured microphysical, thermodynamic, kinematic, and simulated radiative structures of the J25acs for both time periods would also be similar.

Summary of Results

We found the measured and simulated structures of the J25acs observed between 16:30 and 17:00 UTC to be both similar to and different from those observed in cumulus rising into stratocumulus. The similarities can be summarized as follows. The liquid phase microphysical measurements show a transition from a broken structure in the cumuliform layer to an almost continuos distribution of cloud elements in the stratiform layer. Thermodynamic measurements indicate that the cumuliform layered cloud was positioned in a moist and conditionally unstable layer of air while the stratiform layered cloud was positioned in a moist and absolutely stable layer of air. Kinematic measurements indicate that, in the cumuliform layer, regions of rising motion were relatively intense and narrow while regions of sinking motion were broad and weak. In the upper portions of the stratiform layer, regions of both intense sinking and rising motion were observed. Radiative transfer simulations suggest that the system was undergoing radiative destabilization. Owing to its elevated nature, we find two important difference between the structures of the J25acs observed between 16:30-17:00 UTC cloud and cumulus rising into stratocumulus: 1) the J25acs was not coupled to a well-mixed surface-based marine boundary layer and 2) was composed of liquid water droplets and ice crystals .

We found the measured and simulated structures of the J25acs observed between 17:30 and 18:00 UTC to be both similar to and different from those of stratocumulus clouds. The similarities can be summarized as follows. Microphysical measurements indicate that that the cloud layer was composed of cellular cloud elements, and, in these elements, liquid water contents increased towards cloud top. Thermodynamic measurements indicate that the cloud layer was situated at the base of a relatively deep and dry absolutely stable layer of air and above a shallow moist adiabatic layer of air. Evidence of cloud-top entrainment is found in both the thermodynamic and kinematic measurements. Radiative transfer simulations indicate that the cloud layer was being radiatively destabilized. An important difference

between the J25acs (observed between 17:30 and 18:00 UTC) and stratocumulus, is that the J25acs was not coupled to a well-mixed surface-based marine boundary layer.

Outline of Thesis

The outline of this thesis is as follows. In Chapter II, the definition and a summary of results from previous observational studies of altocumulus clouds are given. Chapter III consists of an overview of the J25 experiment; large-scale meteorological observations are presented and a detailed description of the J25 experiment is given. In the experiment description, the relative position of the aircraft measurements in the J25acs and the observed cloud structure are both identified. In Chapter IV, we describe the aircraft instrumentation, the methodology for aircraft measurement analysis, and the methodology used to examine the radiative structure of the J25acs. In Chapter V, aircraft measurements and results from radiative transfer calculations in the J25acs are presented and are used to examine its microphysical, thermodynamic, kinematic, and radiative structures at the separate time periods of the experiment. In Chapter VI, we summarize the main results of this research and also draw conclusions from these results. Possible areas of future research are discussed.

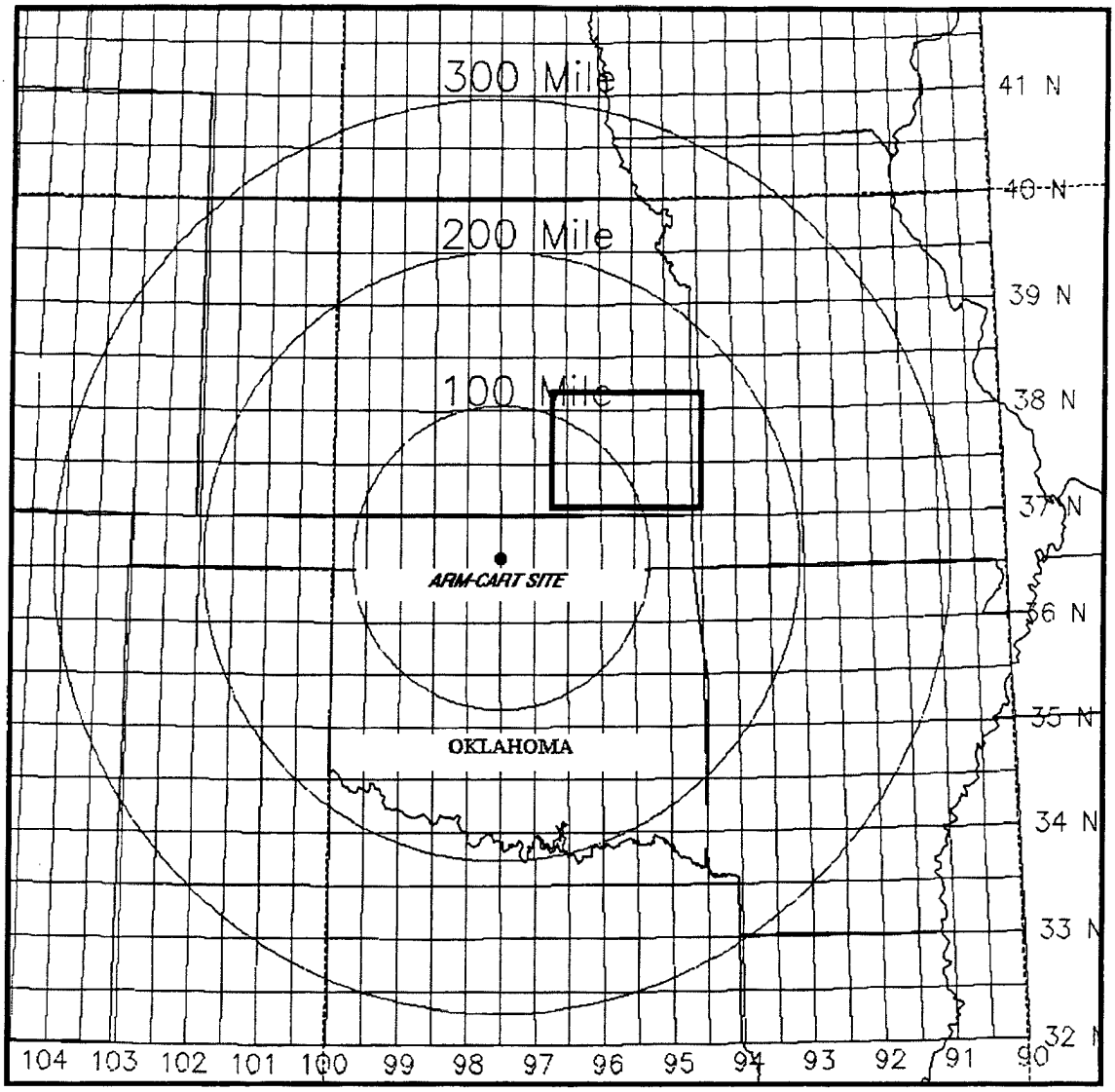

Fig. 1.1 Map of Clex region of focus. Box within Kansas identifies the June 25 experiment region.

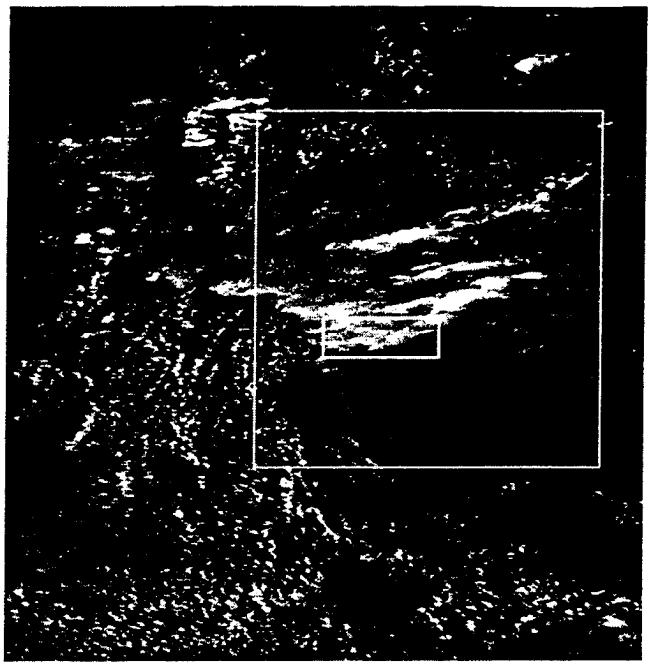

Fig. 1.2 16:31 UTC Goes 8 0.7 μm image of the J25acs. Large box encloses J25acs. Small box identifies southern portion of the J25acs where level flight legs were performed between 16:30 and 17:05 UTC as a part of the J25 experiment.

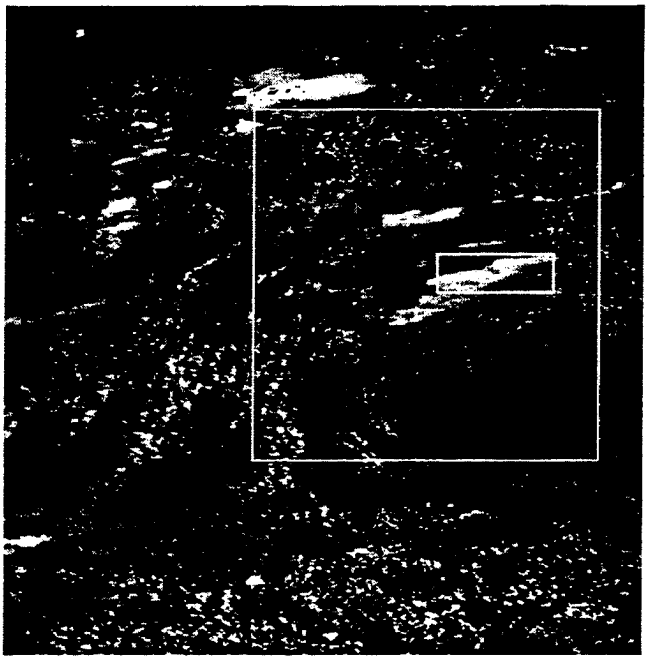

Fig. 1.3 17:15 UTC Goes 8 0.7 μm image of the J25acs. Large box encloses J25acs. Small box identifies northern portion of the J25acs where level flight legs were performed between 17:05 and 17:20 UTC as a part of the J25 experiment.

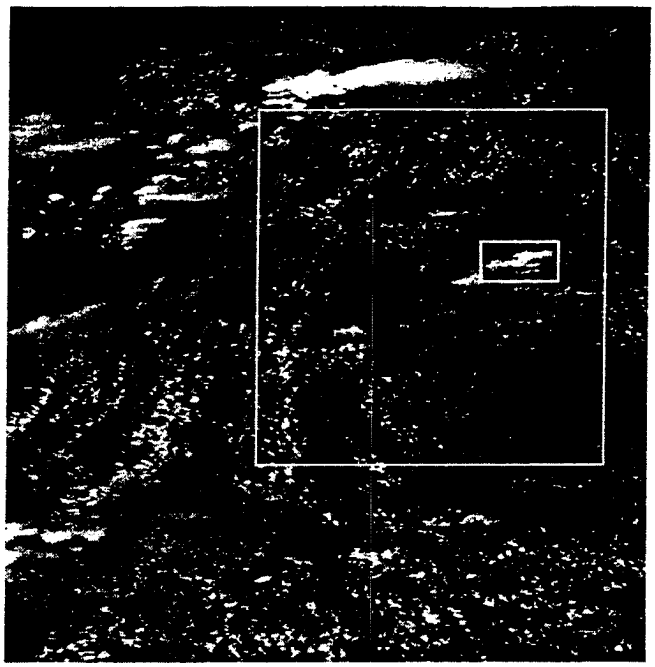

Fig. 1.4 17:45 UTC Goes 8 0.7 μm image of the J25acs. Large box encloses J25acs. Small box identifies portion of the J25acs where spiral sounding was performed between 17:40 and 18:10 UTC as a part of the J25 experiment.

CHAPTER II

BACKGROUND

Introduction

There have been a handful of in-situ observational studies within Ac clouds. In this chapter, we summarize the results from these studies. Through this summary, we attempt to identify our current understanding of Ac cloud microphysical properties and the cloud-scale dynamical processes found to be important for their development, maintenance, and dissipation. This serves to identify the context of our research. We use the results from these studies, where possible, to aid the interpretation of aircraft measurements and radiative transfer calculations presented in Chapter V. We begin this chapter by providing the definition and known formation mechanisms of Ac clouds.

2.1 Altocumulus Clouds: Their Definition and Formation Mechanisms

Altocumulus clouds are defined in terms of their visual appearance by the World Meteorological Organization as a

> White or grey, or both white and grey, patchy, sheet, or layer of cloud generally with shading, composed of laminae, rounded masses, rolls, etc. which are sometimes partly fibrous or diffuse and which may or may not be merged. Most of the regularly arranged small elements usually have an apparent width of between one and five degrees. (WMO 1956 p. 19)

They are further divided into four species: Ac statiformis, lenticularis, castellanus, and floccus (WMO 1956). Their possible formation mechanisms have been discussed by Gedzelman (1988) and Heymsfield et al. (1991). Together they identify the following four mechanisms:

1) "Humid air uplifting from and moving ahead of a lower level humidity source in a sheared environment, often in frontal situations"(Heymsfield 1991);
2) "Moist air expelled from spreading and decaying convective towers and anvils of cumulonimbus" (Heymsfield 1991);
3) "Humid air condensed in the crests of mountain waves" (Heymsfield 1991); and
4) Radiative cooling at the top of thick layers of moist maritime tropical air (Gedzelman 1988).

We see that the presence of moisture at middle levels is critical for the formation of Ac clouds. In the first and second mechanisms, the means by which moisture is transported to these levels is identified. The fourth mechanism indicates that radiative processes alone can lead to the formation of Ac clouds.

2.2 Aircraft Observational Studies

There have been two types of aircraft observational studies within Ac clouds. In the first type of study, measurements within a large number of different cloud layers are analyzed to identify the statistical properties of their microphysical structure. These studies are useful in that they provide an understanding of what sorts of conditions we should expect to see in Ac clouds. In the second type of study, aircraft measurements within an individual cloud layer are analyzed to determine the microphysical, kinematic, and dynamic structure of that layer. These are useful in that they provide an understanding of the dynamical processes which lead to the observed cloud structure. The first type of study has been performed by Borovikov (1961), Lewis (1951), and Hobbs (1985). The second type of study has been performed by Heymsfield et al. (1991). In the following paragraphs, we provide a brief description of each investigator's study and identify their significant results. We give special attention to the second type of study because it matches our study.

Borovikov et al. (1961) analyze measurements from more than 500 flights though altocumulus clouds in the USSR. Their analysis considers the cloud microstructure as a function of temperature and

season. Their results were summarized by Feigel'son (1964 and 1973). Borovikov et al. (1961) find that altocumulus clouds are primarily composed of liquid water. 81.5 % of a total of 508 observed altocumulus clouds are measured to contain only liquid water while 15.9 % are measured to consist of both liquid water and ice. The average liquid water content of altocumulus clouds is observed to depend on both season and cloud temperature. The average liquid water contents for summer and winter are 0.24 g m^{-3} and 0.16 g m^{-3}, respectively. The average liquid water content is 0.21 g $m^{-3}$for cloud temperatures between -5° C and 0° C and decreases to 0.12 g m^{-3} for cloud temperatures between -25° C and -20° C. Borovikov et al. (1961) report the mean vertical extent of altocumulus clouds to be roughly 300 m and the mean radius of cloud droplets to be between 4.5 and 5.0 μm.

Lewis (1951) analyze measurements from 246 flights through Ac and As clouds over the US. He focuses on the relationship between the geographic location of the cloud and the cloud microstructure. His results are summarized by Hobbs (1986). Lewis reports the average liquid water content to range between 0.01 and 0.41 g m^{-3}, with a median value of 0.1 g m^{-3}. He finds the mean moments of the drop size distribution within Ac and As clouds to depend on their geographic location. The reported average droplet diameter and number concentration for 112 clouds measured in the Pacific coast region are 9.4 μm and 35 cm^{-3}, respectively. The reported average droplet diameter and number concentration for 128 clouds measured in other regions of the US are 7.1 μm and 75 cm^{-3}.

Hobbs and Rango (1985) analyze in situ microphysical measurements of 31 Ac clouds sampled over the northwestern US. In their analysis, they focus on the relationship between the droplet size distribution and the presence of ice crystals within clouds. They find, for cloud top temperatures between -6.0° and -32.0° C, a strong relationship between the width of the droplet size distribution at cloud top and the maximum ice particle concentrations. Based on this relationship, they postulate that cloud droplets in Ac clouds with cloud top temperatures less than -6° C, which grow to sizes of ~20 μm in diameter and are exposed to dry air, freeze due to contact nucleation. Because the growth of these newly formed frozen cloud droplets is more favorable to that of the remaining super-cooled cloud droplets (because the supersaturation with respect ice is lower that that for water for temperatures below 0 ° C), they grow by vapor deposition at the expense of the droplets (this is referred to as the Bergeron Fendieson process and is

discussed by Cotton (1989)). As the ice crystals grow and deplete the liquid water, they reach sizes where their gravitational fall speeds are significant and then precipitate out of the cloud. This can lead to a rapid dissipation of the cloud and is referred to as glaciation.

Heymsfield et. al. (1991) analyze the microphysical, thermodynamic, and radiative structure of two Ac clouds measured by the NCAR King Air research aircraft during FIRE. The first Ac cloud layer was sampled near Green Bay, Wisconsin on October 28, 1986, while the second was sampled on October 25, 1985 over Wausau Wisconsin. The vertical extent of the Oct. 28 cloud was 100 m while the vertical extent of the Oct. 25 cloud was 400 m. The thermodynamic structure of each layer is as follows. The Oct. 28 cloud is characterized by neutral or absolute stability, while the Oct. 25 cloud is present within a conditionally unstable layer. Temperature inversions are present both above and below the Oct. 25 cloud. The relative humidity decreases substantially above both cloud layers. In-cloud temperatures near the tops of both clouds are measured to be slightly colder than out-of-cloud temperatures.

Heymsfield et al. (1991) describe the horizontal structure of each layer as cellular and find that both contain liquid and ice particles. They report ice water contents to be relatively low and number concentrations to be generally less than 0.1 L^{-1}. Figs 2.1a-d show vertical profiles of the cloud droplet number concentration, mean droplet diameter, LWC, and water vapor and total (water vapor + liquid) water mixing ratio measured during a vertical descent through the Oct. 25 layer. They attribute fluctuations in each profile to be a result of the aircraft penetrating horizontally separate cloud elements. Figs 2.1a-d show that the LWC, and mean cloud droplet size to increase with height and reach a maximum value at cloud top while the cloud droplet number concentration is a maximum at cloud base and rapidly decreases above that level. The total water and water vapor mixing ratio both decrease with height.

Heymsfield at al. (1991) simulate the measured microphysical structure of each cloud layer using a one dimensional cloud droplet growth model based on diffusion droplet growth theory and modified to include the effects of dry air entrainment. Their model considers an initial distribution of cloud condensation nuclei within a moist adiabatically ascending parcel. The effects of dry air entrainment by the parcel are parameterized by reducing the available amount of water vapor for condensation. The CCN distribution is assumed equal to previously observed distributions. The vertical velocity of the parcel is

assumed constant and is set equal to the maximum updraft speed measured in cloud (0.75 m s^{-1}). The results from their simulations in the Oct. 25 cloud are shown in Figs. 2.1 a-c. Based on their results, they conclude that droplet growth is relatively insensitive to the initial distribution of CCN but is sensitive to the specified vertical velocity of the parcel and the amount of dry-air entrainment. They conclude that the effect of entrainment is to modulate the upward increase in liquid water content so that it is below saturated adiabatic values.

Heymsfield et al. (1991) use both aircraft microphysical measurements and a radiative transfer model to examine the solar and thermal radiative structures of each cloud layer. In their calculations, they neglect the effects of the ice phase microphysics. Figs. 2.2a and b show results of heating rate calculations for each cloud layer. The Oct. 25 cloud layer shows net warming at cloud base and net cooling at cloud top while the Oct. 28 cloud layer shows net cooling throughout its depth. They conclude that the overall effect of the absorption of solar radiation is to reduce the net cloud-layer cooling. In the case of the Oct. 25 cloud, the reduction is by 40 % and the overall net cooling rate of the layer is 0.15 C hr^{-1}.

Based on their simulations of the radiative structures and the entrainment process, Heymsfield et al. (1991) develop an idealized conceptual model (adjusted to agree with aircraft measurements) to identify the effects of each on the dynamic structure of the Oct. 25 cloud. Their model considers a parcel of air which is advected along an idealized path through the cloud. Along this path, they calculate the effects of radiation and entertainment on the buoyancy of the parcel. Based on results from their model, they argue that radiative cooling and

> its resulting negative parcel buoyancy is presumably the major driving mechanism for downdraft motion in the cloud. In the situation modeled here, entrainment acts to partially counter the radiatively driven convective instability by warming the cloudy parcel and reducing the parcel LWC, both of which are positive buoyancy factors. [Heymsfield et al. (1990)]

From the above result, Heymsfield et al. (1991) conclude that the Ac clouds which they observed are similar both structurally and dynamically to stratocumulus clouds.

Summary

In this chapter, previous observational studies within Ac clouds were discussed. The results from these studies indicate what type of liquid phase microphysical properties we should expect to see in the J25acs. They also indicate that a number of different dynamical processes are important for determining the evolution and maintenance of Ac clouds. We summarize these processes with the aid of a schematic diagram shown in Fig. 2.3 We consider this diagram to summarize our current understanding of Ac clouds. In the next chapter, we describe the aircraft experiment and cloud system which were the focus of this research.

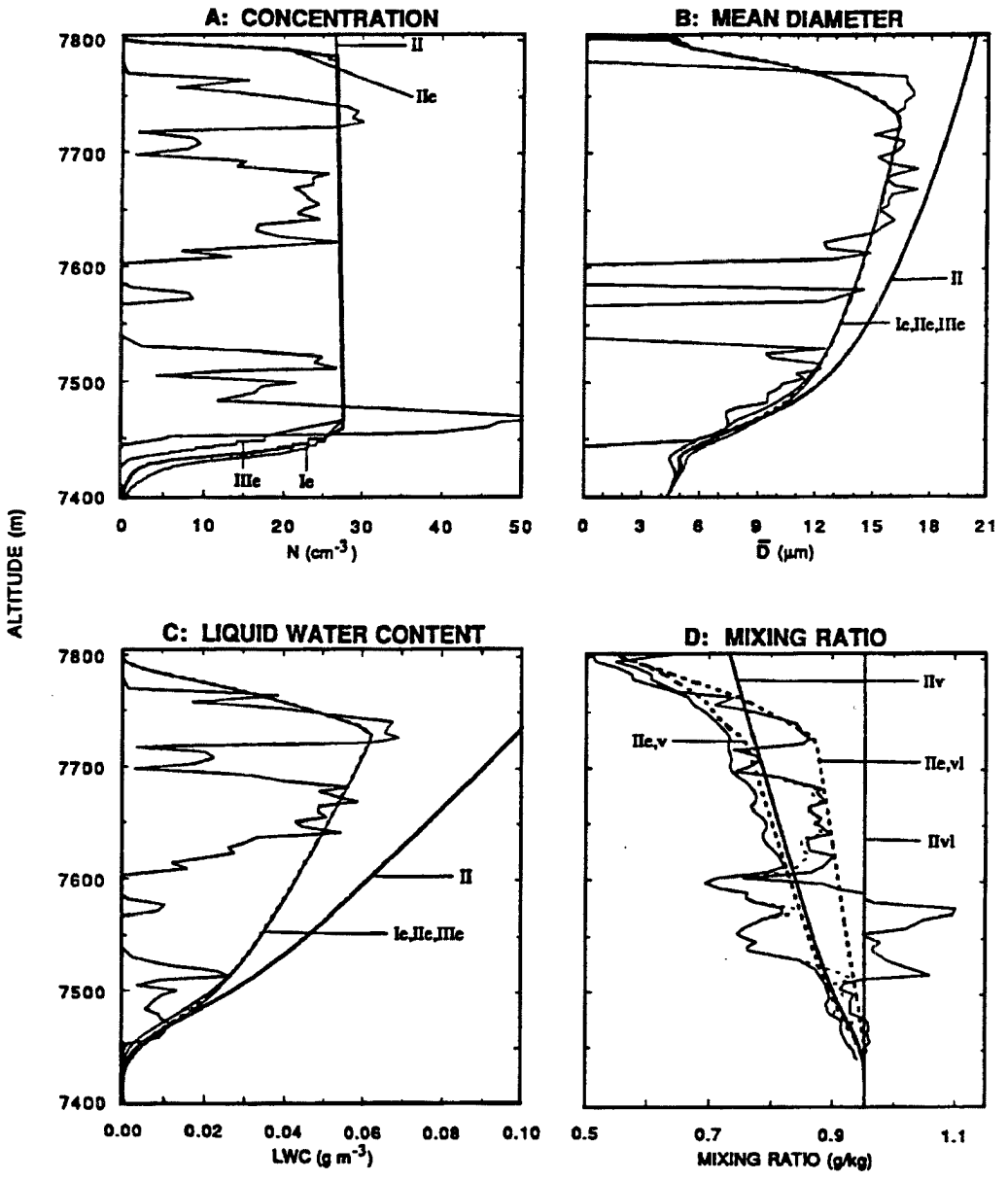

Fig. 2.1 Comparison of microphysical measurements as in Fig. 8 (not shown) with model results, for the 25 October Case. Roman numerals correspond to the CCN spectra defined in Table 1 (not shown), where an appended "e" indicates entrainment was considered. The notation "v" indicates vapor mixing ratio and "vl" indicates vapor plus mixing ratio. [Taken from Heymsfield et al. (1990)]

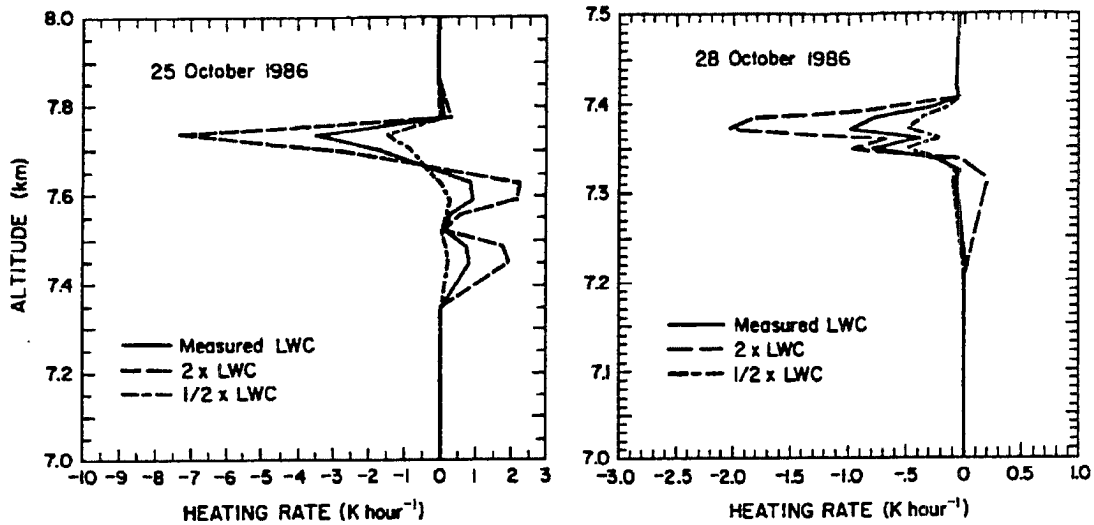

Fig. 2.2 Net radiative heating rates calculated from the radiation schemes for 25 October (left) and 28 October (right using the flux profiles shown in Fig. 13 (not shown). Heating rates are shown for observed liquid water contents and for half and twice these values. [Taken from Heymsfield et al. (1990)]

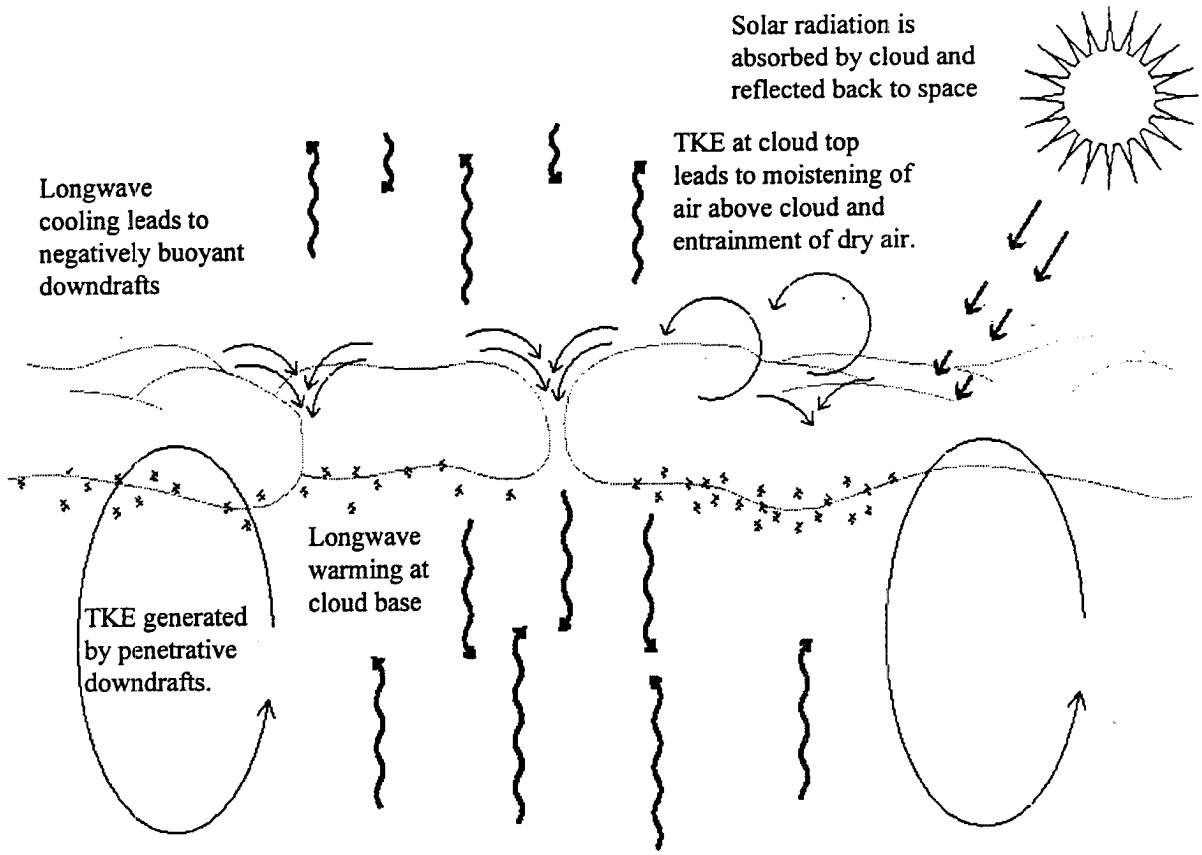

Fig. 2.3 Schematic diagram of physical processes which occur in altocumulus cloud layers.

CHAPTER III

THE JUNE 25 EXPERIMENT AND THE J25ACS

Introduction

A brief overview of the J25 experiment was provided in Chapter I. This chapter contains a more detailed description of the experiment. Meteorological observations made roughly 6 hours prior to the experiment are first presented. The meteorological observations serve to identify the prevailing meteorological conditions in which the J25acs developed and also indicate what the meteorological conditions may have been like during the J25 experiment. Next, a description of the J25 experiment for the time periods: 16:30 - 17:00 UTC, 17:00 - 17:30 UTC, and 17:30 - 18:00 UTC, is given. The observed cloud structure, the method used to obtain measurements, and relationships between the measurements and the observed cloud structure for each time period are identified. The material presented in this chapter is important for the interpretation of the aircraft measurements presented in chapter V and also motivate our methodology of aircraft data analysis described in chapter IV.

3.1 Meteorological Setting

In this section, we present large-scale meteorological observations for time period between 06:35 and 12:35 UTC June 25, 1996. These observations serve to identify the meteorological conditions in which the J25acs formed. Since the J25 experiment took place roughly seven hours subsequent to these observations, they also provide some indication as to what the meteorological conditions were like during the experiment. Appendix A presents and discusses a sequence GOES-8 10.7 μm satellite observations made of the J25acs and experiment region for the time period: 10:15 and 18:15 UTC. These satellite observations indicate how the meteorological conditions may have changed between 12:35 UTC and 16:30 UTC. They also show that the J25acs formed over central KS between 11:15 and 12:15 UTC and then moved eastward and northward into the J25 experiment region. Therefore, our focus here is mainly on

meteorological observations within or near the state of KS. Also, special attention is given to those vertical levels at which the J25acs formed.

500 mb Height and Surface Analysis (NMC)

The 12:00 UTC June 25, 1996 500 mb NMC analyzed height field and surface map are shown in Figs. 3.1a and b, respectively. The 500 mb height field shows a deep upper-level trough just off the west coast of the US, and a ridge over the central plain states. The ridge axis runs through KS. The jet stream is well to the north of KS, which is consistent with the relatively light winds over the state. The fluctuations in the 5880 m contour and the low pressure center over central OK both suggest the presence of weak trough within the CLEX region. This is supported by the wind field which indicates cyclonic rotation over KS and OK (winds are from the northwest over western KS and are from the southwest over eastern MS).

The surface map shows a stationary frontal boundary running from WNW to ESE through Kansas and Nebraska and an area of low pressure centered on the OK panhandle. The air south of the frontal boundary within KS and OK is relatively moist and is generally moving from the SE to the NE while the air north of the frontal boundary is relatively dry and is moving from the ENE to the WSW. Since air is moving parallel to the frontal boundary within KS, it is concluded that the air at the surface was not experiencing any forced frontal ascent at this time.

Radar Summaries

The 06:35 UTC, 10:35 UTC and 12:35 UTC NMC radar summaries are shown in Figs. 3.2a, b, and c respectively. The 06:35 UTC summary shows radar echoes on the northern, southern, and western borders of KS. The echo tops are between 40,700 ft and 43,900 ft for those on the KS, OK border. The heights of these tops suggest that deep penetrative convection was occurring in this region and at this time. The 10:35 and 12:35 UTC summaries show an extensive echo region on the western borders of KS and OK. The echo tops for this regions range between 41000 ft and 44000 ft. The echo region on the southern border of Kansas is no longer apparent. Therefore, we conclude that between 06:35 and 12:35 UTC, the

area of deep convection within northern OK dissipated and new convection formed on the western border of KS.

Upper Air Soundings

The NWS 12:00 UTC upper air soundings for Dodge City and Topeka, KS are shown in Figs. 3.3a and b. Both of these soundings indicate the presence of moisture at middle levels. The Topeka sounding identifies a thin layer of saturated air at 600 mb sandwiched between relatively deep layers of drier air. The temperature profile shows that air above this moist layer was relatively stable as compared to air below this layer. A quasi-temperature-inversion is indicated between roughly 490 and 476 mb.

The Dodge City sounding identifies the presence of two moist layers at 460 and 600 mb. Since the dew-point depressions within each layer are less than 2° C, clouds may have been present at each of these levels. Each layer is sandwiched between dry air, and above them, the air is relatively stable as compared to that below.

Isentropic Height Fields.

The 12:00 UTC June 25 316, 318, 320, and 322 K potential temperature height fields with superimposed wind vectors and relative humidity contours are shown in Figs. 3.3 and 3.4. These potential temperatures match those measured within and just below the J25acs during the experiment. The 316 K surface was measured just below the cloud system, while the 318 K, 320 K, and 322 K, surfaces were measured near the base, middle, and upper levels of the system, respectively. The maps were produced using a Barnes analysis applied to the 12:00 UTC upper data.

Within central and eastern KS, the wind vectors on both the 316 and 318 K maps show a light southerly to southwesterly flow. The relative humidities on the 316 K map within central KS are between 55 and 65 %, while on the 318 K map values are between 48 and 55 %. Both maps show that air was relatively moist to the south of KS. The heights of both the 316 and 318 K surface increase to the NW across KS. The height of the 316 K surface increases from roughly 3800 to 4600 m, while the height of the 318 K surface increases from roughly 4400 to 5100 m.

Within central and eastern KS, the wind vectors on both 320 and 322 K maps show a light westerly flow and the relative humidities are around 40 %. The relative humidity contours on the 322 K map show the relative humidity to decrease across the state of KS from 50 % in the southwestern corner to 30 % in the northwestern corner. The heights of both the 320 and 322 K surface increase to the north across KS. The height of the 320 K surface increases roughly 5100 to 5400 m while the height of the 322 K surface increases from 5700 to 6000 m.

Discussion of the Meteorological Setting

The synoptic meteorological conditions within and near KS have been presented using both synoptic and radar data collected 6 hours prior to the experiment. A summary of the conditions are as follows:

- Deep penetrative convection was present on the western and southern border of KS.
- A large scale upper level ridge was positioned over KS while a stationary frontal boundary was running northwest to southeast through the state.
- The 318 - 322 K flow within central KS was relatively light; the winds veered with height; and the air was relatively dry.
- At middle levels over both Dodge City KS and Topeka KS, shallow layers of moist air were sandwiched between deeper layers of dry air and the static stability of the air above each moist layer was larger than the static stability of the air below each moist layer.

These were the prevailing conditions in which the J25acs formed. Since upper-air observations were not made during the time period of the experiment, it was not possible to identify the large-scale meteorological conditions for that time. Therefore, the conditions just described are the best indication as to what the conditions were like during the time period of the experiment.

3.2 The June 25 Experiment Description

In this section, we provide a description of the J25 experiment for the time periods 16:00 -17:00 UTC, 17:00 -17:30 UTC, and 17:30 - 18:00 UTC. A more detailed description may be found in Appendix B. For each time period, we identify 1) the measurement strategy of the aircraft (how the measurements

were taken), 2) the observed cloud structure (what the cloud looked like), and 3) the position of the aircraft within the J25ac system (where the measurements were taken relative to the observed cloud structure). The relationships among these three pieces of information must be established to allow for interpretation of the aircraft measurements in chapter V and also motivate our methodology for data analysis. Given the importance of these three pieces of information, we developed a system to identify each as simply and as clearly as possible. In the following paragraphs, we describe our system.

Measurement Strategy

The aircraft made use of level and profile flight legs to obtain measurements within the J25acs and its environment. During level flight legs, the aircraft was at constant altitude. During profile flight legs, it was changing altitude. Thirteen separate level flight legs were executed. They are referred to as level flight legs L0-L12. Nine separate profile flight legs were executed. They are referred to as profile flight legs P0-P7 and profile flight leg S1. Table 3.1 contains a summary of the heading, length, altitude, and time period of each flight leg. The level flight legs were of two types : 1) constant heading and 2) changing heading. The profile flight legs P0-P7 were all at a constant heading. The S1 profile flight leg was a spiral sounding flight leg. In the experiment description presented here, we discuss the locations of those flight legs (L1, L2, L4, L7, L9, L10, L11, L12, and S1) used to analyze the structure of the J25acs. In the detailed experiment description contained in Appendix B, the location of each level flight leg is identified.

Cloud Structure

We identify the cloud structure with the aid of schematic cloud diagrams and GOES-8 0.7 μm and 10.7 μm satellite imagery. The schematic cloud diagrams are horizontal cross sections through the J25acs. They show both the observed horizontal and vertical cloud structure and were constructed from a synthesis of our visual observations made during the experiment and of an in-flight video recording of the experiment. The in-flight video was recorded by either a downward-looking or forward-looking camera mounted on the aircraft. Observations made of the in-flight video are presented in Appendix C. The

reader may want to refer to these observations for a more in depth explanations of how the cloud system appeared during each portion of the experiment.

We used GOES-8 10.7 μm brightness temperature maps (IBTM) of the J25acs to identify the horizontal shape and extent of the system. The IBTMs were created using the standard NOAA calibration technique and an IDL contouring algorithm applied to the raw GOES-8 McIDAS image. Within each map, the region enclosed by the 265 K contour was used to identify the horizontal extent and shape of the J25ac system. We chose the 265 K contour because of the correspondence between the location of aircraft flight legs and this contour. Each of the flight legs which were visually identified to be in cloud was also found to be contained within the region enclosed by the 265 K contour. We used GOES-8 0.7 μm images of the J25ac system to identify the horizontal cloud structure. The resolution of the GOES-8 0.7 μm satellite image is 1 km. Thus, cloud structures on these scales were identified.

Position of the aircraft within the J25ac system

We identified the position of the aircraft within the J25acs for each time period by superimposing flight tracks on each GOES-8 IBTM and by indicating the aircraft position within each schematic cloud diagram. The first method showed the horizontal location and orientation of each flight track within the J25acs while the second method shows the relative vertical position of the flight track within the system.

Experiment Description

16:30 -17:00 UTC

Between 16:30 and 17:00 UTC, the J25acs was observed to consist of two separate cloud layers and was sampled during four straight and level flight legs (flight legs L1, L2, L4, and L7). These legs were positioned in the southern portions of the system. The horizontal extent of the cloud system (estimated using GOES-8 satellite data) was between 600 and 900 km^2. The upper layer (cloud layer B) was more stratiform in appearance while the lower layer (cloud layer A) was more cumuliform in appearance. Some of the cumuliform cloud elements of layer A appeared to be rising into layer B. The top of cloud layer B was observed to be smooth and to consist of mounded elements with horizontal dimensions between 100

and 500 m. Cloud layer A was sampled during level flight legs L1 and L2 which were positioned near the base and upper portions of the layer, respectively. Cloud layer B was sampled during straight and level flight legs L4 and L7 which were positioned near the top and middle portions of the layer. Fig. 3.6 is a schematic diagram which shows the observed cloud structure and the relative position of each level flight leg within this structure. We emphasize that the level flight legs were not vertically collocated, were of different lengths, and were made at different headings.

Fig. 3.7a contains the 16:31 UTC GOES-8 10.7 μm IBTM. The location of level flight legs L1 and L2 are indicated by the straight lines. Both flight legs are shown to be in the southern portions of the system and on the boundary of a quasi-circular region with brightness temperatures of 260 K. Based on the 265 K contour, the system is estimated to be greater than 900 km^2 in extent and is complex in shape. The northern and western edges of the system are more ragged while its southern and eastern edges are more uniform. The visible image for this time period, Fig. 3.7b, shows that on the largest scale the J25acs was broken and was composed of cloud patches. The southern and eastern boundaries of the system are sharply outlined. The northwestern portion of the system appears more diffuse and tenuous. Within the southern region of the system, where flight legs L1 and L2 are located, the cloud texture indicates cellularity.

Fig. 3.8a contains the 16:45 UTC GOES-8 10.7 μm IBTM. The location of level flight legs L4 and L7 are indicated by the straight lines. Notice that they were made at different headings than level flight legs L1 and L2. The horizontal shape and extent of the J25acs are different from those of the 16:31 UTC image. The 265 K contour now encloses three distinct regions. The largest of these regions extends from points 0 and 40 in the eastward coordinate and points 12 and 30 in the northward coordinate and is estimated to be 600 km^2 in horizontal extent. Level flight legs L4 and L7 are both contained within this region. The 16:45 UTC visible image, Fig. 3.8b, shows that, on its southwestern boundary, the system is less sharply defined and is darker than within the 16:31 UTC image. The texture of the system within the region where flight leg L4 and L7 are positioned suggests a cellular cloud structure and does not appear much different from the previous image.

17:00 - 17:30 UTC

Between 17:00 and 17:30 UTC, the J25acs was observed to consist of two separate layers and was sampled during straight and level flight legs L9, L11, and L12 and turning level flight leg L10. Flight legs L10, L11, and L12 were executed in the northern portions of the system. In this region, the upper cloud layer (cloud layer B) appeared stratiform and the lower cloud layer (cloud layer C) appeared cumuliform. In certain regions, the two cloud layers were clearly separated by a cloud free layer of air. Cloud layer B was sampled during straight and level flight leg, L9, which was positioned in the lower portions of the layer. Cloud layer C was sampled during two straight and level flight legs, L11 and L12, which were positioned near the top and middle portions of the layer. The clear layer of air separating cloud layers B and C was sampled during level flight leg L10.

Fig. 3.9 is a schematic cloud diagram which shows the observed cloud structure and the relative positions of the level flight legs within the observed cloud structure. While level flight legs L1 and L12 were both positioned at the same vertical level, 5125 m, a comparison of Figs. 3.7 and 3.9 shows that the observed structure of the cumuliform cloud layer was different. In particular, the bases of cloud layer C are lower than those of cloud layer A. This was clearly evident in the downward looking video which showed cloud elements below the aircraft during level flight leg L12.

Fig. 3.10a is the 17:15 UTC IBTM with the location of level flight legs L9,L10, L11 and L12 also plotted. Notice that level flight leg L9 is positioned in the southern portions of the system and in the same general location as flight leg L7. Flight legs L10, L11 and L12 are positioned in the northern portions of the system. Based on the 265 K contour, the system is estimated to be roughly 300 km^2 in horizontal extent. Thus, the system decreased in horizontal extent between 16:45 and 17:15 UTC. A comparison between Figs. 3.8a and 3.10a also shows that that the shape of the system (shape of the 265 K contour) changed between 16:45 and 17:15 UTC and that the system moved slightly east and north of its previous position. The system is obviously more narrow in the northwest-southeast direction. The change in shape can be attributed to an increase in brightness temperatures in the region of the system north and west of the location of level flight legs L7 and L9.

The 17:15 UTC GOES-8 0.7 μm image , Fig. 3.10b, shows the system to be brighter in its northern portions relative to its southern portions. A comparison of this image with the 16:31 UTC 0.7μm image shows that cloud elements dissipated to the west and north of the region where flight legs L7 and L9 were positioned while the cloud texture in this region was nearly the same. Thus, those regions of the J25acs sampled by the aircraft remained fairly constant in cloud structure while other regions were rapidly dissipating. This is consistent with our visual observations made of the upper cloud layer during the time period including flight legs L7 and L9.

17:30 - 18:00 UTC

Between 17:30 and 18:00 UTC, the aircraft sampled the cloud layer during and its environment during the S1 spiral sounding profile. The J25acs was observed to consist solely of a stratiform cloud layer (cloud layer D). A lower cumuliform layer was not observed. The rate of descent and radius of the spiral sounding were roughly 5 m s^{-1} and 5.8 km. Top down observations made of the J25acs during the spiral sounding identified the cloud layer D to consist of closely spaced cellular cloud elements with horizontal dimensions between 100 and 500 m. As the aircraft passed through cloud layer D, several of these cloud elements were encountered. Figs. 3.11 and 3.12 show the observed cloud structure and the location of the aircraft within this structure.

Figs. 3.13a and b show the 17:45 UTC GOES-8 10.7 μm IBTM and 0.7 μm image of the system. The location of the S1 profile is also shown in Fig. 3.13a. Based on the 265 K contour, the system is estimated to be 25 km^2 in size and is both smaller and different in shape than in the 17:15 UTC GOES-8 10.7 μm IBTM.

Results of the Experiment Description

Schematic diagrams, GOES-8 0.7 μm images, and GOES-8 10.7 μm IBTMs were used to identify the horizontal shape, extent, and appearance of the J25acs for three separate time periods of the experiment. Taken together, these figures and diagrams characterized the J25acs for the entire experiment. A summary of the characterization is as follows. The J25acs dissipated during the experiment and

consisted of either one or two separate cloud layers. The upper layer (cloud layers B or D) was stratiform in appearance and its top was smooth and consisted of mounded elements. The lower layer (cloud layers A or C) was cumuliform and broken in appearance. The vertical cloud structure of the J25acs was different in its southern and northern portions. In its southern portion, some of the cloud elements of layer A appeared to be merged with cloud layer B. The base of cloud layer A and the top of cloud layer B were observed to be at roughly 5125 and 5800 m, respectively . In its northern portion and in certain regions, cloud layers B and C were clearly separated by a layer of cloud free air. The base of the cloud layer C was not measured but was visually identified to be lower than that of cloud layer A. The GOES-8 0.7 μm visual texture of the J25acs was similar in both the southern and northern portions and indicated a cellular cloud structure at scales greater than 1 km The dissipation of the J25acs was such that the southern portion disappeared faster than the northern portion

The location of flight legs on the schematic diagrams and on the GOES-8 IBTMs showed how the measurements were taken and also showed the relationship between the measurements and the observed cloud structure. A summary of the results of these figures is as follows. All of the straight and level flight legs were executed within the 265 K contour. Level flight legs L4, L7, and L9 were executed at two levels, were positioned in the same location of the J25acs, and were along the same or opposite headings. Level flight leg L4 was positioned near the tops of the cloud layer B while level flight legs L7 and L9 were positioned in its lower portions. Level flight legs L1 and L2 were executed at two levels, were along the same heading, and were in different locations of cloud layer A. Level flight leg L1 was in the base of the layer while level flight leg L2 was in the middle portions of the layer. Flight leg L10 was a turning flight leg positioned in a clear layer of air separating cloud layers B and C. Level flight legs L11 and L12 were made at two levels, were made along the same heading, and were in different horizontal locations of cloud layer C. The S1 profile was made between 368 and 914 mb, and sampled the cloud layer both vertically and horizontally.

Discussion of the Experiment

Based on the results of the experiment description, two facts become apparent. First, the J25 experiment was made in a complex and evolving cloud system. Second, the methods used to collect

measurements in this system were not systematic and are only representative of conditions in limited regions and at certain time periods within the evolution of a large and complex evolving cloud system. These facts ultimately dictated how aircraft measurements were analyzed and used to determine the radiative structure of the J25acs. These methods are described in the next chapter. Briefly, we chose to analyze the measurements in groups defined do that the methods used to obtain them were systematic and the cloud appearance was uniform. The purpose of the experiment description was to identify the relationship between measurements collected during the experiment and the observed cloud structure. These relationships are important for the interpretation of measurements and simulations presented in Chapter V.

Summary and Conclusions

In this chapter, large scale meteorological observations and a description of the J25 experiment were presented. The meteorological observations characterized the meteorological conditions for the J25acs and its environment for time periods prior to and during the experiment. The experiment description identified the context of the measurements within the J25acs and also characterized the J25acs for separate time periods during the experiment. The meteorological observations indicate that the J25acs formed in weak south westerly flow, south and east of a stationary frontal boundary, and east of regions of deep penetrative convection. The air at middle tropospheric levels within KS was shown to be partly moist and partly dry air. In the J25 experiment description, the observed structure of the J25acs, the methods used to collect the measurements, and the relative position of the measurements within the J25acs were identified for separate time periods of the experiment. The experiment description served to characterize the J25acs for the time period of the experiment.

a)

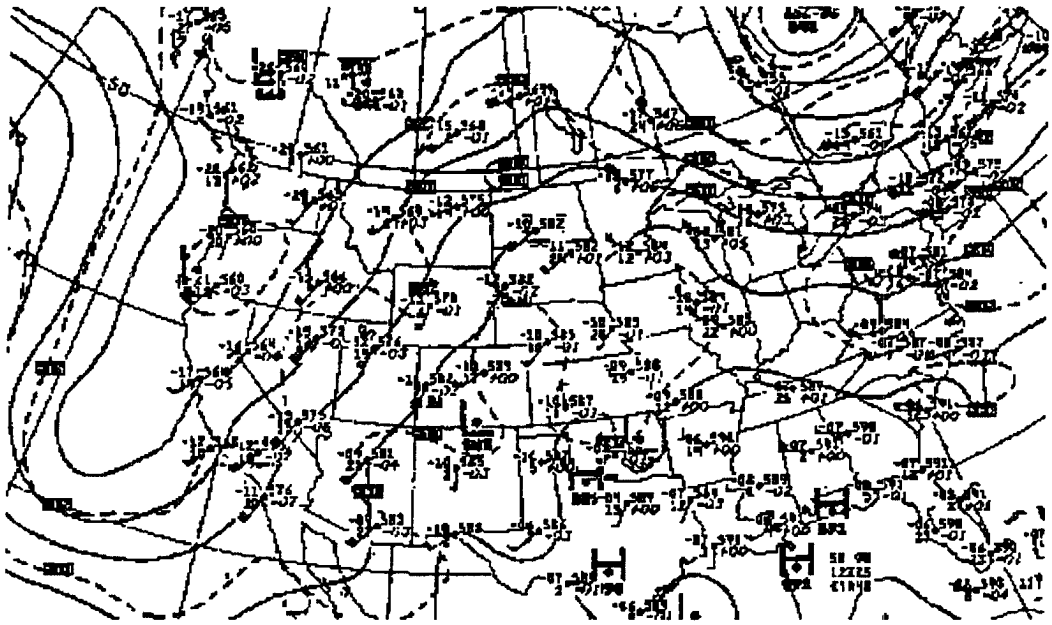

b)

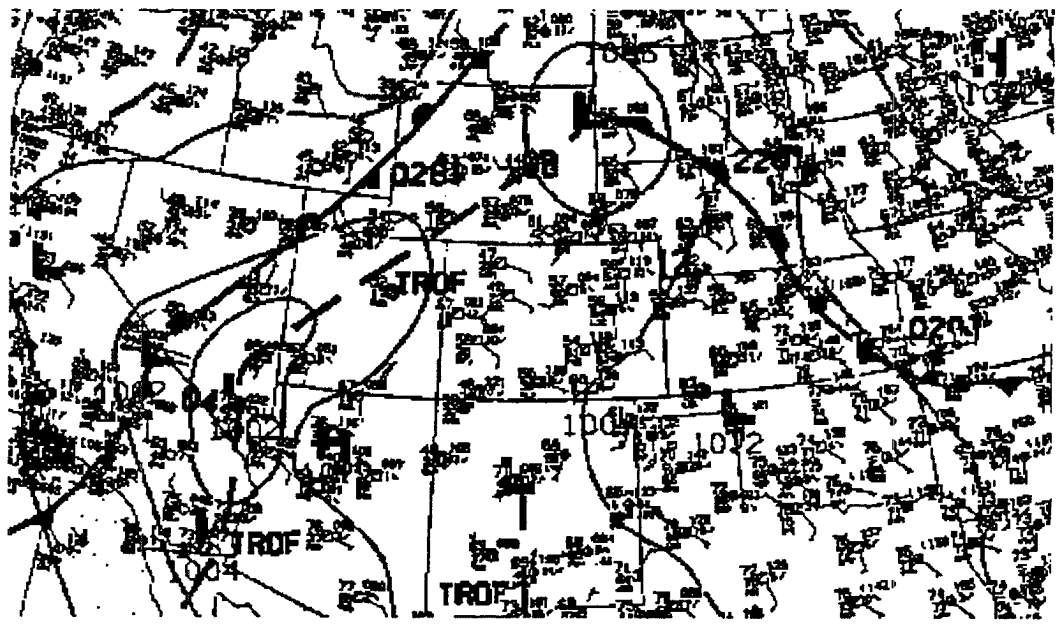

Fig. 3.1 June 25, 1996 12:00 UTC a) 500 mb NMC analyzed height and temperature field and b) surface analysis .

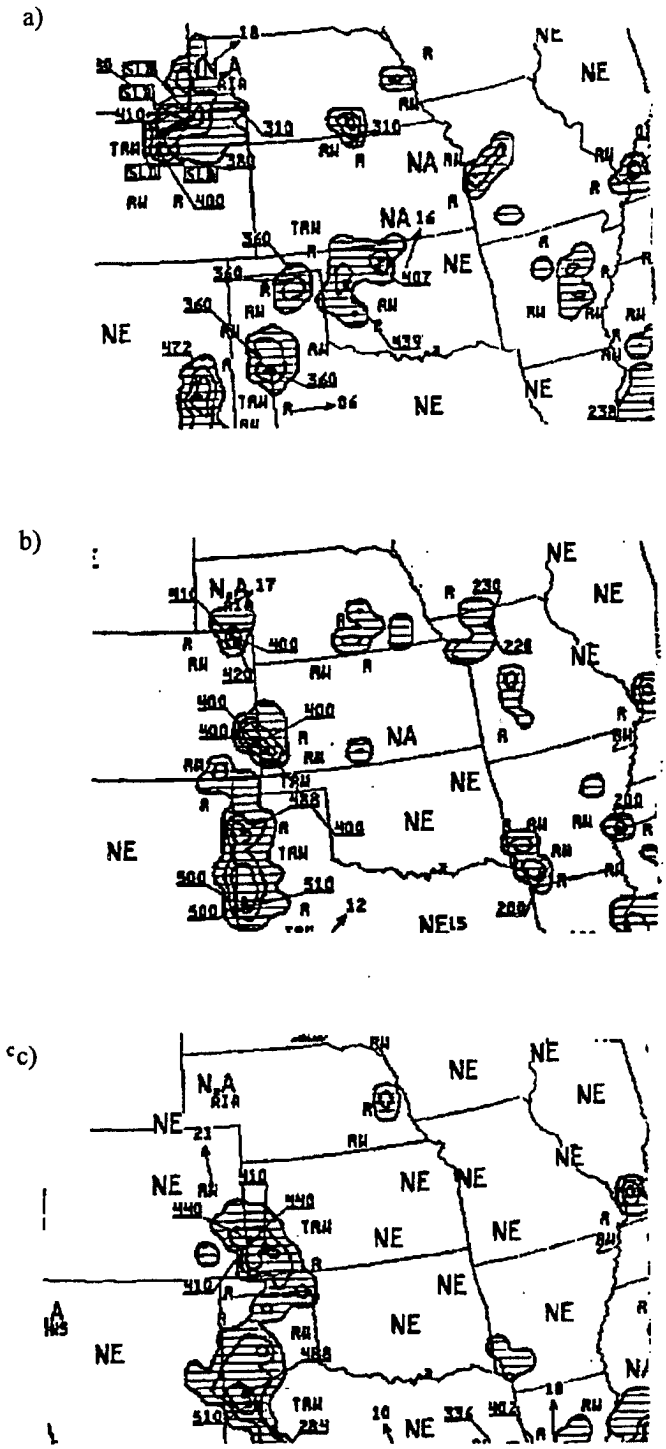

Fig. 3.2 June 25, 1996 NMC radar summaries for a) 06:35 UTC, b) 10:35 UTC and 12:35 UTC.

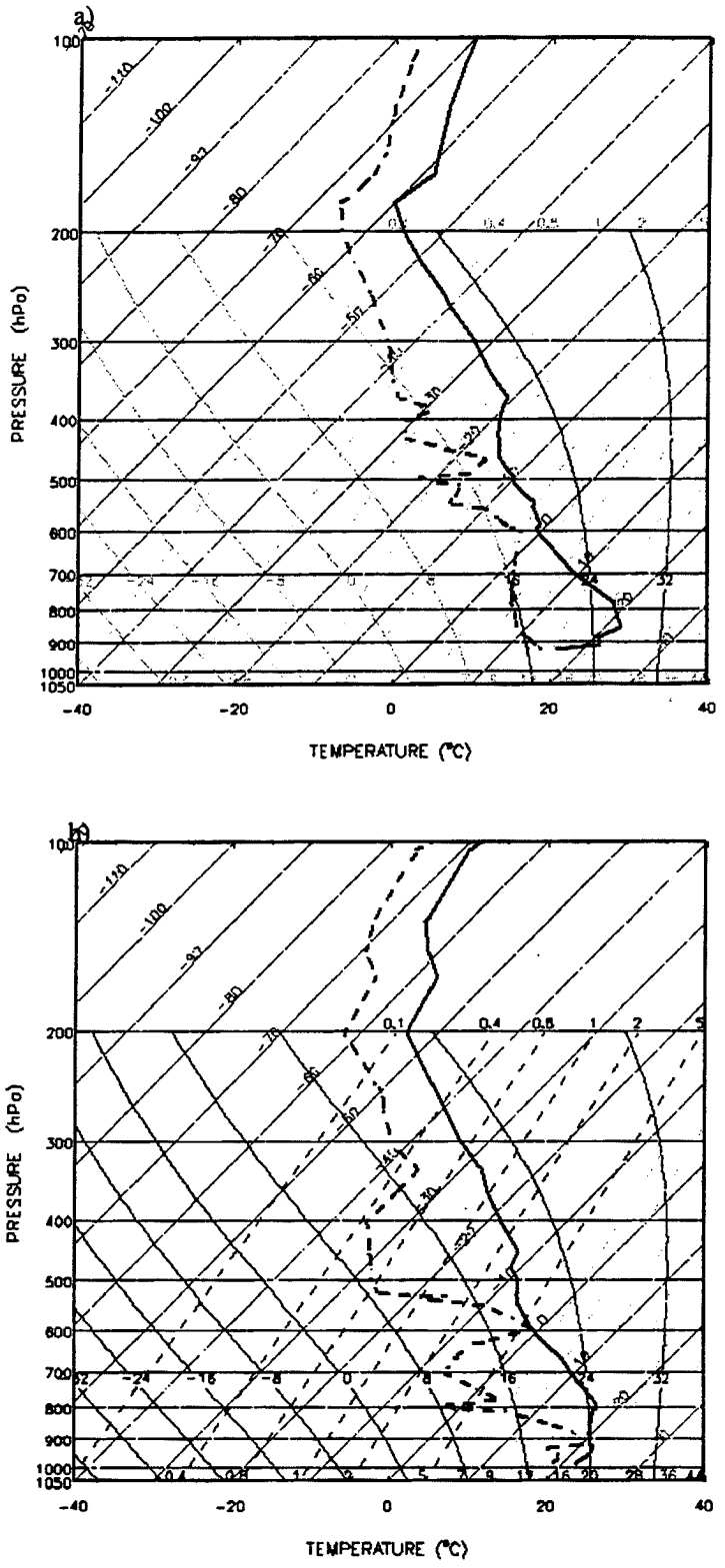

Fig. 3.3 a) 12:00 UTC June 25, 1996 NWS upper air sounding profiles for a) Dodge City, Ks and b) Topeka, KS.

a)

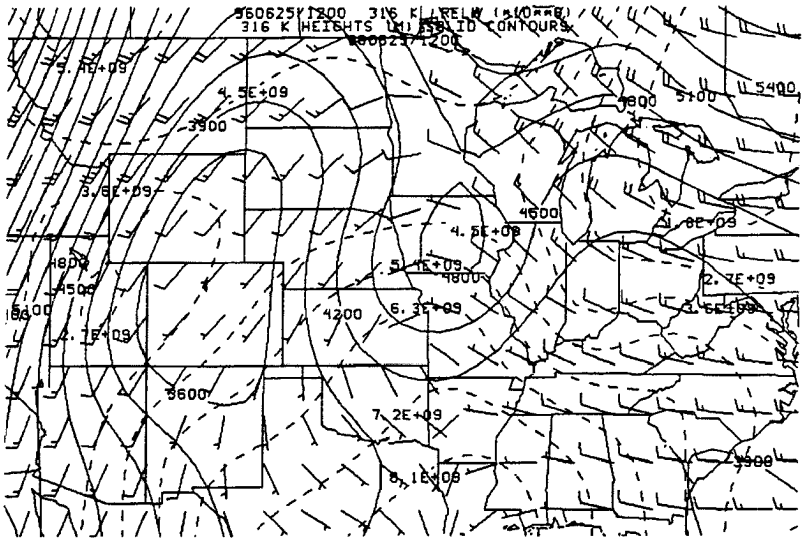

b)

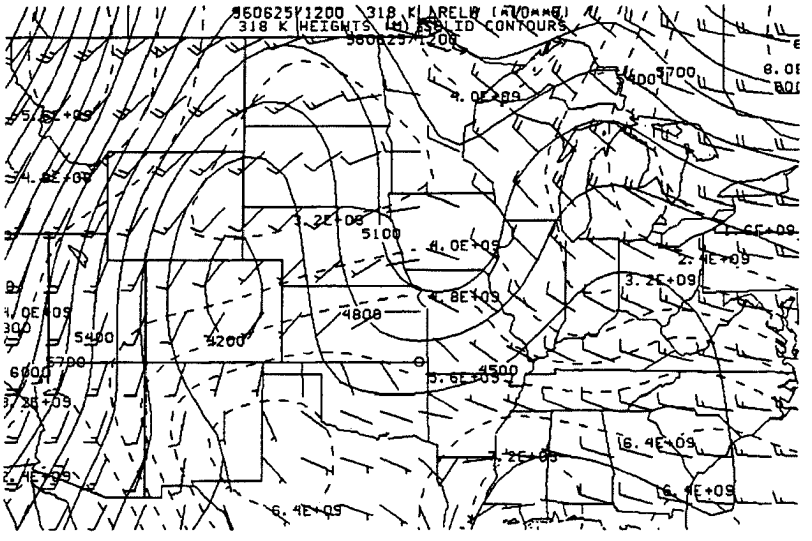

Fig. 3.4 a) 316 K and b) 318 K heights, winds and relative humidity. Units are given in m/s for winds, m for height, and percent*(10**8) for relative humidity. Analysis was performed on the United States National Weather Service radiosonde network upper air data for June 25 1996 12:00 UTC.

a)

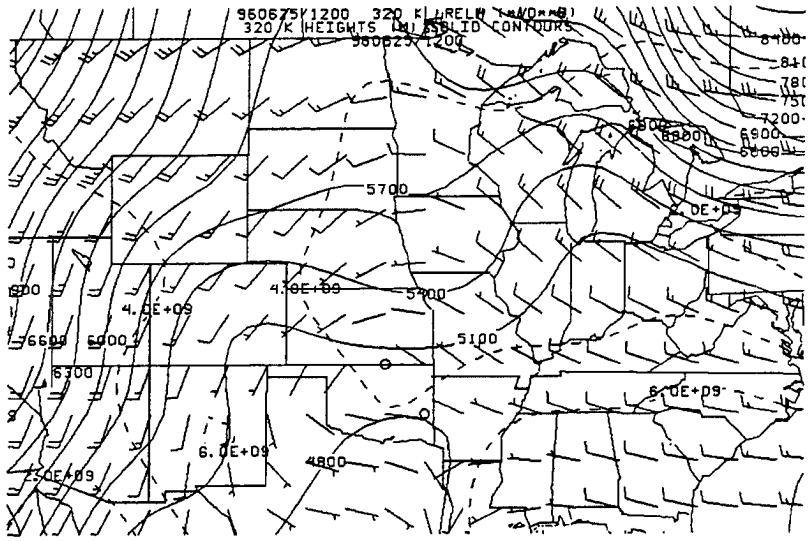

b)

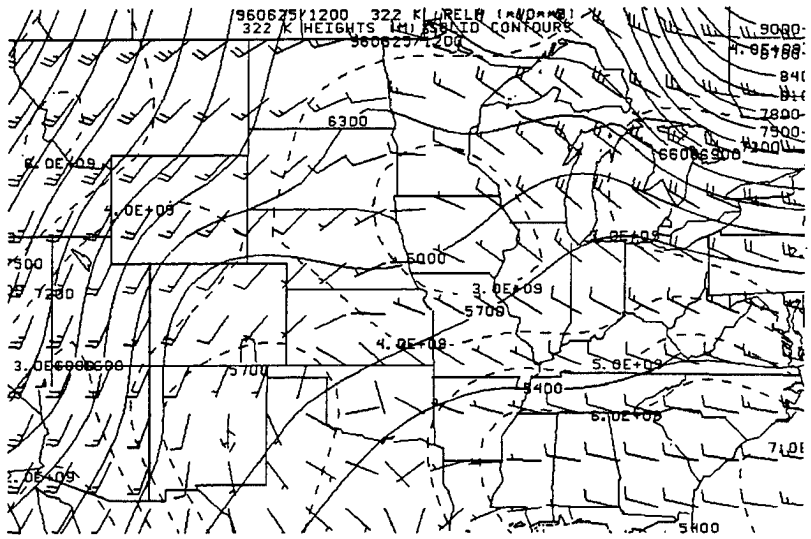

Fig. 3.5 a) 320 K and b)322 K height surfaces, winds and relative humidity. Units are given in m/s for winds, m for height, and percent*(10**8) for relative humidity. Analysis was performed using the United States National Weather Service radiosonde network upper air data for June 25 1996 12:00 UTC.

Table 3.1 Summary of Flight Leg Information for each flight leg made during the J25 experiment.

Flight Leg	Time (UTC)	Heading (deg)	Altitude (m AGL)	Pressure (mb)	Distance Traveled (km)
L0	16:16-16:27	358-61	4500	575	66.6
P0	16:27-16:32	61-136	4500-5125	575-531	27.5
L1	16:32-16:35	136	5125	531	18.0
P1	16:35-16:36	136	5125-5383	531-526	12.2
L2	16:38-16:41	136	5383	526	12.4
P2	16:38-16:41	136	5383-5807	526-486	18.0
L3	16:41-16:44	136-47	5807	486	16.5
L4	16:44-16:50	47	5807	486	38.3
L5	16:50-16:53	47-234	5807	486	14.0
L6	16:53-16:55	234	5807	486	13.3
P3	16:55-16:55	234	5807-5655	496	02.8
L7	16:55-17:01	234	5655	496	33.4
L8	17:01-17:05	234-55	5655	496	23.3
L9	17:05-17:11	55	5655	496	35.5
P4	17:11-17:12	55	5655-5500	496-506	00.3
L10	17:12-17:15	55-22	5500	506	18.9
P5	17:15-17:15	22	5500-5261	522	00.3
L11	17:16-17:17	22	5261	522	10.5
P5	17:17-17:18	22	5261-5125	531	06.7
L12	17:18-17:20	22	5125	532	9.00
P7	17:20-17:42	22-197	5125-7119	368	133.7
S1	17:42-18:11	Spiral	7119-608	917	174.0

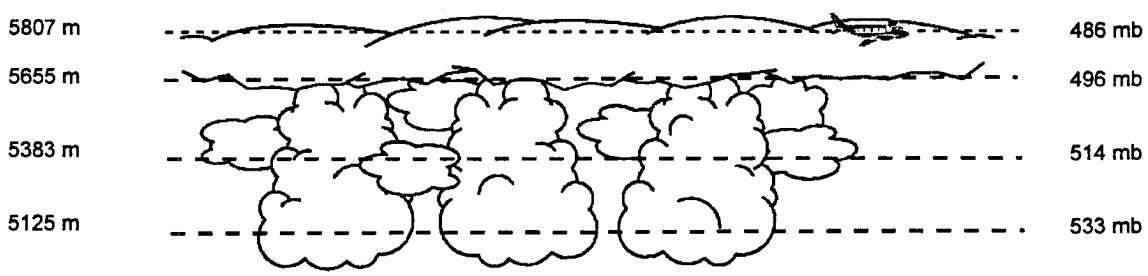

Fig. 3.6 Schematic diagram of J25acs cloud structure observed between 16:30 and 17:00 UTC. Relative positions of level flight legs L1, L2, L7, and L4 (from bottom to top) indicated by dashed lines. Level flight legs were not vertically collocated in space.

a)

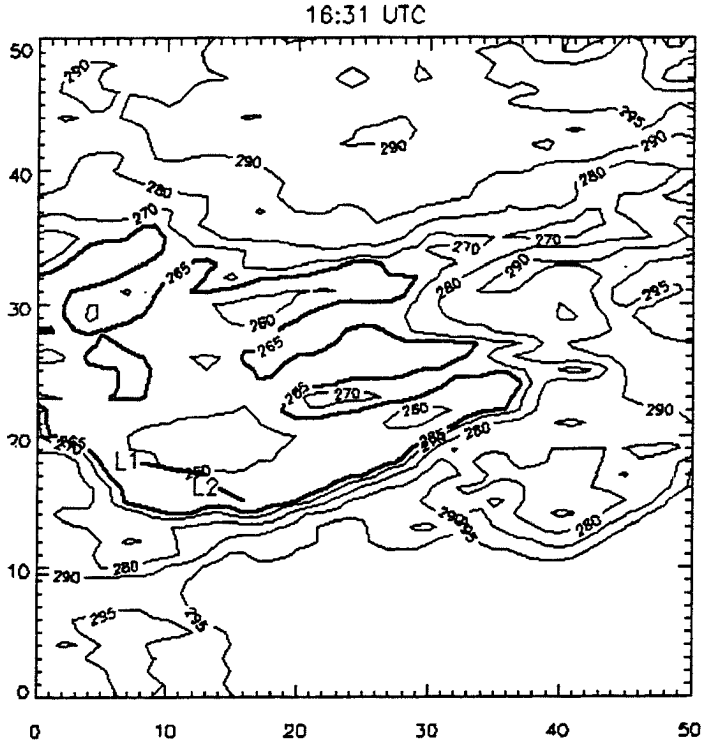

b)

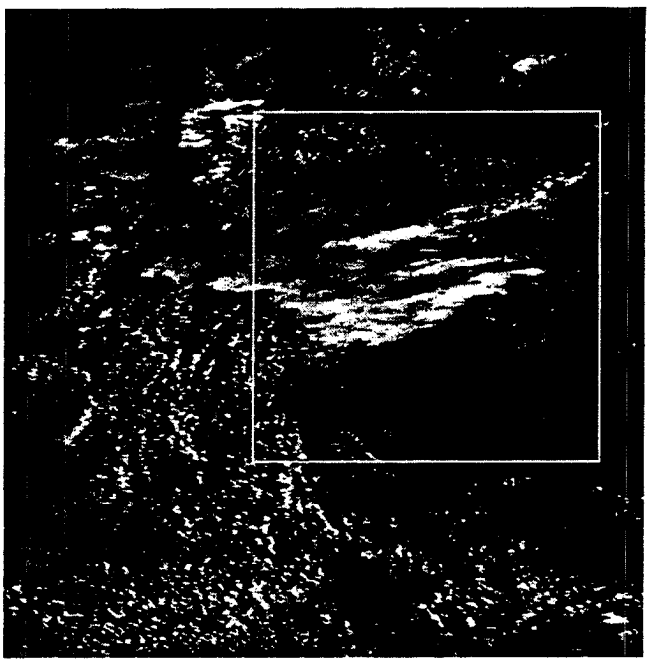

Fig. 3.7 a) 16:31 UTC GOES-8 10.7 μm brightness temperature map of the J25acs with level flight legs L1 and L2 also shown. b) 16:31 UTC GOES-8 0.7 μm image of the J25acs.

a)

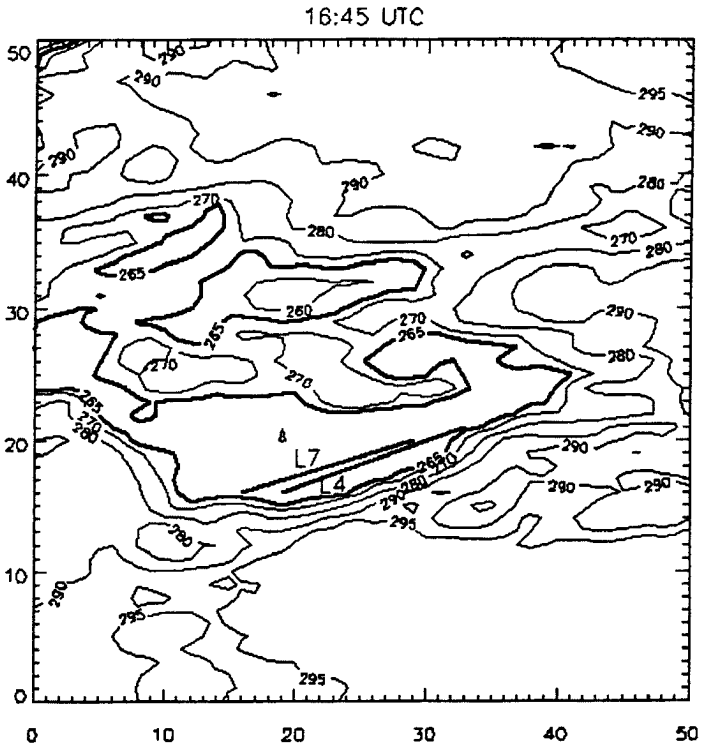

b)

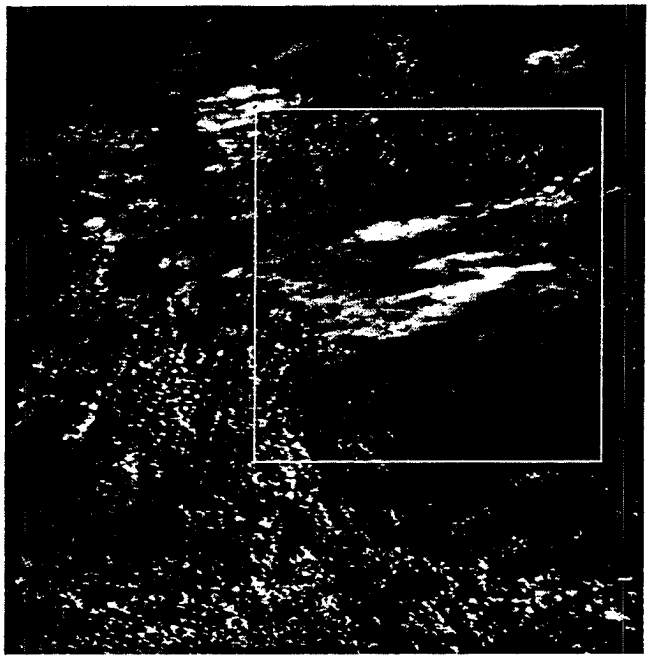

Fig. 3.8 a) 16:45 UTC GOES-8 10.7 μm brightness temperature map of the J25acs with level flight legs L4 and L7 also shown. b) 16:45 UTC GOES-8 0.7 μm image of the J25acs.

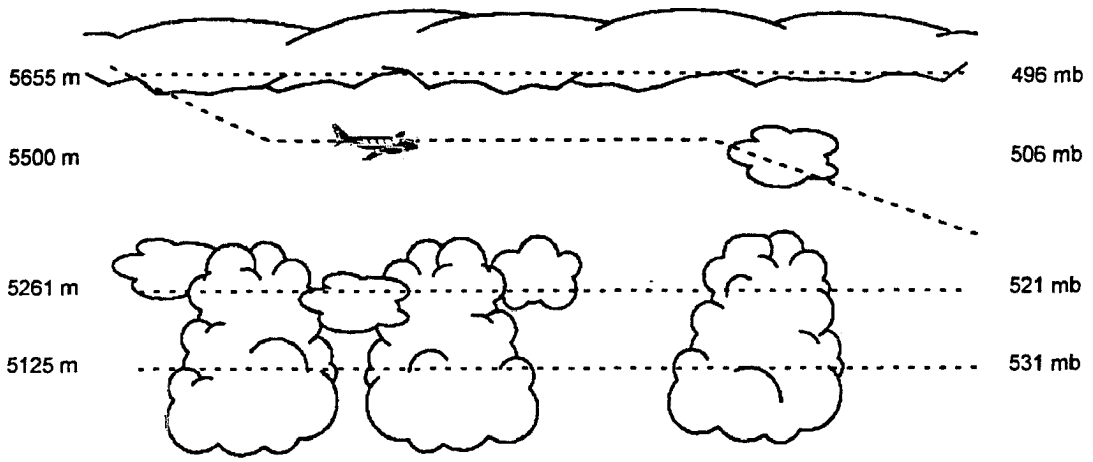

Fig. 3.9 Schematic diagram of J25acs cloud structure observed between 17:00 and 17:30 UTC. Relative positions of level flight legs L12, L11, L10, and L9 (from bottom to top) indicated by horizontal dashed lines. Level flight legs were not vertically collocated in space. During level flight leg L10, aircraft was turning.

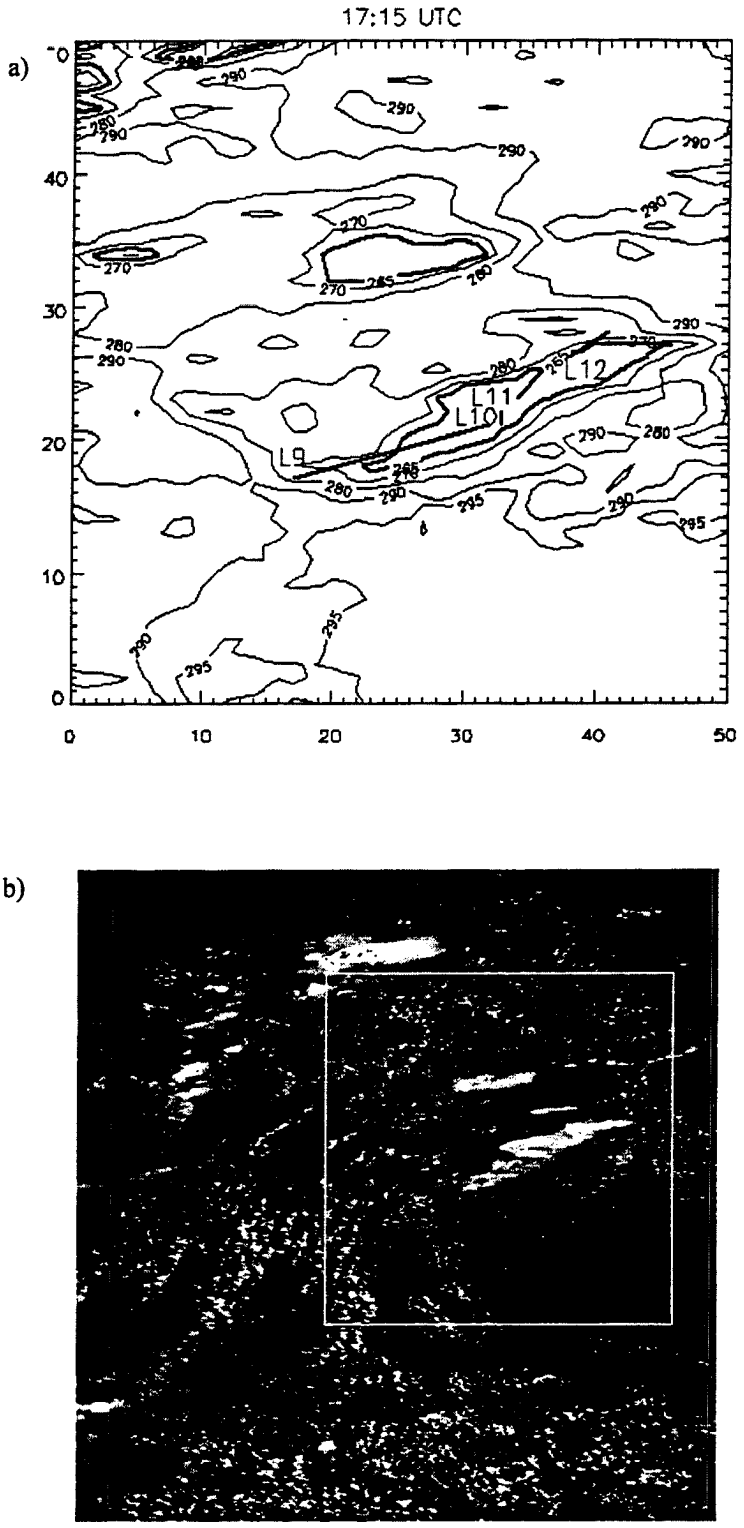

Fig. 3.10 a) 17:15 UTC GOES-8 10.7 μm brightness temperature map of the J25acs with location and orientation of flight legs L9, L10, L11, and L12 also shown. b) 17:15 UTC GOES-8 0.7 μm image of the J25acs.

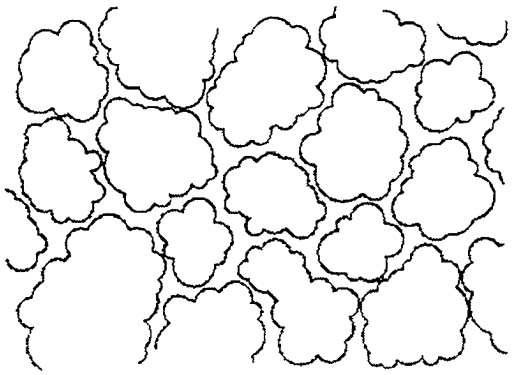

Fig. 3.11 Observed cloud structure of J25acs during profile leg S1.

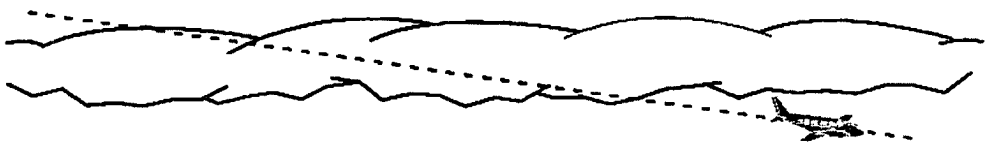

S1

Fig. 3.12 Observed cloud structure during S1 sounding profile. Location of flight leg indicated by the dashed line.

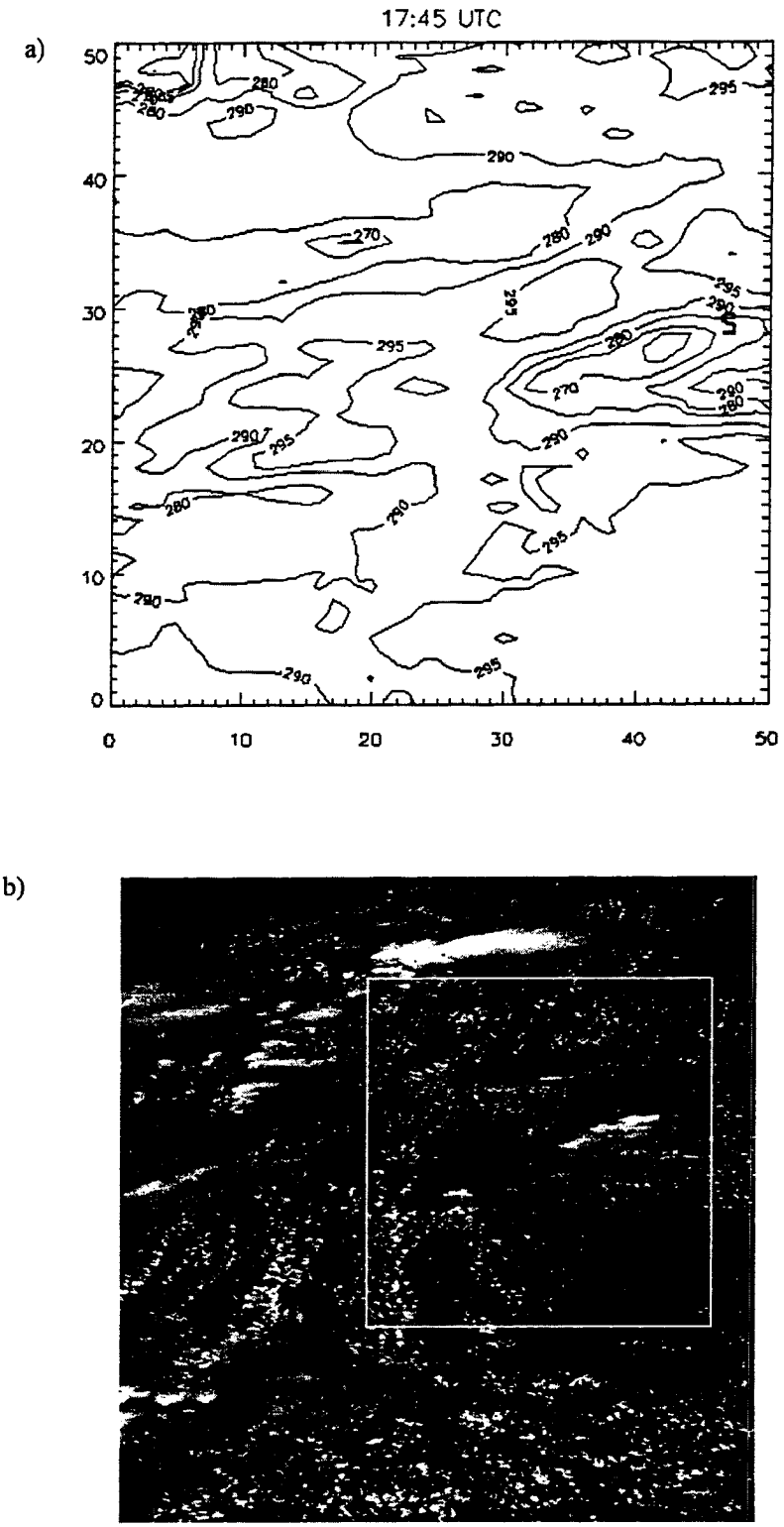

Fig. 3.13 a) 17:45 UTC GOES-8 10.7 μm brightness temperature map of the J25acs with location of sounding profile S1 also shown. b) 17:45 GOES-8 0.7 μm image of the J25acs.

CHAPTER IV

METHODOLOGY

Introduction

Our primary objectives in this research were to use aircraft measurements and a radiative transfer model to examine the microphysical, thermodynamic, kinematic and radiative structure of the J25acs. In the previous chapter, we described how aircraft measurements were collected and also characterized the J25acs for separate time periods of the experiment. In this chapter, we describe how the aircraft measurements were analyzed. We begin by outlining our aircraft measurement classification system. Briefly, we decomposed the set of aircraft measurements into five basic groups : A, B, C, D and M. In our data analysis and presentation, we used this system to identify sets of measurements collected at different locations and within different clouds layers of the J25acs. The chapter proceeds with a description of the aircraft instrumentation and our methodology of aircraft measurement analysis. The operating principles and performance of the aircraft instrumentation are discussed. The methodology of aircraft measurement analysis is designed to examine the microphysical, thermodynamic, and kinematic structure of the J25acs. As will be discussed, we analyzed the set of measurements within each data group: A, B, C, D and M separately. The relationships among the analyzed groups of measurements were then used to infer both the spatial and temporal structures of the J25acs. The chapter concludes with an overview of our methodology for examination of the radiative structure of the J25acs. In summary, we constructed cloud optical property profiles which were based on the microphysical measurements collected within the cloud layers A, B and D and in flight observations made of the J25acs. The cloud optical property profiles along with a constructed profile of atmospheric optical properties were then used as input into the Spherical Harmonic Discrete Ordinate Method (SHDOM) radiative transfer model.

4.1 Aircraft Data Classification System

In this section, we describe a classification system which we developed to identify sets of aircraft measurements collected during the J25 experiment. A classification system was required because aircraft measurements were made at different locations, times, and at different headings within a complex and evolving multi-layered cloud system. In our classification system, measurements were organized into various groups over which the aircraft sampling strategy was systematic and the observed cloud structure was homogeneous. This allowed for analysis of the structure of the J25acs in the corresponding location of each group of measurements. We used the relationships between each group of measurements to examine the spatial and temporal structures of the J25acs.

Our classification system made use of the previous set of level flight legs L0-L12, and the profile flight leg S1 (described in Chapter III) to identify sets of aircraft measurements collected during the experiment. The flight legs were grouped according to their location and orientation within the J25acs. Table 4.1 summarizes our system . Data group A contains the set of measurements collected during level flight legs L1 and L2. These flight legs were in the same direction and were positioned at two separate levels within cloud layer A. We refer to flight legs L1 and L2 as flight legs A_l and A_u (where "l" indicates lower and "u" indicates upper flight leg). Data group B contains the set of measurements collected during the level flight legs L4, L7, and L9. Each of these flight legs was straight and level , was oriented in the same or opposite direction, was in the same region of the J25acs, and was positioned at one of two levels within cloud deck B. The upper flight leg, L4, was referred to as flight leg B_u. To distinguish the set of measurements collected during the two lower flight legs, L7 and L9, we referred to them as flight legs B1 and B2, respectively. Data group M contains the set of measurements collected during flight leg L10. The aircraft was level and turning during this flight leg and was positioned in a clear layer of air between two distinct cloud decks. Therefore, we refer to this flight leg as flight leg M (where M stands for middle) Data group C contains the set of measurements collected during flight legs L11 and L12. These level flight legs were in the same direction and region of the J25acs and were positioned at two different levels within

cloud deck C. We refer to them as flight legs C_u and C_l, respectively. Data group D contains the set of measurements collected during the S1 sounding profile which passed through cloud layer D.

We used the classification system outlined in table 4.1 to refer to the aircraft measurements collected during the J25 experiment. The relative position of these measurements within each cloud layer were illustrated with aid of schematic diagrams in Chapter III and were also summarized in the previous discussion.

4.2 Aircraft Instrumentation and Data Analysis

The aircraft measurements were archived in a GENPRO format by the UWRAF at 1 Hz. Since the aircraft was traveling at roughly 100 m/s during horizontal flight legs, each measurement collected by the aircraft may be thought of as an average value over a 100 m distance.

A list of the instruments used in this research and their measured parameters, range, accuracy, detection limits, and sampling rate is shown in table 4.2. The accuracy of an instrument is defined to be "the closeness of the agreement between the result of a measurement and a true value of the measurand" (WMO 1996). The detection limit or resolution of an instrument is "the smallest change in the primary input that produces a detectable change in the primary output" of the instrument (Brock 1995). We used the measurements collected by the instrumentation listed in table 4.2 to examine the microphysical, thermodynamic, and kinematic structure of the J25acs. The following sections describe the method of aircraft data analysis and the operation principles of each instrument listed in table 4.2.

4.2.1 Microphysical Parameters, Instrumentation, and Analysis

The microphysical parameters considered in our research were the cloud LWC, the cloud droplet number concentration, and the cloud droplet effective radius. These were computed from measurements made by the FSSP-100 optical particle probe. A description of the operating principles and the performance characteristics of this instrument is provided below. This description follows that given by Hobbs et al. (1981).

The FSSP-100 measures the number concentration of cloud water droplets within 15 evenly spaced diameter size bins between 2 and 30 μm. The instrument consists of a Helium-Neon laser focused to a diameter of 200 μm. Drops which pass through the instrument scatter the laser radiation in all directions. The instrument measures the forward scattered component of this radiation. Mie theory and pre-flight calibration are then used to estimate the cloud droplet size from the measured forward component. The droplet size is recorded to obtain a total number count within each droplet size bin. The number concentration of cloud particles within each size bin is computed from the ratio of the total number of drops within the bin and the sample volume of air. The sample volume is determined by the speed of the aircraft, the He Ne laser beam width (with edge corrections taken into account), and the depth of field of the instrument. The sampling rate of the instrument is 10 Hz. At an aircraft cruising speed of 100 m/s, the instrument sample volume for one second is roughly 25 cm^3 (personal communication, Dr. Alfred Rodi).

Microphysical Parameters

The LWC and the cloud droplet effective radius were computed from the FSSP measured cloud particle size distributions as follows:

$$LWC = \frac{\pi \rho_w}{6} \frac{\sum_{i=1}^{m} N_i d_i^3 \Delta d_i}{\sum_{i=1}^{m} \Delta d_i}, \tag{4.1}$$

$$r_e = \frac{1}{2} \frac{\sum_{i=1}^{m} N_i d_i^3}{\sum_{i=1}^{m} N_i d_i^2}, \tag{4.2}$$

where

ρ_w = density of water,

N_i = number concentration of cloud droplets in size channel i,

d_i = diameter of cloud droplet in size channel i,

Δd_i = width of size channel i,

r_e= cloud droplet effective radius.

Equation 4.2 shows that the effective radius is the ratio of the third and second moments of the droplets size distribution. It is useful for identifying whether a droplet size distribution is characterized by larger or smaller droplets. It has also been found to be the property of a droplet size distribution which is most important for determining the optical properties of the distribution (Hu et al. 1992).

Errors in Microphysical Parameters

It was difficult to quantify the errors in the microphysical parameters used in this research. Therefore, we used values reported by Hobbs et al. (1981) as a guideline. They state that the FSSP measured number concentration can be measured to within ± 20 % and that the mean volume diameter can be measured to within ± 1 to 2 μm. Since, the LWC depends on both the number concentration and the third moment of the droplet size, the error is considerably larger, at ± 50 %.

Since the J25acs was found to be composed of both liquid water drops and ice crystals, errors in the FSSP measurements should also be expected due to the spurious detection of water droplets caused by ice crystals passing through this instrument. Heymsfield et al. (1989) studied the effects of ice crystal contamination by examining FSSP measurements in conditions where water droplets were known not to be present. Heymsfield et al (1991, p. 942) summarize the results of this study as follows,

> 1) concentrations of 2.5 cm^{-3} or less in any FSSP size channel could have been produced by ice particles, ... 3) concentrations above this threshold were almost certainly water droplets, and 4) signal contamination by ice primarily affected the higher size channels.

In their study of two mixed phase Ac clouds, Heymsfield et al. (1991) attempt to compensate for these possible errors by reducing the droplet concentration within each size bin by 2.5 cm^{-3}. They claim that this results in an underestimation of their cloud droplet number concentration by at most 5%.

In our research, we did not account for the possible effects of ice crystal contamination. However, based on the work of Heymsfield et al. (1991), we expect that our measured cloud droplet number concentrations (flight leg mean values ranged between roughly 130 and 200 cm $^{-3}$) could be overestimated by as much as 10 %.

Microphysical Data Analysis

FSSP measurements obtained during flight legs through cloud layers A, B, C and D were analyzed to determine the microphysical structure of each cloud layer. The relationships between the structure of each cloud layer and measurements for flight leg M were then used to infer the microphysical structure of the J25acs at separate time periods of the experiment. Because the sampling strategy for flight legs A,B and C was different than that for the flight leg through cloud layer D, the measurements within these sets of cloud layers were analyzed in different manners.

The microphysical measurements collected during flight legs through cloud layers A, B, and C, and flight leg M were examined in two formats: 1) horizontal LWC profiles and 2) flight leg statistics. The horizontal profiles were subsets of FSSP LWC measurements obtained during the upper and lower level flight legs within each layer plotted in a bar graph format as a function of horizontal distance. The bar graph format was chosen to emphasize that each measurement is representative of the LWC over a certain horizontal domain. Since the aircraft speed was fairly constant at around 100 m s^{-1} ± 5 m s^{-1}, each measurement represents the LWC over 100 m ±5 m.

The flight leg statistics computed from each set of measurements were the LW cloud fraction, the flight leg mean LWC, the in-cloud mean LWC, the mean cloud droplet effective size, the mean cloud droplet number concentration, and the mean normalized cloud droplet size distribution. The LW cloud fraction was computed by dividing the number measurements where the LWC greater than 0.001 g m^{-3} by the total number of sample volumes for a flight leg. This is the same criterion used by de Roode et al. (1996) in their study of cumulus rising into stratocumulus. In the case of cloud layer B, statistics for both of the lower level flight legs, B1 and B2, are presented. The flight leg statistics were used to identify the mean microphysical properties (cloud droplet effective radius, cloud droplet size distribution shape, and

number concentration) measured at two different levels within each cloud layer. An understanding of the mean measured properties was required, because they were used to determine the optical properties of each cloud layer. We interpreted relationships between the values computed for each level flight leg to indicate vertical trends in the statistical microphysical properties of each layer. The relationships between the mean statistics of flight legs B1 and B2 were interpreted to indicate temporal trends in the mean microphysical properties of cloud layer B.

We examined the microphysical structure of cloud layer D by plotting measurements of the LWC, cloud droplet effective radius, and the cloud droplet number concentration obtained during the S1 profile as a function of height. Because the aircraft sampled cloud layer D along a slantwise flight path, the measurements collected during this profile are representative of both the horizontal and vertical microphysical structure of this layer..

4.2.2 Thermodynamic Parameters, Instrumentation, and Analysis

Thermodynamic Parameters

The thermodynamic parameters considered in this research were the virtual potential temperature, θ_v, and the relative humidity, RH. In the following sections, we discuss how the virtual potential was computed, the motivations for its use, its absolute error, and the instruments used for its computation. Next, we discuss how thermodynamic measurements in the data groups A, B, C, D, and M were analyzed.

Virtual Potential Temperature

The virtual potential temperature was computed so that the stability of a layers of air with respect to saturated and dry vertical parcel displacements (the moist and dry static stability of a layer) could be examined. The static stability was examined by way of the parcel method. Appendix D contains an overview of this method. The following paragraphs discuss the relationship between virtual potential temperature and buoyancy and also discuss the method used to examine the static stability of a layer .

The virtual temperature is a useful parameter for examining the buoyancy of a moist air parcel with respect to its environment. This is because the virtual temperature is

> the temperature that dry air must have to equal the density of moist air at the same pressure...Virtual potential temperatures are analogous to potential temperatures in that they remove the temperature variation caused by changes in pressure altitude of an air parcel (Stull, 1988).

In our research, we computed the virtual potential temperature of a parcel of air as (Stull, 1988)

$$\theta_v = \theta(1+.61r_v - r_l - r_i), \tag{4.3}$$

where r_v, r_l, and r_i are the water vapor, liquid water, and ice water mixing ratio respectively and θ is the dry potential temperature of the air parcel. The buoyancy force, B, experienced by a parcel of air is proportional to the virtual potential temperature difference between the parcel and it's environment and is given by (Stull 1988),

$$B = g\frac{\theta_{v\,parcel} - \theta_{v\,environment}}{\theta_{v\,environment}} \tag{4.4}$$

where g is the acceleration due to gravity. Together, equations 4.3 and 4.4 imply that air parcels which contain more water vapor relative to their environment will be positively buoyant while air parcels which contain more liquid water and or ice water relative to their environment will be negatively buoyant. The latter effect is referred to as liquid water loading (Stull 1988).

Instrumentation

The measurement of θ_v required measurements of pressure, temperature, water vapor content, liquid water content, and ice water content within an air parcel. The liquid water content of an air parcel was determined from FSSP measurements as described in section 4.2.1. The IWC of an air parcel was computed by the UWRAF during data processing using a mass size relationship based on 2D-C measurements. The following paragraphs briefly describe the operating principles and performance characteristics of the instruments (see table 4.2) used to measure the temperature, pressure, and water vapor content of an air parcel.

The Minco temperature element measures the temperature of an air parcel by measuring the change in the resistance of a platinum wire maintained at constant voltage. The platinum wire element is contained in a housing which prevents its exposure to cloud hydrometeors. The reported accuracy and

detection limits of the Minco instrument is ± 0.5° C and 0.006° C respectively (UWRAF, personal communication).

The EG &G hygrometer measures the water vapor content of an air parcel by determining the dew-point or frost-point of the parcel. The instrument determines the dew or frost-point by measuring changes in the reflective properties of a mirror's surface as its temperature is changed. The reflective properties of the mirror's surface are monitored by photo-resistors in an optical sensing bridge. The temperature of the mirror is varied by a Peltier thermoelectric cooler and it is monitored by a platinum resistance wire. As ambient air passes through the instrument, the temperature of the mirror is varied to that at which water vapor in the air just begins to condense on its surface. The condensate changes the reflective properties of the mirror's surface which is then registered by the photo-resistors. The temperature at which moisture just begins to condense is then taken to be the dew-point or frost-point of the ambient air. The reported accuracy of this instrument is ± 1.0° C for temperatures greater than 0° C and ± 2.0° C for temperatures less than 0° C (NCAR web page). The instrument response depends on the water vapor content of the air parcel. In humid conditions, the response time is 2 s. In regions where the dew point depression is greater than 20° C, the response time can be as large as 20 s (NCAR web page).

Because of the poor response of the EG&G hygrometer, the UWRAF (in their data processing) do not use measurements from this sensor where the first 0.1 s FSSP measurement shows droplet concentrations greater than 10.0 cm^{-3}. In these air parcels, the dew point temperature is assumed equal to the measured air temperature of the parcel i.e. the air parcel is assumed to be just saturated with respect to water. This is assumption is certainly not valid. Previous observational studies have identified that the relative humidity within small cumulus clouds can range between values of 70 % and 107 % (Pruppacher 960). In future research, we propose that the water vapor measurements are analyzed to detemine the saturation state of cloudy air parcels.

The Rosemont 1501 pressure transducer measures the static air pressure by measuring the pressure which air exerts on a sensing diaphragm mounted on the side of the aircraft. The sensing diaphragm is one plate of a parallel plate capacitor. The pressure of air on the diaphragm changes the

capacitance which is then converted to a digital representation of pressure. The reported accuracy and detection limits of the instrument are ± 1.0 mbar and 0.034 mbar respectively (UWRAF).

Thermodynamic Data Analysis

The measurements of θ_v and RH collected during each flight leg in cloud layers A, B and C and flight leg M were analyzed statistically. The computed statistics of θ_v for each flight leg were the flight leg mean, the in-cloud mean, the out-of-cloud mean, the maximum and minimum measurement, and the standard deviation. We analyzed the measurements of θ_v in this format so that: 1) differences between measurements of θ_v in cloud and cloud-free air parcels could be identified, 2) the moist static stability of each cloud layer could be examined and 3) the degree of horizontal variability in θ_v could be assessed. The computed statistics of RH for each flight leg were the out-of-cloud mean and standard deviation. These statistics were computed so that the relative moisture content and the variability in the relative moisture content of air could be assessed.

The flight leg mean values of θ_v were used to examine the moist static stability of each cloud layer. As discussed Appendix D, the determination of the moist static stability of a layer requires a knowledge of the virtual potential temperature lapse rate for the layer under consideration. Because of the aircraft sampling strategy, it was not possible to determine the actual lapse rate between the levels of each flight leg within each cloud layer. Therefore, we computed "hypothetical" lapse rates by linearly interpolating the flight leg mean values for the upper and lower legs. In the case of cloud layer B, we chose to use the mean value measured during flight legs B_u and B1 because these flight legs were closely spaced in time. We realize that the significance of these hypothetical lapse rates depends on the degree to which θ_v is unchanging in the horizontal. To asses the degree of horizontal variability, we examined the standard deviation, the maximum and the minimum in the set of measurements for each flight leg.

We also used the flight leg mean values to construct "hypothetical"θ_v profiles for the J25acs in the northern and southern portion of the system. Our methodology used to construct these profiles was as follows. For the southern portion of the system, we assumed a linear variation with height between the mean values of θ_v computed for flight legs A_u, A_l, B1, and B_u. Table 3.1 shows that roughly 20 minutes

elapsed between the beginning and ending of these flight legs (L1-L7). Figures 3.13a ,3.15a, and 3.19a show that the midpoints of these flight legs were separated by a distance no greater than 12 km (the largest separation distance is between flight leg A_l [L1] and flight leg B_u [L4]). For the northern portions of the system, we assumed a linear variation with height between the mean values computed for flight legs B2, M, C_u, and C_l. Table 3.1 shows that roughly 15 minutes elapsed between the time period of the beginning and ending of these flight legs (L9-L12). Figures 3.19a and 3.22a show that the midpoints of these flight legs were separated by a distance no larger than 15 km (the largest separation distance is between flight legs B2 [L9] and C_l [L12]).

The θ_v structure of cloud layer D and its environment were examined by plotting the measurements collected during the S1 profile as a function of height. Since the aircraft sampled cloud layer D and its environment horizontally and vertically during the S1 profile, these plots were interpreted to indicate both horizontal and vertical structure in the virtual potential temperature field.

The flight leg mean values of the virtual potential temperature were also plotted as function of height on the S1 profile. This was done so that the relationships between the flight leg mean values within each cloud layer, the mean values for flight leg M, and the measurements obtained during the S1 profile could be identified.

4.2.3 Kinematic Parameters, Instrumentation, and Analysis

Parameters and Instrumentation

The kinematic parameters considered in this research were the eastward, u, northward, v, and vertical, w, velocity components of air parcels with respect to the rotating earth . These parameters were computed by the UWRAF using measurements collected by the Honeywell Inertial Reference System and the Rosemont model 858 differential pressure probe. The following section gives a brief discussion of how the wind velocity is computed from these instruments. A more in depth discussion may be found in Lenschow (1986)

The velocity of air, $\bar{u}$, with respect to the rotating earth is computed from the sum of the measurement of the velocity of the aircraft relative to the earth, $\bar{u}_p$, and the measurement of the velocity of

air relative to the aircraft, $\vec{u}_a$, and may be written as (Lenschow 1986)

$$\vec{u} = \vec{u}_p + \vec{u}_a . \tag{4.5}$$

The Rosemont model 858 differential pressure probe was used to measure the velocity of air relative to the aircraft. The probe computes the air velocity by measuring the pressure difference between ports at two locations on the probe. The Honeywell IRS was used to measure the velocity of the aircraft relative to the earth. The instrument consists of an orthogonal triad of accelerometers whose output is integrated to obtain the aircraft velocity. The errors in the wind measurements are known to increase in time due to the integration of errors in velocity measurements in time. The reported accuracy of the wind measurements is $\pm$ 1.0 m s^{-1}. The reported detection limit of the instruments is 0.05 m s^{-1}.

Kinematic Measurement Analysis

We analyzed measurements of the horizontal wind, u and v, and the vertical wind, w, collected during flight legs through cloud layers A, B, and C, flight leg M and profile S1in separate fashions . The horizontal wind measurements collected during flight legs through cloud layers A, B and C and flight leg M were analyzed in terms of their flight leg mean values. These were then used to compute a Richardson number (a description of how this parameter is computed is given below) for each cloud layer. They, along with measurements collected during the S1 profile, were also plotted as a function of height to identify the vertical and horizontal mean kinematic structure of the J25acs. The vertical wind measurements for flight legs through cloud layers A, B and C were analyzed by plotting subsets of them and LWC as a function of horizontal distance. We used this format so that the horizontal structure in the vertical wind field of each cloud layer could be visually examined. We also analyzed these subsets statistically so that the horizontal structure in the vertical wind measurements could be interpreted.

The mean horizontal wind measurements were used to compute a Richardson number for cloud layers A, B, and C. The Richardson number, R_i, for a layer depends on both the vertical wind shear, S, and

the static stability, σ,of the atmosphere and may be written as (Cotton 1989):

$$R_i = \frac{g}{\theta_v} \cdot \frac{\gamma}{S^2}, \tag{4.6}$$

where

$$\gamma = \frac{\partial \theta_v}{\partial z}, \tag{4.7}$$

and

$$S = \left| \frac{\partial \bar{u}}{\partial z} \right|. \tag{4.8}$$

The Richardson number is useful parameter for determining whether a layer of fluid may become unstable due to Kelvin Helmholtz instability (Drazin 1981). Equation 4.6 shows that R_i is the proportional to the ratio of the static stability and the square of the vertical wind shear. In the case where R_i is less than ¼, the layer is said to be unstable and Kelvin Helmholtz stability may occur. Physically, we may interpret this to mean that if the static stability of the fluid is large then it will tend to damp out turbulent kinetic energy which is produced by the mean flow. In this research, we used the Richardson number criterion to establish whether mean kinematic structure of each layer played a role in generating turbulence within the layer.

The skewness parameter, s, was computed for each flight leg set of vertical wind velocity measurements. The skewness is defined as (de Roode 1996)

$$s = \frac{\overline{w'^3}}{\left(\overline{w'^2}\right)^{3/2}}, \tag{4.9}$$

where w' is the difference between a vertical velocity wind measurement and the flight leg mean value. In cases where the skewness is positive, "this means that upward motions are greater and occupy a smaller fractional area than the downward motions, and vice versa" (de Roode 1996). In their observational

studies within cumulus clouds rising into stratocumulus clouds, de Roode et al. (1996) find that the skewness is greater than one in the cumulus layer and is slightly negative in the stratocumulus layer. A physical explanation for the negative skewness values is that radiative cooling at the top of the stratocumulus layer leads to narrow and intense downdrafts.

4.3 Radiative Transfer Model and Radiative Structure Analysis Methodology

We examined the thermal and solar radiative structure of the J25acs using the Spherical Harmonic Discrete Ordinate Method (SHDOM) radiative transfer model and aircraft measurements. A detailed description of the SHDOM model solution procedure, its performance, and comparisons with other models may be found in Evans (1998). In the following section, we briefly describe the model, identify how it was employed in our research, and describe how the radiative structure of the J25acs was examined.

4.3.1 The SHDOM model and how it was used

SHDOM employs the discrete ordinate and spherical harmonic methods within an iterative solution procedure to solve the equation of transfer on a discrete grid of points. The model can compute 1D, 2D, or 3D broad-band or monochromatic radiative transfer within a spatially varying absorbing and scattering medium with both thermal emission and a collimated solar source. A brief overview of the model's solution procedure and a description of how radiometric quantities are computed may be found in Appendix E.

SHDOM uses the correlated k-distribution method developed by Fu et al. (1991) (CKDFU) to perform broadband radiative transfer within a vertically inhomogeneous atmosphere. A detailed description of the method is discussed by Fu et al. (1991), and is not repeated here.. In the CKDFU method, the thermal spectrum is divided into twelve bands and the solar spectrum is divided into six bands. The vertical variation in the absorptive properties of CO_2, O_3, H_20,N_20 and NH_4 are considered. Both the continuum and line absorption properties of H_20 are considered and approximate methods are used to represent absorption overlap. Table 4.3 shows the spectral intervals for the CKDFU bands and the gases which are represented in each band.

The SHDOM model was used in an eight-stream plane-parallel broadband format. The model input parameters including the cell splitting accuracy (SPLITACC), the spherical harmonic accuracy (SHACC), and the solution convergence criterion (SOLACC) were chosen based on the advice of Evans (1998). The delta-M approximation was used in all radiative transfer calculations. A description of this approximation is given by Wiscombe (1977). The parameters required by the model as input (in plane-parallel broadband format) were: 1) vertical profiles of the extinction, phase function, and single scattering albedo defined at a discrete number of grid points for each of the eighteen broadbands, 2) the vertical profile of temperature and pressure defined on the discrete grid of points, 3) the solar zenith angle, and 4) the lower boundary surface temperature and optical properties. In this research, the model grid was specified to range from 0 to 70 km. The resolution of the grid was specified to be a maximum (5 m) for cloudy grid points and a minimum (1 km) near the grid boundaries.

4.3.2 Raditive Structure Analysis Method

The previous section described the SHDOM radiative transfer model, outlined how we used this model, and also listed parameters which were required as input to run the model. In this section, we describe our methodology used to simulate the radiative structure of the J25acs.

How the model-required-parameters were specified

A brief overview of our methodology for specification of the model-required-parameters is as follows. Aircraft measurements obtained during the S1 sounding profile, climatology, and surface observations were used to "construct" vertical atmospheric gaseous extinction and temperature profiles for each of the eighteen broadbands (of the SHDOM model). A number of different broadband cloud optical property profiles were then "constructed" and placed in this vertical gaseous extinction and temperature profile. Aircraft microphysical measurements collected during the level flight legs within cloud layers A and B and Mie scattering theory were to construct "mean" cloud optical property profile for each of the these respective cloud layers. We referred to these cloud optical property profiles as cloud optical property profiles A and B. A multiple cloud layer optical property profiles was then constructed by placing cloud

optical property profile B above cloud optical property profile A. This multiple cloud layer profiles was referred to as cloud optical property profile BA . Aircraft measurements obtained during the S1 profile through cloud layer D and Mie scattering theory were used to construct an "instantaneous" cloud optical profile for this cloud layer. We referred to this profile as cloud optical property profile D. The lower boundary conditions were specified based on visual observations of the surface type cross referenced against previously reported values.

In the following sections, we provide a detailed description of 1) how aircraft measurements and Mie scattering theory were used to construct the "mean" cloud broadband optical property profiles A, B, and the "instantaneous" cloud optical property profile D, 2) how the vertical profile of the broadband atmospheric extinction and temperature was constructed, and 3) how the boundary conditions were specified. We emphasize that a number of approximations were made in the determination of the cloud optical property profiles. These approximations were chosen based on results from a sensitivity study. The methodology and results from this study are presented in Appendix G. In the sensitivity study, we examined the effects of changes in 1) the vertical profile of liquid water, 2) the liquid water path, 3) the presence of cloud layers above and below, and 4) the cloud droplet effective radius on the radiative heating rate properties of Ac-like cloud layers.

Construction of Broad Band Cloud Optical Property Profiles A, B and D

We used a Mie scattering code, the broad band averaging method of Slingo et al. (1982), and "constructed" cloud layer microphysical profiles to construct the broadband cloud optical property profiles A, B and D. In the following section, we describe how the microphysical profiles were constructed. Next, we describe the Mie scattering code, the band averaging method of Slingo et al. (1982), and how they were used to compute the broadband cloud optical properties.

Construction of Microphysical profiles for cloud layers A, B, and D

In this section, we describe the procedure used to construct the microphysical profiles for the cloud layers A, B, and D. These microphysical profiles were used in construction of the cloud optical property profiles. There were both similarities and differences in the procedure used to construct the

microphysical profiles for cloud layers A and B and cloud layers D. In the following paragraph, we identify the similarities. Next, the procedures for cloud layers A and B and cloud layer D are separately discussed.

The microphysical profile for each cloud layer was constructed using the FSSP measurements as a guideline. The 2D-C measurements in each cloud layer were neglected and thus, we did not consider the ice phase microphysics in our calculations. In all cloud layers, the cloud droplet size distribution was set to be of the same form: a modified gamma distribution. The measured form of the cloud droplet size distribution was not considered. The normalized form of the modified gamma distribution may be written as (Hansen, 1971)

$$n(r) = \frac{(a \cdot b)^{2b-1/b}}{\Gamma[(1-2b/b)]} r^{1-3b/b} e^{-r/ab}, \qquad (4.10)$$

where a is the effective radius, r_e, and b is the effective radius variance, v_e, of the distribution itself. Since the distribution is normalized, the integral of the distribution over all radii is equal to one:

$$\int_0^\infty n(r)dr = 1 \qquad (4.11)$$

The effective radius and the effective radius variance are statistical moments of the distribution and they may be written as (Hansen, 1971)

$$r_e = \frac{\int_{r_1}^{r_2} \pi r^3 n(r)dr}{\int_{r_1}^{r_2} \pi r^2 n(r)dr} = \frac{1}{G}\int_{r_1}^{r_2} \pi r^3 n(r)dr \text{ ,and} \qquad (4.12)$$

$$v_e = \frac{1}{Gr_e^2}\int_{r_1}^{r_2} (r-r_e)^2 \pi r^2 n(r)dr, \qquad (4.13)$$

where G is the cross-sectional area of particles per unit volume.

We chose the normal gamma distribution to represent the shape of the droplet distributions because a large number of optical property calculations were required. Because the normal form of the gamma distribution is specified in terms of two moments, this meant that cloud droplet size distributions

could be completely specified in terms of the cloud droplet number concentration and the statistical moments, r_e and v_e, of the distribution. This allowed for computational speed in the construction of the cloud optical property profiles. Also, through a survey of the literature, we found that the most important parameter for computation of optical properties of a cloud droplet size distribution is the effective radius (Hu et al. 1992). The shape of the droplet size distribution is found to be unimportant. The next section describes how we constructed the vertical profiles of r_e, v_e, and the cloud droplet number concentration profiles for each cloud layer.

Microphysical Profiles of Cloud Layers A and B

The microphysical profiles for cloud layers A and B were constructed using FSSP measurements collected during the level flight legs. Each profile was constructed such that the r_e and v_e of the cloud droplet size distribution was the same at all points within that layer while the number concentration of cloud droplets was allowed to vary with height. The respective values of r_e and v_e were specified to be the average of the flight leg mean values within the layer. (We chose to neglect the vertical variation in r_e within each cloud layer, based on the results obtained in our sensitivity study). The profile of the cloud droplet number concentration was constructed by scaling the number concentration to match a specified profile of LWC. For a particular LWC(z) value at point z and in a particular layer (A or B), the number concentration, N (z) at point z, was determined by

$$N\ (z) = \frac{1}{4\rho_w/3} \frac{LWC(z)}{\int \pi r^3 n(r) dr}, \qquad (4.14)$$

where n(r) was the normalized gamma droplet distribution for the particular layer. As an example, a liquid water content of 0.1 g m^3 within cloud layer B yielded a cloud droplet number concentration of 132.8 cm^{-3}. The vertical profile of LWC within each cloud layer was constructed by linear interpolation of the in-cloud mean LWCs computed for the upper and lower level flight legs. The LWC was set to zero above and below the upper and lower flight legs.

Microphysical Profile of Cloud Layer D

We constructed the microphysical profile of cloud layer D using the FSSP measurements obtained during the S1 profile. The profile was constructed such that r_e, v_e, and the cloud droplet number concentration varied with height. The vertical profile of r_e and v_e was constructed by first breaking cloud layer D up into three separate vertical layers (each layer was roughly 40 m in depth). In each layer, the mean r_e and v_e were computed from the set of FSSP measured droplet size distributions in that layer. Next, we set the cloud droplet size distribution in each layer to a be a normal gamma distribution with r_e and v_e equal to the mean values computed for that layer The vertical profile of the cloud droplet number concentration in each layer was then constructed by scaling the number concentration to match the FSSP measured profile of LWC. The scaling was performed in the same manner as described for cloud layers A and B.

Broadband Cloud Optical Property Calculations

A computer code, MIEAVG, was used to compute the broadband extinction cross section, asymmetry parameter, and single scatter albedo for each of the fixed normal gamma cloud droplet size distributions specified in cloud layers A, B and D. The MIEAVG code was developed by Peter Flatau in his Ph. D. research (Jerry Harrington, personal communication). The code employs a Mie scattering code, a drop size distribution integration routine, and a spectral band averaging routine to compute the broadband optical properties of an arbitrary normalized distribution of cloud droplets. The Mie scattering code is the same code as found in Bohren et al. (1983, Appendix A). The broadband averaging routine is based on the band averaging method of Slingo et al. (1982). In the following sections, we outline how the MIEAVG code computes the broadband extinction cross section, asymmetry parameter, and single scatter albedo for an arbitrary normalized distribution of cloud droplets.

The MIEAVG code calls the Mie scattering code to compute the optical properties of a single water drop with radius, r, at a given wavelength, λ. The references used by the code to determine the refractive index of water droplets for a given wavelength are listed in table 4.4. The optical properties of

the normalized distribution of drops are then computed by integrating the Mie optical properties over the distribution as follows

$$\sigma_{ext}^{s}(\lambda) = \int_0^\infty \pi r^2 Q_{ext}(x, n_r, n_i) n(r) dr , \tag{4.15}$$

$$\varpi_0(\lambda) = \frac{\int_0^\infty \pi r^2 Q_{sca}(x, n_r, n_i) n(r) dr}{\int_0^\infty \pi r^2 Q_{ext}(x, n_r, n_i) n(r) dr}, \tag{4.16}$$

$$g(\lambda) = \frac{\int_0^\infty \pi r^2 g(x) n(r) dr}{\int_0^\infty \pi r^2 n(r) dr}, \tag{4.17}$$

$$x = \frac{2\pi r}{\lambda}, \tag{4.18}$$

where σ_e^s is the extinction cross section, x is the size parameter, g is the asymmetry parameter, and ϖ_0 is the single scatter albedo. The spectrally averaged optical properties over a spectral band are computed by weighting each optical property by the distribution of radiative energy within the band. For an optical property $o(\lambda)$, the broadband average was determined by

$$o = \frac{\int_{\lambda_1}^{\lambda_2} o(\lambda) E(\lambda) d\lambda}{\int_{\lambda_1}^{\lambda_2} E(\lambda) d\lambda}, \tag{4.19}$$

where λ_1 and λ_2 are the limits of the spectral band, and $E(\lambda)$ is the distribution of energy within the band. For the solar bands, the distribution of energy was specified using the extra-terrestrial solar source function from the LOWTRAN 7 model. For the thermal bands, the distribution of energy was specified using the Planck function.

Cloud Optical Property Profiles

The vertical profile of the broadband volume extinction coefficient, single scatter albedo, and the scattering phase function for each layer was determined using the MIEAVG computed parameters (for each of the normal gamma size distributions in cloud layers A, B and D and the corresponding cloud droplet number concentration profiles. The broadband volume extinction coefficient profile was determined by multiplying the extinction cross-section and the cloud droplet number concentration profile. The single scatter albedo and the phase function were the same at all points within the cloud layers A and B and were vertically varying in cloud layer D.

The phase function was approximated using the Henyey-Greenstein (HG) function and the MIEAVG computed asymmetry parameter. The HG function was chosen based on the simplicity of its expansion in terms of Legendre polynomials. The HG function and its expansion are given by (AT 721 Class Notes)

$$P_{HG}(\mu) = \frac{1-g^2}{(1+g^2-2g\mu)^{3/2}} = \sum_l (2l+1) g^l P_l(\mu) \qquad (4.20)$$

where g is the asymmetry parameter. The HG function is different from the actual Mie phase function in that it does not capture the forward and backward peak of the Mie phase function. (Stephens AT721 Class notes). The change in the computed fluxes due to the HG phase function approximation should be at most a few percent (Wiscombe 1977). Since we were only concerned with fluxes and heating rates, the HG approximation is believed to be a valid approximation.

With the delta-M approximation and using eight streams, the phase function was given by (Wiscombe 1977)

$$P(\mu) = 2g^{16}\delta(1-\mu) + (1-g^{16}) \sum_{l=0}^{15} \frac{(2l+1)(g^l - g^{16}) P_l(\mu)}{1-g^{16}} \qquad (4.21)$$

The delta-M approximation was used to reduce the error due to the truncation of the phase function.

Atmospheric Profile of Temperature and Gaseous Extinction

To determine the vertical profile of gaseous extinction and thermal source function, vertical profiles of temperature, pressure, and gaseous constituents (CO_2, O_3, H_20,N_20 and CH_4) were required. These profiles were constructed using the N2Uw measurements, local sonde measurements, surface observations and climatology. The concentrations of CO_2, N_20, and CH_4 are uniform with height and were set to be 340.0, 0 .3, and 1.5 ppmv respectively (Liou, 1980). The vertical profile of O_3 was specified using values reported for the McClatchey midlatitude summer atmosphere profile (McClatchey et al., 1972). The profiles of temperature, pressure, and water vapor were determined using the S1 profile, measurements obtained from an ARM 11:30 UTC June 25 radiosonde launched at the U.S. SGP CART site , and values reported for the McClatchey et al. (1972) midlatitude summer atmosphere profile. The vertical levels at which each set of measurements were used are contained in table 4.5. The measurements taken by the ARM sonde were chosen because they were the closest in temporal and spatial proximity to the J25 experiment (the sonde was launched at the start of the experiment and the SGP CART site is located approximately 300 km south and west of the experiment). The surface pressure and water vapor mixing ratio were determined using the nearest co-located June 25 18:00 UTC surface observations.

Boundary Conditions

The in flight video showed that the J25ac system occurred over a vegetated surface. Measured values of the thermal emissivity (8-12 μm) for certain soil types were found in Houghton (1985), but none matched the type observed during the experiment. Houghton notes that the measurements for vegetated surfaces are relatively sparse but may be assumed close to unity. Therefore, the surface thermal emissivity for all spectral bands was assumed equal to unity. Since the reported values for natural earth surfaces range between 0.90 and 0.99, the error in the assumed thermal emissivity is expected to be at most 10%. It was found the for the assumed ground temperature of 305.9 K (90 F) , reducing the emissivity by 10% had the same effect as decreasing the ground temperature by 8.0 K. Values of the albedo of various surface types averaged over the solar spectrum are reported in Liou (1992). The reported value for croplands is

0.15. This value was used for the surface albedo in each spectral band. The zenith angle was found to range between 14° and 19° for the experiment. A value of 15° was chosen .

4.3.2.2 Model Output and Analysis

Each of the cloud optical property profiles B, BA, and D, along with the atmospheric extinction and temperature profile, and the specified boundary conditions were used as input for the SHDOM radiative transfer model. We used the model output from these calculations to examine the radiative heating rate structure of the J25acs in the location where each cloud layer was observed.

The model output from the calculation in cloud optical profile D was plotted as a function of height to examine the vertical distribution of thermal and solar heating in that cloud layer. The net cloud layer thermal and solar heating rates were also computed. Appendix F describes how the net layer heating rate was computed.

We used the model output from calculations in optical property profiles BA and B and the measured horizontal cloud LWC profiles in cloud layers B and A (described in section 4.2) to examine both the vertical and horizontal net radiative heating rate structure of the J25acs in its southern portions where cloud layers A and B were observed. This was achieved by first computing the net layer heating rate for layers A and B from the model simulated heating rates in the cloud optical property profiles B and BA. Next, we placed the computed heating rates on a schematic cloud diagram meant to represent the observed horizontal and vertical cloud structure of the J25acs in its southern portions. We referred to this diagram as a hypothetical net heating rate diagram. Fig. 4.1 shows how the net heating rates computed for layers B and A from calculations in cloud optical property profiles B and BA were placed on the schematic cloud diagram to construct the hypothetical net heating rate diagram for the J25acs in the southern portions of the system where cloud layer A was observed below layer B.

Because flight leg mean values of LWC and r_e were used to construct the optical property profiles B and BA, we chose to interpret the schematic heating rate diagram shown in Fig. 4.1 as follows. The net heating rates computed for layer B in cloud optical profile B were interpreted to indicate the possible net heating rates in that layer in regions of the J25acs where this layer was solely present. The net heating

rates computed for layer B in cloud optical profile BA was interpreted to indicate the possible the net heating rate in that layer in regions of the J25acs where cloud elements of layer B were positioned above cloud layer A. The net heating rate computed for layer A in cloud optical property profile B, was interpreted to indicate the possible net heating rate of the cloud free layer of air between elements of layer A below layer B. The net heating rates computed for layer A in cloud optical profile BA were interpreted to indicate the possible net heating rates of cloud elements of layer A in regions of the J25acs where this layer was positioned below cloud layer B. Because a number of approximations were made in the construction of the cloud optical property profiles, our main interest in the schematic net heating rate diagrams was their implied spatial net heating rate structure. This is because the spatial heating rate structure of the cloud could have implications towards the cloud dynamics.

Chapter Summary

In this chapter, we described our methodology used to examine the microphysical, thermodynamic, kinematic, and radiative structure of the J25acs. To summarize, we broke down the set of aircraft measurements into groups A, B,C, D and M. In each group, measurements were obtained in a systematic fashion and the observed cloud structure was similar. We then analyzed each group of measurements separately. The radiative structure was analyzed by constructing cloud optical property profiles. These profiles were used as input into the SHDOM radiative transfer model.

Table 4.1 Aircraft measurement and cloud classification system used in this research. NA means not applicable.

Data Group	Flight Leg	Altitude (m)	Pressure (mb)	Heading (deg)	Cloud Type	Cloud Layer
A	L1=A_l	5126	531	136	Cumuliform	A
	L2=A_u	5383	526	136	Cumuliform	
B	L4=B_u	5807	486	47	Stratiform	B
	L7=B1	5655	496	234	Stratiform	
	L9=B2	5655	496	55	Stratiform	
C	L11=C_u	5261	522	22	Cumuliform	C
	L12=C_l	5125	531	22	Cumuliform	
M	L10=M	5500	506	55-22	Clear Air	NA
D	S1	7119-608	368-917	Spiral	Stratiform	D

Table 4.2 List of the aircraft instruments (used in this research) and their measured parameters, range, accuracy, detection limits, and sampling rates . NR stands for not reported. Reference for each instrument indicated below instrument

Instrument	Measured Parameters	Range	Accuracy	Detection Limit	Sampling Rate
FSSP (Hobbs et al. 1981)	Cloud Drop Diameter	2.0-30.0 um	± 2.0 um	NR	10 Hz
	Cloud Droplet Number Conc.	NA	20 %	NR	10 Hz
Reverse Flow Minco Element (UWRAF)	Temperature	-50.0 - 50.0 ° C	0.5 ° C	0.006 ° C	10 Hz
HG&G Model 137 Hygrometer (UWRAF)	Dew Point Temperature	-40.0 - 30.0 ° C	±0 .5° C (>0° C) ± 1.0 ° C (< 0 ° C)	0.006 °C	10 Hz
1501 Rosemont Pressure Transducer (UWRAF)	Static Air Pressure	0.0 - 1080.0 mb	± 1.0 mb	0.034 mb	10 Hz
Honeywell Laseref SM IRS & Rosemont Pressure Probe (NCAR RAF)	Vertical and Horizontal Wind Velocity	± 200.0 m/s	± 1m/s	± 0.05 m/s	10 Hz

Table 4.3 CKDFU solar and thermal spectral band intervals. H_2O refers to line absorption and H_2Oc refers to continuum absorption.

Solar Band #	Gases	Wavelength Interval (μm)	Thermal Band #	Gases	Wavelength Interval (μm)	Thermal Band #	Gases	Wavelength Interval (μm)
1	O_3	0.2-0.7	1	H_20	4.5-5.3	7	H_20, H_20c	10.2-12.5
2	H_20	0.7-1.3	2	H_20	5.3-5.9	8	H_20, H_20c, CO_2	12.5-14.9
3	H_20	1.3-1.9	3	H_20	5.9-7.1	9	H_20, H_20c, CO_2	14.9-18.5
4	H_20	1.9-2.5	40	H_20	7.1-8.0	10	H_20, H_20c, CH_4, N_2O	18.5-25.0
5	H_20	2.5-3.5	5	H_20, H_20c	8.0-9.1	11	H_20, H_20c, CH_4, N_2O	25.0-35.7
6	H_20	3.5-4.0	6	H_20, H_20c, O_3	9.1-10.2	12	H_20	35.7-100.0

Table 4.4 References used by MIEAVG code to determine complex index of refraction of water

Spectral Interval (μm)	Reference
0.2-0.69	Hale et al. 1972
0.7-2.0	Palmer et al. 1974
2.0-100.0	Downing et al. 1975

Table 4.5 Sources of data used to construct the vertical profile of temperature, pressure, and water vapor for all radiative transfer calculations in the J25acs

Vertical Levels (km)	Data Source (T, P, w)
25.0-70.0	McClatchey mid-latitude summer atmosphere
7.9-25.0	Arm-Cart June 25, 16:30 UTC sonde
.5-7.9	N2Uw S1 profile

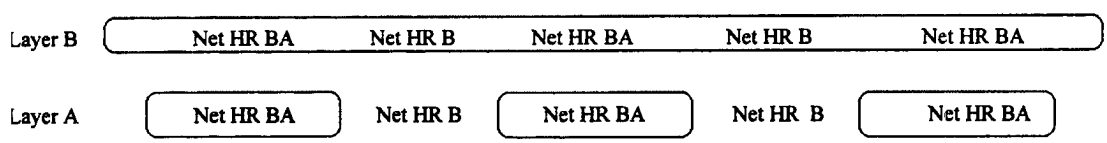

Fig. 4.1 Example of schematic cloud net heating rate diagram, used to examine spatial net heating rate structure of the J25acs in the southern portions of the system where cloud layers B and A were observed. Net HR BA and B are the net heating rate computed for a layer in cloud optical property profiles BA and B, respectively.

CHAPTER V

AIRCRAFT MEASUREMENTS AND RADIATIVE TRANSFER CALCULATIONS

Introduction

In this chapter, we present aircraft measurements collected during level flight legs in and between cloud layers A, B, C, and D and results from radiative transfer calculations in cloud optical property profiles B, BA and D. The relationship between the aircraft measurements in each data group are used to examine the spatial and temporal microphysical, thermodynamic, and kinematic structure of the J25acs and its environment. The results from the radiative transfer calculations are used to examine the spatial and temporal radiative structure of the J25acs. Comparisons between the measured and simulated structures of the J25acs and those observed in previous cloud studies are made. The chapter is organized into four sections : 1) microphysical measurements, 2) thermodynamic measurements, 3) kinematic measurements, and 4) radiative transfer calculations.

5.1 Microphysical Measurements

In this section, we present and discuss microphysical measurements for the set of flight legs through cloud layers A, B, C, and D and flight leg M. The measurements are used to examine the microphysical structure of each cloud layer. The relationships between the microphysical structure of each cloud layer are then used to examine the spatial and temporal microphysical structure of the J25acs. An understanding of the microphysical structure of the J25acs is important for two reasons: 1) the microphysical structure provides evidence that certain dynamical processes were occurring in the cloud and 2) it allows interpretation of radiative calculations presented in section 5.4.

As stated in Chapter IV, errors in the LWC, cloud droplet number concentration, and the cloud droplet effective radius can be as large as $\pm$ 50 %, $\pm$ 20 %, and $\pm$ 2 μm respectively. Given these uncertainties, we found it difficult to identify whether actual horizontal or vertical structure in the

microphysical properties of each cloud layer was present. This is because, in many instances, the standard deviation in the set of measurements for each flight leg was below the uncertainty in the measurements themselves. Also, the differences between the upper and lower level flight leg mean microphysical properties within each cloud layer were, in most cases, below the uncertainty in the values themselves. In our discussion of the vertical trends in the mean statistics, we will identify trends in the statistics, even though, in many cases these trends are below the accuracy of the measurements. In our discussion of the LWC profiles, we will identify horizontal fluctuations in the measurements even though they are, in many cases, below the accuracy of the measurements themselves. Comparisons between the horizontal profiles and observations are used to validate the LWC cloud structure

Cloud layer A

Figs 5.1a and 5.1b show subsets of the LWC measurements collected during flight legs A_u and A_l plotted as a function of distance. Both profiles show a number of horizontally distinct LW cloud regions separated by regions of LW cloud free air. Since observations identified this deck to be cumuliform in structure, we interpret these LW cloud regions to indicate horizontally distinct cumulus cloud elements. In the lower profile, the widths of cloud regions are between 100 and 300 m. In the upper profile, the widths of cloud regions are between 100m and 1000 m. Since the width of the cloud regions is larger in the upper profile as compared to the lower profile, this indicates that the cumulus elements of cloud layer A increased in width with height. In the lower profile, the LWCs range between 0.02 and 0.14 g/m^3 and the cloud regions appear to be regularly spaced every 5000 m. In the upper profile, LWCs are between 0.02 and 0.2 g/m^3 and LW cloud regions appear to be arranged in three distinct cloud groups. The width of these groups are between 1500and 2000 m, and they are regularly spaced every 4000m.

Table 5.1a show the microphysical flight leg statistics computed for flight legs A_u and A_l. A comparison of the liquid phase statistics for each leg, shows that the mean LWC, mean droplet number concentration, and the mean cloud droplet effective radius were computed to be 0.05 g m^{-3}, 66 cm^3, and 0.82 μm larger for the upper leg. Fig. 5.2 shows the mean FSSP droplet size distributions for each flight leg. Both distributions peak at a radius of 3 μm. The upper leg mean size distribution is slightly broader

than the distribution for the lower leg and the number concentrations of cloud droplets with $r \geq 2$ μm are all larger. The relationships between the mean droplets size distributions indicate that both the size and number concentrations of cloud droplets increased with height in cloud elements of layer A.

Cloud Layer B

Fig. 5.3a and 5.3b are subsets of FSSP LWC measurements obtained during flight legs B_u and B1 plotted as a function of horizontal distance. In both profiles, LWCs range between 0.05 g m^{-3} and 0.42 g m^{-3}. The upper profile shows an almost continuous distribution of LW cloud elements. The lower profile shows two distinct LW cloud regions which are roughly 4000 m in length and which are separated by a region of LW cloud free air which is 1000 m in length. Together , these profiles suggest that cloud layer B was composed of a more or less continuous distribution of cloud elements. This is consistent with visual observations presented in Chapter III which characterized layer B as a continuous and stratiform cloud layer. It is also consistent with GOES-8 0.7 μm imagery presented in Chapter III which showed continuous cloud coverage within the regions of the J25acs where measurements for these respective flight legs were obtained. The lower profile shows a more broken cloud structure than the upper profile. A possible interpretation of this trend is that the horizontally extensive cloud regions at lower levels expanded and merged with height to form the almost continuous distribution of cloud elements at upper levels in layer B.

Both the upper profile and the first extended cloud region within the lower profile show fluctuations in LWC of 0.05 and 0.1 g m^{-3} at spatial scales of 100 - 500 m. While these fluctuations may be due to instrument error, they indicate that cloud layer B was cellular in structure at these scales. This is consistent with our visual observations presented in Chapter III.

In the lower profile, LWCs within the first extended cloud region are consistently larger than the values within the second region. The LWCs in the first region are around 0.3 g m^{-3}, while LWCs in the second region are around 0.1 g m^{-3}. In the upper profile, certain extended regions are also characterized by consistently larger or smaller LWCs. Between 5000 and 7000 m, LWC values are around 0.3 g m^{-3} while between 2500 and 4500 m, LWC values are around 0.1 g m^{-3}. Since these differences are larger than

50 % possible errors in the LWCs, they indicate that there was large scale horizontal inhomogeneity in the LWC cloud structure of layer B. This is consistent with interpretations made of GOES-8 0.7 μm satellite imagery of the J25acs in chapter III. The cloud texture in the respective regions of each flight leg was interpreted to identify a cellular cloud structure. Because the resolution of the imagery is 1 km, this cellular structure must have been at scales greater than 1 km.

Tables 5.2 show the microphysical flight leg statistics computed for the flight legs B_u, B1 and B2. A comparison between the statistics for flight leg B_u and B1, shows that the LW cloud fraction, the FL mean LWC, and the mean cloud droplet effective radius were measured to be 0.37, 0.06 g m^{-3}, and 0.8 μm larger for flight leg B_u, while the mean cloud droplet number concentration was measured to be 38 cm^{-3} smaller. A comparison of the liquid phase statistics computed for flight legs B1 and B2 shows that the in-cloud mean LWC, the mean number concentration, and the mean effective radius were measured to be 0.04 g m^{-3}, 21 cm^{-3}, 0.4 μm smaller for the latter flight leg, while the cloud fraction was measured to be nearly the same.

Fig. 5.4 shows the mean FSSP droplet size distributions for flight legs B_u and B1. Each distribution is bimodal with peaks in radius at 3 and 7 μm. A comparison of each distribution shows that the mean number concentrations of cloud droplets with radii, $r \leq 8$ μm, are smaller and radii, $r > 8$ μm, are larger in the upper level distributions. Because each flight leg was horizontally collocated and were separated by a time period of 10 minutes, the relationships between each distribution indicate that the number concentrations of smaller cloud droplets decreased while the number concentrations of larger droplets increased with height in cloud elements of layer B. Also, because the mean LWC of cloud elements was measured to be the same while the number of cloud elements encountered during the upper leg was larger (the cloud fraction was larger), the larger flight leg mean LWC at upper levels must be a result of the larger number of cloud elements encountered at upper levels.

Fig. 5.5 shows the mean FSSP droplet size distributions computed for the lower level legs B1 and B2. The shape of the B2 distribution is similar to that of the B1 distribution and shows peaks at radii of 3 and 7 μm. The number concentrations of cloud droplets with radii , $r \leq 3$ μm, are larger while the number concentrations of cloud droplets with radii, $r \geq 4$ μm, are smaller in the B2 distribution. Since flight legs

B1 and B2 were in the same horizontal location and level of cloud layer B and were separated by a time period of 10 minutes, the relationships between these distributions indicate that the number concentration of cloud droplets with radii, $r \leq 3$ μm, increased while the number concentrations of cloud droplets with radii, $r \geq 4$ μm, decreased within cloud elements of layer B between the time period of each flight leg.

Cloud Layer C

Figs. 5.6a and 5.6b are the complete sets of FSSP LWC measurements for flight legs C_u and C_l plotted as a function of horizontal distance. The upper profile shows eight distinct LW cloud regions separated by regions of LW free air. The width of these regions range between 200 m and 1800 m and LWCs are between 0.01 and 0.49 g m^{-3}. These regions appear to be arranged into two distinct groups. The first group is between 0 and 4000 m and the second group is between 6000 and 9000 m. The lower profile shows a nearly continuous LW cloud region surrounded by regions of LW cloud free air. The width of this region is roughly 5000 m and LWCs are between 0.01 and 0.48 g m^{-3}. Because the width of regions in the upper profile are smaller than the region in the lower profile, it appears that cloud layer C became more broken with increasing height.

Fluctuations in the LWC which are as large as 0.5 g m^{-3} and which occur over scales of 100 to 500 m are shown in both profiles. Since these fluctuations are larger than the 50 % possible error in the LWC, they show that cloud layer C was highly cellular at scales of between 100 and 500 m. Cellularity at these scales is consistent with visual observations which characterized layer C as broken and cumuliform cloud layer. Therefore, we interpret these fluctuations to be a result of the aircraft encountering distinct cumuliform cloud elements with horizontal dimensions of between 100 and 500 m.

Taken together, the upper profile and the lower profile also suggest horizontal cloud structure at large spatial scales. Since the upper and lower level flight legs were separated by a distance of 600 m and were executed at the same heading within layer C, the LW cloud free region between 0 and 2000 m in the lower profile must be interpreted to correspond to a clear region of air separating the last cloud region encountered during the upper leg and the extensive cloud region encountered during the lower leg. Thus,

during flight legs C_u and C_l, the aircraft encountered three distinct cloud groups (each roughly 3000 - 5000 m) in length and separated by regions of cloud free air each roughly 2000 m in width.

Table 5.3 shows the liquid phase flight leg statistics for flight leg C_u and C_l. A comparison of the statistics computed for each flight leg shows that the in-cloud mean LWC, the mean effective droplet size, and the mean cloud drop number concentration were measured to be 0.01 g m^{-3}, 0.5 μm, and 7 cm^{-3} larger for the upper leg as compared to the lower leg. Fig. 5.7 shows the mean measured size distributions for the upper and lower level legs through cloud layer C. Each distribution is bimodal in shape with peaks at radii of 3 and 7 μm. A comparison of each distribution shows that the mean number concentrations of cloud droplets with radii, $r \geq 9$ μm and $r \leq 4$ μm, are larger while the mean number concentrations of cloud droplets with radii, $r \geq 5$ μm and $r \leq 8$ μm, are smaller in the upper leg. The relationships between these distributions indicate that within cloud elements of layer C, the number concentrations of cloud droplets with radii, $r \leq 3$ μm and $r \geq 9$ μm, increased while the number of cloud droplets with radii, $r \geq 5$ μm and $r \leq 7$ μm, decreased with height.

Flight leg M

This section presents microphysical measurements collected during flight leg M. The measurements are presented in the same format as for cloud layers A, B, and C. Since flight leg M was flown just above cloud layer C and just below cloud layer B, the measurements from this leg identify the horizontal LW cloud structure at this level. However, since the aircraft was turning during this leg, the measurements are not a systematic sample of the J25acs and should be examined with caution.

Fig. 5.8 show a subset of FSSP LWC measurement for flight leg M. Since flight leg M was executed between cloud layers B and C, this profile indicates that the region of air in between these two cloud decks was relatively LW cloud free. This is consistent with observations presented in chapter III. The profile also shows that several cloud elements were encountered towards the end of the leg. The values of the LWC within these cloud elements are between 0.25 and 0.43 g m^3. Because visual observations identified that cumulus cloud elements were rising out of cloud layer C, we interpret these LWC measurements to represent the aircraft encountering these cumulus cloud elements.

Table 5.4 shows the liquid phase microphysical flight leg statistics for flight leg M. The relatively small standard deviations in the drop size effective radius and number concentrations show that these parameters were similar in each of the cloud elements encountered during the leg. Fig. 5.9 shows the mean drop size distribution measured within these cloud elements. The distribution is bi-modal with peaks at radii of 3 and 7 μm. Unlike previous distributions the number concentration of droplets with radii of 7 μm is larger than the number concentration of droplets with radii of 3 μm. Through comparisons of this distribution with the mean distributions for flight legs C_u and C_l (fig 5.7), we found that the number concentrations of droplets with radii, $r \leq 6$ μm, were smaller while the number concentrations of droplets with radii, $r \geq 7$μm, were larger in the flight leg M size distribution. Since observations identified that the cloud elements measured during flight leg M were rising out of layer C, this indicates that the number concentrations of cloud droplets with radii, $r \geq 7$ μm, increased while the number concentrations of cloud droplets with radii, $r \leq 6$ μm, decreased with height in these cloud elements.

Relationships Among Flight Leg Statistics for Cloud Layers A, B and C and flight leg M

In the previous section, we identified the horizontal LW cloud structure of cloud layers A, B, and C at two different levels within each layer, vertical trends in the microphysical properties of each cloud layer, and the horizontal LW cloud structure encountered during flight leg M. In this section, we identify relationships between the microphysical statistics computed for flight legs within cloud layers A, B and C and flight leg M. These relationships serve to indicate both vertical and horizontal spatial trends in the statistical microstructure of the J25acs.

The relationships between the statistics for each leg are identified with aid of figures which show the flight leg statistics for each flight leg plotted as a function of height. Values for each leg are distinguished by plotting the cloud layer identifier next to the respective statistic. Because the flight legs with cloud layers A and C were at the same levels but at different locations (flight legs A_u, A_l, were in the southern portion while flight legs C_u and C_l were in the northern portions) in the J25acs; the relationships between the statistics for these legs serve to indicate horizontal trends in the statistical microstructure of the J25acs. Because the flight legs within cloud layer B were positioned above and to the north of flight legs

in layer A and above and to the south of flight legs in layer C and flight leg M; the relationships between the statistical properties computed for these legs serve to indicate both horizontal and vertical trends in the statistical microstructure of the J25acs. Since flight leg M was flown subsequent to the lower flight leg (B2) through cloud layer B and prior to the upper flight leg through cloud layer C; the relationships between these flight legs indicate the vertical trend in the microstructure of the J25acs in the location of flight leg M.

LW Cloud Fraction

Fig. 5.10 shows the LW cloud fraction computed for each flight leg within cloud layers A, B, C and flight leg M plotted as function of height. This figure indicates that the J25acs transitioned from a more broken structure at lower level to continuous cloud structure at upper levels. The relationships between the values for the level flight legs C_u, M, and B2 indicate that the cloud fraction first decreased and then increased rapidly with height in the northern portion of the J25acs where flight leg M was positioned. This is consistent with observations presented in chapter III, which showed that cloud layers B and C were separated by a relatively clear region of air in the location of flight leg M.

The almost linear increase in the cloud fractions for flight legs A_u, A_l, B1, B2, and B_u indicates that the cloud fraction increased linearly with height in the southern portion of the J25acs where flight legs A_u and A_l were positioned. Because the cloud fractions for flight legs C_u and C_l are larger than the fractions for flight legs A_u and A_l, this indicates that the cloud fraction at the vertical levels of these legs increased from the south to the north.

In-Cloud Mean LWC

Fig. 5.11 shows the IC mean LWC measured during flight legs within cloud layers A, B, and C and flight leg M plotted as function of height. Since the IC mean LWCs for flight legs C_u, C_l, B_l, B1 and B2 are close to the same in value, this indicates that IC mean LWC was constant with height in the northern portion of the J25acs where flight legs C_u and C_l were positioned. Taken together, the relationship between values for flight legs C_u, B2, and M indicate that the IC mean LWC increased and then decreased

with height in the northern portion of the J25acs where flight leg M was positioned. The relationship between values for flight legs A_u, A_l, B1, B2, and B_u indicates that the IC mean LWC increased with height in the southern portion of the J25acs where flight legs A_u and A_l were positioned. The relationships between the values for flight legs A_u, A_l, C_l, and C_u indicate that the IC mean LWC increased towards the north at the vertical levels of the J25acs where these flight legs were positioned.

Mean Effective Radius

Fig. 5.12 shows the mean cloud droplet effective radius measured during flight legs within cloud layers A, B, and C and flight leg M plotted as a function of height. Values range between 4.5 μm and 8.0 μm. Because values for flight legs C_u, C_l, B1, B2, and B_u are similar, this indicates that the mean effective cloud droplet effective radius was constant with height in the northern portion of the J25acs where flight legs C_l and C_u were positioned. The relationships between the values for flight legs A_u, A_l, B1, B2, and B_u indicate an almost linear increase with height in the mean cloud droplet effective radius in the southern portion of the J25acs where flight legs in A_u and A_l were positioned. The values for the flight legs C_u, C_l, and flight leg M also appear to indicate a linear increase with height. Since the values for flight legs C_u and C_l are roughly 1.5 μm larger than the values for flight legs A_u and A_l, this indicates that the mean drop size effective radius increased towards the northern portions of the J25acs at the levels where these flight legs were positioned.

Mean Number Concentration

Fig. 5.13 shows the mean number concentration of cloud drops measured during each flight leg within cloud layers A, B, and C and flight leg M plotted as a function of height. The values range between 134 cm^{-3} and 222 cm^{-2}. The relationship between the values for flight legs B2, C_u,, C_l, and M indicates that the mean number concentration of cloud droplets within cloud elements remained constant and then decreased with height in the northern portion of the J25acs where flight legs M, C_u, and C_l were positioned. The relationships between the values for flight legs A_u, A_l, B1, B2, and B_u suggest that the

mean number concentrations of cloud droplets within cloud elements increased and then decreased with height in the southern portion of the J25acs where flight legs A_l and A_u were positioned.

Cloud Layer D

Figs. 5.14-5.16 show measurements of the LWC, the cloud droplet effective radius, and the cloud droplet number concentration obtained during the S1 profile through cloud layer D plotted as a function of height. Because the aircraft sampled cloud layer D both horizontally and vertically during the S1 profile, these figures indicate both the horizontal and vertical microphysical structure of layer D. The vertical profile format was chosen to emphasize the vertical trends in the measurements.

Figs. 5.14-5.16 show that during the S1 profile through cloud layer D, three distinct LW cloud regions were encountered. Since cloud layer D was observed to be cellular in structure, we interpret each of these regions to represent horizontally distinct LW cloud elements. Since the aircraft was traveling at roughly 100 m s^{-1} during this profile and given the above interpretation , then the widths of these cloud elements were between 500 and 900 m and they were separated by clear regions of air which were between 500 and 700 m in width. Since the uppermost and lowermost LWC measurements were at 5995.0 m and 5832.0 m, we assume that these levels identify the top and base of the layer. This assumption leads to a cloud thickness of 163 m. In each LW region, Fig. 5.14 shows an increase in LWC with height. In Figs. 5.14-5.16, the profiles show an overall increase in the LWC and the cloud droplet effective radius with height and an overall decrease in the number concentration of cloud droplets with height. The lowermost and uppermost measurements of the effective radius are 3.4 and 7.5 μm, respectively. Measurements in the lower and upper portions of the number concentration profile are around 175.0 and 100.0 cm^{-3}, respectively. Assuming that the microphysical properties of each cloud element were similar, then these vertical trends indicate that, within cloud elements of layer D, the LWC and the cloud droplet effective radius increased with height while the cloud droplet number concentration decreased with height.

Summary of the Microstructure

Microphysical measurements collected during flight legs within cloud layers A, B, C, and D, and during flight leg M were used to examine the horizontal and vertical LWC cloud structure of each layer. A summary of their structure is as follows. Cloud layer A was composed of relatively narrow and widely spaced cloud regions which increased in width with height. Cloud layer B was composed of horizontally extensive cloud regions (≥ 4000 m) which increased in width with height such that the layer was composed of an almost continuous distribution of cloud elements at upper levels. While the distribution of cloud elements was continuous at upper levels, fluctuations in the LWC at spatial scales of between 100 and 500 m and between 2000 and 4000 m was present. Cloud layer C was composed of extensive cloud regions (≥4000m) which became more broken and more narrow with increasing height. Significant cellularity at scales of between 100 and 500 m was present in the layer. Cloud layer D was composed of LW cloud elements which were between 500 and 900 m in width and which were separated by clear regions of air between 500 and 900 m in width. Within cloud elements of layer D, the LWC and the effective radius of cloud droplets increased while the number concentrations of cloud droplets decreased with height.

The mean statistics were plotted as function of height to indicate spatial trends in the microphysical structure of the J25acs. A summary of these trends is as follows. In the southern portion of the J25acs where flight legs A_u and A_l were positioned and between the levels of flight legs A_l and B_u: the effective radius of cloud droplets, the width of cloud regions, and the LWC of cloud elements increased while the number concentrations of cloud droplets increased rapidly above cloud base and then decreased with height towards cloud top. In the northern portion of the J25acs where flight leg M was positioned and between the levels of flight legs B2 and C_u: the width of cloud regions decreased and then increased with height, the number concentrations remained constant and then decreased, and the effective radius of cloud droplets increased and then decreased with height. In the region of the J25acs where flight legs C_l and C_u were positioned and between the levels of flight legs C_l and B_u: the width of cloud regions decreased and then increased with height, the effective radius of cloud droplets remained constant with height, the number concentrations of cloud droplets remained constant and then decreased with height.

Implications of the Microstructure of the J25acs

The microphysical measurements within the J25acs indicate that several different dynamical and microphysical processes may have been occurring in the cloud. In the following paragraphs, we identify those measurements which we feel are significant, their correspondence between previous studies, and cite theories which have been used to explain them.

The mean cloud droplet size distributions measured at two levels within cloud layers B and C were shown to be bi-modal with peaks at radii of 3.00 and 7.00 μm. Also, the relationships between the mean distributions for the lower and upper level legs in layer B indicate that the distribution broadened with height in that layer. Previous aircraft studies, including those by Warner (1969), also observe these trends. Pruppacher (1987) summarizes the results from these studies and states that the "the tendency of the drop size distribution to be bimodal increased with height above cloud base and with decreasing stability of the environment". One possible explanation for these observations has been proposed by Baker et al. (1980). Using both theoretical arguments and laboratory simulations, they were able to show that a cloud droplet size distribution within a cloudy volume of air can develop a bi-modal spectrum and may also broaden due to the entrainment of discrete blobs of non-cloudy and under saturated air. Based on their results, the implications of the microphysical measurements presented in this study are that cloud elements in layers C and B may have been entraining discrete blobs of under saturated air.

The flight leg statistics for cloud layer A indicate that the number concentrations, cloud droplet sizes, and LWC increased with height above the bases and towards the middle portions of cloud elements in this layer. The S1 profile also showed similar trends at the base of cloud layer D. In Chapter II, results from the study by Heymsfield et al. (1991) were presented. Comparison of their results with ours shows that the vertical trends in the LWC, number concentrations, and effective radius are similar. As previously discussed, they were able to simulate the measured increase in droplet size and number concentration above cloud base by considering the condensational growth of an activated distribution of CCN within a saturated parcel of air ascending moist adiabatically (modified to include the effects of entrainment). Based on their success and the similarity in the measured trends from their study and ours , we believe that

cloud droplets within cloud elements at the base of layers A and D grew by condensation in ascending parcels of saturated air.

The relationships between the upper and lower level LW cloud profiles for layers A and B both indicate that horizontally distinct cloud regions (in these decks) were increasing in width with height. This was also revealed in the vertical trend in the flight leg LW cloud fraction which showed an almost linear increase from values of 0.08 to 0.97 between flight leg A_l and B_u. While these flight legs were not collocated and were executed at different headings, they suggest that the cumuliform cloud elements of layer A were expanding in width with height to form an almost continuous distribution of cloud elements at the top of layer B (in the southern portions of the J25acs). Previous aircraft studies within the cloud type, cumulus rising into stratocumulus, have also measured a similar vertical trend in the cloud fraction. One example is the study by de Roode et al. (1996). They show the cloud fraction to increase from values less than 0.1 at cloud base to 0.72 at cloud top.

To summarize, the microphysical measurements presented here indicate that entertainment and condensational growth of cloud droplets within updrafts may have occurred in the J25acs. They also indicate that in the southern portions of the system, cloud elements were expanding in width with height to form an almost continuous distribution of cloud elements at upper levels. In the next section, we explore the role which the thermodynamic structure of each layer might have played in determining the observed cloud structure.

5.2 Thermodynamic Measurements

In this section, we present measurements of the virtual potential temperature, θ_v, and relative humidity , RH, obtained during flight legs within cloud layers A, B and C, flight leg M, and the S1 sounding through cloud layer D. The measurements collected during flight legs in cloud layers A, B, C and flight leg M are presented in terms of flight leg statistics and hypothetical lapse rates.

We state here that the absolute uncertainty in the values of θ_v and the RH were generally around ± 0.9 K and 13 %, respectively. However, we are <u>not</u> concerned with the true values of θ_v. Rather, we are concerned with the relative differences in the measurements of θ_v. This is because these differences are

used to identify the static stability of each layer. Also, because we are interested in the static stability of each layer, we are primarily interested in the relative differences between the mean value for each leg.

S1 Sounding Profile of Temperature and Dew Point Temperature in SKEW-T Log-p Format

Fig. 5.15 shows the S1 sounding profile of temperature and dew point temperature between 368 mb and 914 mb plotted in a skew-T log-p format. Cloud layer D was encountered during the S1 profile between pressure levels of 474 and 485 mb. Cloud layers A, B and C were sampled between pressure levels of 486 and 530 mb. The temperature profile shows the presence of a quasi-isothermal layer between roughly 470 and 410 mb. Below this layer and down to roughly 600 mb, the temperature profile appears to follow the moist adiabatic lapse rate. The dew point temperature profile shows that the quasi isothermal layer was relatively dry as compared to air at the levels where cloud layers A, B, C, and D were sampled. Cloud layer D is identifiable within the dew point temperature profile as the relatively narrow saturated layer of air situated just below the base of the isothermal layer. The dew point profile shows that the moisture content of air decreased both above and below cloud layer D. The relative humidity of air 100 m above the top and 400 m below the base of the layer is 50 % and 70 % respectively. Between the pressure levels where cloud layers A, B and C were encountered, the dewpoint profile shows that a layer of dry air was sandwiched between layers of relatively moist air. A similar structure is also apparent between the levels of 530 and 590 mb. A comparison of the S1 T and T_d profiles with those in the Topeka and Dodge City sounding (Figs. 3.3 a and b) illustrates that similar features were measured in each profile.

Thermodynamic Measurements in Cloud Layers A, B ,and C

Cloud Layer A

Table 5.6a, b, and c show flight leg statistics of θ_v and RH measurements obtained during flight legs A_u and A_l and hypothetical lapse rate of θ_v computed for the atmospheric layers between flight legs A_u and A_l. The hypothetical lapse rate of θ_v for the layer between flight leg levels A_l and A_u indicates that the atmosphere was conditionally unstable between these levels and in the locations of these flight legs. The out-of-cloud mean relative humidities for both legs indicate that the cloud free air separating cloud

elements was moist. The difference between the in-cloud mean and out-of-cloud mean θ_v for each flight leg shows that cloud elements of layer A were measured to be warmer than their surrounding cloud free environment. This might be explained by the assumed saturation state of cloudy air parcels. Table 5.4b shows that all measurements of θ_v for the upper leg were within 0.7 K and measurements for the lower leg were within 0.5 K of one another. Because the measurements range by this amount, we must emphasize that the lapse rate within specific locations could have been different from the hypothetical lapse rates shown in Table 5.4c.

Cloud Layer B

Table 5.6a, b, and c show flight leg statistics for θ_v and RH measurements obtained during level flight legs B_u and B1 and the hypothetical lapse rate of θ_v computed for the atmospheric layer between flight legs B_u and B1. The out-of-cloud mean relative humidities for both legs indicates that cloud free air encountered at each level was moist. The hypothetical lapse rate of θ_v is greater than the moist adiabatic lapse rate indicating that the atmosphere was absolutely stable between the levels and in the locations of these flight legs. The differences between the in-cloud and out-of-cloud mean values of θ_v show that cloud elements at level B1 were measured to be slightly colder than the surrounding cloud free air. Table 5.5b shows that all measurements of θ_v for the upper leg were within 0.8 K and measurements for the lower leg were within 1.2 K of one another. Once again, because the measurements ranged by this amount, we must emphasize that the lapse rate within specific locations of the J25acs (where these flight legs were positioned) could have been completely different.

Cloud Layer C and Flight leg M

Table 5.7a,b and c show flight leg θ_v and RH statistics for flight legs C_u and C_l and hypothetical lapse rates of θ_v for the atmospheric layer between flight leg levels C_u and C_l. The relationship between the upper and lower level out-of-cloud mean RH indicate that the atmosphere was more moist at level C_l than at level C_u. The lapse rate of θ_v for both sets of flight legs indicate that the atmosphere was conditionally unstable between the levels and in the locations of these flight legs. The difference between

the in-cloud and out-of-cloud mean θ_v for the lower flight legs show that the mean θ_v measured in cloud elements was less than the mean θ_v measured in the cloud free environment. Table 5.7b shows that measurements of θ_v for the upper leg and lower leg were within 0.5 K of one another.

Tables 5.8a and b show θ_v and RH flight leg statistics for measurements obtained during flight leg M and the hypothetical lapse rate of θ_v for the atmospheric layer between flight leg levels M and B2. The mean and standard deviation in the out-of-cloud RH measurements indicate that the layer of air sampled during flight leg M was dry and that there was significant spatial variability in the moisture content of this layer. Because flight leg M was positioned above layer C, this indicates that the moisture content of air decreased with height above that layer C. The hypothetical lapse rate of θ_v indicates that the atmosphere was absolutely stable between the levels and in the region of flight legs M and B2. Also, the difference between the in-cloud and out-of-cloud mean θ_v shows that the mean θ_v measured in cloud elements was less than that in cloud free air.

Cloud Layer D

Figs. 5.18 a and b show measurements of θ_v, LWC, and RH collected during the S1 profile through cloud layer D and its environment plotted as a function of height. The saturated moist adiabatic lapse rate, ~ 3.7 K km^{-1}, is shown as the straight diagonal line. The S1 profile of θ_v and RH indicate that cloud layer D was situated at the base of a dry and absolutely stable layer of air and above a relatively shallow moist and quasi-saturated neutral layer of air. The RH profile shows a rapid decrease above the top of cloud layer D and up to roughly 6300 m. Above that level, values are stationary at roughly 45 %. The quasi-saturated neutral layer, below cloud layer D, is roughly 100 m deep and below it; the atmosphere is shown to be absolutely stable. Within cloud layer D, the profiles of θ_v and RH both show fluctuations. RH values in air parcels where LWC was measured should be neglected because these parcels were assumed saturated. The maxima and minima in fluctuations of θ_v differ by as much as ~2.0 K and they are separated by a depths of roughly 20 m. Because the differences between the maxima and minima are larger than the uncertainty (~± 0.9 K) in the measurements, we interpret this to mean they are real. Because the aircraft was traveling horizontally at roughly 100 m s^{-1}, then the horizontal separation distance between the maxima and minima is roughly 400 m and the implied horizontal gradient in θ_v between them is

roughly 5.0×10^{-3} K m^{-1}. A comparison of θ_v and LWC measurements shows that those air parcels measured to contain LWC were measured to have colder values of θ_v than those measured to be cloud free. Also, the measurements of θ_v in cloud elements appear to increase with height at roughly the moist adiabatic lapse rate. We also see that the maxima in θ_v at roughly 5960 m is similar in value to air measured above that level at 6050 m.

Given the relationships between measurements of θ_v and measurements of LWC, we interpret the S1 profile of θ_v measurements to indicate that cloud elements of layer D were colder than cloud free elements situated at similar vertical levels, and, within these cloud elements, the lapse rate was close to the saturated adiabatic lapse rate. Also, because air above layer D is shown to be roughly 3 K warmer than air measured in cloud, we conclude that, if a saturated cloud parcel were displaced upwards into this air, it would be negatively buoyant and would tend to return to its original level. Since air with values of θ_v similar to that measured 100 m above the cloud was also measured at levels within the cloud, it appears that entrainment processes may have been occurring in this layer.

Hypothetical Profiles of θ_v in the Northern and Southern Portions of the J25acs

In this section, we examine the relationships among the flight leg mean values of θ_v. These relationships are used to infer vertical trends in the mean θ_v of the J25acs in its northern and southern portions. We refer to these vertical trends as "hypothetical" profiles of θ_v.

Fig. 3.19a shows the hypothetical profile of θ_v in the southern portions of the system where flight legs A_u and A_l were positioned. The saturated adiabatic lapse rate, roughly 3.8 K km^{-1}, is indicated by the straight line. The standard deviations in the set of measurements for each flight leg are indicated by the horizontal bars. In the following paragraph, we invoke the parcel method to predict the vertical motion of a saturated parcel displaced upwards in this hypothetical profile.

The saturated parcel, if displaced upwards at level A_l, would immediately be warmer than its environment and would continue to rise via latent heat release and buoyancy. During its ascent, the parcel would gain momentum owing to continued upward acceleration. Arriving at a level of roughly 5800 m, the parcel would at the same θ_v as its environment, and would, therefore, experience a net downward

acceleration. Any momentum gained by the parcel would be lost and it would tend to remain at a level of roughly 5800 m.

Based on the predictions of the parcel method, one should expect that all saturated parcels of air, if displaced upwards in this hypothetical atmosphere at the level A_l, would arrive at and remain at a level close to where the top of cloud layer B was observed. Furthermore, if saturated air parcels were continuously displaced upwards in this atmosphere, one should also expect to find a continuous distribution of these elements at levels where cloud layer B was observed. Given that a number of cloud elements of layer A were observed to be merged with and rising into cloud layer B (in the southern portions of the systems) and cloud layer B was observed to consist of an almost continuous distribution of cloud elements, we note that these expectations are consistent with the observed cloud structure. They are not completely consistent with observations, however, because not all cloud elements of layer A appeared to be merged with cloud layer B.

Fig. 3.19b shows the hypothetical profile of θ_v in the northern portions of the system where flight legs M, C_u, and C_l were positioned. Invoking the parcel method for this hypothetical atmosphere, it is clear that a saturated parcel, if displaced upwards at level C_l, would continue to rise via latent heat release and buoyancy. However, in this case, the limit of moist free convection is at roughly 5600 m. Notice that this level is below that of flight leg B2. Given that cumuliform cloud elements were visually observed to be rising out of cloud layer C and were encountered at flight leg level M, we notice that the parcel method applied to this hypothetical profile can explain this observed cloud structure. Also, because these cumuliform cloud elements did not appear to be merged with cloud layer B (in the location of flight leg M), we see that the parcel method can explain this observed cloud structure, as well. However, based on the prediction made by the parcel method, we should expect that all saturated and displaced parcels at level C_l would continue to rise and remain at a level of 5600 m. This expectation is not consistent with observations. In fact, only a relatively small number of cumuliform cloud elements were observed in the location of flight leg M.

The S1 Profile of θ_v and RH

Fig. 5.20a and b show measurements of θ_v and RH obtained during the S1 profile with flight leg mean values also plotted as function of height. The top and bottom of cloud layer D are indicated by the horizontal dashed lines. In Fig. 5.20a, the saturated moist adiabatic lapse rate is indicated by the solid diagonal line.

The S1 profile of θ_v and the flight leg mean values both show a similar vertical structure. Between flight leg levels (A_l, C_l) and M, the S1 profile shows the atmosphere to be conditionally unstable. Between the levels of flight leg M and flight leg B_u, the profile shows the atmosphere to be absolutely stable. Between 4500 m and flight leg level (C_l ,A_l), the S1 profile shows two unstable layers. The first is between roughly 4500 and 4800 m and is conditionally unstable. The second is between roughly 4975 and 5025 m and is absolutely unstable. Above flight leg level B_u, the S1 profile shows several rapid fluctuations. Above 6100 m, the atmosphere is shown to be absolutely stable.

The S1 profile of RH measurements and the out-of-cloud flight leg mean values show a similar vertical structure, as well. Between flight leg levels B1 and B_u, both the S1 profile and flight leg mean values are above 90 %. Between level B1 and M, the S1 profile and the value for flight leg M both show RH to decrease with decreasing height and reach a local minimum (roughly 70 %) at level M. Between levels M and A_l, the profile shows the RH to increase with decreasing height and reach a local maximum of roughly 80% at level A_l. The flight leg mean values for layers A and C also indicate this trend however they are larger than the S1 profile values at all levels. Between 4900 and level A_l, the profile shows a similar structure as that above it. Values decrease with decreasing height towards a local minimum (~50%) at roughly 4900 m and then increase towards value of roughly 85 % at 4500 m.

Because the S1 profile was in a different location and time period than the level flight legs, we can not, a priori, assume that the profiles of θ_v and RH measurements shown in Figs. 5.19a and 5.19b represent the actual vertical structure of θ_v and RH above and below the J25acs in its southern and northern portions where the set of level flight legs were positioned. However, because the profiles and the flight leg mean values both show similar vertical structures, we believe they provide a good indication as to what the vertical structure of θ_v and RH above, below, and within the J25acs may have been like in these locations.

In the following paragraphs, we discuss the implications of the measured vertical profile of θ_v and RH towards the dynamics of the J25acs.

Above flight leg level B_u, the S1 profile indicates that the atmosphere was dry and absolutely stable. Because of the fluctuations associated with cloud layer D, we are not certain as to how dry or how stable the air was right above cloud layer B. However, we are fairly confident that at some point (within 100 m above level B_u) the relative humidity decreased with height while θ_v increased with height at a rate greater than the moist adiabatic. This thermodynamic structure implies that a saturated parcel of air, if displaced upwards at flight leg level B_u, would be negatively buoyant and would tend to return to its original level of displacement. Given that clear sky was visible above flight leg B_u and visual observations identified the aircraft to be positioned at the top of cloud layer B during this leg, we see that the implications of the static stability structure and visual observations are consistent.

Between flight leg level B1 and flight leg levels C_u and A_u, both the S1 profile and flight leg M mean value of RH indicate that air at that level was relatively dry as compared to air above and below this level. The implications of this vertical moisture structure may be understood by considering a rising cumulus cloud element of layer A or C positioned below this dry layer of air. As discussed by Hess (1959), if some fractional amount of dry air from aloft were mixed in with this element, then cloud droplets within it would evaporate and the temperature of the parcel would decrease. Thus, the buoyancy of the parcel would be reduced and the lapse rate traced out by the parcel would be less than the adiabatic lapse rate.

Between the levels of 4500 and 4800 m, the S1 profile of θ_v shows the atmosphere to be conditionally unstable. Thus, a saturated parcel of air, if displaced upwards at 4500 m in this atmosphere, would immediately be warmer than its environment and would continue to rise. Assuming that this parcel did not mix with its environment and no compensating motions took place, then we would expect this parcel to rise up to a level of roughly 4750 m. We observe that this is the same level at which cloud layer B was encountered. However, if the parcel were to mix with its environment, then we would expect it to rise at some rate below the moist adiabatic (Hess 1959) and hence, to some equilibrium level between 4500 and 5750 m. The relationship between the moist adiabatic lapse rate and the S1 profile, shows that the

slightest deviation from a moist adiabatic ascent by the saturated and rising parcel would result in a limit of free convection at about 4950 m. Because cumulus were observed below cloud layer C (during flight leg C_l), and the S1 profile shows the atmosphere to be conditionally unstable between 4500 and 4800 m, this is evidence that these cloud elements may have formed due to conditional instability. Further evidence is in the S1 profile of RH, which indicates that air at 4500 m was moist and that the relative moisture content was similar to air encountered at level C_l and C_u.

Summary of θ_v and RH measurements and conclusions

Measurements of θ_v and RH collected during flight legs through cloud layer A, B, and C, flight leg M, and the S1 profile have been presented. These measurements were used to examine the thermodynamic structure of each cloud layer and it's environment. A summary of the structure of cloud layers A, B and C is as follows. The flight leg mean statistics indicate that cloud elements of layers A and C were imbedded in a relatively moist and conditionally unstable layer of air while cloud elements of layer B were imbedded in a moist and absolutely stable layer of air. The mean θ_v of cloud elements in layer A was found to be 0.1 K greater than the mean θ_v in cloud free elements. The mean θ_v of cloud elements encountered during the lower leg of through layer C was found to be 0.1 K colder than the mean θ_v in cloud free elements.

While there is some degree of uncertainty as to the exact vertical structure of θ_v and RH in a particular location of the J25acs and at a particular time period within its evolution, based on the relationships between the flight leg mean statistics and the S1 profile of measurements, we conclude that the mean thermodynamic structure of the J25acs in its southern portions and for the time period between 16:30 UTC and 16:55 UTC was as follows:

- air within 100 m above the J25acs (above flight leg level B_u) was absolutely stable and was relatively dry
- air at upper levels of the J25acs (between levels B_u and B1) was moist and absolutely stable

- air at lower levels of the J25acs (between the levels of flight legs A_u and A_u) was conditionally unstable and moist
- the limit of moist free convection for a saturated parcel displaced upwards at a level of 5125 m (flight leg levels A_l) in the southern portions of the system was 5800 m

A comparison of the above described structure for the southern portions of the system between 16:30 UTC and 16:55 UTC with that observed by de Roode et al. (1996) in their study of cumulus rising into stratocumulus shows similarities. They find the cumulus layer to be imbedded within a conditionally unstable layer and below an absolutely stable layer. Within the stratocumulus layer, they find the lapse rate to be close to the moist adiabatic.

While their are similarities between the thermodynamic structure of the J25acs observed between 16:30 UTC and 16:55 UTC and the structure observed by de Roode et al. (1996), there is one important and obvious difference which should not be overlooked. In their study, de Roode et al. (1996) find the cumulus cloud layer to be situated on top of a well-mixed surface-based marine boundary layer. In the J25acs, we are not certain as to the vertical profile of θ_v below the J25acs observed between 16:30 and 17:00 UTC, however, we are certain that the J25acs was not coupled to a well-mixed surface-based marine boundary layer.

The S1 profiles of θ_v and RH measured during descent through cloud layer D were used to examine the thermodynamic structure of this cloud layer and its environment. A summary of our interpretations of this structure is as follows. Cloud layer D was situated below a dry, relatively deep, and absolutely stable layer of air and above a relatively shallow and moist quasi-saturated neutral layer. Within cloud elements of layer D, the lapse rate was close to the moist adiabatic. Also cloud elements near cloud top were colder than cloud-free elements at similar vertical levels. The values of θ_v within cloud free elements was similar to those encountered just above the top of the layer suggesting that these elements had been entrained into cloud layer D.

The thermodynamic structure of cloud layer D is similar to that observed within the two separate altocumulus layers studied by Heymsfield et al. (1991) A summary of the thermodynamic structure of each layer may be found in chapter II. In their study, Heymsfield et al. (1991) conclude that the

thermodynamic structure of their observed cloud layers is similar to that found within stratocumulus clouds. They state that, "the clouds were structurally and thermodynamically similar to stratocumulus, with extensive cloudtop entrainment, a capping temperature inversion, and a dry layer above." Because the thermodynamic structure of cloud layer D is similar to the structure of the Ac cloud layers observed by Heymsfield et al. (1991), we also draw similar conclusions. However, we conclude that cloud layer D was structurally similar to stratocumulus clouds decoupled from a well-mixed surface-based moist boundary layer.

Kinematic Measurements

In this section, we present measurements of u, v, and w winds obtained during flight legs in cloud layers A, B, and C, flight leg M, and the S1 sounding profile. The measurements of u and v winds obtained during level flight legs are presented in terms of their flight leg statistics. The statistics presented here are the flight leg mean and variance, the in-cloud mean, and the out-of-cloud mean. Our main attention is given to the relationships among the various flight leg mean values. These relationships serve to indicate the mean vertical and horizontal kinematic (u and v) structure of the J25acs. They also were used to examine the stability of each layer with respect to Kelvin-Helmholtz instability. To identify relationships among the mean values, we plotted them as a function of height on the same figure as the S1 profile.

The measurements of w winds obtained during level flight legs in cloud layers A, B, and C are presented in terms of horizontal profiles and flight leg statistics. The horizontal profiles are 100 s subsets of w wind velocity measurements. These profiles serve to indicate the horizontal structure in the measured w wind field in each cloud layer. To identify possible relationships between the horizontal LW cloud and w wind velocity structure, LWC cloud measurements are also shown on these profiles. In our discussion of the w wind velocity profiles, we focus on the relative differences among the measurements. We do not give attention to the actual values themselves. This is because, in most profiles, w wind velocity measurements are below the absolute accuracy of the measurement. To aid in identification of the relative differences between measurements, we plotted the mean value (computed for each 100 s subset) on the

horizontal profile. It will be our interpretation that measurements which are 0.05 m s^{-1} above the mean value identify regions of "rising" motion and measurements which are 0.05 m s^{-1} identify regions of "sinking" motion. When we say "rising" or "sinking" motion, we implicitly mean that the air is rising or sinking relative to air in its surrounding environment (in this case the environment is considered to be the region of atmosphere encountered during the 100 s subset of each flight leg) . We chose a value of 0.05 m s^{-1} as a threshold to identify regions of rising and sinking motion, because this is the reported minimum detection limit of the instrument. We also performed a statistical analysis of the subset of w measurements for each flight leg. In this analysis, we computed the fractional coverage of regions of rising motion and sinking motion, the mean, maximum values of rising and sinking motion, and the skewness.

u and v Wind Measurements

Figs. 5.20 a and b show u and v wind velocity measurements obtained during the S1 profile and flight leg mean values for flight legs in cloud layers A, B, C and flight leg M plotted as a function of height. Focusing on the u wind measurements, the S1 profile shows winds to transition from light easterly values at 4500 m to westerly values of roughly 5 m s^{-1} at 5700 m. The flight leg mean values for flight legs C_u, C_l, and M show the same vertical trend as the S1 profile (between their respective levels). The relationship between flight leg mean values B1 and B_u indicate that u wind speeds increased with height in cloud layer B. Between the levels of cloud layer D, the S1 profile shows fluctuations which appear to be correlated with fluctuations in the LWC profile. These correlations indicate that cloud elements within layer D were characterized by more easterly momentum than cloud free air. Examination of the flight leg statistics in table 5.10 also indicates that for flight legs B_u, B1, M, C_u and C_l, cloud elements were characterized by more easterly momentum than cloud free elements. For example, the in-cloud mean values computed for flight legs M and B_u are 2.1 and 1.4 m s^{-1}, respectively, more easterly than the out-of-cloud mean value.

Focusing on v wind velocity measurements, the relationship among the flight leg mean values indicate that v winds were light (values are around 5 m s^{-1}) and southerly at all levels. The S1 profile also indicates this vertical trend and shows similar values between flight leg levels B_u and A_l. Just above cloud

layer D, the S1 profile shows a rapid increase in v winds by roughly 3 m s^{-1}. Above that level, the profile increases more gradually towards a maximum value of 10 m s^{-1}. Between the levels of cloud layer D, the S1 profile shows several rapid and relatively small fluctuations in the lower portions of the layer and then a rapid increase and decrease in the upper portion of the layer. The maximum value (~ 8 m s^{-1}) associated with the rapid increase is similar to values of v wind velocity measured in air just above cloud layer D. A comparison of the v wind velocity profile and LWC profiles also shows that the maximum value was measured in cloud free air. Thus, it appears that, in its upper portions, cloud layer D was composed of a mixture of air with distinctly different values of v momentum. Because the momentum of an air parcel is a conserved quantity in the absence of mixing or acceleration, one possible interpretation of Fig. 5.20b might be that the cloud free air parcel encountered during the S1 profile through cloud layer D with momentum values similar to air above it was just brought down into cloud layer D (i.e. that this air parcel was entrained into cloud layer D).

Table 5.11 shows the Richardson number computed for cloud layers A, B, and C. Because the number for each layer is larger than 0.25, it does not appear that vertical wind shear played a role in the generation of TKE in the observed cloud layers.

w Wind Velocity Measurements in Cloud Layers A, B, and C

Cloud Layer A

Fig. 5.21a and b show subsets of w wind velocity and LWC measurements obtained during flight legs A_u and A_l plotted as function of horizontal distance. Focusing on the lower profile, we see that regions of rising motion are generally narrow (100-200 m in width) and values are as large as 0.70 m s^{1}. Regions of sinking motion are more extensive and values are as large as -0.50 m s^{-1}. The regions of most intense rising motion are shown to occur in the same general location as regions where LWC cloud elements were encountered. Focusing on the upper profile, we see that regions of rising motion are between 300 and 1500m in width and values range between roughly +0.05 and +2.0 m s^{-1}. Regions of sinking motion appear to be more extensive than regions of rising motion and values of sinking motion

range between -0.1 and -0.4 m s^{-1}. Regions of rising motion are generally shown to occur in the same locations as regions where LWC cloud elements were encountered.

Table 5.11 shows the rising and sinking motion statistics computed for the upper and lower level subsets of wind velocity measurements obtained during flight legs A_u and A_l. We notice that for both legs, the fractional area covered by regions of rising motion is smaller than for regions of sinking motion, while the maximum value of rising motion is roughly a factor of two greater than the maximum value of sinking motion. Given these statistics and the visual appearance of the w wind velocity measurement profiles , we might expect that the skewness should be positive. Table 5.11 shows that the skewness computed for both the upper and lower profiles was positive.

Cloud Layer B

Fig. 5.22a and b show subsets of w wind velocity and LWC measurements obtained during flight legs B_u and B1 plotted as function of distance. Focusing on the lower profile, we see that both regions of intense rising and sinking motion were encountered during flight leg B1. The regions of intense sinking motion are relatively narrow (100-200 m in width) and the maximum value of sinking motion is -1.0 m s^{-1} (see Table 5.11). Regions of intense rising motion are between 300 and 1000 m in width and the maximum value of rising motion is 1.5 m s^{-1}. A comparison of the LWC profile and the w wind velocity profile shows that at large spatial scales regions of rising motion and values of LWC are related. Between points 0 and 4000, the w profile generally shows rising motion and values of LWC are relatively large. Between points 5000 and 10000, the w profile generally shows sinking motion and values of LWC are either zero or are relatively small.

The upper w profile shows fluctuations at both large and small spatial scales. The large scale fluctuations appear to be correlated with the large scale fluctuations in the LWC profile. For example, between points 4500 and 7000, LWC values are relatively large and w measurements generally show rising motion. Between points 3000 and 4000, LWC values are relatively small and w measurements generally show sinking motion. The small scale fluctuations in the w profile indicate that relatively narrow (200-500 m in width) and intense regions of rising and sinking motion were both encountered during flight leg B_u.

Table 5.11 shows the rising and sinking motion statistics computed for the upper and lower level 100 s subsets of wind velocity measurements obtained during flight legs B1 and B_u. We see that for the subset of measurements obtained flight leg B1, the fractional area covered by regions of rising motion was slightly smaller than that covered by regions of sinking motion; the mean values (of rising and sinking motion) were the same; and the maximum value of rising motion was 0.5 m s^{-1} larger than the maximum value of sinking motion. The statistics computed for the upper level subset are different. They show that the fractional area covered by regions of rising motion was slightly larger than that covered by regions of sinking motion, and that the maximum value of sinking motion was 0.2 m s^{-1} larger than the maximum value of rising motion.

Cloud Layer C

Figs. 5.23a and b show the entire set of w wind velocity and LWC measurements obtained during flight legs C_u and C_l plotted as a function of distance. In the lower w profile and between points 4000 and 7000, w values indicate that air was generally rising. This region is surrounded by regions where air is shown to be generally sinking or stationary. The shape of the w profile appears to be the same as that of the LWC profile. Intense fluctuations at scales of between 200-500 m are shown in the same region where the most intense rising motion is indicated. These fluctuations indicate that the regions of most intense rising motion were relatively narrow and were separated by regions where air that was stationary or was sinking.

Focusing on the upper w profile and between points 0 and 3500, we see a number of relatively intense and narrow (100-500 m) regions of rising motion separated by regions of narrow and intense sinking motion. The shape of w and LWC profile appear to be similar in this region. Between points 3500 and 5500, the w profile shows relatively small fluctuations and regions of sinking and rising motion are both shown. Between points, 6000 and 10000, the w profile shows several regions of relatively intense rising motion separated by regions of relatively weaker sinking motion. The most extensive region of rising motion is roughly 1200 m in width and the maximum value of rising motion in this region is 2.2 m s

[1]. The shape of the w profile appears to be similar to that of the LWC profile. For example, between points 7000 and 9000, the LWC profile and w profile both show increase and then decrease.

Table 5.11 shows the rising and sinking motion statistics for the set of w measurements obtained during flight legs C_u and C_l. The statistics for the upper and lower flight legs both show that the fractional coverage by regions of rising motion was smaller than by regions of sinking motion while the maximum and mean values of rising motion were both greater. Given these statistics and the visual appearance of each horizontal profile, we might expect positive values of skewness to be computed for the set of w measurements shown in Figs. 5.23a and b. Table 5.11 shows that skewness values for each subset were computed to be positive.

Relationships Between w Wind Measurements in Cloud Layers A, B and C

A comparison of the statistics computed for flight legs A_u, A_l, B_l, and B_u, indicate that the fractional area occupied by regions of rising motion (relative to surrounding air) increased with height while the fractional area occupied by regions of sinking motion (relative to surrounding air) decreased with height between the levels of these flight legs and in the southern portion of the J25acs where flight legs A_u and A_l were located. They also show that maximum value of rising motion was measured at flight leg level A_u, while the maximum value of sinking motion was measured at flight leg level B_u.

A comparison of the statistics for flight legs A_u and A_l and flight legs C_u and C_l reveals both similarities and differences. Both sets of flight legs show the fractional area covered by regions of rising motion to be smaller than the fractional area covered by regions of sinking motion while the maximum and mean values of rising motion are greater. However, the maximum and mean values of rising and sinking motion are relatively larger for flight legs C_u and C_l. This is especially true for flight legs C_l and A_l, where the maximum and mean values of rising motion computed for flight leg C_l are a factor of three larger and the maximum and mean values of sinking motion are a roughly a factor of four larger.

5.4 Radiative Transfer Calculations

In this section, we present results of radiative transfer calculations in the cloud optical property profiles B, BA and D. We use these results as a guide for understanding what the radiative heating rate structure of the J25acs may have been like in the locations where flight legs A_u, A_l, B_u, and B1 were positioned and in the location where cloud layer D was observed. Fig. 5.25 shows the atmospheric sounding profile in which each of the cloud optical property profiles was placed. Fig. 5.26 shows the profile of liquid water used to construct the cloud optical property profiles B and BA. Table 5.11 shows the cloud drop effective radius, the effective radius variance, the 10.2 -12.5 μm optical properties and 0.2-0.7 μm optical properties computed for cloud layers A and B . As discussed in Chapter IV, the LWC profiles for each layer was constructed by linear interpolation of the in-cloud mean values for the upper and lower flight legs in the layer. The cloud droplet effective radius and effective radius variance were set to be the same at all points in each layer.

Calculations in Cloud Optical Property Profiles B and BA.

Fig. 5.27 shows a schematic diagram of the hypothetical net thermal heating rate structure of the J25acs in its southern portions where cloud layer A was observed below cloud layer B. In all regions, cloud layer B shows net cooling. Cloud elements of layer A show net heating rates while the cloud free regions surrounding cloud layer A show zero net heating rate. The horizontal net thermal heating rate structure of layer B shows that the radiative effect of cloud layer A on cloud layer B, in these calculations, was to increase its cooling rate by a factor of two.

Fig. 5.28 shows a schematic diagram of the hypothetical net solar heating rate structure of the J25acs in its southern portions where cloud layer A was observed below cloud layer B. Layers A and B both show net solar heating rates. The net solar heating rates of layer B are larger than those in layer A. In regions where cloud elements of layer A are below layer B, solar heating rates for each layer are 0.2 C hr^{-1} larger than the surrounding regions. This is due to reflection of solar radiation by layer A back into layer B where it is further absorbed.

Fig. 5.29 shows a schematic diagram of the hypothetical net thermal+solar heating rate structure of the J25acs in its southern portions where cloud layer A was observed below cloud layer B. A comparison of this figure with Fig. 5.27, shows that the effects of solar radiation on the hypothetical spatial net radiative heating rate structure of the J25acs are substantial. Cloud layer B still shows net cooling rates in all regions while layer A shows net heating rates in all regions. However, the horizontal cooling rate structure in layer B now shows substantially larger gradients than those shown in Fig. 5.27. The cooling rates differ by a factor of six.

The implications of the hypothetical net radiative heating rate structure shown in Fig. 5.29 are summarized as follows. Because layer B shows a net cooling rate while layer A shows a net heating or zero heating rate, we should expect that, if this heating rate structure were to persist, the lapse rate between the levels of layer B and layer A would tend to become unstable. Thus, this heating rate structure would tend to promote convection between the levels of layers B and A. Because the net cooling rates and net heating rates of layers A and B are larger in regions where cloud elements of layer A were positioned below layer B, this implies that the destabilization effect would be more pronounced in these regions. Because the net heating rates of cloud elements of layer A are larger than the heating rate in the cloud free surrounding air at the same level, we expect that if this horizontal heating rate structure were to persist then cloud elements of layer A would become warmer than their surrounding cloud free environment and hence positively buoyant. For these calculations, cloud layer A would be 0.2 C warmer than surrounding cloud free air in 10 minutes. Because the net cooling rate structure of layer B shows horizontal differences, we should expect that, if this heating rate structure were to persist, then certain regions of cloud layer B would become colder and hence negatively buoyant with respect to surrounding regions. These negatively buoyant regions would then tend to sink. Thus, based on the results from these calculations, one might expect to find regions of intense sinking motion within cloud layer B. Given that regions of sinking intense sinking motion were observed in cloud layer B, we notice that there is consistency between the implications of the radiative structure and the w wind measurements.

Calculation in Cloud Optical Property Profile D

This section presents and interprets results from the radiative transfer calculations in cloud optical property profile D. Table 5.13 shows the three effective radii and effective radius variances used to construct the optical property profile for layer D , the vertical levels between which they were specified to be constant with height, and the MIEAVG computed 10.2 - 12.5 μm and 0.2 -0.7 μm optical depth, single scatter albedo, and asymmetry parameter for each of the layers. The vertical profile of LWC for layer D is shown in Fig. 5.14.

Fig. 5.30a and b show the calculated thermal and solar heating rate profiles within cloud optical property profile D. The thermal heating rate profile shows relatively intense cooling rates in the upper portions and weaker thermal heating rates in the lower portions of the profile. The maximum cooling rate is at the top of the profile and is 18.9 C hr^{-1}. The maximum thermal heating rate is positioned 20 m above the base of the profile and is 1.4 C hr^{-1}. The solar heating rate profile shows the maximum value, 2.6 C hr^{-1}, at the top of the profile and a decrease below that level.

Fig. 5.31c shows the simulated thermal+solar radiative heating rate profile. A comparison with Fig. 5.31a shows that the effect of solar radiation is to decrease the simulated cooling rates in the upper portions of the profile and to increase the heating rates in the lower portions of the layer. The net thermal, solar, and thermal plus solar heating rates calculated for layer D are -1.2, 0.7, and -0.5 C hr^{-1}. Thus, the effect of solar absorption is to decrease the net cooling rate of the layer by roughly 50 %. Because this simulated profile shows cooling in the upper portions and heating in the lower portions, we expect that, if it were to persist, then the lapse rate within cloud layer D would tend to become unstable and convective overturning would occur.

Chapter Summary

In this chapter, aircraft measurements and results from radiative transfer calculations were presented. The aircraft measurements were used to examine the spatial and statistical microphysical, thermodynamic, and kinematic structure of cloud layers A, B, C, and D. The relationships among the measurements obtained in each of these layers and those obtained during flight leg M were used to

examine the vertical and horizontal structures of the J25acs. The radiative transfer calculations in cloud optical property profiles B and BA were used to examine the net radiative structure of the J25acs in its southern portions where cloud layer B was observed above cloud layer A. The radiative transfer calculations in cloud optical profile D were used to examine the radiative heating rate structure of the J25acs observed between 17:45 and 18:10 UTC.

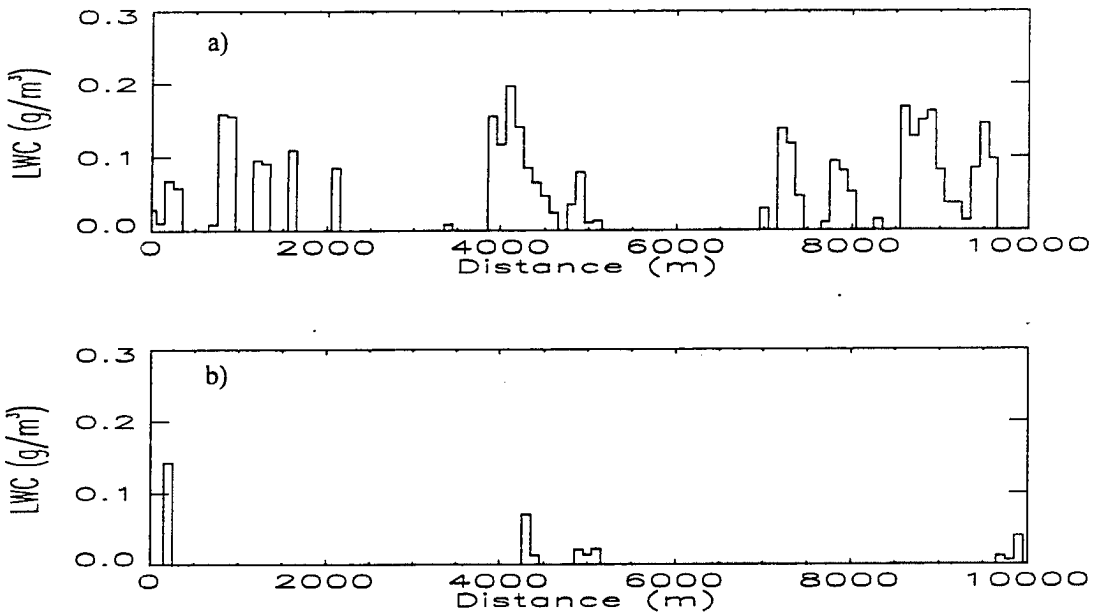

Fig. 5.1 FSSP measured LWC as a function of distance for flight legs a)A_u and b) A_l through cloud layer A. Uncertainty in LWC measurements are ± 50 % of measurement.

Table 5.1 Liquid phase microphysical statistics for the two level flight legs in cloud layer A. Mean statistics are reported as mean ± standard deviation in measurements. Uncertainty in the in-cloud mean LWC, mean cloud droplet effective radius, and mean number concentration are ± 50 %, ± 2.0 μm, and 20 % respectively.

flight leg	cloud fraction	flight leg mean LWC (g m^{-3})	in-cloud mean LWC (g m^{-3})	mean cloud droplet effective radius (μm)	mean number concentration (# cm^{-3})
A_u	0.35	0.028	0.08 ± .053	5.3 ± 0.8	200 ± 101
A_l	0.08	0.003	0.03 ± .036	4.5 ± 0.8	134 ± 88

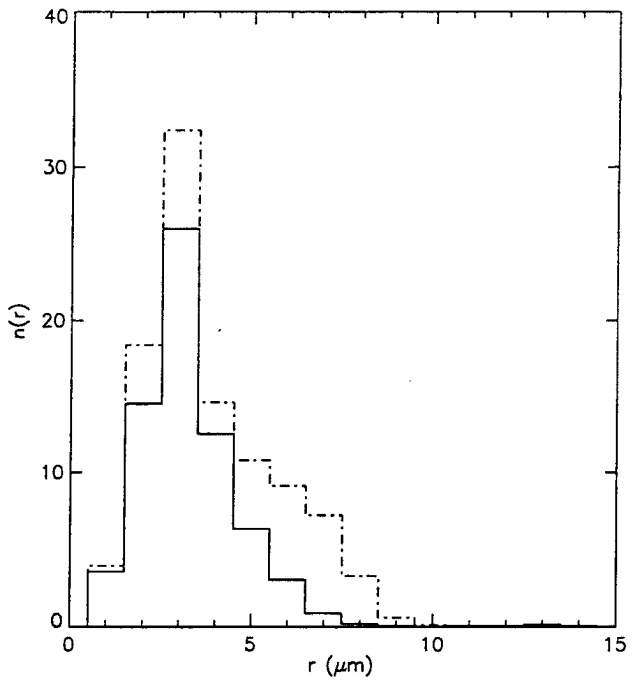

Fig. 5.2 Mean FSSP droplet size distributions computed for flight legs A_u(dashed line) and A_l (solid line) through cloud layer A. Uncertainty in number concentration are ± 20 % of measurement.

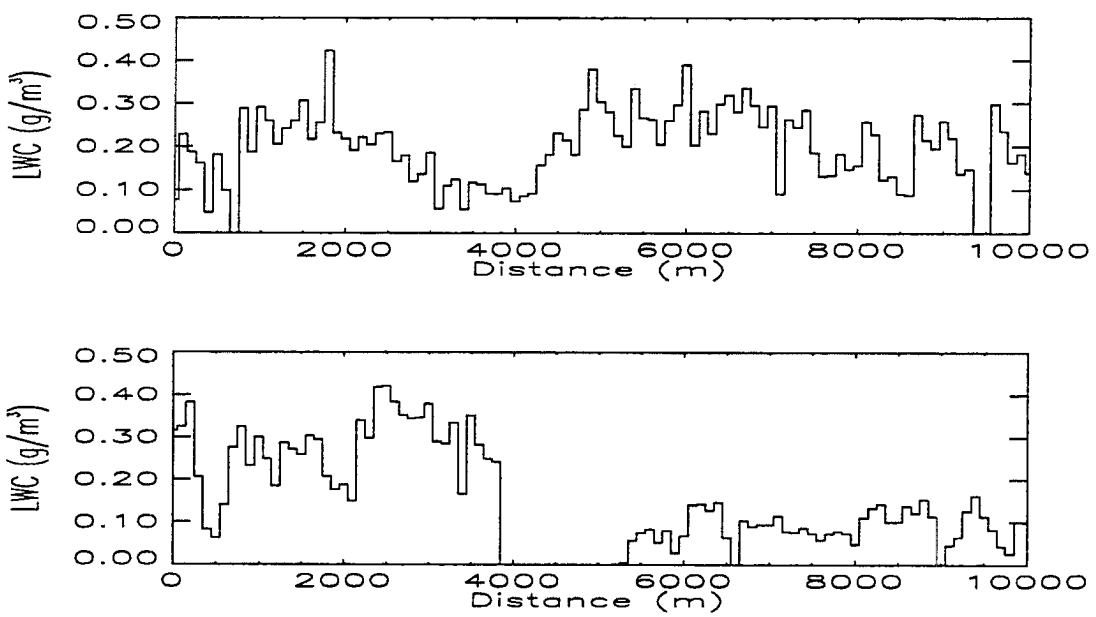

Fig. 5.3 Subsets of FSSP measured LWC as a function of distance for flight legs a) B_u and b) B1 Uncertainty in LWC measurements are ± 50 % of measurement.

Table 5.2 Liquid phase microphysical flight leg statistics for flight legs B_u, B1, and B2. In-cloud mean statistics are reported as mean ± standard deviation in measurements. Uncertainty in the in-cloud mean LWC, mean cloud droplet effective radius, and cloud droplet number concentration are ± 50 %, ± 2.0 μm, and 20 % respectively.

flight leg	cloud fraction	flight leg mean LWC (g m^{-3})	in-cloud mean LWC (g m^{-3})	mean cloud droplet effective radius (μm)	mean number concentration (# cm^{-3})
B_u	0.93	0.14	0.15 ± 0.09	7.1 ± 1.3	138 ± 56
B1	0.56	0.09	0.15 ± 0.12	6.3 ± 1.2	176 ± 74
B2	0.57	0.06	0.11 ± 0.10	5.9 ± 1.4	155 ± 69

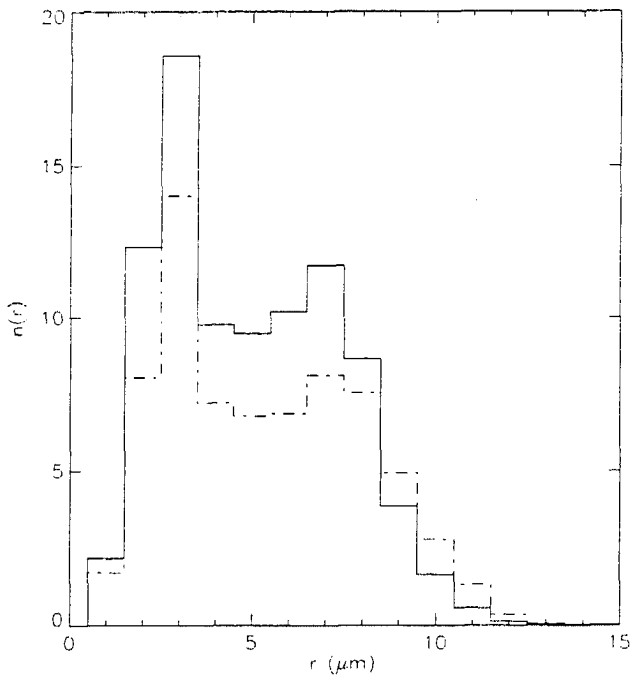

Fig. 5.4 Mean FSSP droplet size distributions for the upper level (dashed line) flight leg and lower level (solid line) flight leg B1 through cloud layer B. Uncertainty in number concentrations are ± 20 %. Number concentrations 2.5 cm^{-3} could be due to ice contamination

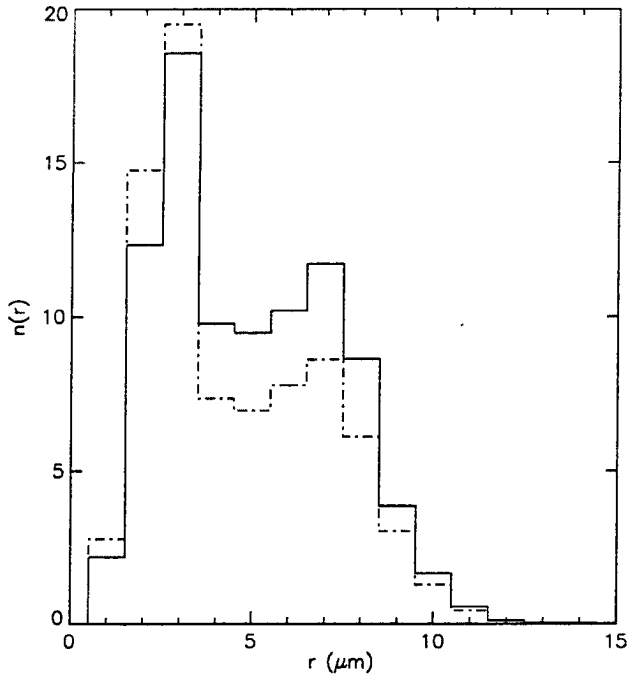

Fig. 5.5 Mean FSSP droplet size distributions for flight leg B2 (dashed line) and B1 (solid line) through cloud layer B. Uncertainty in number concentrations are ± 20 %. Number concentrations < 2.5 cm^{-3} cloud be due to ice contamination.

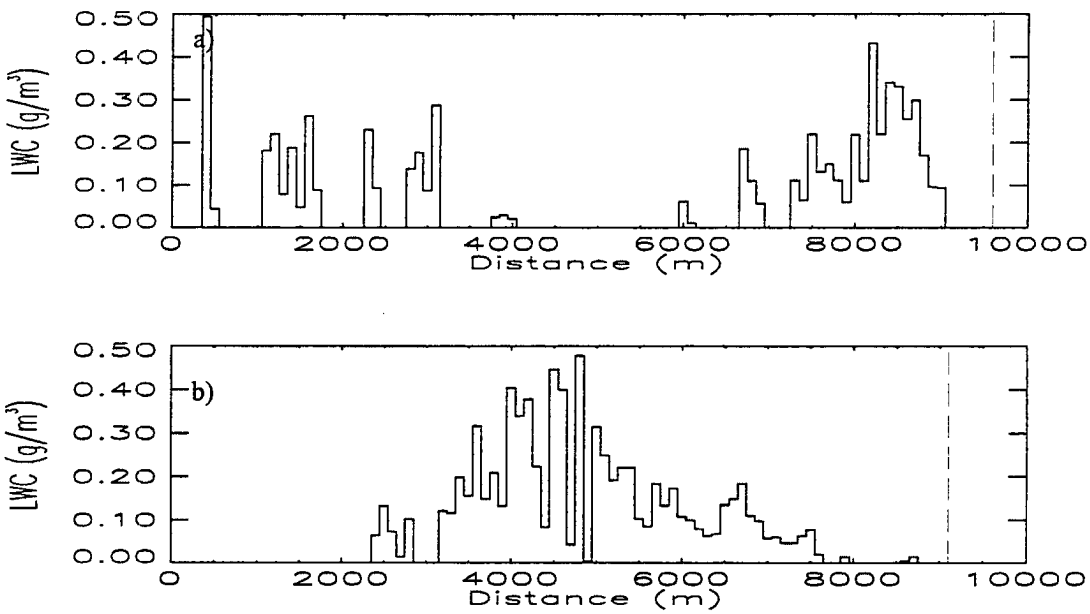

Fig. 5.6 FSSP measured LWC as a function of distance for flight legs a) C_u and b) C_l through cloud layer C. Dashed line identifies end of flight leg. Uncertainty in each LWC measurements is ± 50 % of measurement.

Table 5.3 Liquid phase microphysical statistics for flight legs C_u and C_l through cloud layer C. In-cloud mean statistics are reported as mean ± standard deviation. Uncertainty in the in-cloud mean LWC, mean cloud droplet effective radius, and cloud droplet number concentration are ± 50 %, ± 2.0 μm, and 20 % respectively.

flight leg	cloud fraction	flight leg mean LWC (g m^{-3})	in cloud mean LWC (g m^{-3})	mean cloud droplet effective radius (um)	mean number concentration (# cm^{-3})
C_u	0.44	0.068	0.16 ± 0.11	6.6 ± 0.7	218 ± 114
C_l	0.59	0.088	0.15 ± 0.12	6.2 ± 1.0	211 ± 93

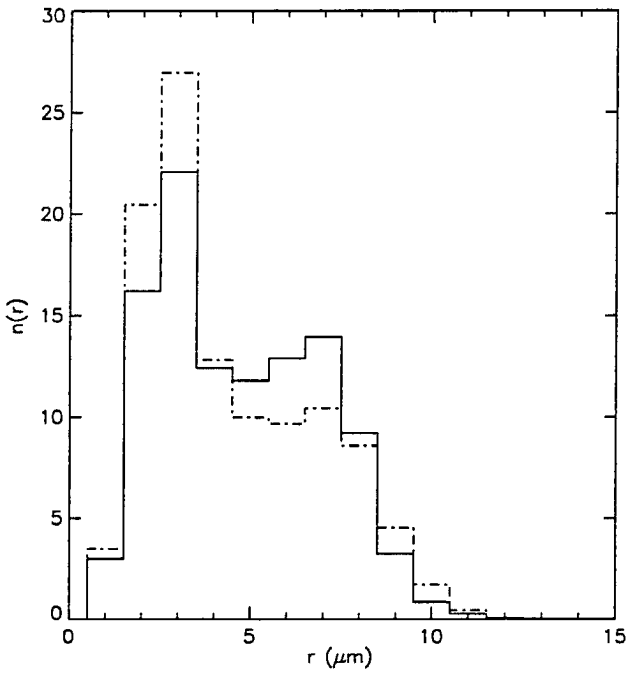

Fig. 5.7 Mean FSSP droplet size distributions for flight legs C_u (dashed line) and C_l (solid line) through cloud layer C. Uncertainty in number concentrations are ± 20 %. Number concentrations < 2.5 cm^{-3} could be due to ice contamination.

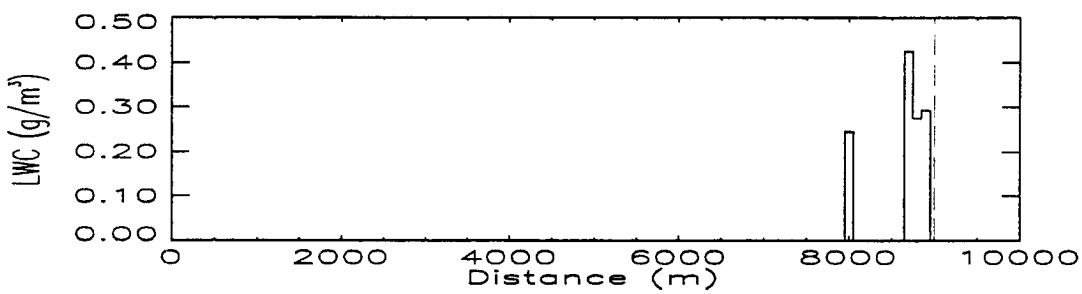

Fig. 5.8 FSSP LWC measurements as a function of horizontal distance for flight leg M. Dashed line identifies end of flight leg. Uncertainty in LWC measurements are ± 50 % of measurements.

Table 5.4 Liquid phase microphysical statistics for the upper level and lower level flight legs through cloud layer M. In cloud statistics are reported as mean ± standard deviation. Uncertainty in the in-cloud mean LWC, mean cloud droplet effective radius, and cloud droplet number concentration are ± 50 %, ± 2.0 μm, and 20 % respectively.

flight leg	cloud Fraction	flight leg mean LWC ($g\ m^{-3}$)	in-cloud mean LWC ($g\ m^{-3}$)	mean cloud droplet effective radius (μm)	mean number concentration ($\#\ cm^{-3}$)
M	0.02	0.006	0.31 ± .11	8.0 ± 0.00	221± 14

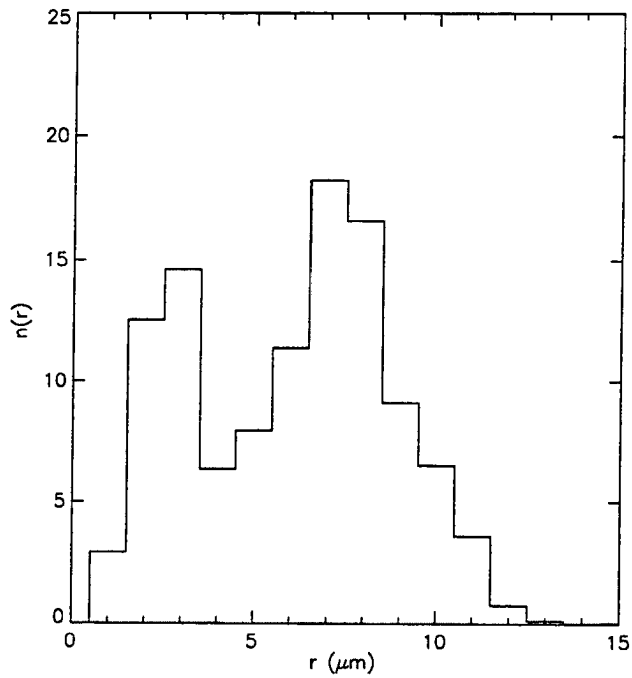

Fig. 5.9 Mean FSSP droplet size distribution for flight leg M. Uncertainty in cloud droplet number concentrations are ± 20 %.

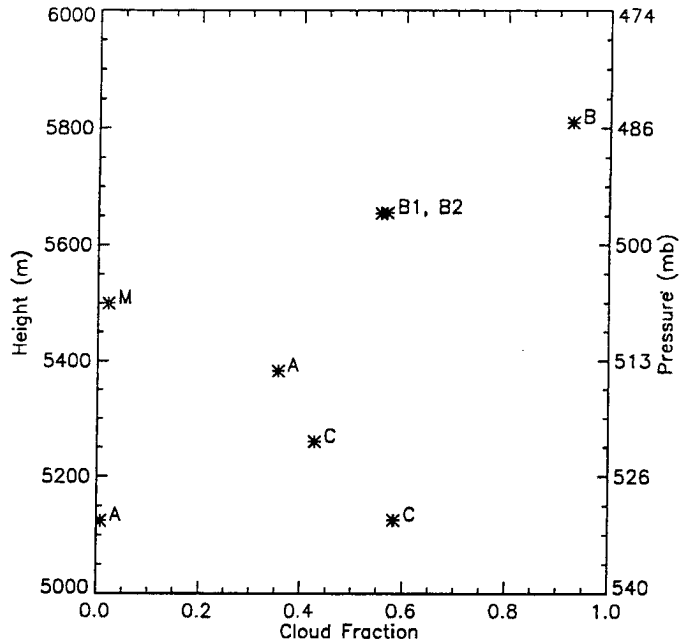

Fig. 5.10 Cloud fraction for level flight legs in cloud layers A, B and C and flight leg M. Cloud fraction is the number of measurements where liquid water is greater than .001 g/kg.

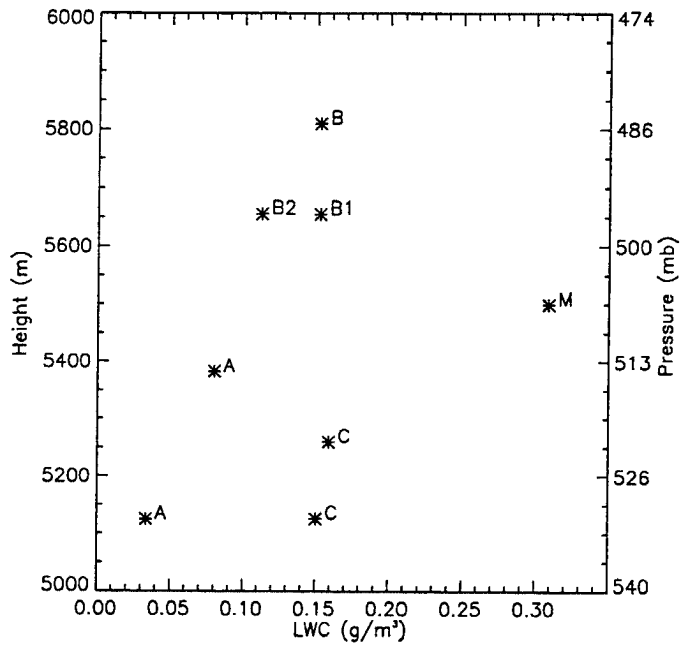

Fig. 5.11 Mean in-cloud liquid water content for flight legs in cloud layers A, B and C and level flight leg M. Uncertainty in measurements of LWC are ± 50 %.

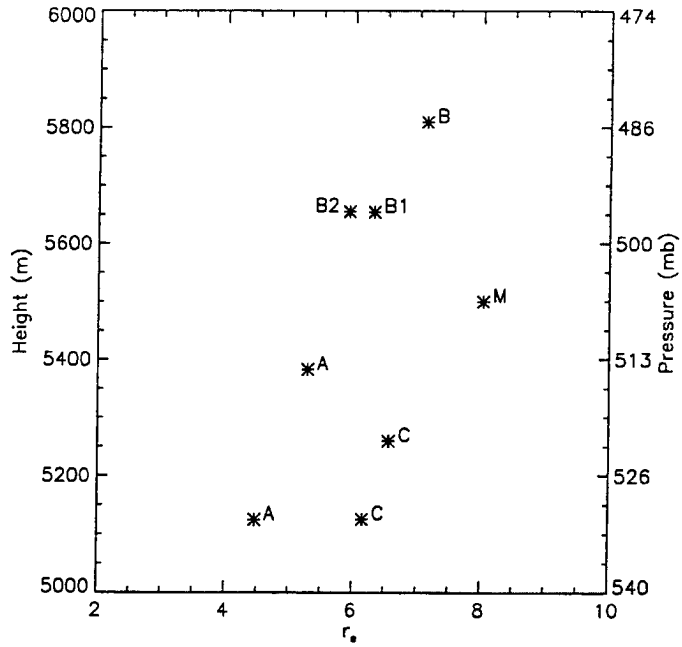

Fig. 5.12 Mean cloud droplet effective radius for flight legs in cloud layers A, B, C, and flight leg M. Uncertainty in mean cloud droplets effective radius is ± 2.0 μm.

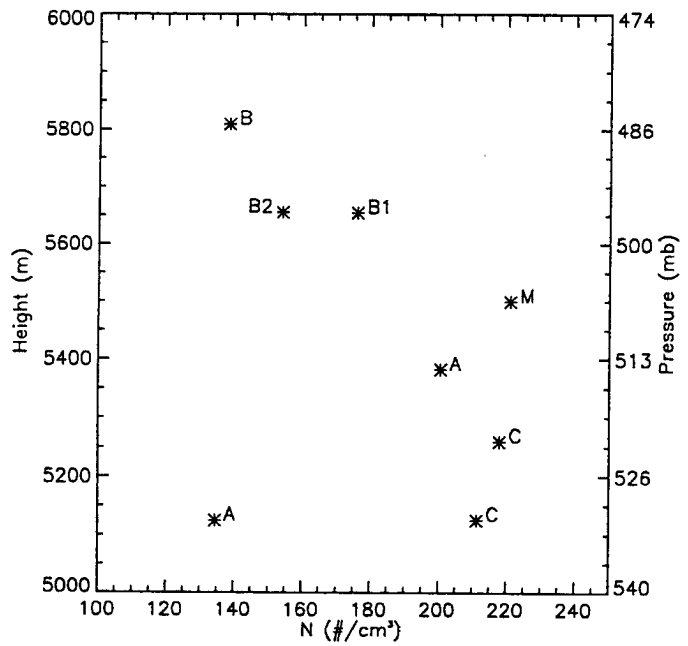

Fig. 5.13 Mean number concentration for level flight legs in cloud layers A, B and C and level flight leg M. Uncertainty in mean number concentrations are ± 20 %.

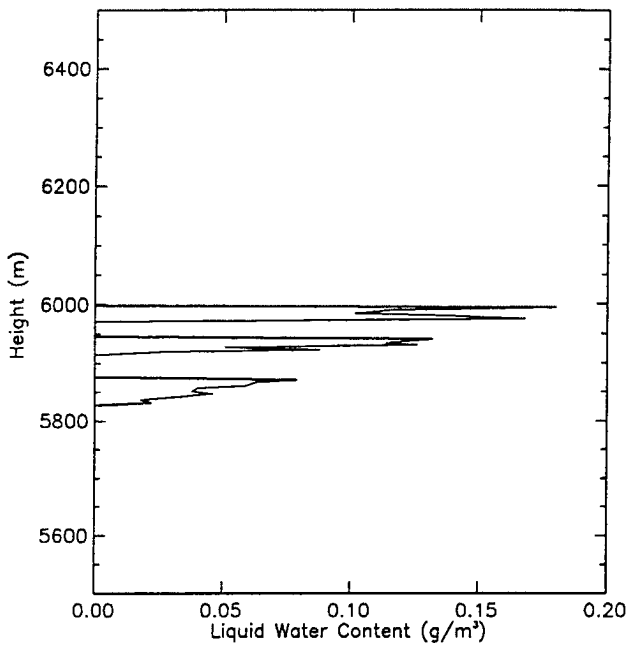

Fig. 5.14 Liquid water profile measured during S1 profile through cloud layer D plotted as a function of height.. Uncertainty in LWC measurements are ± 50 %.

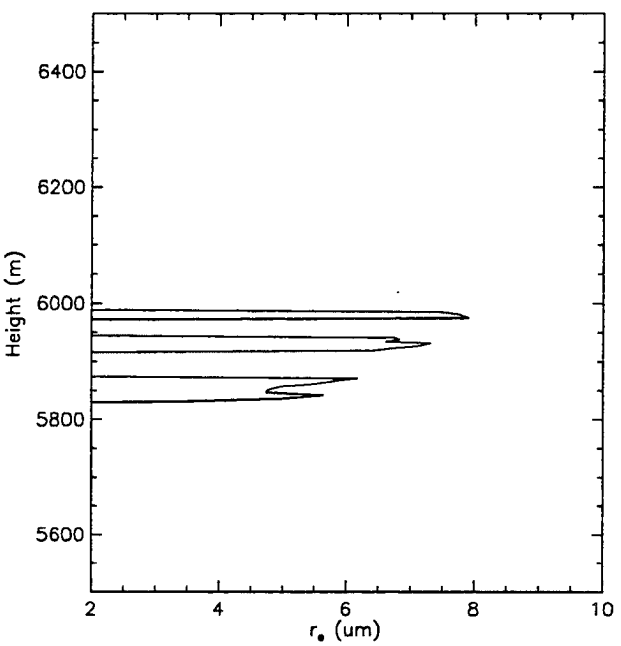

Fig. 5.15 Cloud droplet effective radius measured during S1 profile within cloud layer D plotted as function of height. Uncertainty in cloud droplet effective radius is ± 2.0 μm.

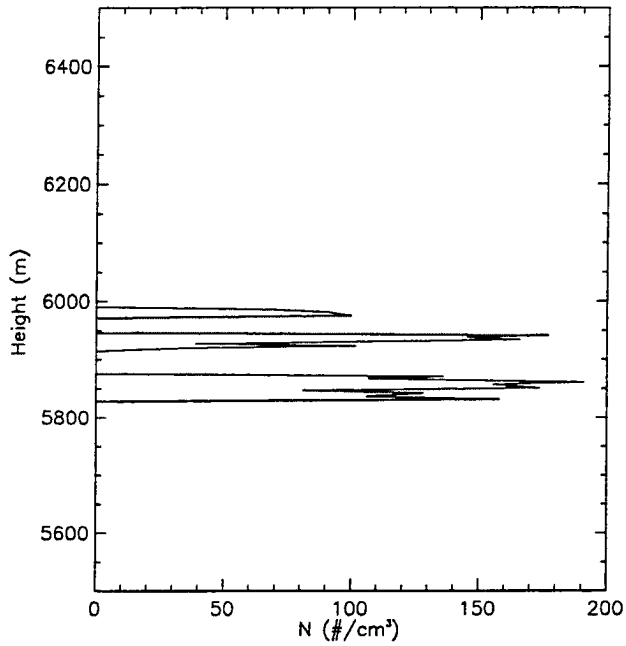

Fig. 5.16 Cloud droplet number concentration measured during S1 profile within cloud layer D plotted as function of height. Uncertainty in cloud droplet number concentration is ± 20 %.

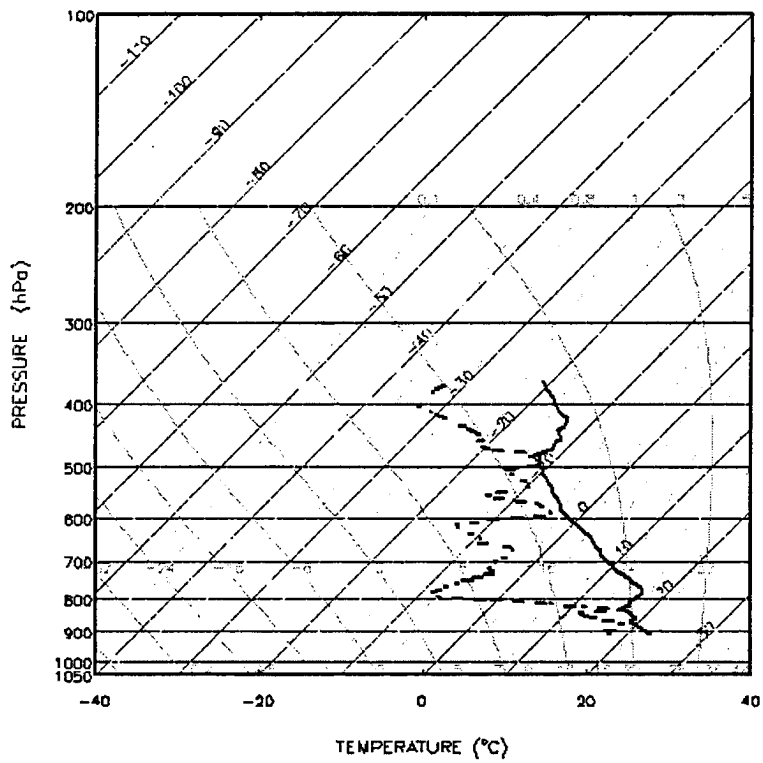

Fig. 5.17 Measurements of T and T_d obtained during S1 sounding profile plotted in a Skew-T Log P format.

Table 5.5 a) Flight leg statistics of θ_v and RH measurements obtained during flight legs A_u and A_l. b) Maximum, minimum, and difference between maximum and minimum value of θ_v for flight legs A_u and A_l. c) Hypothetical lapse rates of θ_v for atmospheric layers between flight leg levels A_u and A_l and between flight leg levels A_u and B1. Uncertainties in θ_v and RH measurements are ± 0.9 K and ± 13 %, respectively.

a)

flight leg	out-of-cloud mean RH ± σ (%)	flight leg mean θ_v ± σ (K)	in-cloud mean θ_v (K)	out-of-cloud mean θ_v (K)	in-cloud - out-of-cloud mean θ_v (K)
A_u	92 ± 4.2	319.6 ± 0.18	319.7	319.6	+0.1
A_l	88 ± 3.7	319.0 ± 0.08	319.0	318.9	+0.1

b)

flight leg	max. θ_v (K)	min. θ_v (K)	max. -min. θ_v (K)
A_u	319.9	319.2	0.7
A_l	319.2	318.7	0.5

c)

layer between flight legs	saturated lapse rate of θ_v (K/km)	hypothetical lapse rate of θ_v (K/km)
A_u and A_l	~3.9	3.0

Table 5.6 a) Flight leg statistics of θ_v and RH measurements obtained during flight legs B_u and B1. b) Maximum, minimum, and difference between maximum and minimum measurement of θ_v for flight legs B_u and B1. c) Hypothetical lapse rate of θ_v for atmospheric layer between flight legs B_u and B1. Uncertainties in θ_v and RH measurements are ± 0.9 K and ± 13 %, respectively

a)

flight leg	out-of-cloud mean RH ± σ (%)	flight leg mean θ_v ± σ (K)	in-cloud mean θ_v (K)	out-of-cloud mean θ_v (K)	in-cloud - out-of-cloud mean θ_v (K)
B_u	97 ± 2.6	321.5 ± 0.14	321.5	321.5	0.0
B1	95 ± 3.0	320.6 ± 0.21	320.6	320.7	-0.1

b)

flight leg	max. θ_v (K)	min. θ_v (K)	max. -min. θ_v (K)
B_u	321.8	321.0	0.8
B1	321.1	319.9	1.2

c)

layer between flight legs	saturated lapse rate of θ_v (K/km)	hypothetical lapse rate of θ_v (K/km)
B_u and B1	~ 3.6	5.4

Table 5.7 a) Flight leg statistics of θ_v and RH measurements obtained during flight legs C_u and C_l. b) Maximum, minimum and difference between maximum and minimum measurements of θ_v for flight legs C_u and C_l. c) Hypothetical Lapse rates of θ_v for atmospheric layer between flight legs C_u and C_l. Uncertainties in θ_v and RH measurements are ± 0.9 K and 13 % respectively.

a)

flight leg	out-of-cloud mean RH ± σ	flight leg mean $\theta_v \pm \sigma$ (K)	in-cloud mean θ_v (K)	out-of-cloud mean θ_v (K)	in-cloud - out-of-cloud mean θ_v (K)
C_u	91 ± 4.9.	319.0 ± 0.13	319.0	319.0	0.0
C_l	93± 2.6	318.6 ± 0.10	318.6	318.7	-0.1

b)

flight leg	max. θ_v (K)	min. θ_v (K)	max. -min. θ_v (K)
C_u	319.3	318.8	0.5
C_l	318.9	318.4	0.5

c)

layer between flight legs	saturated lapse rate of θ_v (K/km)	hypothetical lapse rate of θ_v (K/km)
C_u and C_l	~ 3.9	3.0

Table 5.8) a) Flight leg statistics of θ_v and RH measurements obtained during flight leg M. b) Maximum, minimum and difference between maximum and minimum measurements of θ_v for flight leg M. Uncertainties in θ_v and RH measurements are ± 0.9 K and ± 13 %, respectively

a)

flight leg	Out-of-cloud mean RH ± σ (%)	Flight Leg Mean $\theta_v \pm \sigma$ (K)	In Cloud Mean θ_v (K)	Out of Cloud Mean θ_v (K)	In Cloud - Out of Cloud Mean θ_v (K)
M	64 ± 7.2	319.8 ± 0.09	319.6	319.8	-0.2

b)

flight leg	max. θ_v (K)	min. θ_v (K)	max. -min. θ_v (K)
M	319.9	319.4	0.5

c)

Layer Between Flight Legs	Saturated Lapse Rate θ_v (K/km)	Hypothetical Lapse Rate of θ_v (K/km)
M and B2	~ 3.7	8.2

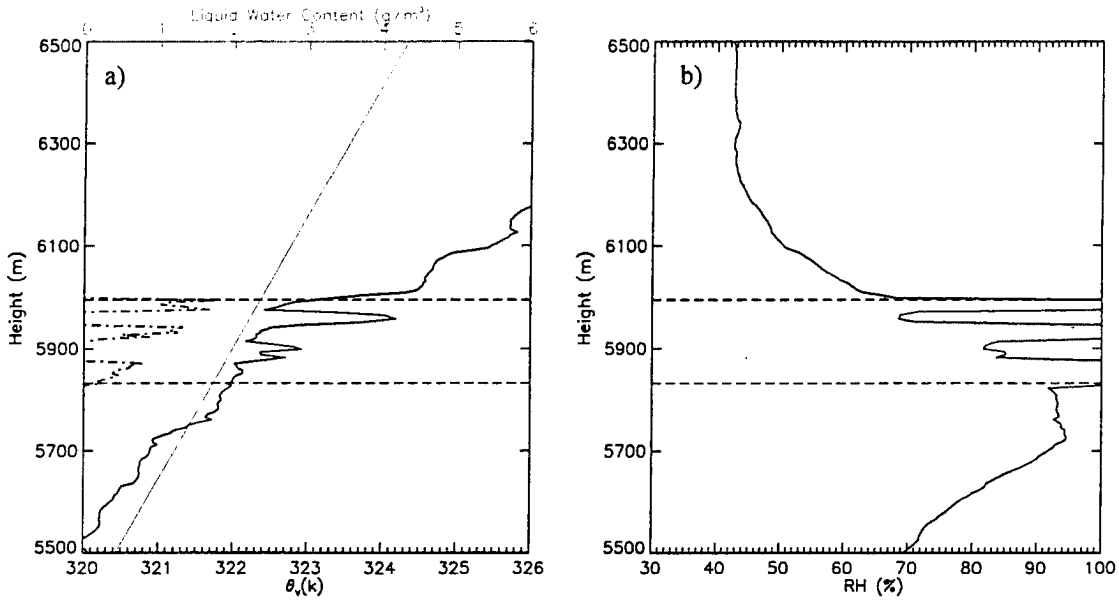

Fig. 5.18 a) Measurements of LWC and θ_v obtained during S1 profile plotted as a function of height. Dashed lines denote lowermost and uppermost LWC measurements. Diagonal solid line indicates moist adiabatic lapse rate of roughly 3.6 K km^{-1}. Uncertainties in θ_v measurements are ± 0.9 K. b) Measurements of RH obtained during S1 profile plotted as a function of height. Dashed lines denote lowermost and uppermost LWC measurements. Uncertainties in RH measurements are ± 13 %. In regions where cloud droplets are measured, RH assumed to be 100 %.

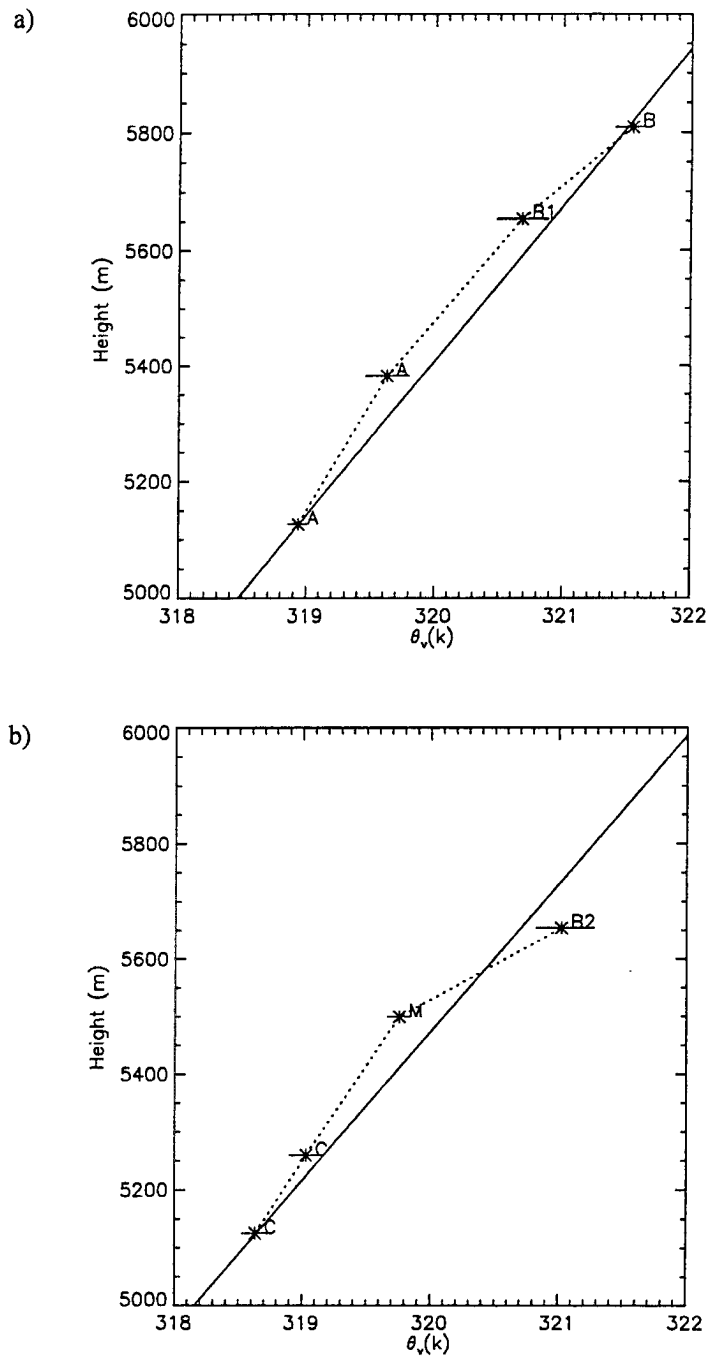

Fig. 5.19 a) Flight leg mean ± σ of θ_v measurements obtained during flight leg A_l, A_u, B_u, and B1 plotted as function of height. b) Flight leg mean ± σ of θ_v measurements obtained for flight legs C_l, C_u, M, and B2 plotted as a function of height Moist adiabatic lapse rate (roughly 3.8 K) indicated by straight line. Uncertainty in θ_v measurement is ± 0.9 K.

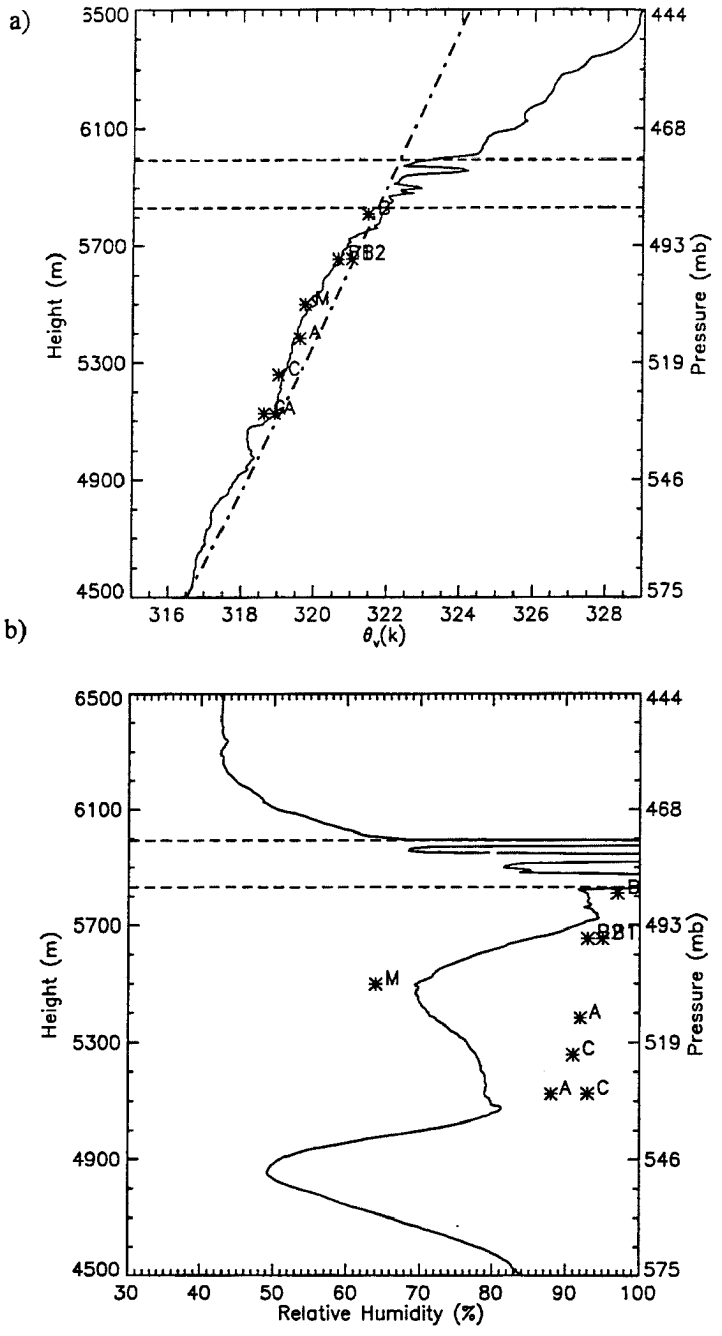

Fig. 5.20 a) Measurements of θ_v obtained during S1 profile and flight leg mean values for flight legs in cloud layers A, B and C and flight leg M plotted as a function of height. Straight solid line indicates moist adiabatic lapse rate: ~4.1 K/km between 4500 -4900 m, ~ 3.9 K/km between 4900 - 5300 m, ~ 3.7 K/km between 5300 - 5700 m, ~ 3.7 K/km between 5700 - 6100 m, and ~ 3.8 K/km between 6100 and 6500m. b) Measurements of RH obtained during S1 profile and flight leg mean values for flight legs in cloud layers A, B and C and flight leg M plotted as a function of height. Dashed lines in Fig. 5.17a indicate the first and last measurements of liquid water within cloud layer D. Uncertainty in θ_v measurements are ± 0.9 K. Uncertainty in RH measurements are ± 13 %.

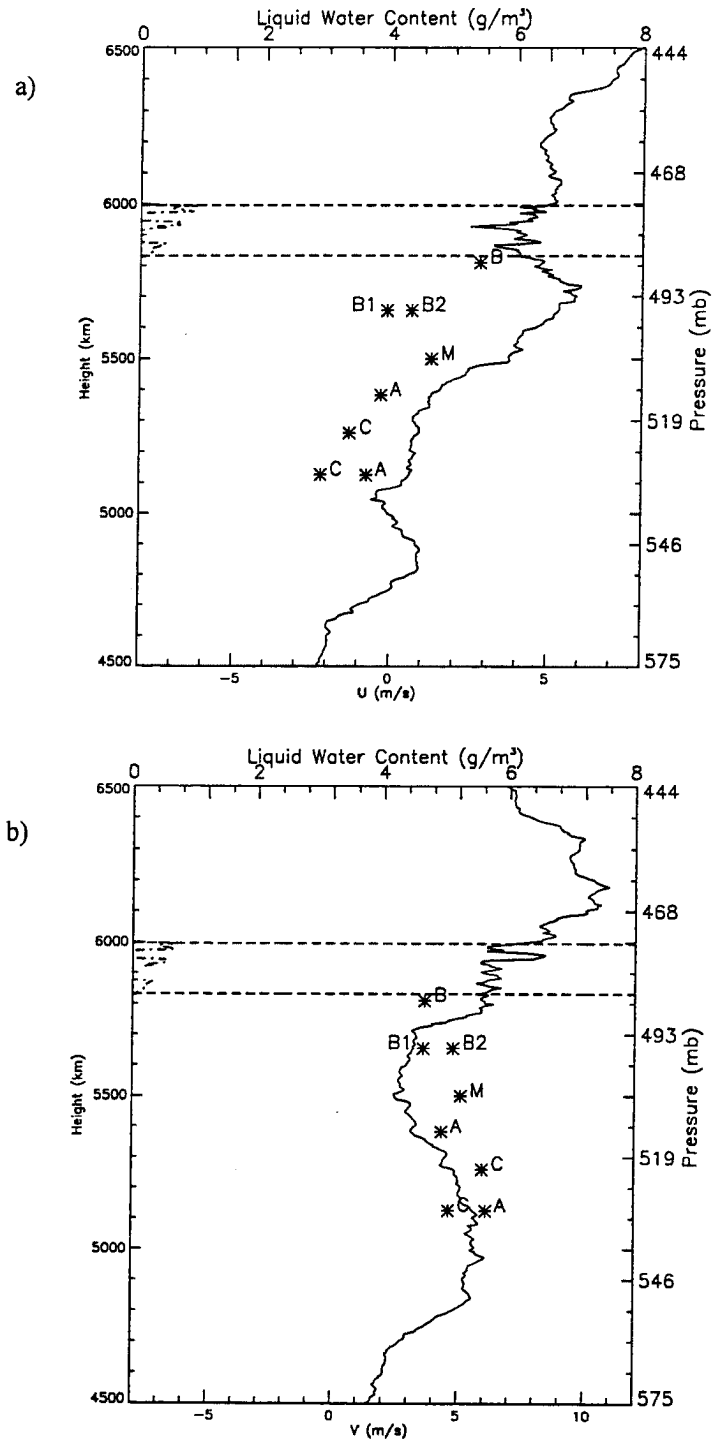

Fig. 5.21 Set of measurements of a) u wind and b) v wind obtained during S1 profile and mean values for flight legs in cloud layers A, B, C and flight leg M plotted as a function of height. Uncertainty in wind measurements are ± 1.0 m s^{-1}.

Table 5.9 In-cloud, out-of-cloud mean, and flight leg variance in measurements of u and v winds for level flight legs in cloud layers A, B, C and flight leg M. Uncertainty in u and v wind measurements are ± 1.0 m s^{-1}.

	in-cloud mean u ($m\ s^{-1}$)	out-of-cloud mean u ($m\ s^{-1}$)	flight leg variance v ($m^2\ s^{-2}$)	in-cloud mean v ($m\ s^{-1}$)	out-of-cloud mean v ($m\ s^{-1}$)	flight leg variance v ($m^2\ s^{-2}$)
B_u	+2.7	+4.1	+1.5	+3.6	+4.0	+0.37
B1	-0.3	+0.0	+1.1	+3.6	+3.6	+0.52
B2	-0.1	+0.5	+1.2	+4.7	+4.7	+0.40
M	-1.2	+1.3	+1.1	+3.9	+3.9	+0.14
A_u	-0.1	-0.2	+0.5	+4.3	+4.3	+0.24
A_l	-0.1	-0.8	+0.2	+6.1	+6.1	+0.67
C_u	-1.7	-1.0	+0.7	+5.9	+5.9	+0.63
C_l	-2.5	-1.8	+0.7	+4.7	+4.7	+0.42

Table 5.10 Richardson number computed for layers A, B and C.

Cloud layer	A	B	C
Richardson Number	2.37	24.01	0.62

Table 5.11 Fractional coverage of, mean value of, and maximum value of rising motion and sinking motion, and Skewness parameter, S, computed from subset of w wind measurements shown in Figs. 5.21-5.23. Rising and sinking motion were computed as w wind measurement - mean w wind measurement (for the subset of measurements).

leg	rising motion			sinking motion			S
	fraction %	mean ($m\ s^{-1}$)	max ($m\ s^{-1}$)	fraction %	mean ($m\ s^{-1}$)	max($m\ s^{-1}$)	
A_u	38.0	0.5	2.0	53.0	0.4	0.9	+2.0
A_l	30.0	0.2	0.7	39.0	0.1	0.4	+1.1
B_u	51.0	0.4	1.0	45.0	0.4	1.2	-0.3
B1	38.0	0.34	1.5	45.0	0.29	1.0	+0.6
C_u	42.0	0.6	2.2	54.0	0.5	1.2	+1.1
C_l	36.0	0.6	2.1	55.0	0.4	1.8	+0.8

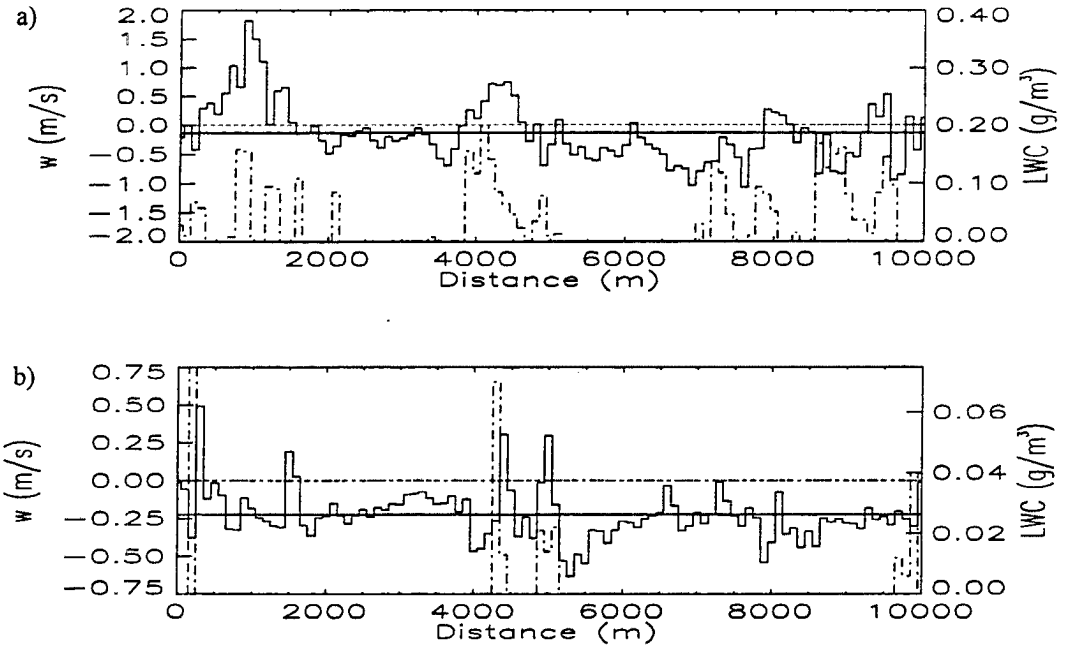

Fig. 5.22 Set of measurements of w wind velocity (solid line) and LWC (dashed and dotted line) for flight legs a) A_u and b) A_l in cloud layer A plotted as a function of distance. Horizontal dashed line indicates mean value of w for the subset of measurements. Uncertainties in w wind measurements are ± 1.0 m s^{-1}.

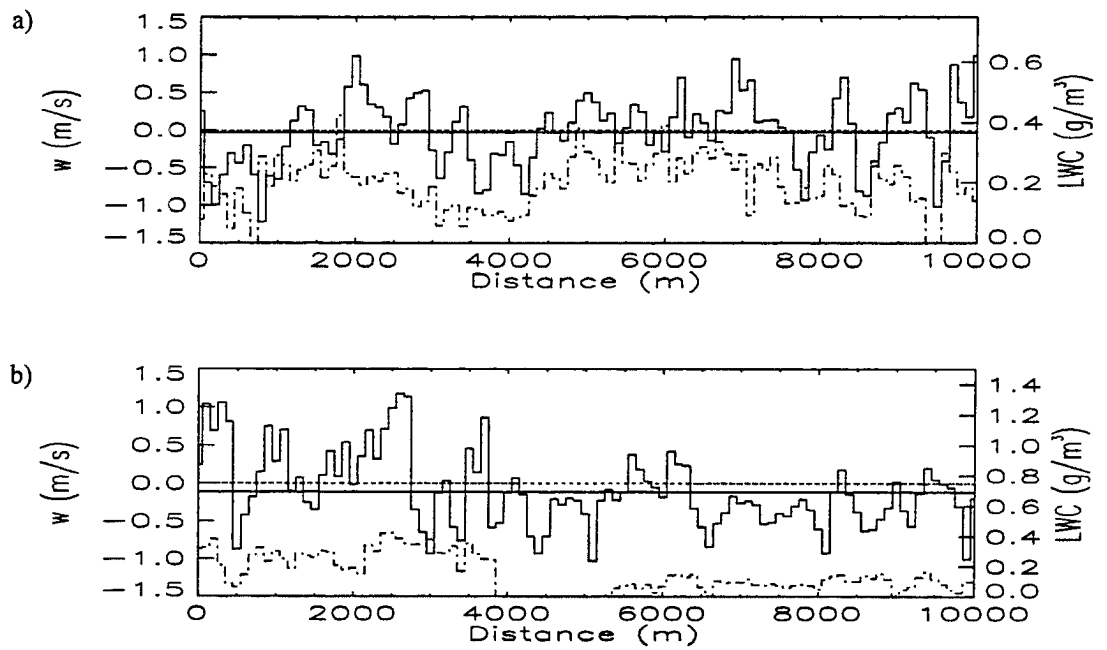

Fig. 5.23 Subset of measurements of w wind velocity (solid line) and LWC (dashed and dotted line) obtained during flight legs a) B_u and b) B1 in cloud layer B plotted as a function of distance. Horizontal dashed line indicates mean value of w for the subset of measurements for each flight leg. Uncertainties in w wind measurements are ± 1.0 m s^{-1}.

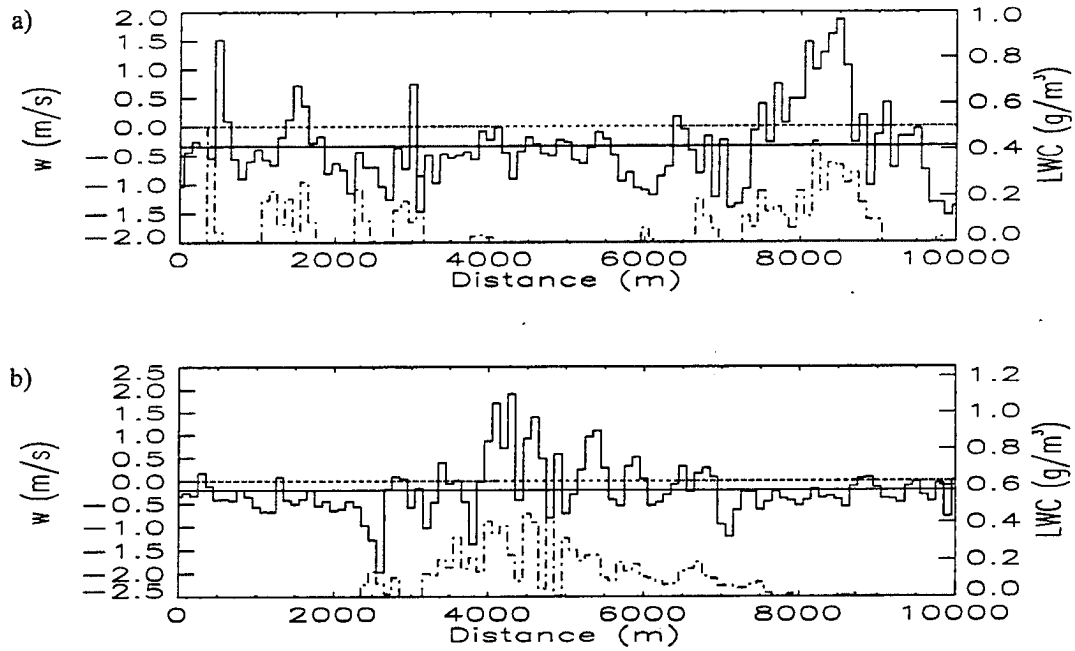

Fig. 5.24 Set of measurements of w wind velocity (solid line) and LWC (dashed and dotted line) obtained during flight legs a) C_u and b) C_l in cloud layer C plotted as function of horizontal distance. Horizontal dashed line indicates mean value of w for the set of measurements for each flight leg. Uncertainties in w wind measurements are ± 1.0 m s^{-1}.

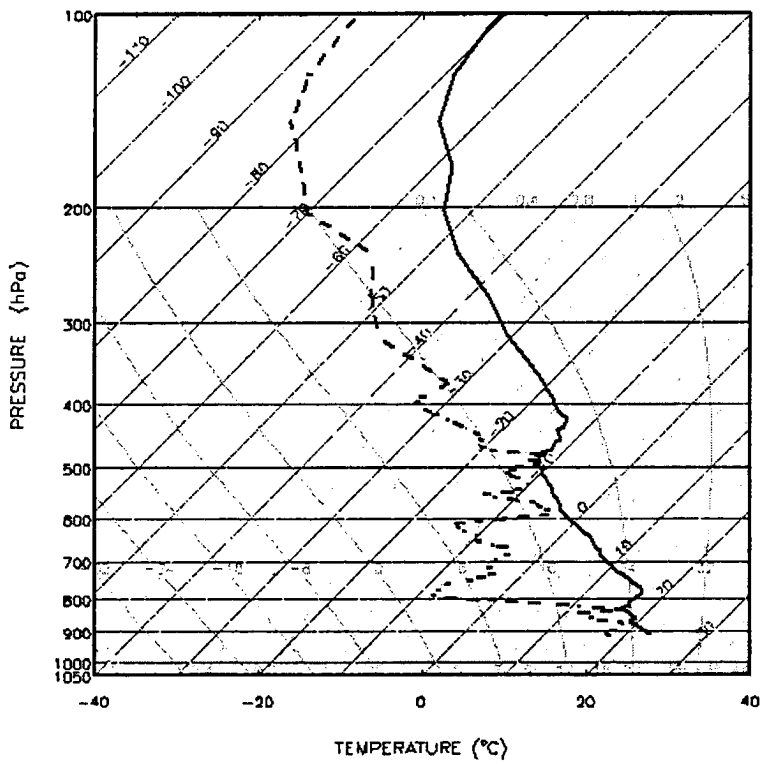

Fig. 5.25 "Constructed" profile of temperature and dew point temperature used in all radiative transfer calculations of the J25acs.

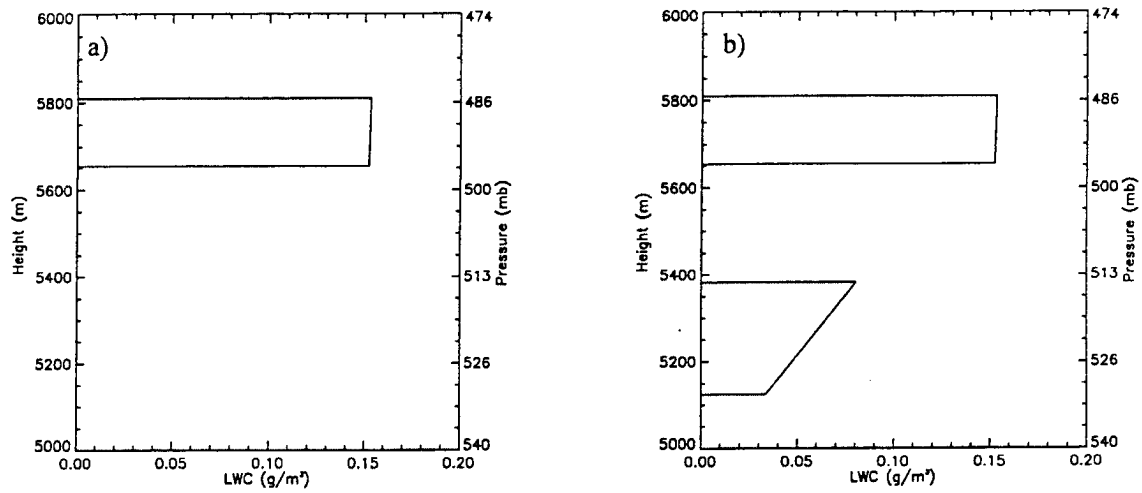

Fig. 5.26 LWC profiles used to construct cloud layer optical property profiles: a) B and b) BA.

Table 5.12 Fixed cloud droplet effective radius, effective radius variance, and MIEAVG computed 10.2-12.5 μm and 0.2-0.7 μm optical properties for cloud layers A and B .

Layer	r_e (μm)	v_e	10.2 -12.5 μm			0.2-0.7 μm		
			opt. depth	ϖ_0	g	opt depth	ϖ_0	g
A	4.9	0.14	2.0	0.336	0.69	4.8	0.999	0.85
B	6.7	0.10	3.1	0.374	0.72	5.8	0.999	0.85

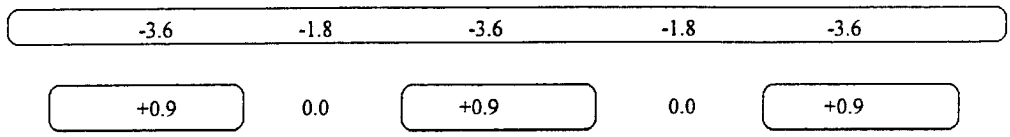

Fig. 5.27 Schematic diagram of hypothetical net thermal radiative structure of J25acs in southern portions of the system where cloud layers B and A were both observed. Net heating rates are for levels of cloud layers B and C in profiles B and BA and clear sky. Clear sky values are at far left hand portion of figure. Figure drawn to approximate scale.

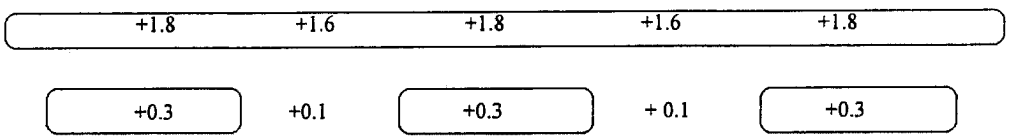

Fig. 5.28 Schematic diagram of hypothetical solar radiative structure of the J25acs and its environment in regions where cloud layers B and A were both observed. Net solar heating rates are for levels of cloud layers B and C in profiles B and BA and clear sky. Clear sky values are at far left hand portion of figure. Figure drawn to approximate scale.

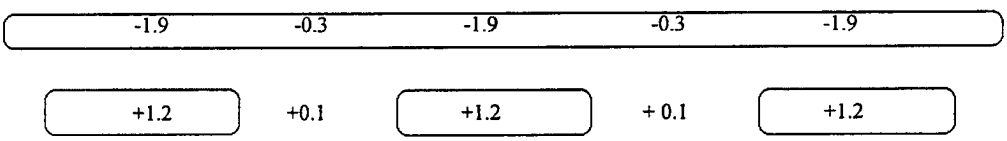

Fig. 5.29 Schematic diagram of hypothetical net solar+thermal radiative structure of the J25acs and its environment in regions where cloud layers B and A were both observed. Net thermal+solar heating rates are for levels of cloud layers B and C in profiles B and BA and clear sky. Clear sky values are at far left hand portion of figure. Figure drawn to approximate scale.

Table 5.13 Vertical profile of effective radius and effective radius variance used to construct cloud optical property profile D. Profile of MIEAVG computed 10.2 - 12.5 μm and 0.2 - 0.7 μm optical depth, single scatter albedo, and asymmetry parameter. Total 10.2-12.5 μm and 0.2-0.7 μm optical depth are 1.0 and 2.0 respectively.

Levels (m)	r_e (μm)	v_e	10.2 -12.5 μm			0.2-0.7 μm		
			opt. depth	ϖ_0	g	opt depth	ϖ_0	g
5995-5945	7.9	0.16	0.41	0.443	0.84	0.82	0.999	0.86
5940-5880	6.8	0.09	0.36	0.361	0.71	0.71	0.999	0.85
5875-5830	5.1	0.16	0.25	0.357	0.71	0.49	0.999	0.84

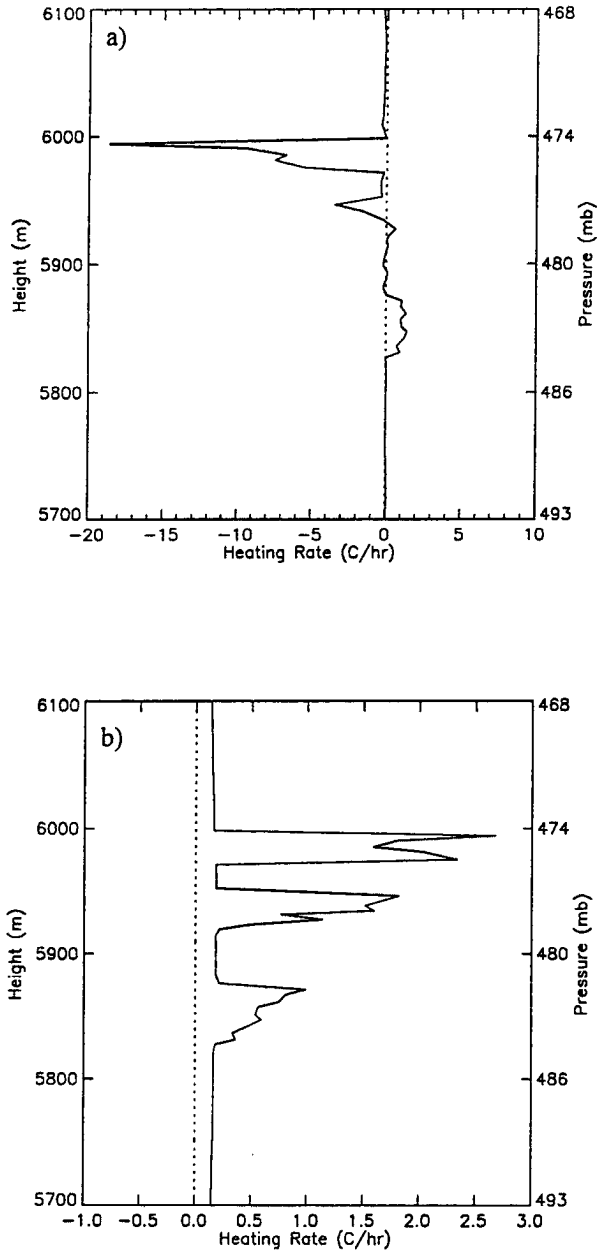

Fig. 5.30 Simulated a)thermal, b)solar heating rate profile for cloud layer optical property profile D.

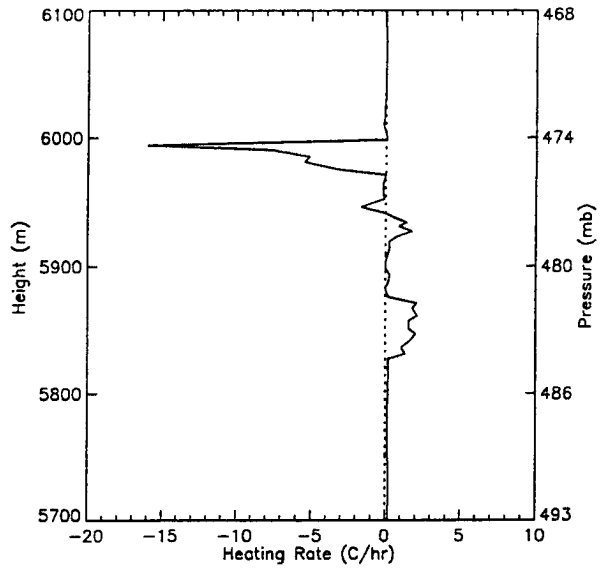

Fig. 5.31 Simulated thermal plus solar heating rate profile for cloud layer optical property profile D.

CHAPTER VI

SUMMARY AND CONCLUSIONS

Altocumulus clouds modify the distribution of diabatic heating within the atmosphere and cover a significant fraction of the Earth's surface. Therefore, they play a role in determining both climate and weather. Because there have been only a handful of observational studies within Ac clouds, our understanding of the physical processes which are important for their development, maintenance, and dissipation is incomplete. In this research, we attempted to increase our understanding of the physical processes which occur in Ac clouds by performing an in-situ observational and radiative transfer simulation study of a complex and dissipating cloud layer observed on June 25, 1996 as a part of CLEX-1.

Thesis Summary

A summary of this thesis is as follows. In chapter I, we defined the objectives and obstacles of our research. As stated, the objectives were to examine the microphysical, thermodynamic, kinematic, and radiative structures of a dissipating multiple layered Ac cloud measured on June 25, 1996 during CLEX using aircraft measurements and a radiative transfer model. The obstacles were that the Ac cloud was complex in structure and aircraft measurements were not taken in a systematic fashion. In chapter II, we presented a summary of previous observational studies within Ac clouds and identified physical processes found to be important in these clouds. In chapter III, the J25acs was characterized for separate time periods during the experiment and an in-depth description of the J25 experiment was given. In the experiment description, we identified how aircraft measurements were taken and the relative position of measurements within the observed cloud structure. In chapter IV, we described our methodology of aircraft data analysis and methodology used to simulate the radiative structure of the J25acs. The set of aircraft measurements obtained during the experiment were arranged into five data groups: A, B,C,M and the J25acs was divided into four cloud layers A, B, C and D. The measurements in each data group were

analyzed according to how they were taken and with the purpose of identifying the structure of the J25acs in the location where the measurements were taken. Our method used to simulate the radiative structure of the J25acs involved the construction of cloud optical property profiles which were based on aircraft FSSP microphysical measurements and then using these profiles as input for the SHDOM radiative transfer model. In chapter V, aircraft measurements in data groups A, B, C, M and D and results from radiative transfer simulations in cloud optical property profiles B, BA and D were presented and discussed. The aircraft measurements were used to examine the microphysical, thermodynamic, and kinematic structure of the J25acs at separate time periods of the experiment. The results from radiative transfer simulations in cloud optical properties B and BA were used to examine the spatial and vertical radiative heating rate structure of the J25acs in its southern portions where cloud elements of layer A were observed below cloud layer B. The results from radiative transfer simulations in cloud optical property D were used to examine the vertical structure of radiative heating within cloud layer D.

Summary of Results

In this section, we summarize the structures of cloud layers A, B, C, and D based on measurements within each cloud layer and results from radiative transfer simulations in the cloud optical property profiles B, BA, and D.

Cloud layer A

Cloud layer A was observed to be cumuliform in appearance and was sampled in the southern portions of the J25acs between 16:30 and 16:38 UTC. Aircraft measurements obtained during flight legs A_u and A_l and radiative transfer simulations in cloud optical property profiles B and BA indicate the following.

- Cloud layer A was composed of horizontally separate and regularly spaced LW cloud regions whose width increased with height.
- The cloud droplet sizes, number concentration, and LWC increased with height in cloud elements of layer A.

- The cloud layer was imbedded within a moist and conditionally unstable layer of air.
- The net radiative heating rate of the layer of atmosphere in which cloud elements of layer A were imbedded was positive.
- Regions of rising motion within layer A occupied a smaller fractional area than regions of sinking motion while mean and maximum values of rising motion were greater than those of sinking motion.
- Regions of rising motion were positioned in roughly the same location as cloud elements of layer A.
- Cloud layer A was stable with respect to Kelvin-Helmholtz instability.

Cloud layer B

Cloud layer B was observed to be stratiform in appearance and to consist of smoothed and mounded elements at cloud top. The cloud layer was visually observed in the southern and northern portions of the system and was sampled between 16:40 and 17:00 UTC. Aircraft measurements obtained during flight legs B_u and B1 and radiative transfer simulations within cloud layer optical property profiles B, and BA indicate the following :

- Cloud layer B was composed of extensive (~4000 m) cloud regions which increased in width with height to form an almost continuos distribution of cloud elements at upper levels.
- Within cloud elements of layer B, the cloud droplet size distributions were bi-modal and they broadened in width with height.
- Cloud elements of layer B were imbedded within a moist and absolutely stable layer of air.
- The net radiative heating rate for the layer of atmosphere in which cloud elements of layer B were imbedded was negative.
- Regions of equally intense rising and sinking motions were present at upper and lower levels of layer B.
- Cloud layer B was stable with respect to Kelvin-Helmholtz instability

Cloud layer C

Cloud layer C was observed to be cumuliform in appearance. The cloud layer was visually observed in the northern portions of the J25acs below cloud layer B and was sampled between 17:15 and 17:20 UTC. Aircraft measurements obtained during flight legs C_u and C_l indicate the following:

- Cloud layer C was composed of extensive cloud regions (~4000 m at level C_l) whose width decreased with height.
- Significant small scale fluctuations in the LWC cloud structure of layer C was present
- Within cloud elements of layer C, cloud droplet size distributions were bi-modal.
- Cloud layer C was imbedded within a moist and conditionally unstable layer of air.
- Regions of rising motion occupied a smaller fractional area than regions of sinking motion and the average and maximum values of rising motion were greater than those of sinking motion.
- Cloud layer C was stable with respect to Kelvin-Helmholtz instability.

Cloud layer D

Cloud Layer D was observed to be stratiform in appearance and to consist of cellular cloud elements. Aircraft measurements obtained during the S1 sounding profile and radiative transfer simulations in cloud optical property D indicate the following:

- Cloud Layer D was composed of horizontally separated cloud elements.
- Within cloud elements, the cloud droplet sizes and LWC increased with height while the cloud droplet number concentration decreased with height.
- The lapse rate within cloud elements was roughly moist adiabatic and cloud elements were colder than the surrounding cloud free air at similar levels.
- Cloud-top entrainment was occurring.
- The lapse rate of the layer air just below cloud layer D was quasi-moist adiabatic and this air was relatively moist.

- Cloud elements of layer D were radiatively cooling at cloud top and heating at cloud base, and the net heating rate for the layer was negative.

The relationships between aircraft measurements obtained during level flight legs in cloud layers B and A, results from radiative transfer simulations in cloud optical property profiles B and BA, and measurements obtained during the S1 profile indicate that the microphysical, thermodynamic, kinematic, and radiative structures of the J25acs in its southern portions between 16:30 and 16:55 UTC were both similar and different to those observed within the cloud type, cumulus rising into stratocumulus. The similarities between our results and those measured by de Roode et al. (1996) in their study of cumulus rising into stratocumulus are listed below:

- The Cloud fraction has a minimum value at cloud base and increases towards maximum values near cloud top.
- The flight leg mean LWCs increase upward from cloud base with maximum values near cloud top.
- A cumulus cloud layer is situated within a conditionally unstable layer and below an absolutely stable layer.
- The relative humidity decreases with height above cloud top.
- The vertical motion field within the cumulus layer is characterized by narrow regions of relatively intense rising motion and broad regions of weak sinking motion.
- Relatively intense regions of sinking motion occur near cloud top.
- Longwave cooling occurs in the upper portions of the cloud and longwave warming occurs in the lower portions of the cloud.

The differences are summarized as follows:

- The sub-cloud layer was not a well mixed surface-based marine boundary layer.
- J25acs was a mixed-phase cloud.

Aircraft measurements obtained during the S1 profile and radiative transfer simulations in cloud optical property profile D indicate that the microphysical, thermodynamic, and radiative structures of the J25acs observed between 17:30-18:00 UTC were similar to those observed in previous studies of altocumulus. We find the following similarities in the structures of the J25acs observed between 17:30-18:00 UTC and the Oct 25. altocumulus cloud studied by Heymsfield et al. (1991):

- The cloud layer was composed of cellular cloud elements.
- The LWC and cloud droplet sizes increase with height and reach maximum values near cloud top.
- The cloud layer is situated below a dry and absolutely stable layer of air.
- Cloud-top entrainment was occurring.
- Calculated radiative cooling occurs in the upper portions and radiative warming in the lower portions of the cloud layer.
- The calculated shortwave heating is largest in upper portions of the cloud layer.
- The calculated net cloud layer radiative heating rate is negative.

We also observe that the measured and calculated structures of cloud layer D are in many ways similar to the structures of stratocumulus clouds. The one important difference is that cloud layer D was not coupled to a well mixed surface-based boundary layer.

Future Research

In this research, the first steps were made towards developing an understanding of the physical processes which occurred in a complex multi-layered dissipating Ac cloud system, the J25acs. There is still, however, much work left to be done in the study of the J25acs and Ac clouds in general. In the following paragraphs, we describe possible areas of future research in the study of the J25acs. Next, we discuss how future aircraft studies in altocumulus clouds should be conducted.

Future study of the J25acs

We propose that the next step in the study of the J25acs should be to examine the ice phase microphysical structure of the system. Study of the ice phase structure is important for two reasons. First, results from this study might indicate what impact ice phase microphysical processes had on the dynamics and evolution of the J25acs. In particular, because ice phase microphysical processes can lead to rapid dissipation of middle level layer clouds through glaciation, results from this study might provide some explanation as to why the J25acs dissipated. A second reason for studying the ice phase structure of the system is so that more realistic radiative transfer simulations of the J25acs may be performed. In this research, measurements of ice phase microphysics were neglected in the construction of cloud optical property profiles.

Based on observations made of the J25acs using a GOES-8 10.7 μm satellite animation loop, we believe that gravity waves may have played a role in the formation and evolution of the J25acs. Therefore, future study of the J25acs should attempt to determine whether gravity wave activity was present in the state of KS (at the vertical levels of the J25acs) prior to and during the J25 experiment time period. A possible methodology for this research might involve analysis of wind profiler network data collected in the state of KS for time periods prior to and during the experiment.

Another area of future research of the J25acs should involve examination of the stability of the system with respect to cloud-top entrainment instability. Given that this type of instability has been proposed as possible mechanism for breakup of stratocumulus cloud layers, the results from such a study might also provide an explanation as to why the J25acs dissipated.

Once the ice phase microphysical structure of the cloud system has been examined, we believe that that an LES modeling study of the J25acs should be performed. The results from this type of study might serve to explain how radiative, thermodynamic, and microphysical processes interacted to produce the observed structure and evolution of the J25acs.

Future aircraft studies in Ac cloud layers

There is a need for more in-situ aircraft studies of Ac cloud layers. The greatest obstacle which faced this research was the non-systematic sampling strategy of the aircraft. Therefore, we propose that, in future in-situ aircraft measurement experiments of Ac cloud layers, the aircraft sampling strategy should be "Lagrangian". This sampling strategy would provide measurements of the same cloudy volume of atmosphere as it is advected by the mean wind. The flight path for future experiments should consist of several straight and level flight legs systematically positioned at levels above, within, and below the cloud layer. A profile flight leg which samples the same vertical levels as the straight and level flight legs should also be performed prior and subsequent to the straight and level flight legs.

Concluding Remarks

The objectives of this research were to examine the microphysical, thermodynamic, kinematic, and radiative structures of a complex and dissipating multi-layered Ac cloud system observed on June 25, 1996 during CLEX. The results from this study indicate that, in many ways, the structures of this system were similar to those observed in boundary layer cloud types, cumulus rising into stratocumulus and stratocumulus. A possible interpretation of these results is that the physical processes which occurred in the observed altocumulus cloud system were also similar to those which occur in boundary layer cloud types, cumulus rising into stratocumulus and stratocumulus. This interpretation and our results are both consistent with previous in-situ observational studies of Ac clouds (Heymsfield et al. 1991).

REFERENCES

Baker, M. B., R. G. Corbin, and J. Latham, 1980: The influence of entrainment of the evolution of cloud droplet spectra. *Quart. J. R. Met. Soc.* **106**, 581-598.

Bohren, C. F., and D. R. Huffman, 1983: *Absorption and Scattering of Light by Small Particles.* Wiley-Interscience, 519 pp.

Brock, F. V., 1995: *Lecture Notes on Meteorological Measurement Systems.* Custom Academic Publishing Company.

Cotton, W. R., and R. A. Anthes, 1989: *Storm and Cloud Dynamics.* Academic Press, Inc., pp. 883.

de Roode, S. R., and P. G. Duynkerke, 1996: Dynamics of cumulus rising into stratocumulus as observed during the first 'Lagrangian' experiment of ASTEX. *Quart. J. R. Met. Soc.*, **122**, 1597-1623.

Downing, H. D. , and D. Williams, 1975: Optical constants of water in the infrared. *Journal of Geophysical Review*, **80**, 1656-1661.

Drazin, P. G., and W. H. Reid, 1981: *Hydrodynamic Stability.* Cambridge University Press. pp. 515.

Evans, K. F., 1998: The spherical harmonic discrete ordinate method for three-dimensional atmospheric radiative transfer. *J. Atmos. Sci.*, **55**, 429-446.

Feigel'son, E. M., 1966: *Light and Heat Radiation in Stratus Clouds.* Israel Program for Scientific Translations, 245 pp.

Feigel'son, E. M., 1973: *Radiant Heat Transfer in a Cloudy Atmosphere.* Israel Program for Scientific Translations, 191 pp.

Fu, Q., and K. N. Liou, 1992: On the correlated *k*-distribution method for radiative transfer in nonhomogeneous atmospheres. *J. Atmos. Sci.*, **49**, 2156-2139.

Gedzelman, S. D., 1988: In praise of altocumulus. *Weatherwise*, **41**, 143-149.

Hale, G., and M. Querry, 1972 : Optical constants of water in the 200 nm to 200 um wavelength region. *Applied Optics* ,**12**, 555-563.

Hansen, J. E., 1971: Multiple scattering in planetary atmospheres. Part II: Sunlight reflected by terrestrial water clouds. J. Atmos. Sci., **28**, 1400-1426.

Hess, S. L., 1959: *Introduction to Theoretical Meteorology.* Holt, Rinehart, and Winston, pp. 361.

Heymsfield, A. J., and L. M. Miloshevich, 1989: Evaluation of liquid water measuring instruments in cold clouds sampled during FIRE. *J. Atmos. Oceanic Technol.* **6**, 378-388.

Heymsfield, A. J., L. M. Miloshevich, A. Slingo, K. Sassen, and D. O. Starr, 1991: An observational and theoretical study of highly supercooled altocumulus. *J. Atmos. Sci.*, **48**, 923-945.

Hobbs, P. V., and A. Deepak, 1981: *Clouds Their Formation, Optical Properties, and Effects.* Academic Press, pp. 493.

Hobbs, P. V., and A. L. Rango, 1985: Ice particle concentration in clouds. *J. Atmos. Sci.*, **42**, 2523-2548.

Hobbs, P. V., 1993: Aerosol-Cloud-Climate Interactions. Academic Press, Inc., 235 pp.

Hu Y. X. and K. Stamnes, 1992: An accurate parameterization of the radiative properties of water clouds suitable for use in climate models. *J. Climate*, **6**, 728-742.

Lenschow, D. H., 1986: *Probing the Atmospheric Boundary Layer.* American Meteorological Society, 269 pp.

Liou, K. N., 1980: *An Introduction to Atmospheric Radiation.* Academic Press, Inc., 392 pp.

Liu, S. and S. K. Krueger, 1996: Numerical simulations of altocumulus with a cloud resolving model. *Proceedings of the Fifth Atmospheric Radiation Measurement (ARM) Science Team Meeting March 19-23 1995 San Diego, California.* United States Department of Energy. 402 pp.

McClatchey, R. A., et al., 1972: *Optical Properties of the Atmosphere.* U. S. Department of Commerce AD-753 075. 94 pp.

Pruppacher, H. R., and J. D. Klett, 1997: *Microphysics of Clouds and Precipitation.* Atmospheric and Oceanographic Science Library, 954 pp.

Palmer, K. F., and D. Williams, 1974: Optical properties of water in the near infrared. *J. of the Opt. Soc. of Amer.*, **64**, 1107-1110.

Slingo A., and H. M. Schrecker, 1982: On the shortwave properties of stratiform water clouds. *Quart. J. R. Met. Soc.* **108**, 407-426.

Starr, D. O., and S. K. Cox, 1985: Cirrus clouds, part II: numerical experiments on the formation and maintenance of cirrus. *J. Atmos. Sci.*, **42**, 2682-2694.

Stull, R. B., 1994: *An Introduction to Boundary Layer Meteorology.* Kluwer Academic Publishers, 666 pp.

Tiedke, M., 1993: Representation of clouds in large-scale models. *Mon. Wea. Rev.*, **121**, 3040- 3061.

Warner, J., 1969: The microstructure of cumulus clouds part I: general features of the droplet spectrum. *J. Atmos Science.*, 20, 1049-1059.

Warren, S. G., C. J. Hahn, J. London, R. M. Chervin and R. Jenne, 1986: Global distribution of total cloud cover and cloud type amount over land. NCAR Tech. Note TN-273 STR, 229 pp.

Warren, S. G., C. J. Hahn, J. London, R. M. Chervin and R. Jenne, 1988: Global distribution of total cloud cover and cloud type amount over the ocean. NCAR Tech. Note TN-317 STR, 212 pp.

Wiscombe, W. J., 1977: The delta-*M* method: Rapid yet accurate radiative flux calculations for strongly asymmetric phase functions. *J. Atmos. Sci.*, **34**, 1408-1422.

WMO, 1956: *International Cloud Atlas*. World Meteorological Organization, 61 pp.

WMO, 1996: *Guide to Meteorological Instruments and Methods of Observation Part I: Measurement of Meteorological Variables*, World Meteorological Organization.

APPENDIX A

GOES-8 10.7 μm OBSERVATIONS

In this appendix, we present an hourly sequence of GOES-8 10.7 μm satellite images focused on the CLEX region. This sequence shows the evolution of cloud features (including the J25acs) within KS for time periods prior to and during the experiment. In particular, the formation and dissipation of the J25acs can be identified. The dissipation of the system occurs during the experiment time periods. The sequence of imagery presented here is actually a subset of 15 minute imagery which was animated using IDL image looping software. Within the animation loop, the motion and evolution of cloud features (including the J25acs) were clearly identifiable. The following section describes the sequence of images.

Satellite Images

10:15-12:15 UTC

Figs. A.1a-c are the 10:15 UTC, 11:15 UTC, and 12:15 UTC GOES-8 10.7 μm images. Identifiable within each image is a relatively large region of bright (cold) cloud situated on the western border of KS, the OK panhandle, and in the northern portion of TX. The size of this cloud region increases with each successive image. Based on the 10:35 and 12:35 UTC radar summary (shown in section 1), this region of cold clouds is interpreted to be a result of deep penetrative convection in its early or mature stages of development. The increase in the size of this cloud region within each image could be due to an increase in the size the convective region, itself, or it could be due to detrainment of cloudy air at the base of the tropopause. Since the radar summaries showed that the height of echo tops and the size of echo regions increased between 10:35 UTC and 12:35 UTC, we interpret these cold cloud features to represent convection in either its mature or growing stage of development. Identifiable, within each image, are a number of linear cloud features over central KS. These features are slightly darker than the convective clouds to the east, and are generally oriented southwest to northeast. Within the animation loop, we observed these features to move eastward in time. Both their motion and shape suggest they were associated with gravity wave activity.

The boxes within the 11:15 and 12:15 UTC images are believed to enclose the J25acs in its initial stage of development. The 11:15 UTC image shows the system to be composed of several distinct cloud elements. The 12:15 UTC image shows the system to be composed of several distinct cloud patches which are larger in size. Within the animation loop, it appeared as if the distinct cloud elements within the 11:15 UTC image rapidly expanded in size to form the cloud patches evident within the 12:15 UTC image. These cloud patches continued to increase in size between 12:15 and 13:15 UTC.

13:15-15:15 UTC

Figs. A.2a-c are the 13:15, 14:15, 15:15 UTC GOES-8 10.7 μm images. In each succeeding image, the region of cold clouds on the western border of KS and the OK panhandle is more ragged in appearance and is slightly larger in size. In the north western portions of KS, the cloudy region is more continuous, while in the southern portions it is more broken. The radar summaries for these time periods showed that the regions of deep convection within the OK panhandle were dissipating while new convective regions were forming in the north western portions of KS. The border of the cold cloud region extends further to the east within each image. This suggests that high cloud elements, detrained from the regions of deep convection, were being advected eastward during this time.

Within the satellite animation loop, we observed the J25acs to evolve in shape as it move moved northward and eastward between 13:15 UTC and 15:15 UTC. Evolution and movement are also evident through comparison of Figs 3.7a and c. The 13:15 UTC image shows the system to be complex in shape

and centered south and west of Hillsboro, KS while the 15:15 UTC images show the system to be quasi circular in shape and centered east of and north of Hillsboro, KS . While it cannot be discerned from the 13:15 UTC image alone, we believe that the complex shape of the system is a direct result of undulations which were observed to pass through the system at this time. We speculate that these undulations were caused by gravity waves propagating through the cloud system.

16:15-18:15 UTC

Figs. A.3 a-c are the 16:15, 17:15, and 18:15 UTC images. The sequence identifies the evolution of the J25acs and its environment during the experiment time period (16:30-18:00 UTC). Within the 16:15 UTC image, the system is shown to be an extended quasi-circular cloud region which is north and east of its previous position at 15:15 UTC. The 17:15 UTC image shows the system to be broken and composed of several distinct cloud patches. Within the 18:15 UTC image, the system is no longer visible.

Summary of the Satellite Images

The sequence of GOES-8 10.7 μm satellite images identified the evolution of the J25acs and other cloud features within the state of KS prior to and during the experiment. A summary of the evolution of the J25acs is as follows: The J25acs formed approximately 7 hours prior to the experiment in a location roughly 200 km west and south of the J25 experiment region. The formation of the system was characterized by an expansion of discrete cloud elements into an extended cloud region. Once formed, the system moved eastward and northward, expanded to a size of roughly 2000 km^2, and became quasi - circular in shape. During the period of the experiment, the J25acs dissipated and was no longer present at 18:15 UTC. The dissipation was characterized by a break up of the cloud into distinct cloud patches. The next section provides a detailed description of the J25 experiment.

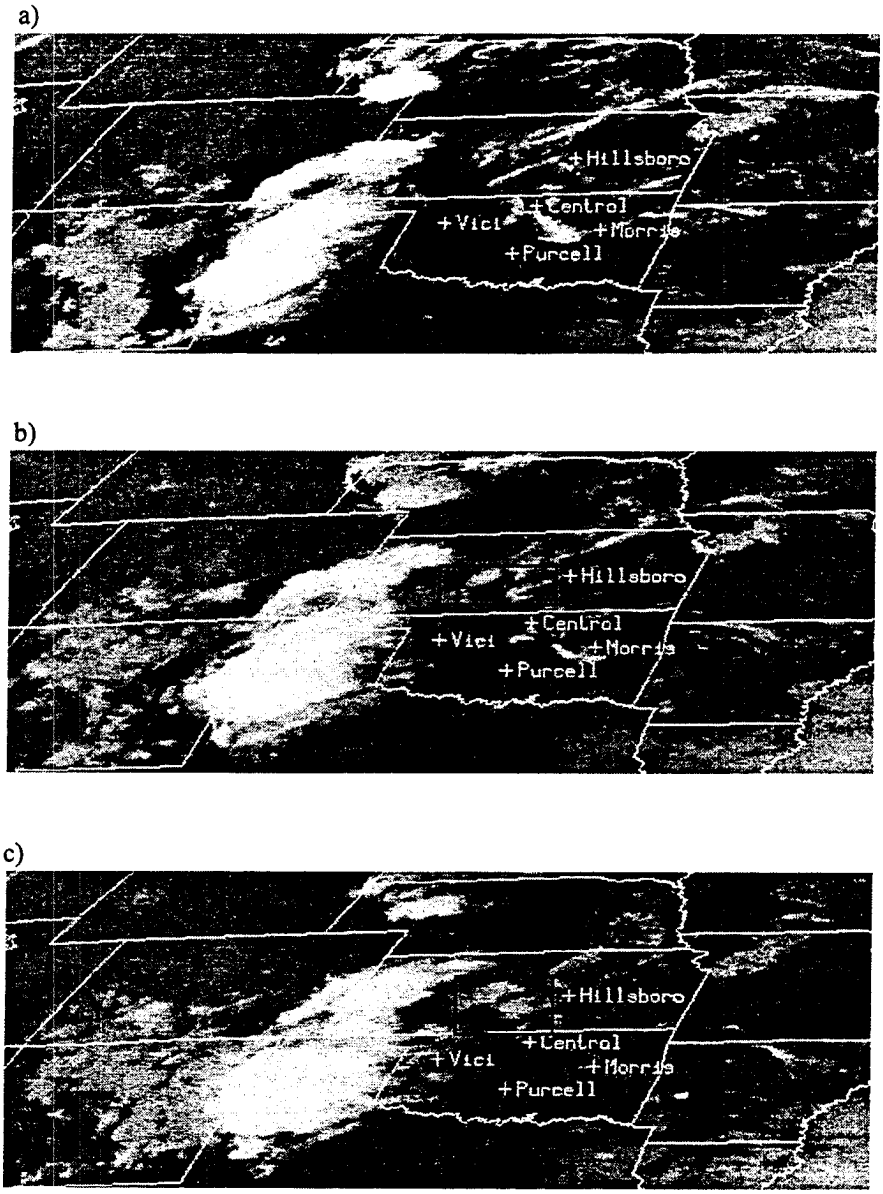

Figure A.1 a) 10:15 UTC, b) 11:15 UTC, and c) 12:15 UTC June 25, 1996 10.7 μm GOES-8 images of central United States. Boxes enclose J25acs.

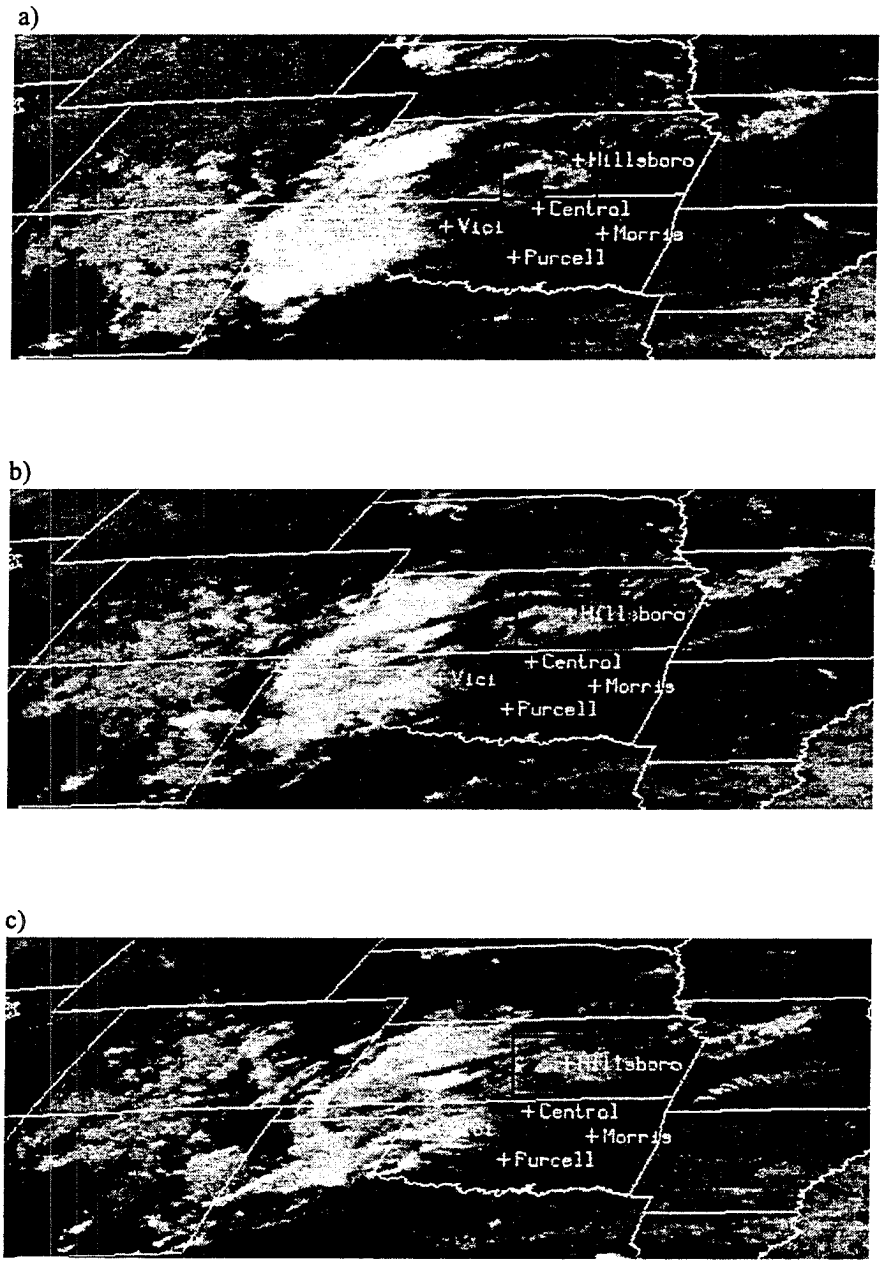

Figure A.2 a) 13:15 UTC, b) 14:15 UTC, and c) 15:15 UTC June 25, 1996 10.7 μm GOES-8 images of central United States. Boxes enclose J25acs.

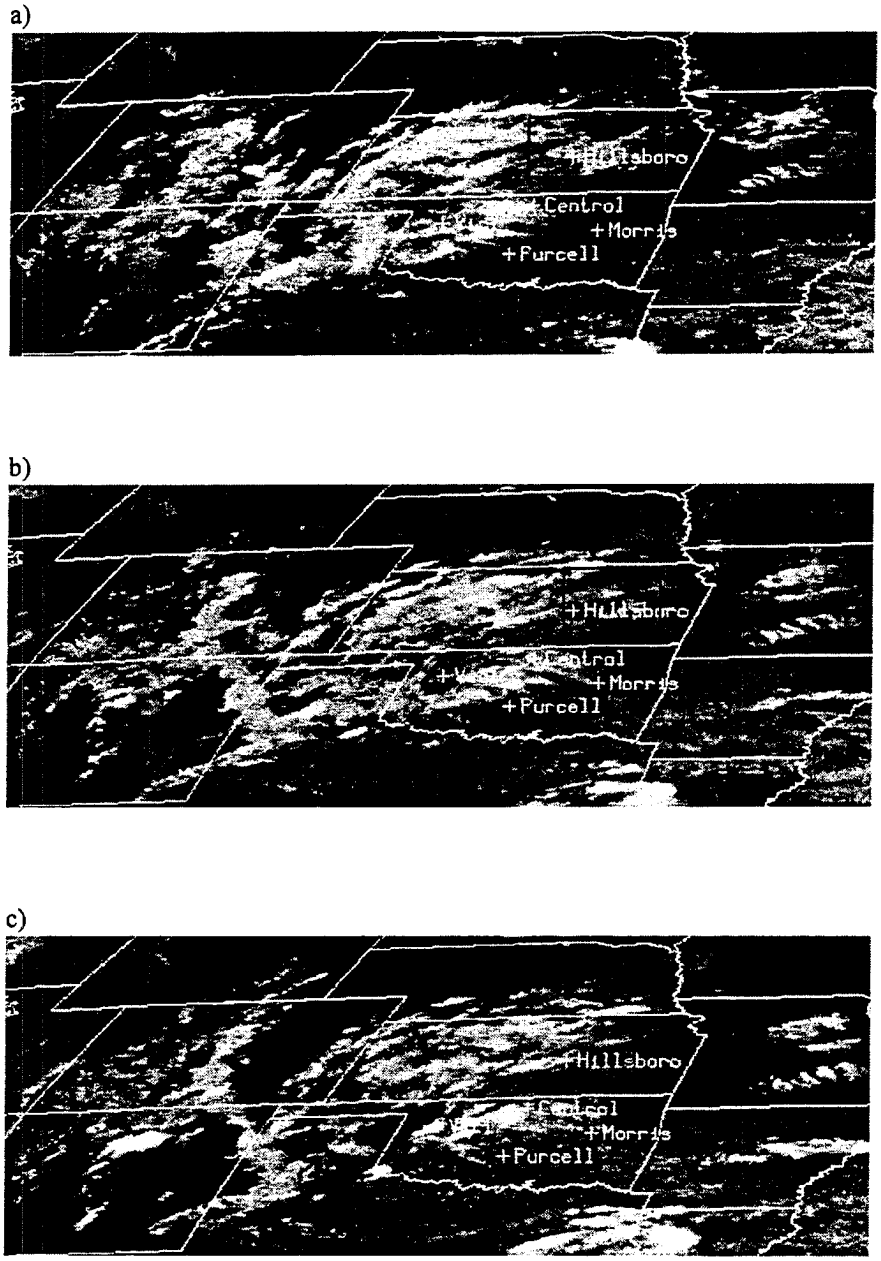

Figure A.3 a) 16:15 UTC, b) 17:15 UTC, and c) 18:15 UTC June 25, 1996 10.7 μm GOES-8 images of central United States. Boxes enclose J25acs.

APPENDIX B

J25 EXPERIMENT DESCRIPTION

In this appendix, an in-depth chronological description of the J25 experiment is given. The description makes use of schematic cloud diagrams and GOES-8 0.7 μm images and IBTMs to illustrate the observed cloud structure and the relative position of the aircraft within the observed structure. The aircraft sampling strategy is identified by the set of level /profile flight legs described and listed in chapter IV.

16:00 UTC - 16:27 UTC
Flight Leg Summary: L0

The N2Uw took off from Ponca City, Oklahoma at approximately 16:00 UTC and headed due North. Between 16:16 and 16:28 UTC, the N2Uw was en route to the J25ac system at a cruising altitude of 4500 m (575 mb). This level flight leg corresponds to flight leg L0.

Between 16:27 and 16:28 UTC, the J25acs was visible in front of the aircraft. The system was observed to consist of two separate cloud layers. The upper layer was thinner and stratiform in appearance, while the lower layer was thicker and was composed of cumuliform cloud elements. Some of the cumulus cloud elements from the lower layer were merged with the upper stratiform layer. Also, trails of virga were apparent below the base of the cumuliform cloud layer. Fig. B.1 depicts the observed cloud structure.

The observation of an upper and lower cloud deck was made during the time period 16:30-17:15 UTC. We refer to the upper cloud deck observed during this time period as cloud deck B. We refer to the lower cloud deck observed between 16:30 and 17:05 UTC as cloud deck A. We refer to the lower cloud deck observed between 17:05 and 17:20 UTC as cloud deck C.

16:28 UTC - 16:38 UTC
Flight Leg Summary: P0, L1, P1, L2

Between 16:28 and 16:31 UTC, the aircraft passed below cloud deck B and ascended to an altitude of 5125 m (533 mb). The ascent corresponds with flight leg P0. The aircraft was ascending in order to intercept cloud deck A which was still visible ahead of the aircraft at this time. Fig. B.2 depicts the observed cloud structure and the location of the aircraft.

Between 16:31 UTC and 16:38 Z, the aircraft sampled cloud deck A. Level flight legs L1 and L2 were flown at the base and middle portions of this deck. Fig. B.3 depicts the observed vertical location of the aircraft within cloud deck A during each flight leg. At the end of flight leg L2, the aircraft exited cloud deck 2. Upon exiting this deck, cloud deck B was still visible above the aircraft. Fig. B.4 depicts the observed cloud structure and the location of the aircraft. This diagram shows that within certain regions of the J25acs, cloud deck B was present above cloud deck A, while in other regions cloud deck B was solely present.

16:31 UTC satellite image

Fig. B.5a is the 16:31 UTC GOES-8 IBTM with flight legs L1 and L2 also plotted. Based on the 265 K contour, the system is estimated to be greater than 900 km^2 in extent and is complex in shape. The northern western edges of the system are more ragged while the southern and eastern edges are more uniform. Both flight legs are shown to be in the southern portions of the system and on the boundary of a quasi circular region with brightness temperatures of 260 K. We stated that cloud deck B was visible

above the aircraft prior to flight leg L1 and subsequent to flight leg L2. Notice that flight legs L1 and L2 are positioned several kilometers from the boundary of the system (the 265 K contour). This indicates that the 265 K identifies the horizontal extent of the upper deck and also suggests that the horizontal extent of the cloud deck 1was larger than the horizontal extent of the lower cloud deck.

The visible image for this time period, Fig. B.5b, shows that on the largest scale the J25acs was broken and was composed of cloud patches. The southern and eastern boundaries of the system are sharply outlined. The northwestern portion of the system appears more diffuse and tenuous. Within the southern region of the system, where flight legs L1 and L2 are located, the cloud texture indicates cellularity.

16:38- 16:55 UTC
Flight Leg Summary: P2, L3, L4

Between 16:38 and 16:44 UTC, the aircraft ascended to an altitude of 5810 m (486 mb), reversed course, and entered cloud deck B. Profile flight leg P2 and level flight leg L3 were made during this period. During flight leg L3, cloud deck B was visible ahead of the aircraft. The top of the deck appeared to consist of smoothed and mounded elements. The size of these mounded elements was estimated to be between 100 and 500 m.

Between 16:44 and 16:50 UTC, level flight leg L4 was made in the upper portion of cloud deck B. Fig. B.6 depicts the observed position of the aircraft within the cloud deck. The top of cloud deck B is shown to be smooth and mounded and the aircraft is positioned at the very top of the deck. During this flight leg, blue sky was visible above the aircraft as the aircraft passed into thinner cloud regions. Towards the end of flight leg L4, the aircraft exited cloud deck 1.

Between 16:50:05 and 16:54:56 UTC, the N2Uw made a course reversal and reentered cloud deck1 on a straight heading. Level flight legs L5 and L6 corresponds to these maneuvers. During flight leg L6 and prior to reentering cloud deck B, the top of the cloud deck B was visually observed. The appearance was similar to that observed during flight leg L3.

16:45 UTC Satellite Images

The 16:45 UTC GOES-8 IBTM, Fig. B.7a, identifies the horizontal extent and shape of the system and also shows the location, length, and orientation of level flight legs L3, L4, and L5. The horizontal shape and extent of the J25acs are different from those of the 16:31 UTC image. The 265 K contour now encloses three distinct regions. The largest of these regions extends from points 0 and 40 in the eastward coordinate and points 12 and 30 in the northward coordinate, and is estimated to be 600 km^2 in horizontal extent. Flight legs L3 and L5 are both on the southern boundary of this region, while flight leg L4 is contained within this region.

For the remainder of the experiment description, we refer to this region as the J25acs. Based on the sequence of images presented in section 2 of this chapter, however, it is clear that this region is a single element of the J25acs which is now breaking up.

The 16:45 UTC visible image, Fig. B.7b, shows that the southwestern boundary of the system is less sharply defined and is darker than within the 16:31 UTC image. The texture of the system within the region where flight leg L4 is positioned suggests a cellular structure in the cloud and does not appear much different from the previous image. This is consistent with our in-flight observations which showed that the top of cloud deck 1 appeared similar both prior and subsequent to level flight leg L4.

16:55 - 17:00 UTC
Flight Leg Summary: P3, L7, L8, L9

Between 16:55 and 17:00 UTC, flight legs P3 and L7 were made in cloud deck B. During profile flight leg P3, the N2Uw descended to an altitude of 5655 m (496 mb). Level flight leg L7 was a straight flight leg through the lower portions of cloud deck B. Fig. B.8 shows the location of the aircraft within cloud deck B and the vertical cloud structure observed during leg L7. Cloud elements are shown to extend from cloud deck A and into cloud deck B. This was observed in the downward looking video. Towards the end of level flight L7, the aircraft exited cloud deck B.

Between 17:00 and 17:10 UTC, the aircraft made a course reversal (level flight leg L8) and reentered cloud deck 1 (level flight leg L9). During flight leg L8, cloud deck A was visible below the aircraft while the aircraft was situated in clear air. The vertical cloud structure observed during flight leg L9 was similar to that observed during flight leg L7. Prior to reentering cloud deck B, its top was observed to consist of smooth mounded elements. Figs. B.9 and B.10 depict the observed cloud structure and the relative position of the aircraft for flight legs L8 and L9 respectively . Fig. B.9 shows cloud deck A to consist of small cumuliform cloud elements within the region of flight leg L8.

17:01 UTC Satellite Images

Fig. B.11a is the 17:01 UTC IBTM with flight legs L6, L7, L8, and L9 also plotted. Flight legs L6 and L8 both cross the 265 K contour, while flight legs L7 and L9 are contained within this contour. Flight legs L7 and L9 are shown to occur in close to the same location. A comparison with the 16:31 UTC IBTM, shows that the locations of flight legs L8 and L1 were also nearly the same. However, a comparison of the observed cloud structure for each of these flight legs (figs. B.9 and B.3) shows that cloud deck B was not identified in the region of flight leg L8. This suggests that cloud deck B either dissipated or advected out of this region between these time periods. There is evidence for both of these processes in the 17:01 and 16:31 UTC IBTMs. Dissipation is indicated because the system is obviously more narrow in the NW-SE direction in the 17:01 UTC IBTM. Advection is indicated because the location of the J25acs is slightly north and east of its original position in the 16:31 UTC IBTM.

The 17:01 UTC GOES-8 0.7 μm image , Fig. B.11b, shows that the system is brighter in its northern portion as compared to its southern portion. A comparison of this image with the 16:31 UTC 0.7μm image also shows that cloud elements have dissipated to the west of the region where flight legs L7 and L9 are positioned while the cloud texture in this region is nearly the same. This suggests that those regions of the J25acs sampled by the aircraft remained fairly constant in cloud structure while other regions were rapidly dissipating. This is consistent with in-flight observations made prior to flight leg L9 which identified the cloud top structure to be similar to that observed during flight legs L6 and L3.

17:11 - 17:20 UTC
Flight Leg Summary: P4, L10,P5, L11, and L12

Between 17:11 and 17:15 UTC, the aircraft descended out of cloud deck B to 5500 m (506 mb), flew at a constant altitude of 5500 m, and then descended into cloud deck C. Flight legs P4, L10, and P5 correspond to each of these maneuvers. Fig. B.12 depicts the observed vertical cloud structure and the relative position of the aircraft during these legs. Cloud decks B and C are shown to be separated by a clear layer of air with the aircraft positioned in this layer. Cloud elements extend from the top of cloud deck C and up to the level of the aircraft. Table 3.1 shows that flight legs L2, L10, and L11 were at similar altitudes. However a comparison of the observations made during flight leg L2 (Fig. B.3) and flight leg L10 (Fig. B.12) shows that the vertical structure of cloud decks A and C were observed to be different in vertical structure.

Between 17:15 UTC and 17:20 UTC, level flight legs L11 and L12 were made in the upper and middle potions of cloud deck C. At the end of flight leg L12, the aircraft exited cloud deck 2. Fig. B.13 depicts the observed cloud structure and the position of each flight leg within cloud deck C.

17:15 UTC Satellite Images

Fig. B.14a is the 17:15 UTC IBTM with level flight legs L10, L11, and L12 also plotted. The approximate horizontal extent of the J25acs is 100 km^2, and flight legs L10-L12 are positioned in the northern portions of the J25acs. Flight legs L10 and L11 are both contained within the 265K contour while flight leg L12 crosses this contour. The visible image, Fig. B.14b, indicates that the cloud structure was cellular within the region of flight legs L10, L11, and L12.

The horizontal structure of the J25acs is significantly different from the horizontal structure shown in the 17:01 UTC IBTM. The change is most noticeable in the region previously sampled by level

flight legs L7, L8, and L9 (see Fig. B.11) where brightness temperature have increased. This indicates that the J25ac system has dissipated within this region.

A comparison of Figs. B.5a and B.14a shows that flight legs L1 and L2 were separated from the location of the flight legs L10, L11, and L12 by a distance of roughly 30 km and that each set of flight legs was positioned in a different location of the J25acs. The first set (L1-L2) was positioned in the southern portions of the J25acs while the second set (L10-L12) was positioned in the northern portions. Given that the vertical structure of cloud deck 2 was observed to be different in the respective regions of these flight legs, this indicates there was horizontal variability in the structure of cloud deck 2.

17:20- 18:11 UTC
Flight leg summary : P7, S1

Between 17:19:49 and 17:42:00 UTC, the aircraft ascended to an altitude of 7920 m (368 mb). This ascent corresponds to flight leg P7. During the ascent, the aircraft remained above the J25acs. Between 17:42 and 18:11 UTC, the aircraft performed a spiral sounding descent (sounding profile leg S1) from 7920 m (368 mb) to 790 m (930 mb) which passed through cloud deck D. The rate of descent for the sounding was 5 m/s while the radius of each spiral was roughly 5.8 km. Top-down observations of the cloud deck were made while the aircraft was above the deck. The cloud deck was observed to be composed of cellular cloud elements which were closely spaced together. The size of these elements was estimated to be between 100 and 1000 m. Fig. B.15 depicts the observed cloud structure. As the aircraft passed through cloud deck 1, its tops were observed to both smoothed and mounded. Fig. B.16 depicts the observed vertical cloud structure and the aircraft flight track. Notice that cloud deck C was not observed during the spiral sounding. This vertical cloud structure is different than the structure observed during flight legs L10,L11, and L12 (figs B.21-B.22) where both cloud decks B and C were identified. The dashed line within Fig. B.16 shows that the aircraft sampled the cloud deck horizontally and vertically during the S1 profile.

17:45 UTC Satellite Images

Fig. B.17a is the 17:45 UTC IBTM with the location of the sounding profile S1 also plotted. The horizontal extent of the J25acs is roughly 25 km^2. A comparison with the 17:15 UTC IBTM (Fig. B.14a) shows that the system has dissipated in its southern portions where flight legs L1-L9 were located. The S1 profile is positioned on the eastern border of the J25acs within a region enclosed by the 280 K. The location of S1 profile is separated from the locations of flight legs L10 -L12 by a distance of roughly 10 km. The cloud texture of the J25acs within the visible image (Fig. B.17b) indicates a cellular cloud structure in the central portions of the system and a more tenuous and uniform cloud structure on its boundaries. While the cloud texture is similar to the texture within the 17:15 UTC visible image, the system appears to be more broken and is less bright in the 17:45 UTC image.

The vertical cloud structures observed during flight legs L10 -L12 and during the S1 profile were shown to be different. Since these flight legs were separated by a distance of 10 km and by a period of 30 minutes, it is not clear as to whether this difference was due to horizontal inhomogeneity or temporal changes in the vertical cloud structure of the J25acs. Given that other regions of the J25acs were encountered where cloud deck B was solely present, horizontal inhomogeneity is certainly possible. Furthermore, this vertical cloud structure was observed on the boundary of the system and the sounding profile S1 was also shown to occur on the boundary of the system.

This concludes the experiment description. The aircraft measurement strategy, the observed cloud structure, and the relative position of the measurements within the observed cloud structure have been identified for separate time periods of the experiment. A summary of the results of the experiment description is given below.

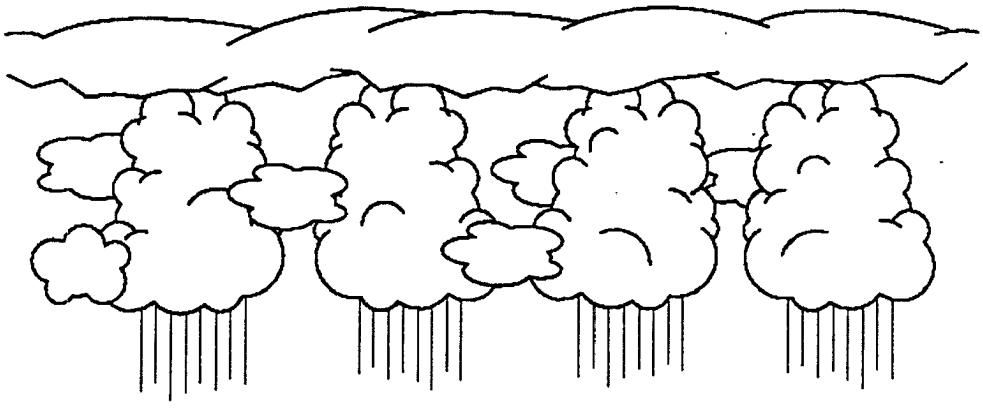

Figure B.1 Observed cloud structure during flight leg P0.

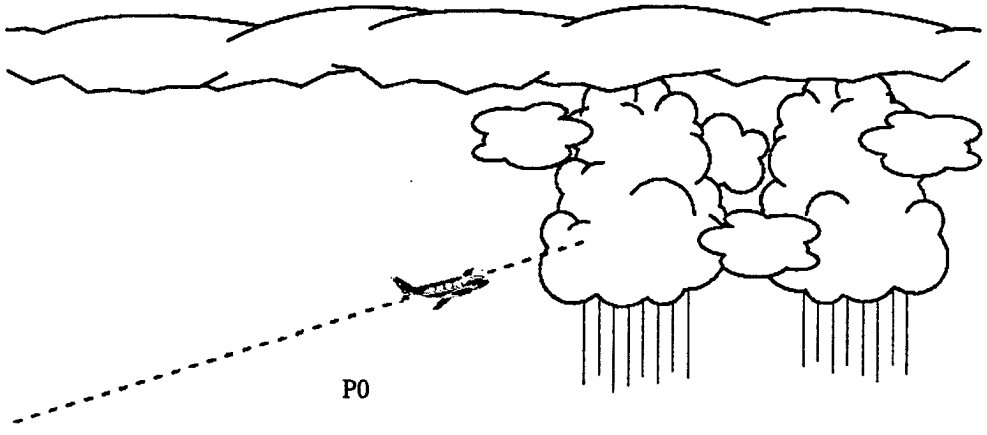

Figure B.2 Observed cloud structure during flight leg P0 and location of aircraft.

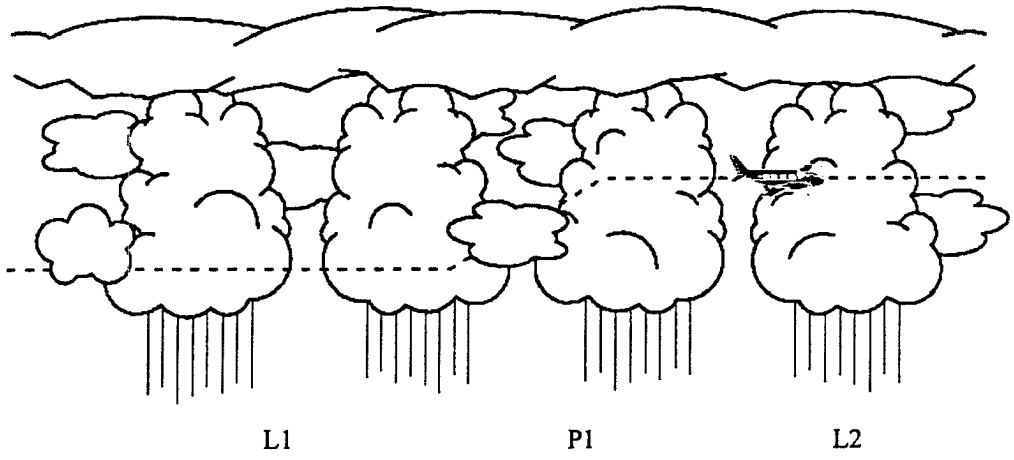

Figure B.3 Observed cloud structure during flight legs L1, P1, and L2. Relative positions of each flight leg within cloud deck 2 indicated by dashed line.

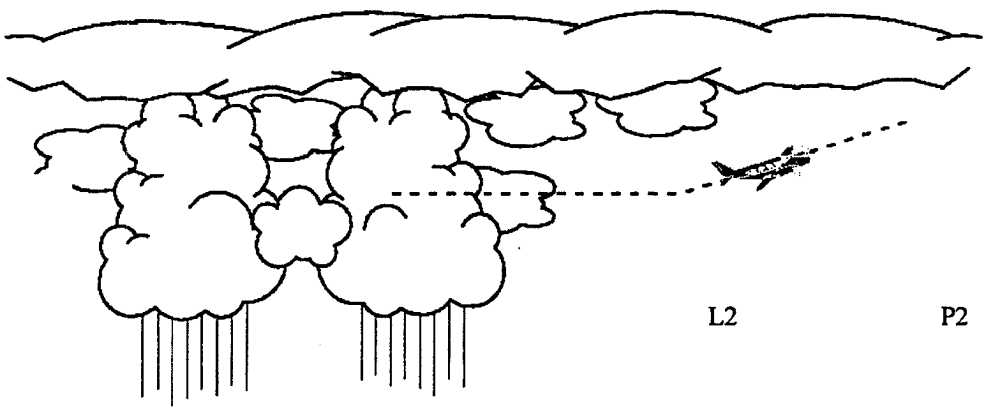

Figure B.4 Observed cloud structure during flight legs L2 and P2. Location of aircraft indicated by dashed line.

a)

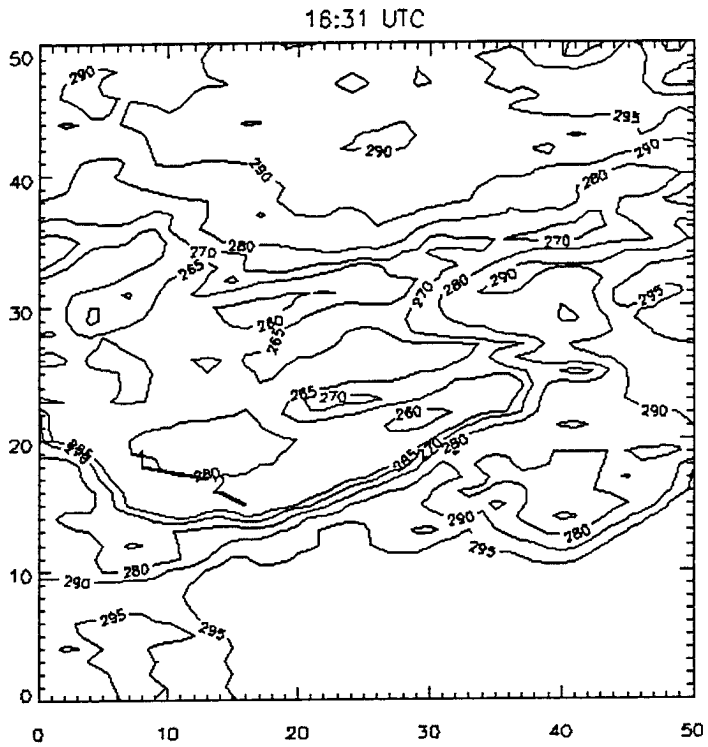

b)

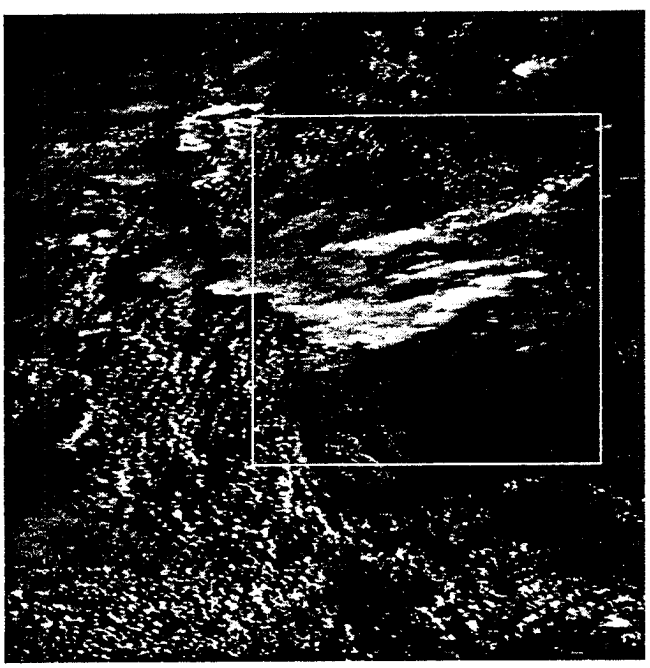

Figure B.5 a) 16:31 UTC GOES-8 10.7 μm brightness temperature map of the J25acs with level flight legs L1 and L2 also shown. b) 16:31 UTC GOES-8 0.7 μm image of the J25acs.

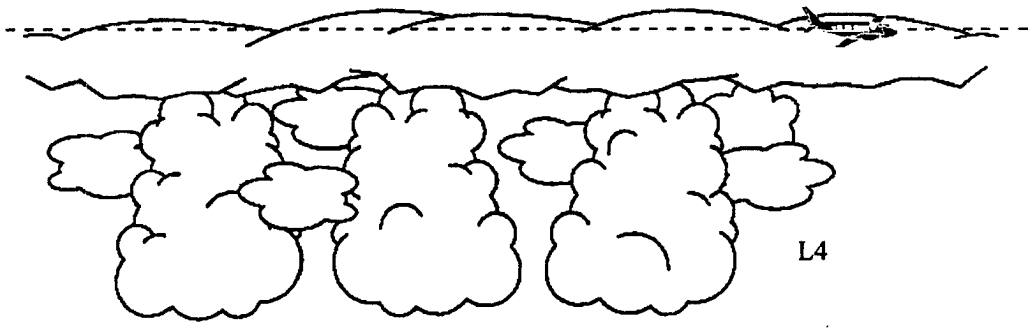

Figure B.6 Observed cloud structure during flight leg L4. Dashed line indicates location of aircraft within cloud deck 1.

a)

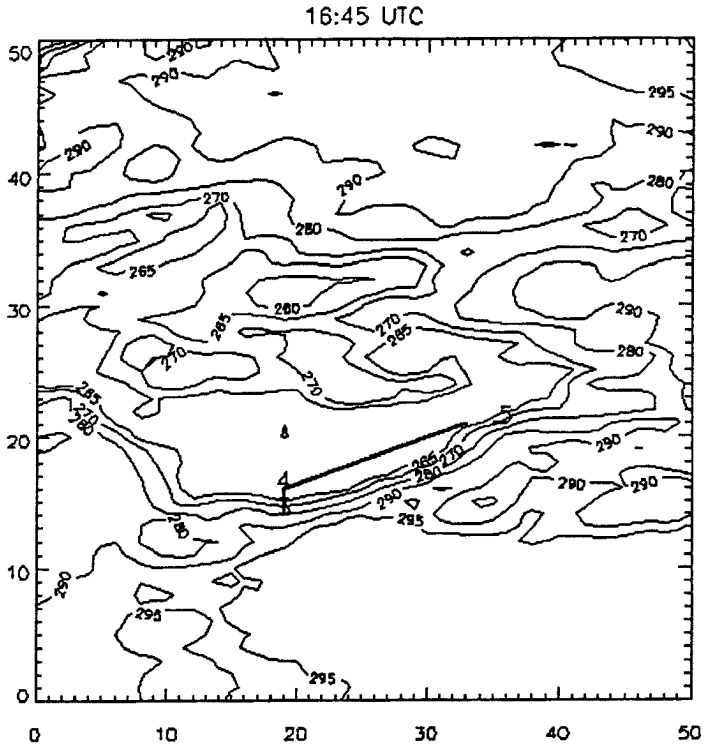

b)

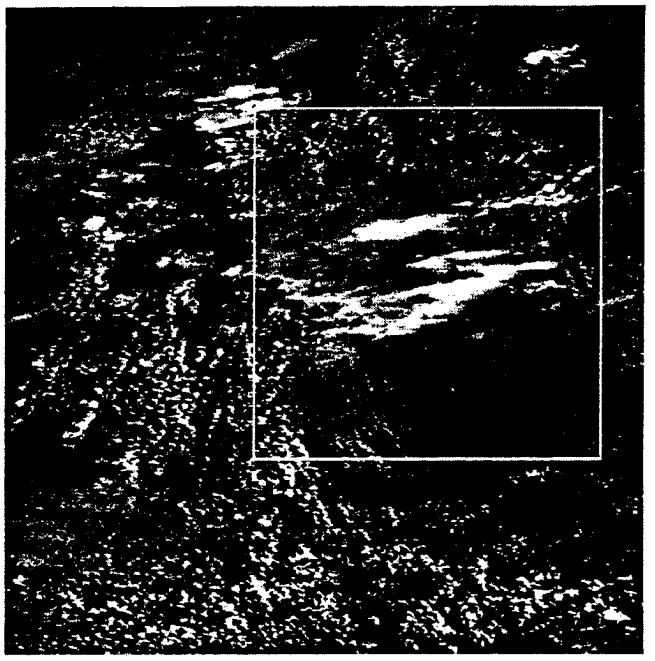

Figure B.7 a) 16:45 UTC GOES-8 10.7 μm brightness temperature map of the J25acs with level flight legs L3,L4 and L5 also shown. b) 16:45 UTC GOES-8 0.7 μm image of the J25acs.

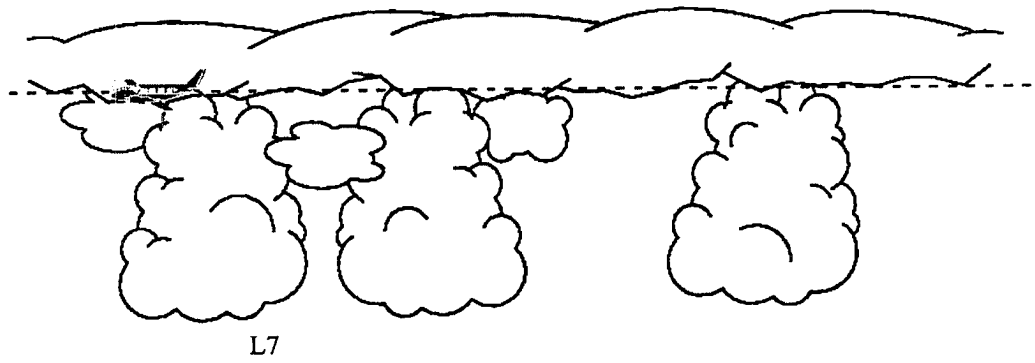

Figure B.8 Observed cloud structure during flight leg L7. Location of the flight leg is indicated by the dashed line.

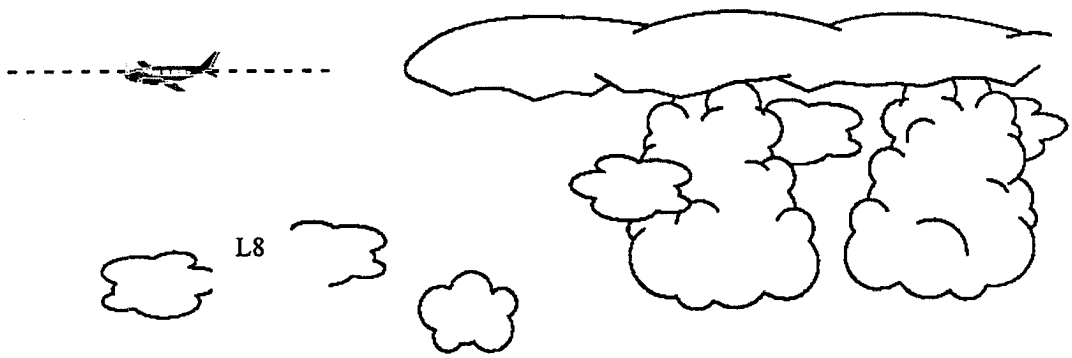

Figure B.9 Observed cloud structure during flight leg L8. Location of the flight leg is indicated by dashed line

8

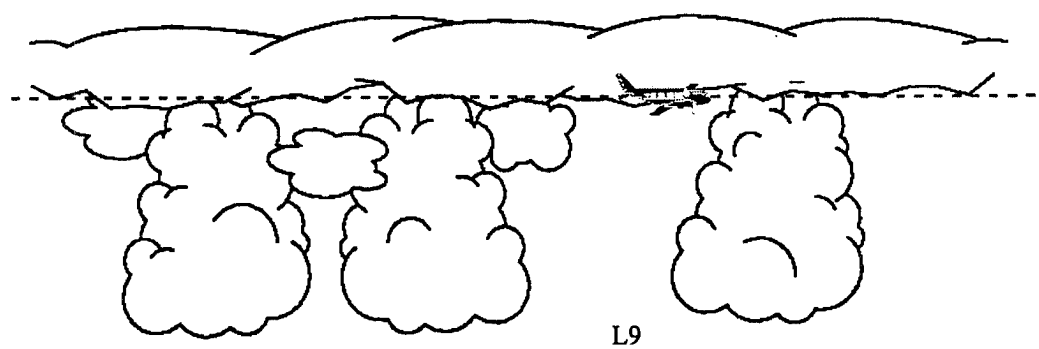

Figure B.10 Observed cloud structure during flight leg L9. Location of the flight leg is indicated by the dashed line

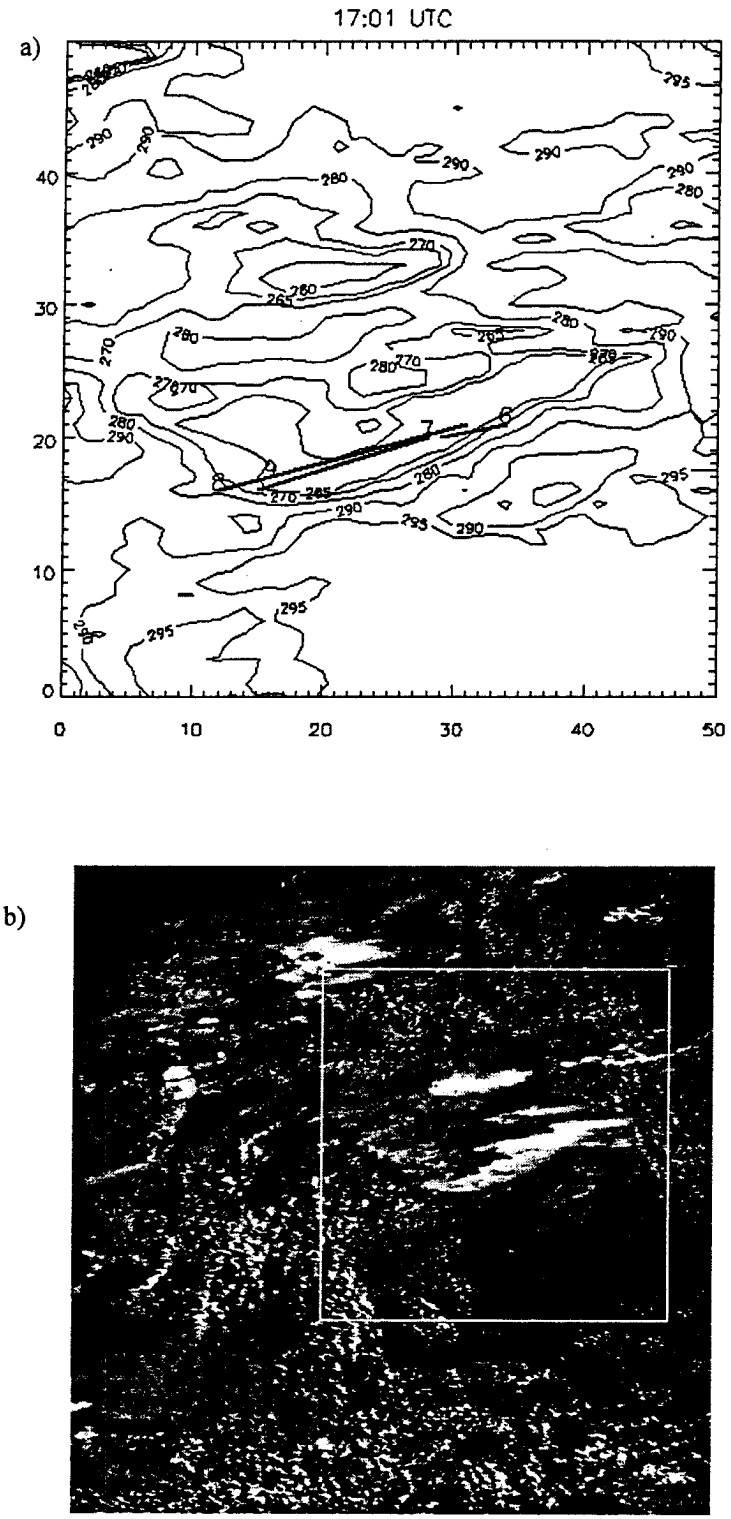

Figure B.11 a) 17:01 UTC GOES-8 10.7 μm brightness temperature map of the J25acs with flight legs L6, L7, L8, and L9 also shown. b) 17:01 UTC GOES-8 0.7 μm image of the J25acs.

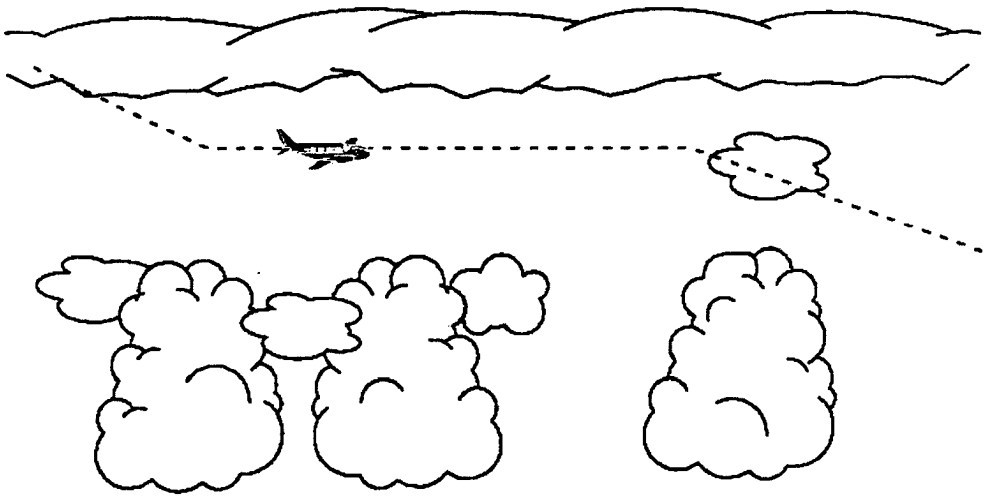

Figure B.12 Observed cloud structure during flight legs P4, L10, and P5. Location of flight leg indicated by dashed line

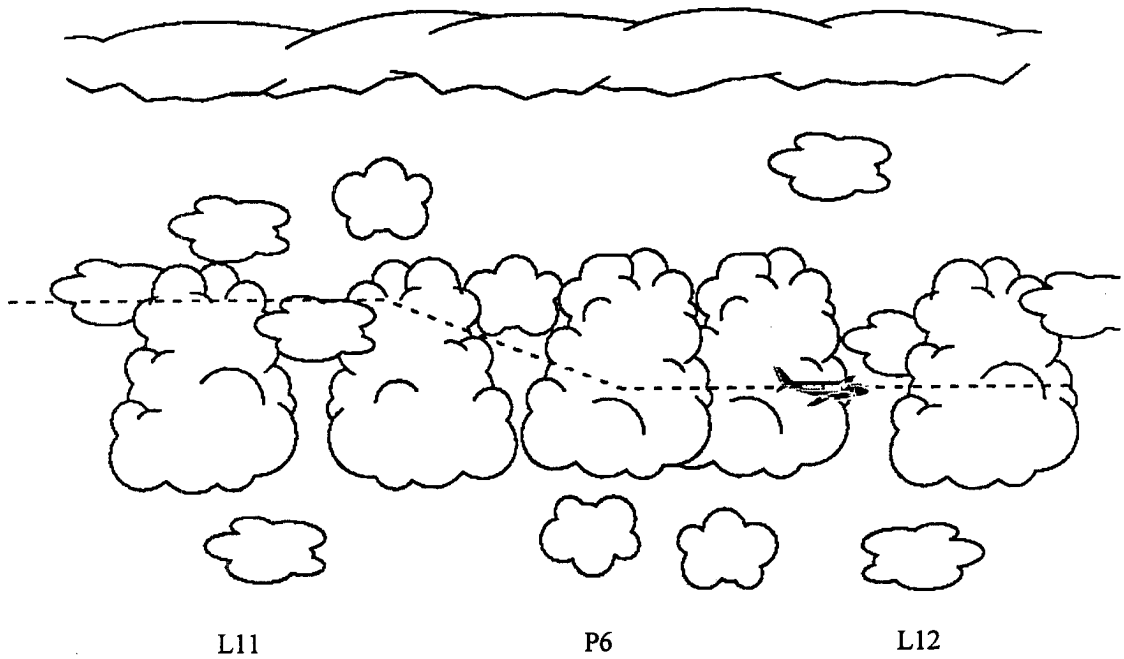

Figure B.13 Observed cloud structure during flight legs L11, P6, and L12. The location of each flight leg is indicated by the dashed line.

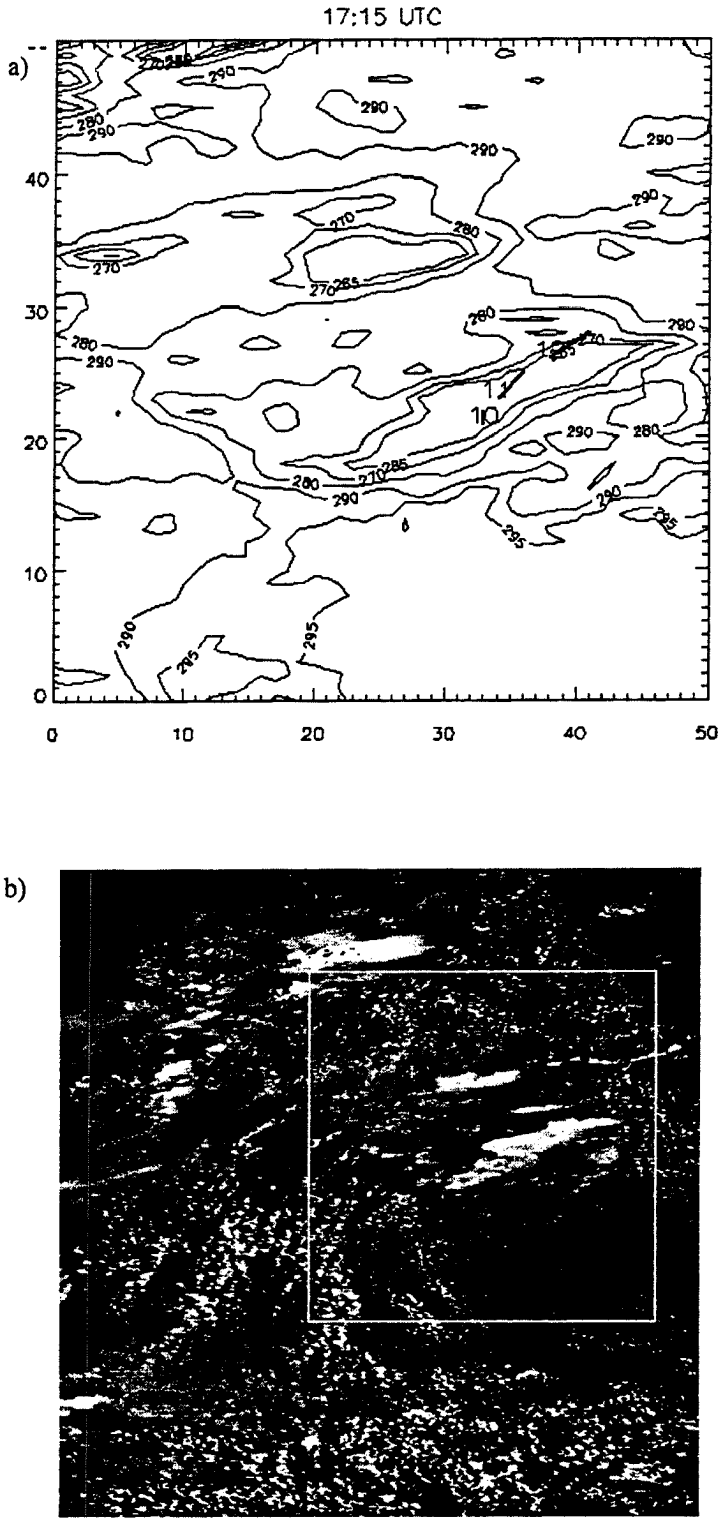

Figure B.14 a) 17:15 UTC GOES-8 10.7 μm brightness temperature map of the J25acs with flight legs L10, L11, and L12 also shown. b) 17:15 UTC GOES-8 0.7 μm image of the J25acs.

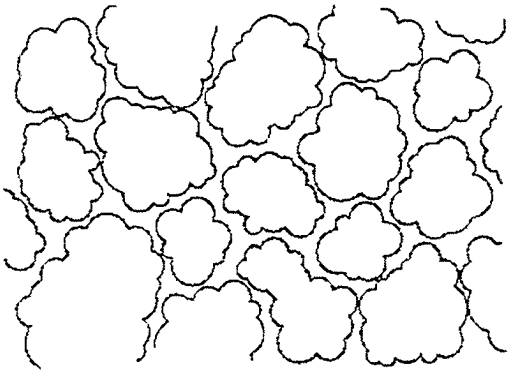

Figure B.15 Observed cloud structure of J25acs during profile leg S1.

S1

Figure B.16 Observed cloud structure during S1 sounding profile. Location of flight leg indicated by the dashed line.

a)

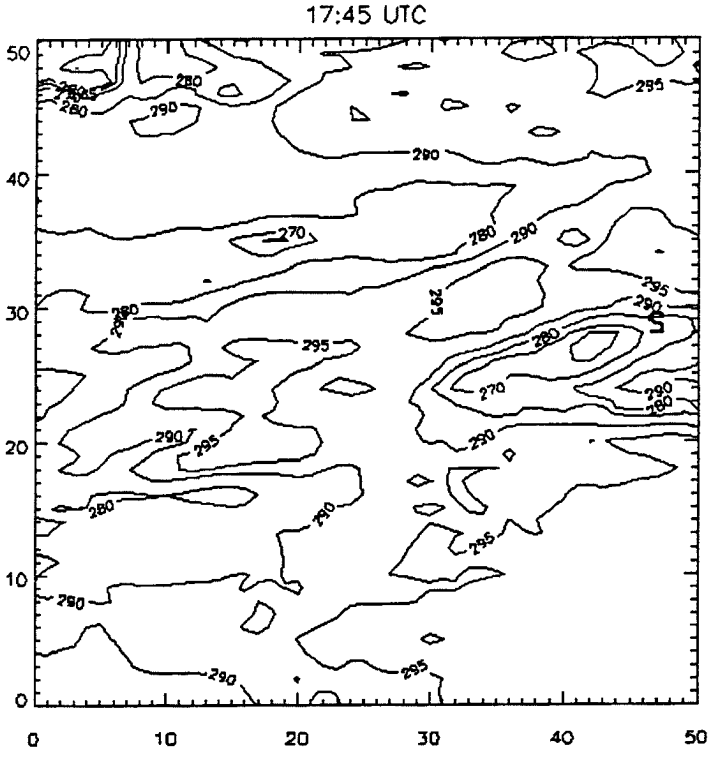

b)

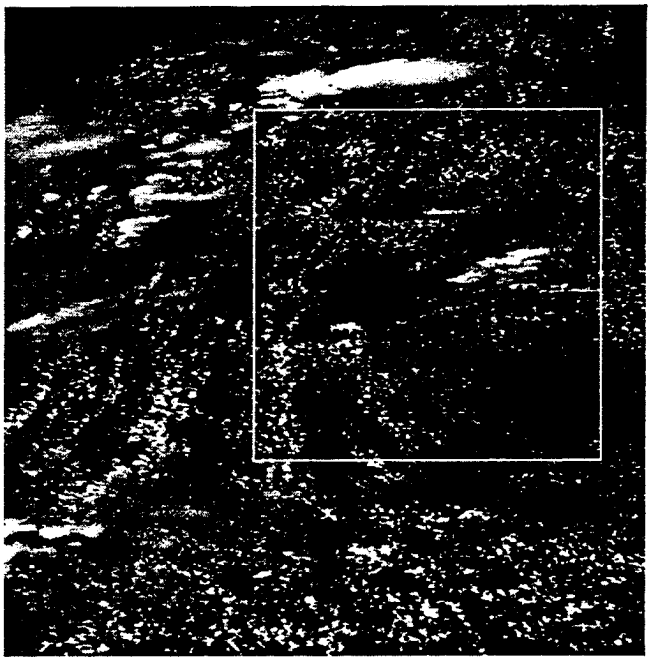

Figure B.17 a) 17:45 UTC GOES-8 10.7 μm brightness temperature map of the J25acs with the location of the sounding profile S1 also shown. b) 17:45 GOES-8 0.7 μm image of the J25acs.

APPENDIX C

OBSERVATIONS OF J25 EXPERIMENT IN-FLIGHT VIDEO

Detailed observations made of the J25 experiment in-flight video are presented in tabular format. The time of each observation (during the experiment), the flight leg (L0-L12, P0-P7, S1), the altitude of the aircraft, and the camera used to record the video (forward looking or downward looking) are included with each observation. Also, observations made by in-flight passenger (in-flight video recording includes sound) are included.

Table C.1 Observations of J25 experiment in-flight video for flight legs L0 and P0 (time period 16:16:12-16:31:54). Time and camera (F indicates forward looking and D indicates downward looking) are indicated for each observation. Observations made by the in-flight passenger are indicated as O. For profile flight legs, initial and final height and pressure are both indicated. For level flight legs, pressure and altitude are indicated.

Type	Flight Leg	Time Interval	Pressure	Height	Observations
L	L0	16:16:12-16:27:18	575 mb	4500 m	16:27:19 F - Thin white stratiform layer cloud in front of aircraft. Large horizontal extent. Blue sky visible through cloud elements. Estimate cloud base is 1000 m above aircraft. Estimate thickness is less 100 - 200 meters. 16:27:19 F - Cumuliform cloud layer visible ahead of aircraft. Virga is visible below the base of the cumuliform cloud layer. Cumuliform cloud layer is below upper thin cloud layer
P	P0	16:27:19-6:31:54	575 mb 531 mb	4500 m 5126 m	16:28:32 F - Thin white stratiform layer cloud above aircraft. Cellular elements visible in cloud layer. Estimated dimension of elements is 50 meters. Estimated cloud thickness is 100 - 200 meters 16:28:32 F - Cumuliform cloud layer ahead of aircraft. Cumuliform cloud layer appears to be at the same altitude as aircraft. Turrets are visible at the top of the cloud layer. Estimated vertical thickness of cloud layer including turrets is 500 m. Base appears dark. 16:30:00 F - Upper stratiform cloud appears more continuos. Blue sky no longer visible. 16:30:09 F - Cumulus cloud layer is still visible. Turrets are ragged in appearance. Upper stratiform cloud layer now appears thicker. Cellular elements no longer visible. Blue sky no longer visible.

Table C.2 Observations of J25 experiment in-flight video for flight legs L1- P2 (time period 16:31:55-16:40:54). Time and camera (F indicates forward looking and D indicates downward looking) are indicated for each observation. Observations made by the in-flight passenger are indicated as O . For profile flight legs, initial and final height and pressure are both indicated. For level flight legs, pressure and altitude are indicated.

Type	Flight Leg	Time	Pressure	Height	Observations
L	L1	16:31:55-16:34:55	531 mb	5126 m	16:31:55 F - Aircraft enters base of cumuliform cloud. 16:33:48 F - In and out of cloud 16:35:10 D -Ground visible. No cloud elements visible below. 16:35:50 O -In the base of the cloud. Appears broken.
P	P1	16:34:56-16:35:50	531 mb 526 mb	5126 m 5383 m	16:35:30 F- In cloud.
L	L2	16:35:51-16:37:54	526 mb	5383 m	16:36:50 F - In and out of cloud. Clear air visible above between cloud elements. 16:36:50 O- Starting to see the tops of the clouds. Right in the middle of the cloud layer.
P	P2	16:37:55-16:40:54	526 mb 486 mb	5383 m 5810 m	16:37:52 F - Exit cloud. Clear directly ahead. Thin white layer cloud visible above. Estimate cloud layer is 1000m above aircraft. Cloud layer appears cellular in texture. Estimated thickness of cloud layer is 100 m. 16:39:29 F - Thin layer cloud right above aircraft. Cloud contains cellular elements. Estimated cloud layer thickness is less than 100m. Blue sky is visible through cloud. 16:40:51 F - Two layers visible ahead. Lower layer is darker than the upper layer. Lower layer top contains cumuliform turrets rising out of layer.

Table C.3 Observations of J25 experiment in-flight video for flight legs L3- L5 (time period 16:40:55-16:52:45 UTC). Time and camera (F indicates forward looking and D indicates downward looking) are indicated for each observation. Observations made by the in-flight passenger are indicated as O. For profile flight legs, initial and final height and pressure are both indicated. For level flight legs, pressure and altitude are indicated.

Type	Flight Leg	Time (UTC)	Pressure	Height	Observations
L	L3	16:40:55-16:43:40	486 mb	5810 m	16:41:35 F - Two distinct decks ahead. Thin white cloud layer above. Blue sky is visible through cloud above. Cloud layer ahead is at aircraft level. Appears thicker than thin diffuse cloud layer above 16:42:59 F - Enter cloud. Blue sky visible above as aircraft passes though cloud elements. Appears as if aircraft is flying at the top of cloud layer.
L	L4	16:43:41-16:50:04	486 mb	5810 m	16:46:36 O- Right at the top. Can see the sun shining through. 16:49:22 D - Cloud layer visible below. Cloud layer is thin and diffuse. Estimate cloud layer is 1000 m below aircraft. Ground is visible through cloud
L	L5	16:50:05-16:52:45	486 mb	5807 m	16:51:41 F - Thin cloud layer above. Blue sky visible through cloud layer. Estimated thickness of cloud layer is less than 100 meters. 16:51:58 F -Top of thick white cloud layer visible ahead. Top appears smoothed or laminar. Mounds are evident on the top of the cloud layer. Extends off in the distance. 16:52:27 F - Thin grayish white cloud layer just above aircraft. Blue sky visible through the cloud. Estimated thickness of cloud layer is 50m.

Table C.4 Observations of J25 experiment in-flight video for flight legs L6- P3 (time period 16:52:43-16:55:25 UTC). Time and camera (F indicates forward looking and D indicates downward looking) are indicated for each observation. Observations made by the in-flight passenger are indicated as O. For profile flight legs, initial and final height and pressure are both indicated. For level flight legs, pressure and altitude are indicated

Type	Flight Leg	Time	Pressure	Height	Observations
L	L6	16:52:43-16:54:56	486 mb	5807 m	16:53:15 F - Thin cloud still above aircraft. 16:53:26 D - Thin layer cloud below. Cloud layer is grayish white. Cloud layer appears diffuse. Ground is visible through cloud layer. Estimate cloud layer is 500-1000m below aircraft. Layer appears very thin and is continuous. Layer appears distinct from aircraft level. 16:54:34 D - Thicker grayish white cloud layer below. Estimate cloud layer is 500 m -1000 m below aircraft. Layer cloud now contains cellular elements. Elements are white to gray and ragged in texture. Estimated horizontal size of elements is 50 - 100m. Ground is visible in between cloud elements. At times cloud elements appear to be right below aircraft and ground is completely obscured.
P	P3	16:54:57-16:55:25	486 mb 495 mb	5807 m 5655 m	

Table C.5 Observations of J25 experiment in-flight video for flight leg L7 (time period 16:55:22-17:00:56 UTC). Time and camera (F indicates forward looking and D indicates downward looking) are indicated for each observation. Observations made by the in-flight passenger are indicated as O. For profile flight legs, initial and final height and pressure are both indicated. For level flight legs pressure, and altitude are indicated.

Type	Flight Leg	Time (UTC)	Pressure	Height	Observations
L	L7	16:55:22-17:00:56	496 mb	5655 m	16:55:25 D - Thick grayish white cellular cloud layer visible below. Ground visible in between cloud elements. Estimated size of elements is 100 m - 200m. 16:56:17 D - Cloud layer below appears thicker and darker. Appears to become connected to cloud layer at aircraft level. Cloud elements right below aircraft. 16:57:50 D - Puffy grayish white cloud elements visible below. Ground is completely obscured. 16:58:48 D - Thick dark cloud below. Ground is obscured by cloud. No visibility. 16:59:06 D - Thick dark cloud below. Cloud elements are still apparent. Ground visible in regions when cloud elements below aircraft become thinner. 16:59:24 D - Cloud elements below aircraft appear separate and ragged. Cloud layer below is more broken than previous observations. Cloud elements are estimated to be 500 m to 1000m below aircraft. 17:00:00 D - Cloud elements below become thicker. Appear to be right below aircraft.

Table C.6 Observations of J25 experiment in-flight video for flight leg L8-L9 (time period 17:00:57-17:10:47 UTC). Time and camera (F indicates forward looking and D indicates downward looking) are indicated for each observation. Observations made by the in-flight passenger are indicated as O. For profile flight legs, initial and final height and pressure are both indicated. For level flight legs, pressure and altitude are indicated.

Type	Leg	Time (UTC)	Pressure	Height	Observations
L	L8	17:00:57-17:04:51	496 mb	5655 m	17:01:20 D -Clear region right below aircraft. Thin white to grey cellular cloud deck visible below clear region. Estimate cloud layer is 500m-1000m below aircraft. Ground visible in between cloud elements. Elements are randomly distributed and have a ragged appearance. 17:03:48 F - White layer cloud visible ahead of aircraft. Cloud top is flat with rounded smoothed elements. Cloud top is well defined. 17:04:42 F - Aircraft right in the tops of clouds. Cloud tops are white. 17:04:51 F - No visibility.
L	L9	17:04:52-17:10:47	496 mb	5655 m	17:07:20 D - White cloud elements visible below as aircraft enters clear regions. Ground visible in between cloud elements. 17:08:26 D - Cloud elements right below aircraft. 17:09:53 D - White cellular cloud visible below. Ground visible in between elements. Estimated vertical extent of cloud elements is 200m - 500m.

Table C.7 Observations of J25 experiment in-flight video for flight leg P4 - P6 (time period 17:10:48-17:18:17 UTC). Time and camera (F indicates forward looking and D indicates downward looking) are indicated for each observation. Observations made by the in-flight passenger are indicated as O. For profile flight legs, initial and final height and pressure are both indicated. For level flight legs, pressure and altitude are indicated.

P	P4	17:10:48-17:11:51	496 mb 506 mb	5655 m 5500 m	17:11:09 F - Two distinct cloud decks visible above and below aircraft. Both decks are white. Upper deck is cellular, with blue sky visible in between elements. Estimated vertical thickness of upper layer is 100 m - 200 m. Lower cloud deck top contains small cumulus turrets. Estimated vertical extent of turrets is 100m - 200m. Lower cloud deck base is not visible. Appears clear in between decks.
L	L10	17:11:52- 17:15:01	506 mb	5500 m	17:14:17 F- Two distinct cloud layers above and below aircraft. Upper layer base is uniform. Elements no longer apparent within upper cloud layer . Estimate upper layer base is 200m - 500 m above aircraft. Blue sky is no longer visible. Lower layer top contains cumulus turrets which are rising up into the clear region at aircraft level.
P	P5	17:15:02- 17:15:34	506 mb 522 mb	5500 m 5261 m	
L	L11	17:15:35-17:17:10	522 mb	5261 m	17:16:00 O - Aircraft is in the upper portions of the lower cumulus deck.
P	P6	17:17:11-17:18:17	522 mb 532 mb	5261 m 5125 m	

Table C.8 Observations of J25 experiment in-flight video for flight leg L12 - S1 (time period 17:18:18-18:11:10 UTC). Time and camera (F indicates forward looking and D indicates downward looking) are indicated for each observation. Observations made by the in-flight passenger are indicated as O. For profile flight legs, initial and final height and pressure are both indicated. For level flight legs, pressure and altitude are indicated.

L	L12	17:18:18-17:19:48	532 mb	5125 m	17:17:37 D - Ground visible below. White cloud elements visible below. Estimate vertical extent of cloud elements is 500 m - 800 m. Cloud elements at times are right below aircraft. At times appear to be 500 m - 1000m below aircraft. 17:19:20 D - White cellular cloud visible below. Appears to become distinct from cloud layer presently sampled.
P	P7	17:19:49-17:42:06	532 mb 368 mb	5125 m 7919 m	17:20:30 F - Cloud layer visible ahead. Cloud layers appear to be at the same altitude as sampled cloud but appears to be a great distance away.
S	S1	17:42:07-18:11:10	368 mb 917 mb	7919 m 608 m	17:48:15 D - Layer cloud visible directly below aircraft. Cellular in appearance Ground is not visible in between cells. Closed cell structure 17:49:15 F - Layer cloud visible above aircraft Layer cloud visible in distance which appears to be at an altitude which is slightly below the layer above the aircraft.

APPENDIX D

OVERVIEW OF THE PARCEL METHOD

This appendix contains an overview of the parcel method. In this method, the relationship between the lapse rate (of the layer), the saturated moist adiabatic lapse rate, and the dry adiabatic lapse rate of θ_v and the saturation state of a displaced air parcel (whether the parcel is saturated or not) are used to establish criteria for determining the static stability of the layer. The atmosphere is said to be

(1) Absolutely stable if $\gamma < \Gamma_s$,

(2) saturated neutral if $\gamma = \Gamma_s$,

(3) conditionally unstable if $\Gamma_s < \gamma < \Gamma_d$,

(4) dry neutral if $\gamma = \Gamma_d$,

(5) absolutely unstable if $\gamma > \Gamma_d$.

Here γ is the environmental lapse rate, Γ_s is the saturated adiabatic lapse rate, and Γ_d is the dry adiabatic lapse rate of the virtual potential temperature at the level of consideration. We now discuss each of the stability criterion in terms of whether a saturated or unsaturated air parcel is displaced upwards (pseudo-adiabatically) in the respective environments. For each criterion, we assume that the saturated parcel of air (if displaced upwards) will rise at the moist adiabatic lapse rate and the unsaturated parcel (if displaced upwards) will rise at the dry adiabatic lapse rate. In both cases, we assume that the pressure of the air parcel immediately adjusts to that of it's environment. Also, two inherent assumptions of the parcel method are that (Hess 1959, p. 95):

(1) no compensating motions occur in the environment as the parcel moves and

(2) the parcel does not mix with its environment and so retains it's identity.

In an absolutely stable atmosphere, both a saturated and an unsaturated parcel of air when displaced upwards will immediately become cooler than their environment. This will result in a downward acceleration, via the buoyancy force, which will tend to return each parcel to it's original level. Since an unsaturated parcel of air should rise at the dry adiabatic lapse rate (which is always less than or equal to the moist adiabatic lapse rate), this parcel would be more negatively buoyant than a saturated parcel.

In a saturated neutral atmosphere, a saturated parcel of air when displaced upwards, will rise at the saturated adiabatic lapse rate and hence will be at the same temperature as its environment. Thus, this parcel will experience no net acceleration. An unsaturated parcel will rise at the dry adiabatic lapse and hence will become cooler than its environment. Thus, this air parcel will experience a downward acceleration towards its original level.

In a conditionally unstable atmosphere, a saturated parcel of air when displaced upwards will be warmer than its environment. This will result in a positive buoyancy force on the air parcel and hence it will continue to rise at an increasing rate. The parcel will continue to experience a net upward force until it encounters a level of the atmosphere where its virtual potential temperature is cooler than that of its environment. At this new level, the air parcel will experience a net downward force, will eventually come to rest, and will then proceed downward until it arrives at a level where its virtual potential temperature is equal to that of its environment. An unsaturated parcel of air when displaced upwards will immediately become cooler than its environment and will therefore experience a downward restoring force towards its original level.

In a dry neutral atmosphere, a saturated parcel of air displaced upwards will proceed in a manner similar to that described for the case of a conditionally unstable atmosphere. An unsaturated parcel of air when displaced upwards will rise at the dry adiabatic lapse rate and hence will have a virtual potential

temperature equal to that of its environment. Hence, the unsaturated parcel of air will remain at this level unless further upward impulse is applied.

In an absolutely unstable atmosphere, both a saturated and an unsaturated parcel of air when displaced upwards will proceed in a manner similar to that described for a saturated parcel of air displaced upwards in a conditionally unstable atmosphere. Thus, it should be expected that the absolutely unstable atmosphere will not persist for long periods of time, due to the rapid mixing of air parcels which would occur in this event. Of course the parcel method can not predict this mixing since the method assumes that no compensating motions will occur.

APPENDIX E

MODEL SOLUTION PROCEDURE

In this appendix, we provide an overview of the model's solution procedure. The overview is based on that given by Evans (1998) . Since the model was used in a plane parallel format, our overview is in the context of plane parallel radiative transfer. Evans (1998) discusses the solution procedure in the more general context of 3-D radiative transfer.

SHDOM solves the equation of transfer on a discrete grid of points. The grid is adaptive such that the spatial resolution of the grid may change as the equation of transfer is solved. The model solves the equation of transfer for the source function by using both the spherical harmonic and discrete ordinate methods within a Picard iteration. The iterative solution procedure is basically a successive order of scattering approach (Evans 1998). During each iteration the following steps occur (Evans 1998):

1. The spherical harmonics source function is transformed to discrete ordinates;
2. The source function is integrated to obtain the radiance field;
3. the radiance field is transformed to spherical harmonics; and
4. the source function is computed from the radiance field in spherical harmonics.

At the end of each iteration, a solution convergence test is made. This test is passed when the rms difference between successive source function fields is below a solution convergence criterion (specified by the user). If the test is passed, then the iterative solution procedure is stopped and radiometric quantities (specified by the user) are output. The following paragraphs explain each of the above listed steps in more detail.

Within step 1, the spherical harmonic source function is transformed to discrete ordinate space. The spherical harmonic representation of the source function at a vertical grid point, s_k , is given by (Evans 1998)

$$J(s_k, \mu) = \sum_l P_l(\mu) J_l(s_k) \qquad \text{(E.1)}$$

where the P_l (μ)s are the normalized associate Legendre polynomials, the J_l.s are the associate Legendre coefficients, and μ is cosine of the zenith angle. The transformation of the spherical harmonic source function to discrete ordinates involves specifying the source function at a discrete number, N_μ ,of Gaussian quadrature angles (ordinates) , μ_j, and is given by (Evans 1998)

$$J(s_k, \mu_j) = \sum_l P_l(\mu_j) J_l(s_k) . \qquad \text{(E.2)}$$

The number of discrete ordinates is specified by the user and they also determine the order of the spherical harmonic expansion. The order of the expansion, L, is given by (Evans 1998)

$$L = N_\mu - 1. \qquad \text{(E.3)}$$

Note, the model allows the user to choose whether the expansion of the source function should be carried out to the maximum number of terms. This is achieved through a user input parameter referred to as SHACC, which determines the minimum value of the expansion terms. If SHACC is zero, then the expansion is carried out to the maximum number of terms.

Within step 2, the integral form of the radiative transfer equation is used to compute the radiance, I, at a particular grid point, s_k ,and along a particular discrete ordinate, μ_j. Because there are N_μ discrete ordinates, a total of N_μ operations are required for each grid point. A backwards integration scheme is used to approximate the integral form of the transfer equation. The scheme is given by

$$I(s_k,\mu_j) = \exp\left[-\int_{s_{j-1}}^{s_k}\sigma_{ext}(s')ds'\right]I(s_{k-1}) + \int_{s_{s-1}}^{s_k}\exp\left[-\int_{s'}^{s}\sigma_{ext}(t)dt\right]J(s',\mu_j)\sigma_{ext}(s')ds'. \quad (E.4)$$

Equation E.1 shows that within the backwards integration scheme, the radiance, I, at the grid point s_k depends on the radiance, I, at the grid point s_{k-1} ,on the extinction, σ_{ext} , at the grid points s_k and s_{k-1} ,and on the product of the source function and the extinction, $J\sigma_{ext}$ at the grid points s_k and s_{k-1} Both σ_{ext} and $J\sigma_{ext}$ are assumed to vary linearly between the grid points s_k and s_{k-1} within the scheme.

In step 2, a check is also made to determine how much $J\sigma_{ext}$ changes between grid points. If the change exceeds a certain criterion, then an extra grid point is added between the two original grid points. The optical properties are then trilinearly interpolated and the radiance is linearly interpolated to the new grid point. Extra grid points are added to increase the accuracy of the second term in the backwards integration scheme (Evans 1997). The criterion for adding new grid points is specified through the input parameter SPLITACC.

In step 3, the radiance field is transformed from discrete ordinate space to spherical harmonic space. The transformation is given by (Evans 1997)

$$I_l(s_k) = \sum_{j=1}^{N_\mu}\omega_j P_l(\mu_j)I(s_k,\mu_j), \quad (E.5)$$

where ω_j are the normalized Gauss-Legendre quadrature weights.

In step 4, the source function is computed from the radiance field by (Evans 1997)

$$J_l(s_k) = \frac{\varpi_0\chi_l(s_k)}{2l+1}I_l(s_k) + S_l(s_k), \quad (E.6)$$

where ϖ_0 is the single scatter albedo, χ_l is lth Legendre coefficient of the scattering phase function $P(\mu)$, and S_l is the lth Legendre coefficient of the solar pseudo-source and /or thermal source respectively. The Legendre coefficients of the scattering phase function are specified by the user at each grid point within the medium and they are given by (Stephens At 722 class notes)

$$\chi_l(s_k) = \frac{2l+1}{2}\int_{-1}^{1}P(s_k,\mu)P_l(\mu)d\mu. \quad (E.7)$$

As stated by Evans (1997), the thermal source is isotropic and so involves just the first spherical harmonic term:

$$S_l(s_k) = (1-\varpi_0)B[T,s_k](4\pi)^{1/2}\delta_{l0} \quad (E.8)$$

where B[T] is the Planck function... The solar pseudo-source of diffuse radiation is

$$S_l(s_k) = \frac{F_0}{\mu_0}e^{-\tau_{s_k}}P_l(\mu_0)\frac{\varpi_0\chi_l(s_k)}{2l+1} \quad (E.9)$$

where F_0 is the solar flux on a horizontal plane, μ_0 is the cosine of the solar zenith angle and τ_s is the optical path from the grid point to the upper domain boundary along the solar direction.. As previously stated, at the end of step 4, a solution convergence test is made. The solution convergence criterion is specified by the user through the input parameter, SOLACC. If convergence is achieved, the iteration procedure is stopped and user specified radiometric quantities are output at each grid point.

Computation of Radiometric Quantities

The radiometric quantities required in our research were the thermal and solar radiative flux divergence and the hemispheric upwelling and downwelling thermal and solar fluxes. Both of these quantities are computed by the model. The hemispheric upwelling and downwelling fluxes at each grid point are computed from the discrete ordinate radiances as follows (Evans 1997):

$$F^{\pm}(s_k) = \sum_{j=1}^{N_\mu/2} \omega_j |\mu_j| I(s_k, \mu_j). \qquad (E.10)$$

The net flux divergence at each grid point is computed by (Evans 1997)

$$-\vec{\nabla}\cdot\vec{F}_{net}(s_k) = \sigma_{ext}(s_k)(1-\varpi_0(s_k))\left[4\pi\bar{I}(s_k) + \frac{F_0(s_k)}{\mu_0} e^{-\tau_{s_k}} - 4\pi B[T, s_k]\right] \qquad (E.11)$$

where $\bar{I}$ is the angular mean radiance and is given by (Evans 1997)

$$\bar{I}(s_k) = \frac{1}{(4\pi)^{1/2}} I_{l=0}. \qquad (E.12)$$

APPENDIX F

COMPUTATION OF NET LAYER HEATING RATE, NET CLOUD TOP THERMAL COOLING RATE, NET CCLOUD BASE THERMAL HEATING RATE, SOLAR TRANSMISSION, AND SOLAR ALBEDO

In this appendix, we describe how the net layer heating rate, net cloud top cooling rate, net cloud base heating rate, and solar transmission and solar albedo were computed from SHDOM model output. The net cloud top cooling rates, net cloud base heating rates, the solar albedo, and the transmission are parameters which were used in the sensitivity studies presented in appendix G.

The net cloud layer thermal or solar heating rate, $\frac{dT}{dt}$, for each cloud was computed as follows

$$\frac{dT}{dt} = \frac{\sum \frac{dT}{dt}(s_k)\Delta s_k}{\sum \Delta s_k} \qquad \text{(F.1)}$$

where $\Delta s_k = \frac{s_{k+1} - s_{k-1}}{2}$ is the mean distance between successive grid points, and $\frac{dT}{dt}(s_k)$ is the thermal or solar heating rate at a grid point in the layer. Thus, the net cloud layer thermal and solar heating rates were simply the average heating rates of a layer.

The net thermal cloud top cooling rate, $\frac{dT^-}{dt}$,for a cloud layer was computed as

$$\frac{dT^-}{dt} = \frac{\sum \frac{dT^-}{dt}(s_k)\Delta s_k}{\sum \Delta s_k}, \qquad \text{(F.2)}$$

where $\frac{dT^-}{dt}(s_k)$ was specified to be zero if the heating rate was positive and was specified to be $\frac{dT}{dt}(s_k)$ if $\frac{dT}{dt}(s_k)$ was negative. Likewise, the net cloud base thermal warming rate, $\frac{dT^+}{dt}$, was computed as

$$\frac{dT^+}{dt} = \frac{\sum \frac{dT^+}{dt}(s_k)\Delta s_k}{\sum \Delta s_k}, \qquad (F.3)$$

where $\frac{dT^+}{dt}(s_k)$ was specified to be zero if the heating rate was negative and was specified to be $\frac{dT}{dt}(s_k)$ if $\frac{dT}{dt}(s_k)$ was positive. The net cloud top cooling rates and net cloud base heating rates were computed so that we could identify the relative contribution of thermal cooling rates (negative heating rates) and thermal warming rates (positive heating rates) towards the net thermal heating rate of a layer.

The albedo r, and transmittance t, for each cloud layer were respectively computed as (Liou 1992)

$$r = \frac{F^+(s_{k_t})}{F^-(s_{k_b})}, \text{ and} \qquad (F.4)$$

$$t = t = \frac{F^-(s_{k_b})}{F^-(s_{k_t})}, \qquad (F.5)$$

where $F^-(s_{k_t})$ and $F^+(s_{k_t})$ are the downward and upward solar flux at the top grid point of a layer and $F^-(s_{k_b})$ and $F^+(s_{k_b})$ are the downward and upward solar flux at the bottom grid point of a layer.

APPENDIX G

SENSTIVITY STUDY

Here, we present results from a sensitivity study using the SHDOM radiative transfer model. The purpose of this study was to determine the effect of: 1) the cloud liquid water profile, 2) the cloud liquid water path, 3) the cloud drop size effective radius, and 4) the presence of additional cloud layers on the SHDOM simulated thermal and solar radiative structure of Altocumulus-like cloud layers. Results from this study were used as guideline for the interpretation of radiative transfer simulations in the cloud profiles B, BA and D.

G.1 Sensitivity of Calculated Radiative Structure to Changes in the Profile LWC

Methodology

Our method used to study the effect of the vertical profile of LWC on the simulated thermal and solar radiative structure of altocumulus-like clouds was as follows. Three cloud optical property profiles were first constructed each with a different profile of LWC but with the same LWP. These cloud layer optical property profiles were referred to as cloud layers 1, 2, and 3. They were constructed in the same manner as cloud layers optical property profiles A and B (see chapter IV). We chose their thickness and altitude to crudely match the observed thickness and altitude of the J25acs. Their geometric thickness was specified to be 300 m and each layer was positioned between 5700 and 6000 m in the McClatchey midlatitude summer atmosphere. The effective radius and the effective radius variance of each layer were set at 6.38 μm and 0.11, respectively. These values were chosen because they are representative of the mean values computed from all FSSP measured droplet size distributions collected during J25 experiment and are therefore also representative of conditions within an observed Ac cloud system. Figure 3.1 shows the LWC profiles for cloud layers 1, 2, and 3. Within cloud layer 1, the LWC increases linearly from 0.0 g m^{-3} at cloud base to 0.1 g m^{-3} at cloud top. Within cloud layer 3, the LWC decreases linearly from 0.1 g m^{-3} at cloud base to 0.0 g m^{-3} at cloud top. Within cloud layer 2, the LWC is constant with height at 0.05 g m^{-3}. Since each cloud layer was specified to have the same LWP and the same droplet size distribution, the optical depth, asymmetry parameter, and single scatter albedo of each cloud layer were the same. Using the MIEAVG code, we computed the 10.2-12.5 μm optical depth, asymmetry parameter, and single scatter to be 1.69, 0.3717, and 0.77. The 0.2- 0.7 μm optical depth, asymmetry parameter, and single scatter albedo were computed to be 3.77, .9999, and .86. Since the cloud droplet size distribution was specified to be constant with height, the asymmetry parameter and single scatter albedo were also constant with height while the extinction coefficient was proportional to the LWC and therefore a linear function in height.

Cloud layer optical profiles 1,2 and 3 were used as input for the SHDOM radiative transfer model. The boundary conditions and the solar zenith angle were specified to be the same as those used for simulations in cloud layer profiles A, B, BA and D. Solar and thermal heating rate profiles and the net radiative properties were computed. Since the optical properties of each cloud layer were the same (the exception being their vertical profiles of extinction), we attributed differences in their simulated structures to be a consequence differences in the shapes of their extinction profile. Results from these simulations and the differences between them are discussed in the following section.

Results

Fig. G.2 shows the thermal radiative heating rate profile for cloud layers 1,2 and 3. Each thermal heating rate profile shows cloud base warming and cloud top cooling. Thus, each cloud layer is absorbing thermal radiation emitted by the warmer atmosphere and lower boundary below while emitting thermal

radiation towards the colder atmosphere aloft. Their are differences in the shape of each profile. The cloud layer 1 profile shows a gradual increase in heating at the base of the layer and then a rapid transition towards cooling in the upper portions of the layer. The depth over which heating and cooling rates occur are nearly the same. The maximum cooling rate is at the top of the layer, while the maximum heating rate is positioned 80 m above cloud base. Relative to the other profiles, cloud layer 1 exhibits the largest maximum cooling rate. The cloud layer 2 profile shows a maximum heating rate at its base with a transition towards cooling rates in the upper portion of the layer. The maximum cooling rate is at cloud top. The depth over which cooling occurs is larger than the depth over which warming occurs. Cloud layer 3 shows a maximum heating rate at cloud base and a rapid transition from heating towards cooling above that level. The depth over which cooling occurs is larger than the depth over which heating occurs. Cloud layer 3 shows the largest maximum heating rate. Through comparisons of each profile, we see that the position and magnitude of the maximum thermal cooling and heating rate depends on the gradient of the extinction at the cloud boundary. A larger gradient in extinction leads to a larger maximum value, and this value is positioned at the boundary of the layer. A smaller gradient in the extinction leads to smaller maximum value, and it is positioned inside the cloud layer.

Fig. G.3 shows the solar radiative heating rate profile for cloud layers 1,2 and 3. Since each profile shows heating, each cloud layer is absorbing solar radiation throughout its depth. The difference in the shape of each profile are a result of the difference in the extinction profile of each layer. In cloud layers 1 and 2, the heating rate increases with height and reaches the maximum value just below the top of the layer. The heating rate decreases with height and reaches a maximum value just above cloud base within profile 3. A comparison of the shape of each profile shows that the position and magnitude of the maximum solar heating rate is dependent on the gradient in the extinction at cloud top. A larger gradient in extinction leads to a larger maximum value and it is positioned at the cloud top. A smaller gradient in extinction leads to a smaller maximum value and it is positioned below the cloud top.

Table G.1 shows the net thermal and solar heating rate parameters computed for each cloud layer (Appendix F shows how each parameter was computed). Because each net thermal cloud layer heating rate is negative, this means that each cloud layer is emitting more thermal radiation than it is absorbing. The net thermal cloud top cooling rates and cloud base heating rates show that the net thermal cooling rate distributed over the layer is a factor of three larger than the net thermal heating distributed over the layer. Notice that the net effect of solar radiation, for these simulations, is to reduce the net cooling rate of the layer by roughly a factor of two. The differences in the net heating rates are less than .05 C hr^{-1}. Since these differences are small, we conclude that the simulated net cloud layer thermal and solar heating rates are insensitive to the vertical profile of extinction. Apparently, changes in the vertical profile of extinction merely act to redistribute the cooling and or heating rates over a different depth within the layer. Because the solar albedo and the transmission of each layer are the same we also conclude that these parameters are insensitive to the vertical profile of the extinction.

G.2 Changes in the LWP

Methodology

To examine the effect of changes in the LWP on the simulated thermal and solar radiative structure of altocumulus like cloud layers, we made use of the same cloud layer profiles (1,2, and 3) from the previous study. Simulations were performed in each layer where its LWP was scaled by constant factor ranging between 0.05 and 8.0 (no changes were made in the shape of the LWC profile). The results from each simulation were identified by the factor used to scale the LWP. Because scaling the LWP profile of each cloud layer scaled its optical depth, we attributed changes in the simulated radiative structure of each layer to be a consequence of changes in its optical depth. The results from these simulations are examined in the following section.

Results

Fig. G.4, G.5 and G.6 contain the thermal and solar heating rate profiles for the 0.05xLWP-8.0xLWP simulations within cloud layers 1, 2 and 3, respectively. The 8.0xLWP simulation profile for cloud layer 1is not shown because the maximum thermal cloud top cooling were so large that, when plotted, it was difficult to visualize the relatively smaller differences within the other profiles. The heating

rate profiles are shown without reference to their corresponding LWP factor because the differences between each profiles are systematically related to the change in the LWP. A description of how the thermal and solar heating rate profiles changed as the LWP factor was changed for each cloud layer is provided below.

As the LWP was increased in cloud layer 1, we observed the following changes in the thermal and solar radiative heating rate profile. The maximum thermal cooling rate increased while the depth of the region of cooling decreased. The maximum thermal heating rate also increased and its position moved towards the base of the cloud. The region over which heating was shown increased and then remained constant. The solar heating rates increased in the upper portions of the layer. For each successive increase in the LWP, the depth of the region (in which the solar heating rate increased) became more shallow while the magnitude of the increase became larger.

As the LWP was increased in cloud layer 2, we observed similar changes as in cloud layer 1. The single exception was in the thermal heating rate profiles where continued increase in the LWP eventually resulted in a region in the middle of the layer which had zero net heating rate.

As the LWP was increased within cloud layer 3, the following changes were observed in the thermal and solar heating rate profile. The maximum thermal cooling rate increased, moved towards higher levels in the cloud, and the depth of the region of cooling became more shallow. The maximum thermal heating rate increased and the depth of the region of heating became more confined towards the base of the layer. For smaller LWPs, the solar heating rates increased near the base of the layer. For progressively larger LWPs, the maximum solar heating rate moved towards the middle and upper potions of the layer while the heating rates near the base of the layer decreased slightly.

Fig. G.7 show the net cloud layer heating rate parameters and the maximum thermal and solar radiative heating rates for cloud layers 1,2, and 3 as a function of the LWP. For a particular LWP, the net thermal heating rates are virtually the same within each cloud layer. Thus, the simulated net layer thermal heating rates are insensitive to the LWC profile (extinction profile) regardless of the LWP (optical depth). However, the net thermal heating rates for each cloud layer are sensitive to the value of the LWP, and this sensitivity depends on the value of the LWP itself. For the net thermal cloud layer heating rate, the largest sensitivity is for LWPs less than 15 g m^2 (10.2 -12.5 μm optical depths less than 1.92). In this range, increase in the LWP results in a rapid increase in cooling. There is relatively little change in the net layer thermal heating rate for LWPs greater than 30 g m^2 (10.2 -12.5 μm optical depths less than 3.83). In the case of the net thermal cloud top cooling and cloud base warming rates, the largest sensitivities are for LWPs less than 30 g m^{-2}. Beyond this value, the heating rates show a more gradual change up to 60 g m^{-2} and then little change beyond that value. Focusing on the maximum thermal cooling rates and heating rates, we see that they increase linearly with increase in the LWP and are largest for profiles with the largest gradient in the extinction at cloud top. In the case of the maximum thermal heating rate, we see that they also increase linearly and are largest for the profile with the largest gradient in the extinction at cloud base.

We explain the trends in the net thermal radiative properties of each layer as follows. As the LWP of each layer is increased, the cloud layer emissivity approaches the limiting value of unity (the blackbody limit). Approaching this limit, the cloud layer emits and absorbs the maximum possible amount of thermal radiation. Further increase in the amount of absorbing material (i.e. LWP) can not increase the emissivity of the layer past unity. Therefore, the net cloud layer heating rate, the net cloud top cooling rate, and the net thermal cloud base heating rate approach fixed values.

Fig. G.8 shows the net cloud layer and maximum solar heating rate for cloud layers 1,2, and 3 as a function of the LWP. We see that, for a particular LWP, the net layer solar heating rate is virtually the same for each cloud layer. Thus, we conclude that for the simulated net solar heating rate are insensitive to the profile of LWC (extinction) regardless of the LWP (optical depth). The net solar heating rate shows the largest sensitivity for LWPs between 0.75 g m^2 and 30 g m^2. Within this range, the net solar heating rate increase from 0.25 to 1.09 C hr^{-1}. Beyond this range, the increase is more gradual and appears to asymptote towards a fixed value.

We explain the relationship between the net layer solar heating rate and LWP as follows. As the LWP in each cloud layer is increased, their optical depth due to absorption is also increased. The increase in the absorption results in an increased heating rate for the layer. We should expect that at some limit the amount of solar radiation available for absorption by the cloud layer will be completely depleted. At this

point, further increase in the LWP (extinction) should not lead to a further increase in absorption; hence, the heating rate will approach a fixed value. The trend in the heating rate profile shows this asymptotic approach.

G.3 Changes Due To the Presence of Upper and Lower Cloud Layers

Methodology

The change in the simulated radiative structure of an altocumulus like cloud layer due to the presence of an additional cloud layer situated above or below this layer was examined by considering two multiple cloud layer profiles: 2u and 2b. In multiple cloud profile 2u, a cloud layer with the same geometric thickness and optical properties as cloud layer 2 was positioned with its base 500 m above the top of cloud layer 2. In multiple cloud profile 2b, a cloud layer with the same optical properties as cloud layer 2 was positioned with its top 500 m below the base of cloud layer 2. These distances were chosen to correspond roughly with the spacing between cloud layers observed in the J25 experiment. To assess the effect of changes in the LWP of the upper and lower cloud layers on the radiative heating rate properties of cloud layer 2, simulations were performed where the LWP of the upper and lower cloud layer was scaled by the same factors as in the previous study (0.05 - 8.00). The results from these simulations are presented and discussed in the next section.

Results

Figs. G.9 and G.10 respectively show the thermal and solar heating rate profiles of cloud layer 2 for simulations in multiple cloud profiles 2u and 2b where the LWP of the upper and lower cloud layers was scaled by constant factors between 0.05 and 8.00. The profiles are shown without reference to the LWP factor because the difference between each profile is systematically related to the change in the LWP. Our observations of how the heating rates in cloud layer 2 changed as the LWP of the upper or lower cloud was changed is given below.

For simulations in profile 2u, as the LWP of the upper layer was increased: the thermal cooling rates in the upper portions of layer 2 increased with the largest increase at cloud top and the solar heating rates at all point within the layer decreased. In simulations with LWP factors ≥ 4.00, the thermal heating rate profile showed no thermal cooling rates.

For simulations in profile 2b, as the LWP of the lower layer was increased: the thermal heating rates in the lower portions of layer 2 decreased with the largest decrease at cloud base while the solar heating rates in the lower portions increased with the largest increase at cloud base. In simulations with LWP factors $\geq$ 4.00, the thermal heating rate profile showed no thermal heating rates.

We explain the observed changes in the heating rate of cloud layer 2 as follows. In the case of multiple cloud profile 2u, the upper cloud layer emits thermal radiation downwards from its base, some of which arrives at the top of cloud layer 2. As the LWP, i.e optical depth, of the upper layer is increased, the amount of downwelling radiation is increased (due to the increased emissivity of the upper layer) . The increased downwelling flux reduces the net flux divergence in the upper portions of layer 2 and hence the cooling rates in these regions are also reduced. The upper cloud layer also absorbs, reflects and transmits solar radiation. Some of this transmitted radiation arrives at the top of cloud layer 2 and may then be absorbed by this layer. As the LWP of the upper layer is increased, the amount of solar radiation available for absorption by cloud layer 2 is reduced due to absorption and reflection by the upper layer. This reduction results in lower heating rates in layer 2.

In the case of the multiple cloud layer profile 2b, the lower cloud layer absorbs upwelling thermal radiation from below, emits thermal radiation upwards from its top, and reflects a certain amount of solar radiation back into layer 2. As the LWP, i.e. optical depth, of the lower cloud layer is increased, the amount of absorbed upwelling thermal radiation and reflected solar radiation by this layer both increase. This reduces the amount of upwelling thermal radiation (because the lower cloud layer tends to emit thermal radiation at its temperature which is colder than the lower boundary and atmosphere) and increases the amount of upwelling solar radiation at the base of layer 2. Thus, the thermal heating rates are decreased and the solar heating rates are increased.

Figs. G.11a, b, and c show the net thermal layer thermal heating, net thermal cloud top and net thermal cloud base heating rates, and the maximum thermal cooling and the maximum heating rates,

respectively, of cloud layer 2 as a function of the LWP factor for the upper cloud layer in simulation 2u and the lower cloud layer in simulation 2b. For simulations in profile 2u, Fig. G.11a shows the net layer thermal heating rate of cloud layer 2 to increase for LWP factors between .05 and 2.00 and asymptote towards a fixed value for LWP factors ≥ 2.00. For simulations in profile 2b, the net layer thermal heating rate of cloud layer 2 shows: cooling for the 0.05xLWP, a rapid transition towards heating for LWP factors between 0.05 and 2.00, and an asymptotic approach towards a fixed value for LWP factors ≥ 2.00.

We explain these results as follows. As the LWP factor of the upper or lower cloud layer is increased, the emissivity of each layer approaches the limiting value of unity and thus, each layer emits at its blackbody temperature. As discussed previously, the effect of the upper cloud layer is to increase the downwelling flux at the top of layer 2 and thus reduce the net flux divergence across the layer. Because there is a limit to the amount of downwelling flux which can be emitted by the upper layer, there is also a limit to the amount of downwelling flux which arrives at the top of layer 2 and thus a limit to the reduction in the net flux divergence of the layer. In the case of the lower layer, its effect is to reduce the upwelling radiation at the base of layer 2 and thus the net flux convergence across it. Because there is a limit to this reduction there is a limit in the reduction in heating.

Figs. G.12a and b show the net layer and maximum solar heating rates, respectively, of cloud layer 2 in simulations 2u and 2b as a function of the LWP factors for the upper and lower cloud layers. For simulations 2u, Fig. G.12a shows that the increase in the upper cloud layer LWP results in a decrease in the net solar heating rate of cloud layer 2. The largest change occurs for LWP factors between 0.05 and 2.00. A comparison with the net layer thermal heating rates for simulations 2u shows that the decrease in solar heating is offset by a larger increase in thermal heating. Thus, the overall effect of a cloud layer positioned above cloud layer 2 is to increase the total heating rate of the layer. In the 4.00xLWP simulation, the increase in the net thermal + solar layer heating rate of layer 2 is roughly 1 C hr^{-1}.

In simulations 2b, the net solar heating rate increases slightly for LWP factors between 0.05 and 2.00, and shows little change beyond this value. The increase in the net solar heating rate is small as compared to the increase in the thermal cooling rate. Thus, the overall effect of a cloud positioned below cloud layer 2 is to increase the total cooling rate of the layer. In the 4.00xLWP simulation, the increase in the thermal+solar net cooling rate of the layer is roughly 0.8 C hr^{-1}.

G.4 Changes in the Effective Radius

Methodology

The effects of changes in the cloud droplet effective radius on the simulated thermal and solar heating rate structure of altocumulus like cloud layers was studied by changing the cloud droplet effective radius within cloud layer 2 while holding the LWP fixed. Simulations were performed where the cloud droplet radii was fixed at 4.0 and 8.0 μm and for LWP factors of 0.25,1.00 and 8.0. Values of 4.0 and 8.0 μm were chosen because they were roughly the minimum and maximum mean flight leg values encountered in the J25acs and are therefore representative of the possible range of values in this cloud.

Changes in the effective radius affect changes in the optical properties of the cloud layer. Table G.2 shows the 9.1-10.2 μm and 10.2-12.5 μm broadband optical properties of cloud layer 2(LWPx1.00) for the stated effective radii. Table G.3 shows the six solar broadband optical properties of cloud layer 1 (LWP x 1.00) for the stated effective radii. We used the optical properties computed from these bands, in the interpretation of results from this portion of the study. Examining table G.2, we see that in the thermal window portion of the spectrum and for equivalent LWPs, cloud layer 2 (r_e=4.0 μm) has a larger absorption optical depth than cloud layers 2 (r_e=6.4 and 8.0 μm). Examining table G.3, we see that for each of the solar bands and for equivalent LWPs, cloud layer 2 (r_e=4.0 μm) has: a larger or close to the same absorption optical depth and a larger single scatter albedo than cloud layers 2 (r_e=6.4 and 8.0 μm).

Results

Table G.4 shows the simulated net thermal and solar heating rate structure of cloud layer 2 with r_e=4.0, 6.38, 8.0 μm and for LWP factors of 0.25,1.00,and 8.00. The net thermal cloud layer heating rates show sensitivity towards changes in r_e for the 0.25xLWP simulation, but do not show sensitivity for the 1.00xLWP and 8.00xLWP. For the 0.25xLWP simulation, the net thermal cloud layer heating rate for cloud layer 2 (r_e=4 μm) are 0.1 C hr^{-1} larger than for cloud layer 2 (r_e=5.0 μm). The net thermal cloud top

and cloud base heating rates show sensitivity towards changes in r_e for both the 0.25xLWP and 1.00xLWP simulations but do not show sensitivity for the 8.00xLWP simulation. In the case of the 1.00xLWP simulation, cloud layer 2 (r_e=4 μm) is shown to have 0.2 C hr^{-1} larger net cloud top cooling rate and 0.15 C hr^{-1} larger cloud base heating rate than cloud layer 2 (r_e=8 μm).

A physical interpretation of these results is as follows. In the case of smaller LWPs (0.25xLWP and 1.00xLWP), the emissivity of each cloud layer (r_e=4.00, 6.38, 8.00 μm) is below unity, and since the absorption of thermal radiation by cloud layer 1 (r_e=4.0 μm) is a factor of two larger than that of cloud layer 2 (r_e=8.0 μm), the emissivity of the former layer is also larger. The larger emissivity of cloud layer 1 (r_e=4.0 μm) results in larger net cloud layer cooling rates, net cloud base heating rates and net cloud top cooling rates. In the case of the 8.0xLWP, the emissivity of each cloud layer (r_e=4.00, 6.38, 8.00 μm) has approached the limiting value of unity; hence, the larger absorption of cloud layer 2 (r_e=4.0 μm) does not lead to an increase in emission.

Table G.4 shows the sensitivity of the net solar heating rate of cloud layer 2 towards changes in r_e to depend on the value of the LWP factor. For the 0.25xLWP and 1.00xLWP simulations, the net solar heating rates for cloud layer 2 (r_e=4.0 μm) are 0.15 and 0.16 C hr^{-1} larger than for cloud layer 2 (r_e=8.0 μm). For the 8.00xLWP simulation, the net solar heating rate for cloud layer 2 (r_e=8.0 μm) is 0.35 C hr^{-1} larger than for cloud layer 2 (r_e= 5.0 μm).

A physical explanation for these results is as follows. For the 0.25xLWP and 1.00xLWP simulations, the optical depths of each cloud layer 2 (r_e=4.0 and 8.0 μm) are relatively small. At these optical depths, photons which enter cloud layer 2 (r_e=4.0 μm) experience a larger number of scattering events (due to the larger number of cloud droplets) than those photons which enter cloud layer 2 (r_e=8.0 μm). The larger number of scattering events leads to larger probabilities that the photon will be absorbed before it is either transmitted through the layer or scattered back out the top of the layer. Those photons which enter cloud layer 2 experiencing a fewer number of scattering events and are forward scattered through cloud layer 2 without being absorbed. For the 8.00xLWP the optical depths of each cloud layer 2 (r_e=4.0 and 8.0 μm) are relatively large. At these optical depths, photons which enters cloud layer 2 (r_e=4.0 μm) experience a large number of scattering events (due to the larger number of droplets) in the upper portions of the layer. The large number of scattering events, in these portions, increase the probability of absorption there, but also increase the probability that a photon is scattered back out of the top of the layer. Being scattered out of the top of layer, this reduces the amount of absorption which may take place at lower levels in the layer. Photons which enter cloud layer 2 (r_e= 8.0 μm) also experience a large number of scattering events (due to the large number of drops) and hence have a large probability of being absorbed. However since the number of droplets is smaller than in cloud layer 2 (r_e= 4.0 μm), those droplets which are not absorbed will have a greater likelihood of being forward scattered further down into the layer. Being forward scattered into the layer they have a greater likelihood of being absorbed before they are eventually transmitted through the layer or scattered out of the top of the layer.

The above arguments are consistent with the larger maximum heating rate shown for layer 2 (r_e=4.0 μm). Since the maximum heating rates occur at the top of the layer , we expect the absorption at this level to be larger. Also notice that for the 8.00xLWP simulation, cloud layer 2 (r_e=4.0 μm) reflects more radiation than transmitted which physically means that a large number of photons are being scattered back out of the top of the layer and few photons are being transmitted further down where they may be absorbed.

Results of the Sensitivity Study

The results from our sensitivity study may be summarized as follows. The shape of the simulated thermal and solar heating rate profiles within Altocumulus like layer clouds were sensitive to both the liquid water profile and also the LWP. The net layer thermal and solar radiative heating rates were found to be relatively insensitive to the shape of the LWC profile but were sensitive to the LWP. The sensitivity was largest for small LWPs. The radiative effects of a cloud layer positioned 500 m above or below altocumulus like cloud layers was found to be substantial. The effects of changes in the drop size effective radius on the net thermal and solar heating rate properties of altocumulus-like clouds was found to depend on the LWP of the layer. For smaller LWPs, the cloud layer with r_e=4μm cooled thermally and heated due to absorption of solar radiation at a slightly greater rate than the cloud with r_e=8μm. For larger LWPs, the

net thermal cooling rate of each cloud layer (r_e=4.00, 6.38, and 8.00μm) was the same while the cloud with r_e=8.0 μm heated due to absorption of solar radiation at a greater rate.

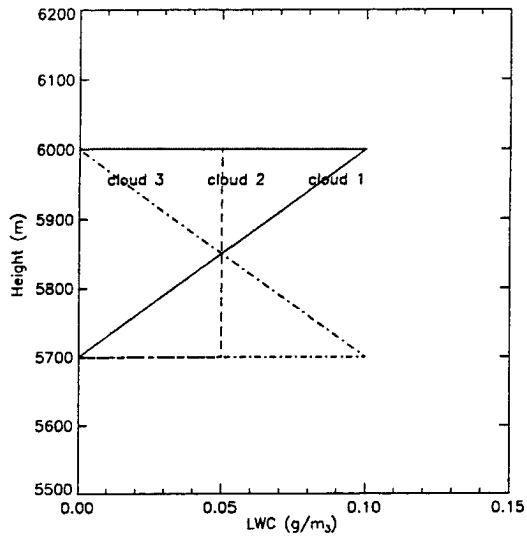

Figure G.1 Liquid water profiles of cloud layers 1, 2, and 3. Each profile has the same liquid water path at 15 g/m2.

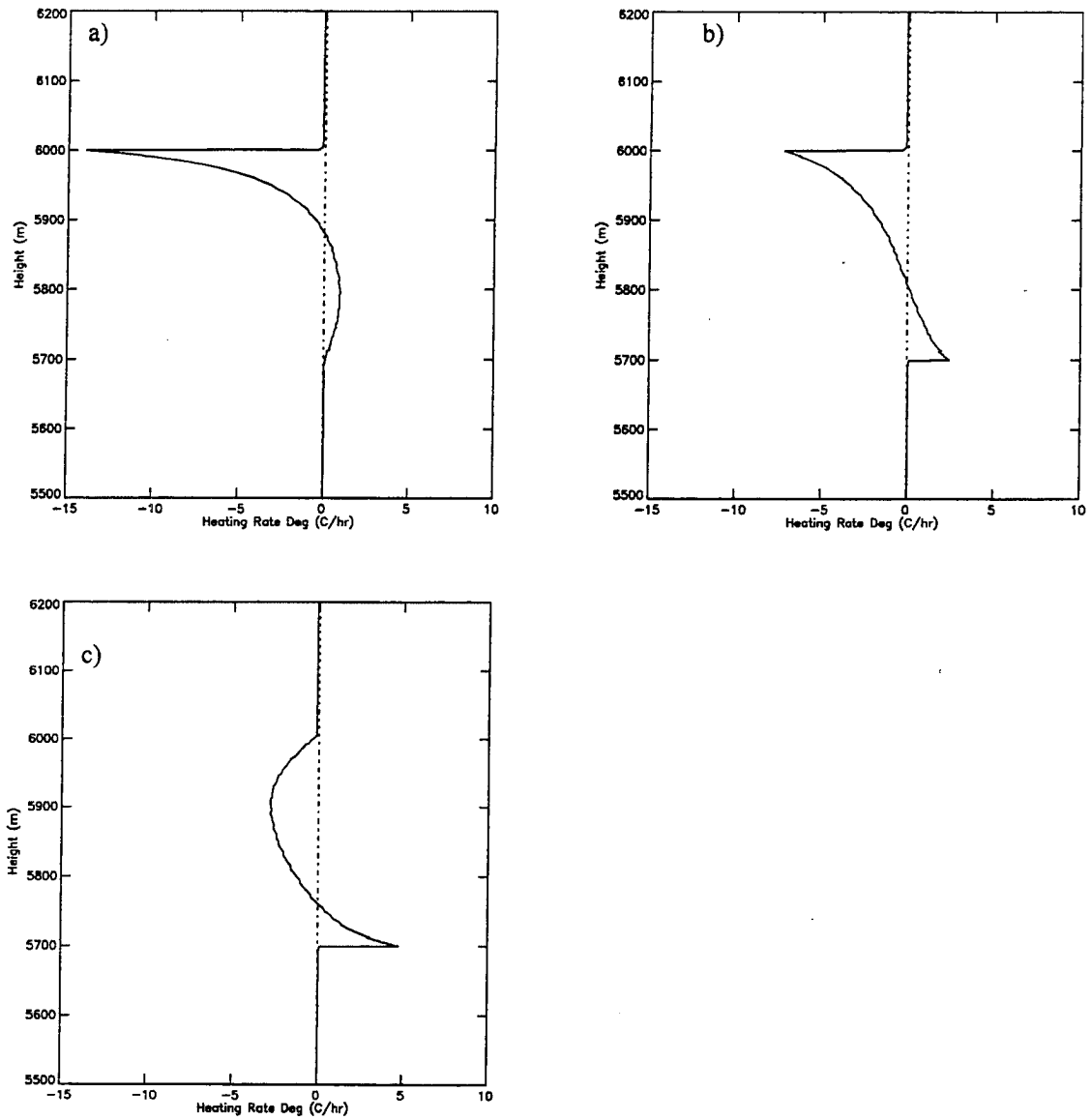

Figure G.2 Thermal radiative heating rate profiles for a) cloud profile 1, b) cloud profile 2, and c) cloud profile 3.

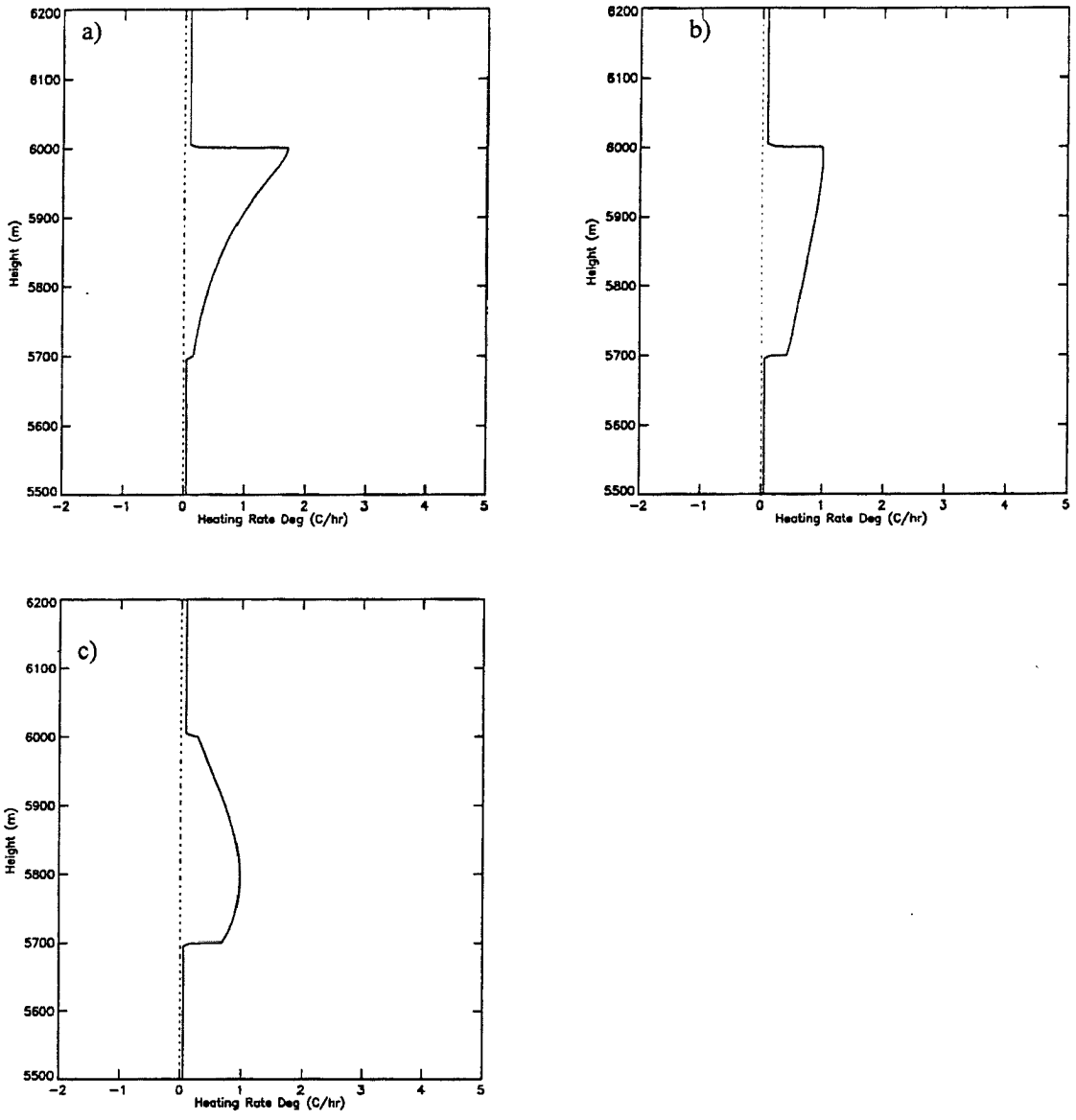

Figure G.3 Solar radiative heating rate profiles for a) cloud profile 1, b) cloud profile 2, and c) cloud profile 3.

Table G.1 Net Thermal and Solar Radiative Properties of Cloud Layers 1, 2, and 3.

	Cloud Layer1	Cloud Layer 2	Cloud Layer 3
Net Cloud Layer IR Heating Rate (C/hr)	-1.10	-1.13	-1.15
Net Cloud Top IR Cooling Rate (C/hr)	1.48	1.49	1.51
Net Cloud Base IR Warming Rate (C/hr)	0.38	0.36	0.36
Net layer solar heating Rate (C/hr)	0.65	0.66	0.65
Net Cloud Layer IR + Solar Heating Rate (C/hr)	-0.45	-0.47	-0.50
Cloud Layer Solar Albedo	0.25	0.25	0.25
Cloud Layer Solar Transmission	0.79	0.79	0.79

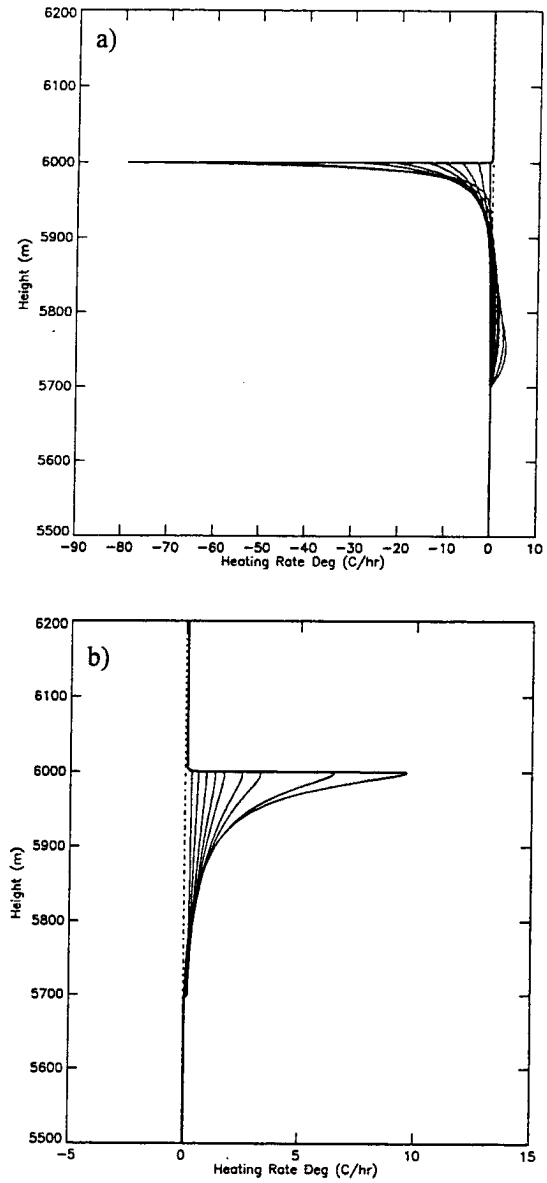

Figure G.4 a) Thermal and b) Solar radiative heating rate profiles for cloud layer 1 and for LWP factors between 0.05-6.0.

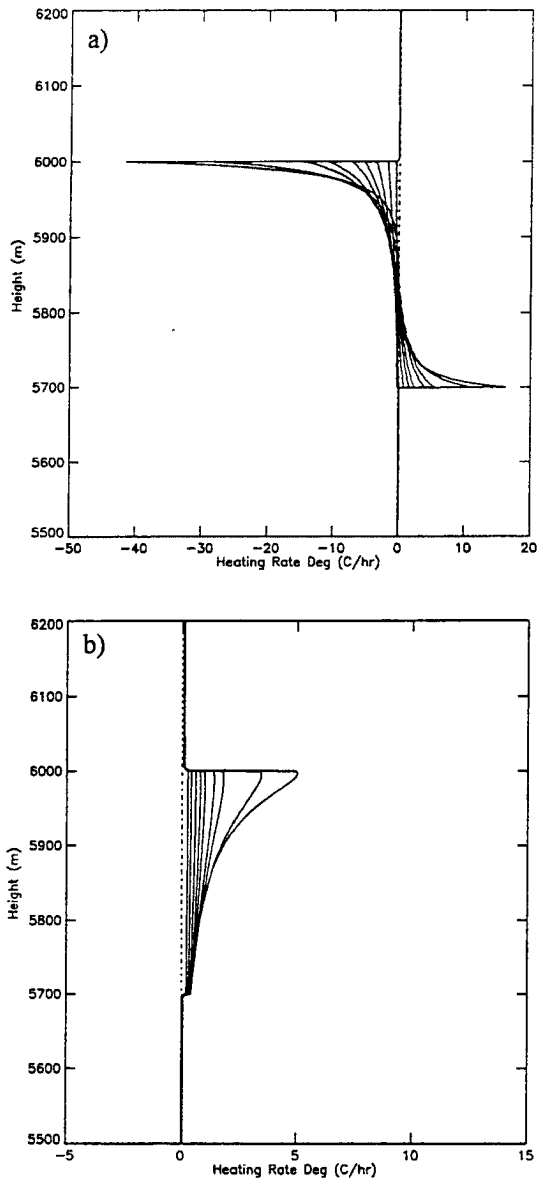

Figure G.5 a) Thermal and b) Solar radiative heating rate profiles for cloud layer 2 where LWP is modified by factors between 0.05 and 8.0.

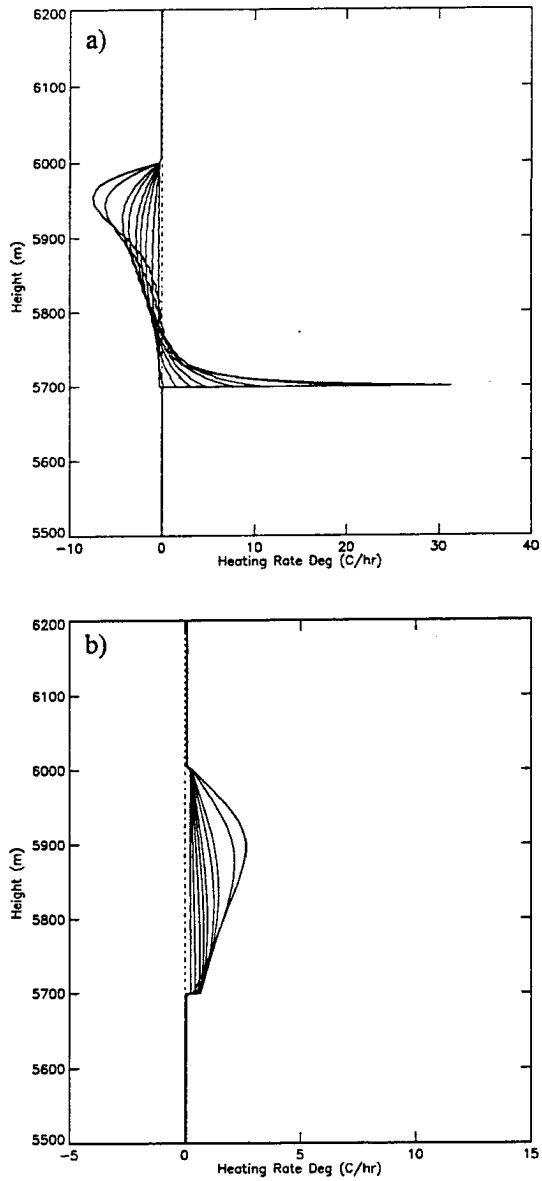

Figure G.6 a) Thermal and b) Solar radiative heating rate profiles for cloud layer 3 where LWP is modified by factors between 0.05 and 8.0.

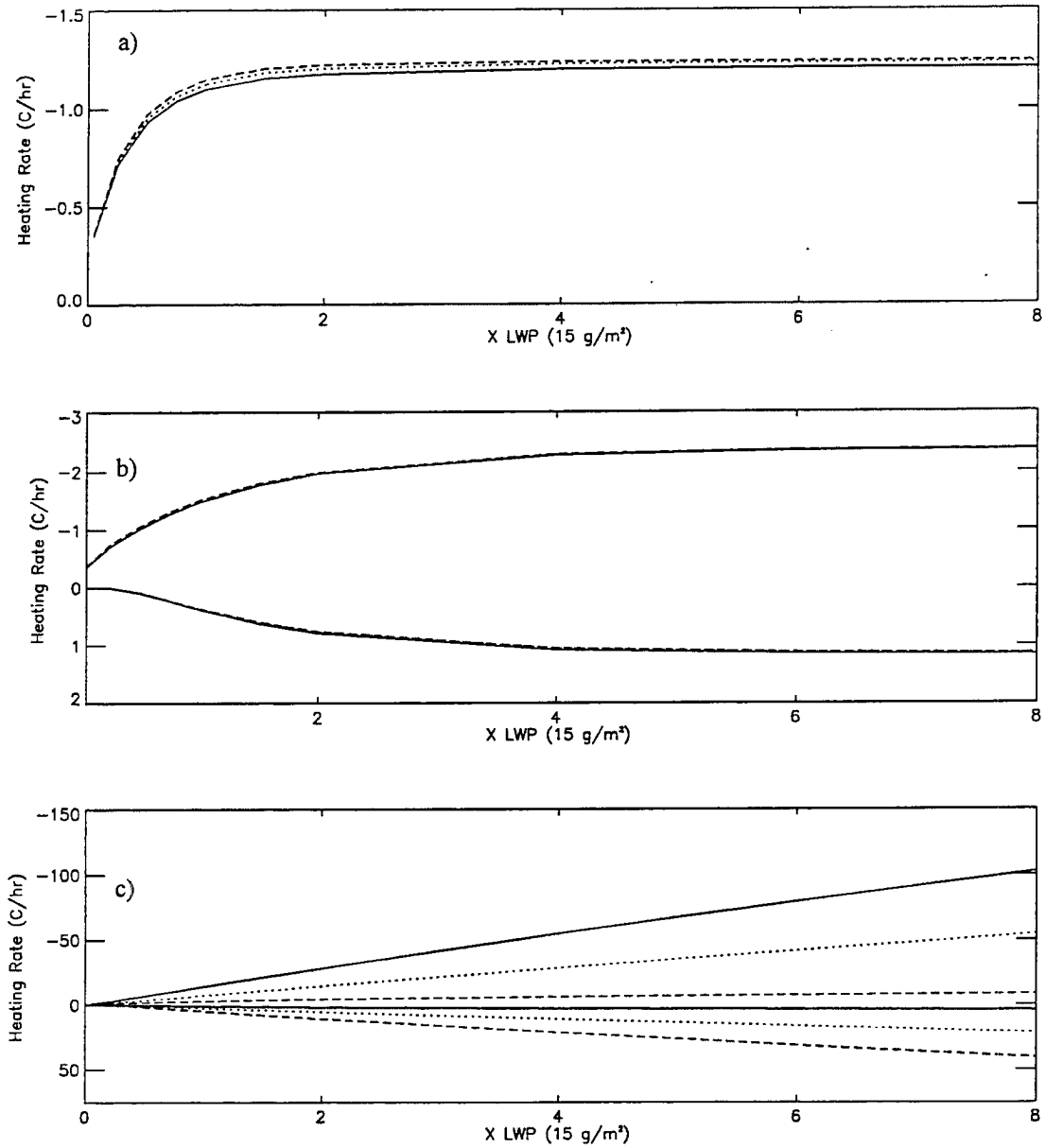

Figure G.7 a) Net layer thermal heating rate, b) Net thermal cloud top cooling rate (negative values) and net cloud base heating rate (positive values), and c) Maximum thermal cooling rates (negative values) and heating rates (positive values) as a function of the LWP for cloud layer 1 (solid line), cloud layer 2 (dashed line), and cloud layer 3 (dotted line).

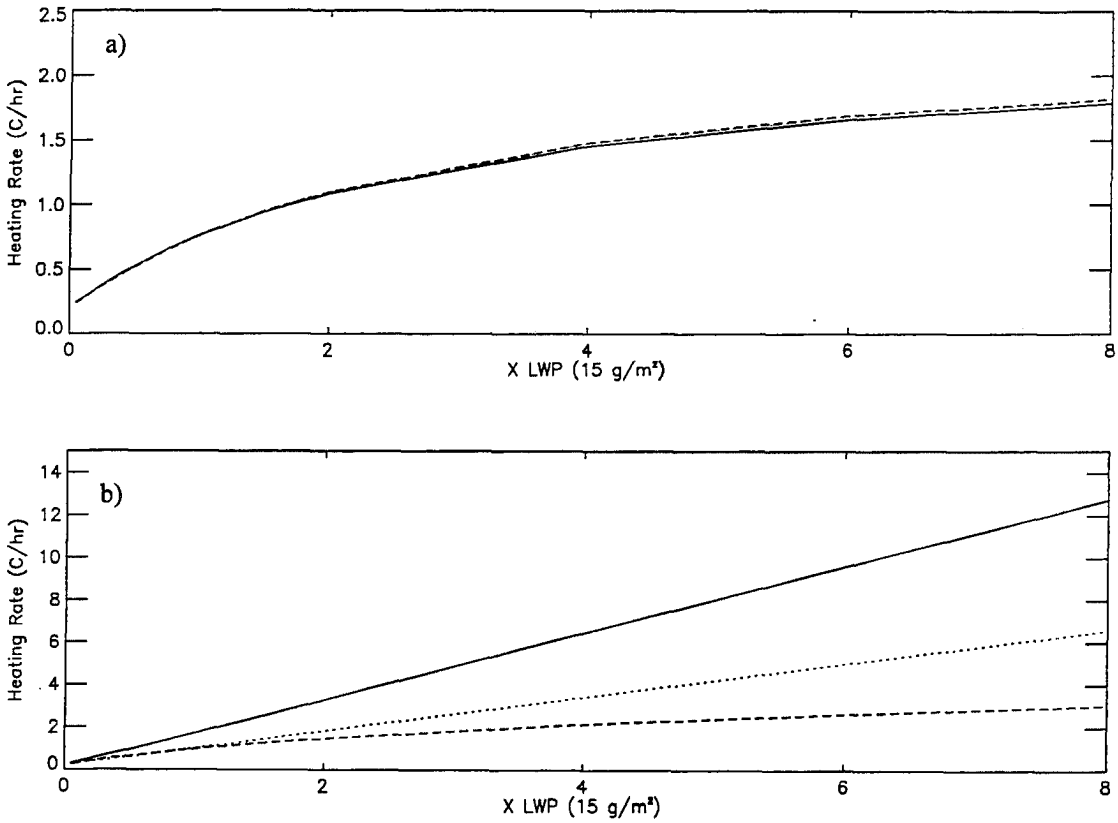

Figure G.8 a) Net layer solar heating rate and b) Maximum solar heating rate as a function of the LWP for cloud layer 1 (solid line), cloud layer 2 (dashed line), and cloud layer 3 (dotted line).

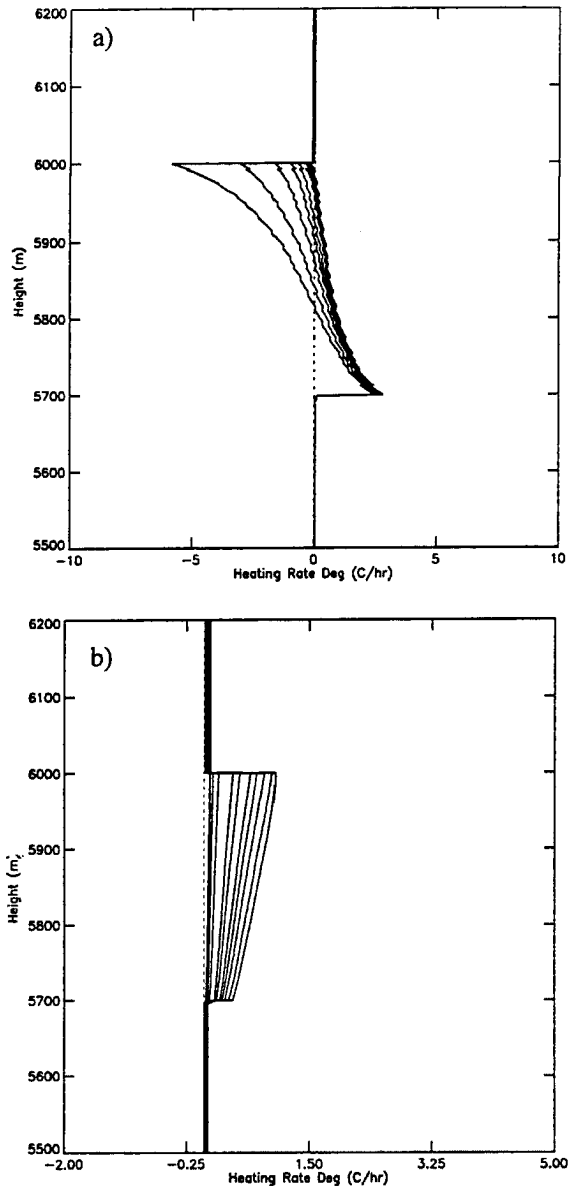

Figure G.9 a) Thermal and b) solar heating rate profiles of cloud layer 2 in simulations 2u where the LWP of upper cloud layer is modified by factors between 0.05 and 8.00.

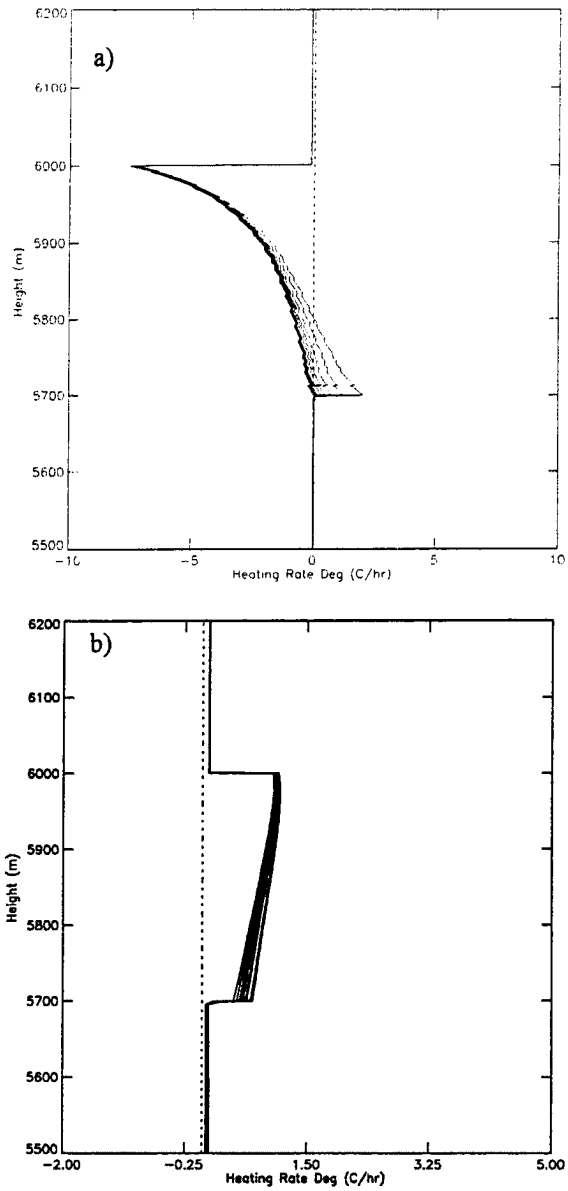

Figure G.10 a) Thermal and b) solar heating rate profiles of cloud layer 2 in simulations 2l where the LWP of lower cloud layer is increased by factors 0.05 between 8.00.

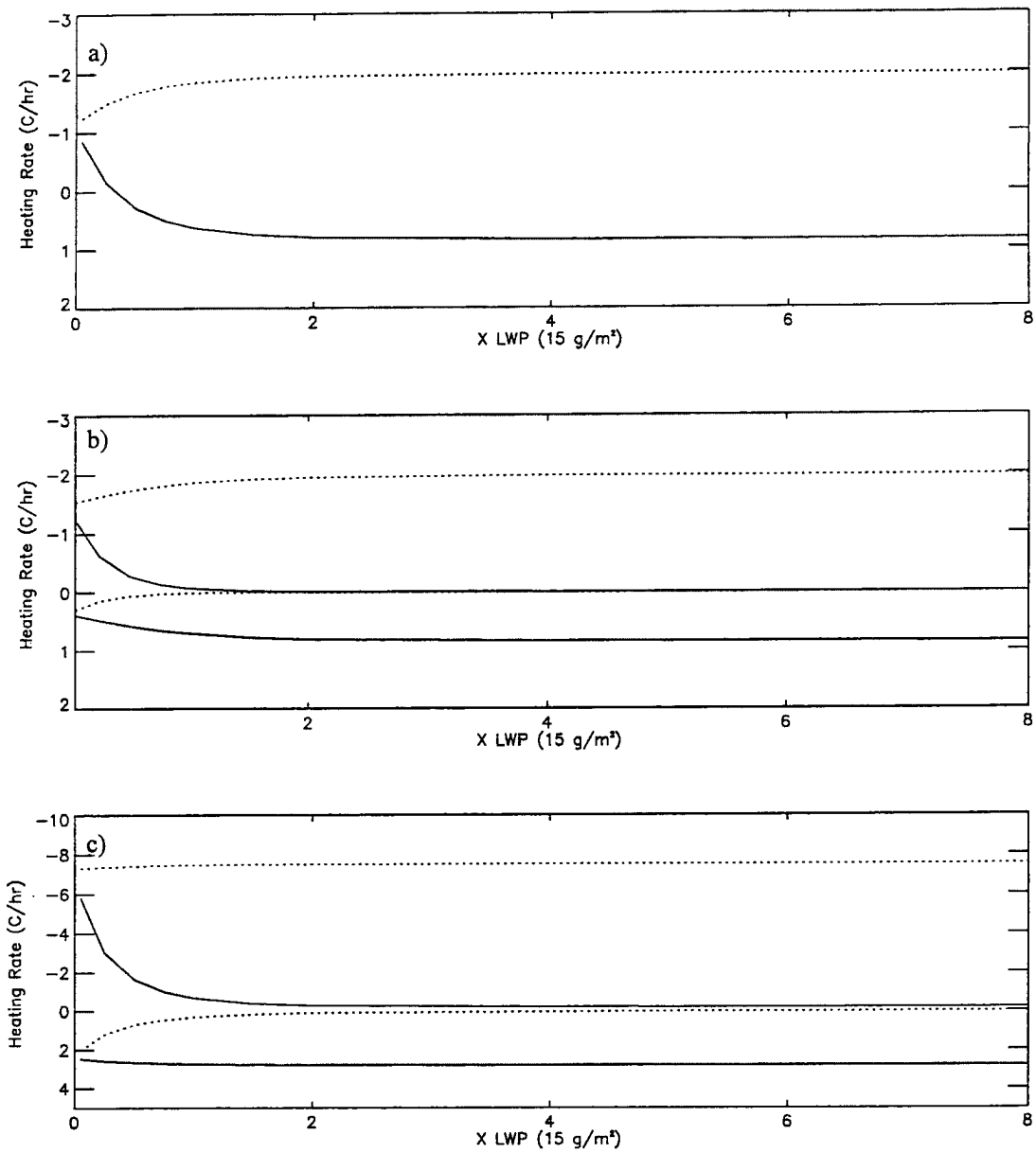

Figure G.11 a) Net layer thermal heating rate, b) Net thermal cloud top cooling rate (negative values) and net cloud base heating rate (positive values), and c) Maximum thermal cooling rates (negative values) and heating rates (positive values) for cloud layer 2 as a function of the LWP factor of the upper cloud layer in simulation 2u (solid line) and the lower cloud layer in simulation 2b (dashed line)

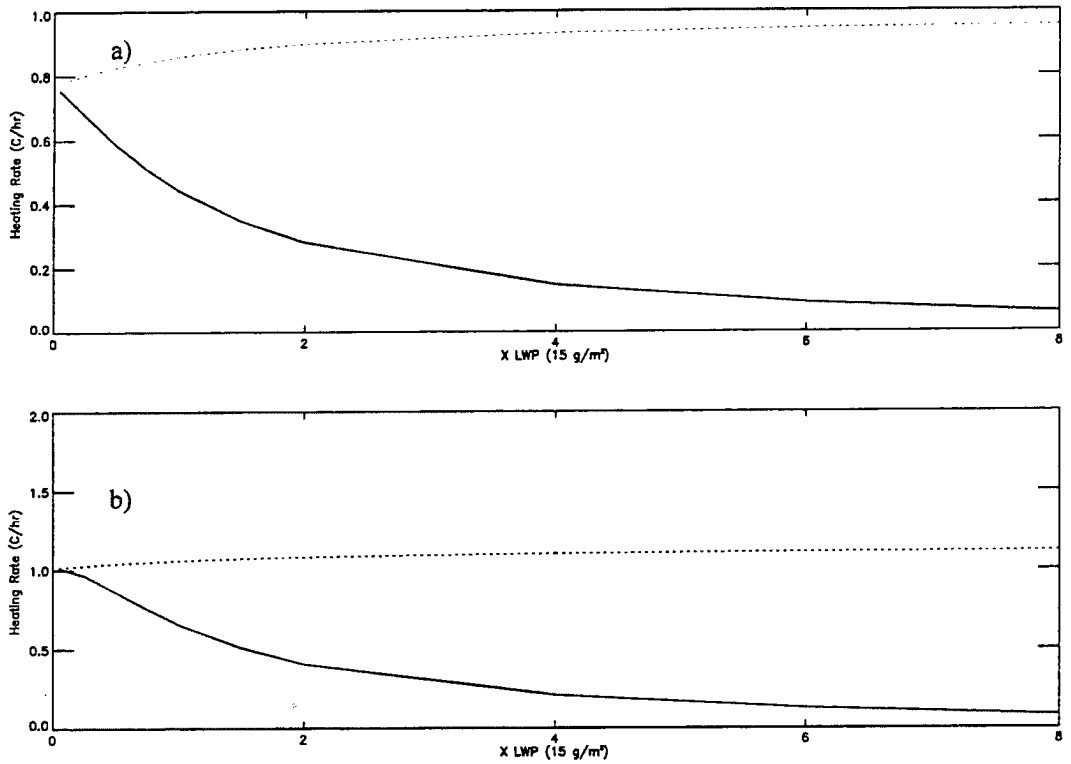

Figure G.12 a) Net layer solar heating rate and b) maximum solar heating rate of cloud layer 2 as a function of the LWP factor in the upper cloud layer for simulation 2u (solid line) and lower cloud layer for simulation 2b (dashed line).

Table G.2 Cloud layer 2 9.1-10.2 μm and 10.1-12.5 μm broad band optical properties for different values of r_e. Optical depth due to extinction (ode) and optical depth due to absorption (oda) corresponds to a LWP of 15 g m^2.

r_e (μm)	9.1-10.2 μm ode	oda	9.1-10.2 μm ϖ_0	9.1-10.2 μm g	10.2-12.5 μm ode	oda	10.2-12.5 μm ϖ_0	10.2-12.5 μm g
4.00	1.91	0.81	0.564	0.64	1.87	1.38	0.256	0.56
6.38	2.46	0.81	0.671	0.81	1.92	1.21	0.372	0.78
8.00	2.59	0.77	0.703	0.86	1.88	1.10	0.421	0.84

Table G.3 Cloud layer 2 solar broadband optical properties for r_e=4.0, 6.38, and 8.0 μm. Optical depth due to extinction (ode) and optical depth due to absorption (oda) computed for a LWP of 15 g m^2.
a)

r_e (μm)	0.2-0.7 μm ode	0.2-0.7 μm oda	0.2-0.7 μm ϖ_0	0.2-0.7 μm g	0.7-1.3 μm optical depth	0.7-1.3 μm	0.7-1.3 μm ϖ_0	0.7-1.3 μm g
4.00	6.14	0.00	0.999	0.84	6.42	0.00	0.999	0.81
6.38	3.77	0.00	0.999	0.85	3.89	0.00	0.999	0.83
8.00	2.96	0.00	0.999	0.86	3.04	0.00	0.999	0.84

b)

r_e (μm)	1.3-1.9 μm ode	1.3-1.9 μm oda	1.3-1.9 μm ϖ_0	1.3-1.9 μm g	1.9-2.5 μm ode	1.9-2.5 μm oda	1.9-2.5 μm ϖ_0	1.9-2.5 μm g
4.00	6.76	0.02	0.997	0.76	7.92	0.11	0.986	0.80
6.38	4.04	0.02	0.994	0.81	4.20	0.10	0.975	0.79
8.00	3.50	0.02	0.993	0.83	3.24	0.10	0.969	0.81

c)

r_e (μm)	2.5-3.5 μm ode	2.5-3.5 μm oda	2.5-3.5 μm ϖ_0	2.5-3.5 μm g	3.5-4.0 μm ode	3.5-4.0 μm oda	3.5-4.0 μm ϖ_0	3.5-4.0 μm g
4.00	7.79	2.16	0.723	0.89	9.85	0.34	0.965	0.81
6.38	4.37	1.32	0.698	0.88	4.54	0.34	0.925	0.72
8.00	3.31	1.04	0.685	0.89	3.41	0.32	0.905	0.74

Table G.4 Net thermal and solar radiative structure of cloud layer 2 with r_e=4.0, 6.38 and 8.0 μm and for LWP factors of 0.25, 1.00, and 8.00.

LWP Factor	0.25			1.00			8.00		
Cloud layer 2 r_e (μm)	4.00	6.38	8.00	4.00	6.38	8.00	4.00	6.38	8.00
Net Cloud Layer IR Heating Rate (C/hr)	-0.8	--0.7	-0.7	-1.2	-1.1	-1.1	-1.2	-1.2	-1.2
Net Cloud Top IR Cooling Rate (C/hr)	0.8	0.7	0.7	1.60	1.5	1.4	2.4	2.4	2.4
Net Cloud Base IR Warming Rate (C/hr)	0.0	0.0	0.0	0.5	0.4	0.3	1.4	1.4	1.4
Net Layer Solar Heating Rate (C/hr)	0.5	0.4	0.4	0.9	0.8	0.7	1.5	1.8	1.9
Maximum Solar Heating Rate (C/hr)	0.5	0.4	0.4	1.4	1.0	0.9	7.0	6.6	5.6
Cloud Layer Albedo	0.16	0.12	0.11	0.38	0.25	0.20	0.76	0.69	0.63
Cloud Layer Solar Transmission	0.90	0.95	0.96	0.64	0.79	0.84	0.11	0.24	0.31